

---

Doctoral Dissertations

Student Theses and Dissertations

---

Spring 2018

## Behavior and temporal-based effects of sustainable self-consolidating concrete in bridge structures

Hayder Hussein Alghazali

Follow this and additional works at: [https://scholarsmine.mst.edu/doctoral\\_dissertations](https://scholarsmine.mst.edu/doctoral_dissertations)



Part of the [Civil and Environmental Engineering Commons](#)

Department: Civil, Architectural and Environmental Engineering

---

### Recommended Citation

Alghazali, Hayder Hussein, "Behavior and temporal-based effects of sustainable self-consolidating concrete in bridge structures" (2018). *Doctoral Dissertations*. 2658.

[https://scholarsmine.mst.edu/doctoral\\_dissertations/2658](https://scholarsmine.mst.edu/doctoral_dissertations/2658)

This thesis is brought to you by Scholars' Mine, a service of the Missouri S&T Library and Learning Resources. This work is protected by U. S. Copyright Law. Unauthorized use including reproduction for redistribution requires the permission of the copyright holder. For more information, please contact [scholarsmine@mst.edu](mailto:scholarsmine@mst.edu).

BEHAVIOR AND TEMPORAL-BASED EFFECTS OF SUSTAINABLE SELF-  
CONSOLIDATING CONCRETE IN BRIDGE STRUCTURES

by

HAYDER HUSSEIN ALGHAZALI

A DISSERTATION

Presented to the Faculty of the Graduate School of the  
MISSOURI UNIVERSITY OF SCIENCE AND TECHNOLOGY

In Partial Fulfillment of the Requirements for the Degree

DOCTOR OF PHILOSOPHY

in

CIVIL ENGINEERING

2018

Approved by:

John J. Myers, Advisor  
Kamal H. Khayat  
Lesley H. Sneed  
Mohamed A. ElGawady  
VA Samaranayake

© 2018

Hayder Hussein Alghazali

All Rights Reserved

## **PUBLICATION DISSERTATION OPTION**

This dissertation consists of the following six articles that have been prepared for submitting for publication as follows:

Paper I (page 35-66), manuscript entitled “Performance Study of Ecological Self-Consolidating Cement Mixtures,” was published in the Journal of Materials in Civil Engineering by the American Society of Civil Engineering (ASCE). Paper II (page 67-96), manuscript entitled “Shear Behavior of Full-Scale High Volume Fly Ash-Self Consolidating Concrete (HVFA-SCC) Beams,” was published in the Journal of Construction and Building Materials by Elsevier. Paper III (page 97-125), manuscript entitled “Bond Performance of High Volume Fly Ash-Self Consolidating Concrete (HVFA-SCC) in Full-Scale Beams,” was prepared and submitted for publication in the ACI Structures Journals published by the American Concrete Institute (ACI). Paper IV (pages 126-156), manuscript entitled “Time-Dependent Prestress Loss Behavior of Girders in Missouri Bridge A7957 Compared with a U.S. Data Set of High Performance Concrete Bridge Girders,” was published in the Precast/Prestressed Concrete Institute (PCI) Journal. Paper V (pages 157-178), entitled “Uniform Thermal Behavior of High Strength-Self Consolidating Concrete Bridge Girders (Field Study),” was prepared and published in the Transportation Research Board Annual Convention-2018. It was presented and published in the proceedings. Paper VI (pages 179-199), entitled “Thermal Gradients and Their Effects on High Strength-Self Consolidating Concrete Bridge Girders,” was prepared to the Precast/Prestressed Concrete Bridge Convention in 2018. It was presented at the convention and published in the proceedings. Appendices A, B, C, D, E and F have been added to supplement this work.

## ABSTRACT

The main objective of this study was to investigate the performance of sustainable self-consolidating concrete (SCC) for highway bridge structures. Two types of concrete were utilized in this study: high volume fly ash-self consolidating concrete (HVFA-SCC) and high strength-self consolidating concrete (HS-SCC). This dissertation consists of two major parts: a laboratory study developing and investigating the overall performance of HVFA-SCC and a field study of time-dependent field-based behavior of HS-SCC in Bridge A7957 MO, USA. In the first part, an experimental program was conducted to develop a new class of SCC incorporating up to 70% cement replacement with fly ash. Three replacement levels (50%, 60%, and 70%) by weight were selected to quantify the effect of cement replacement on the structural performance of HVFA-SCC. Shear behavior and bond performance of HVFA-SCC were investigated in the laboratory. The shear behavior program consisted of twelve full-scale beams, and the bond performance program consisted of twelve full-scale splice test specimens. Analysis of the HVFA-SCC data indicated that concrete with up to 70% cement replacement can be considered for the production of sustainable SCC. The second part of this dissertation presents the total prestress losses and thermal behavior of Bridge A7957 constructed with HS-SCC. A health monitoring system was established on this bridge to monitor the time-dependent behavior of bridge girders using VWSGs and a data acquisition system. HS-SCC girders were monitored for more than two years' worth of field-based data. Both measured prestress losses and thermal data (uniform temperature and thermal gradients) were compared to the current design specifications. Results showed that the investigated specifications require some modifications to accommodate the material composition of HS-SCC.

## ACKNOWLEDGMENTS

Nothing can be accomplished alone, so here I would like to extend a sincere thank you to those who without their support and patience during the completion of this work, I would never have completed my work. To my mentor and advisor, Professor John J. Myers for years of guidance, advice, and inspiration. Words are powerless to express my gratitude. I highly appreciate him for all that he taught me and without a doubt he is one of my best friends. I would like to express my sincere gratitude and appreciation to my advisory committee members: Dr. Kamal H. Khayat, Dr. Lesley H. Sneed, Dr. Mohamed ElGawady, and V. D. Samaranayake for their kind contributions and their suggestions that greatly added to the quality of the final product. A special thank you goes to my sponsor HCED-Iraq and the Iraqi government for supporting me and my family during the years of study. A very special thanks to John Bullock and Mike Lusher for acting as my lab mentors and assisting me with my research no matter when I asked or what I asked them to do. I always consider them as best friends. I would like also to thank Gary Abbot, Greg Leckrone, Jason Cox, and Brian Swift for their hard work and crucial assistance during construction and testing of the specimens. Many thanks to my wonderful colleagues Zuhair Al-Jaberi, Zena Al-Jazaeri, Eli Hernandez, Saipavan Rallabhan, Valter Gora, Wei Wang, Michael Janke, and Alex Griffin. It has been a pleasure getting to know these fellow students throughout my study. Also, I would to thank Emily Seals for her effort to edit my dissertation. I would like to express my everlasting love to my parents, sisters, and brothers for supporting me throughout my life. Without their unconditional love and guidance, I would not have become the man I am today. Dad and Mom, I love you so much. Last but not least, from all of my heart, I would like to express my sincere appreciation to my lovely wife and my children Ali, Noora, and Mohammed for giving me unconditional care and enlightening my life with their love.

## TABLE OF CONTENTS

	Page
PUBLICATION DISSERTATION OPTION .....	iii
ABSTRACT.....	iv
ACKNOWLEDGMENTS .....	v
LIST OF ILLUSTRATIONS.....	xi
LIST OF TABLES.....	xv
SECTION	
1. INTRODUCTION.....	1
1.1. PART 1: DEVELOPMENT AND INVESTIGATION THE OVERALL PERFORMANCE OF HVFA-SCC .....	1
1.1.1 Fly Ash .....	2
1.1.2 High Volume Fly Ash-Self Consolidating Concrete (HVFA-SCC).....	4
1.1.3 Shear Behavior .....	5
1.1.4 Bond Behavior .....	8
1.2. PART 2: TIME-DEPENDENT FIELD-BASED BEHAVIOR OF HS-SCC IN MISSOURI BRIDGE A7957 MO, USA.....	12
1.2.1 Bridge A7957 .....	14
1.2.2 Total Prestress Losses .....	18
1.2.3 Uniform Temperature .....	22
1.2.4 Thermal Gradients .....	26
2. RESEARCH OBJECTIVES.....	31
3. ORGANIZATION OF DISSERTATION.....	34
PAPER	
I. PERFORMANCE STUDY OF ECOLOGICAL SELF-CONSOLIDATING CEMENT MIXTURES.....	35
ABSTRACT.....	35
1. INTRODUCTION .....	36
2. EXPERIMENTAL PROGRAM .....	37
2.1. EXPERIMENTAL DESIGN.....	38
2.2. TESTS PROCEDURES .....	40
3. EXPERIMENTAL RESULTS AND DISCUSSION .....	42

3.1. EFFECT OF OVERALL REPLACEMENT LEVELS ON THE PERFORMANCE OF ECO-SCCM .....	42
3.2. EFFECT OF FLY ASH REPLACEMENT LEVELS ON THE PERFORMANCE OF ECO-SCCM .....	44
3.3 EFFECT OF ADDING HYDRATED LIME TO ECO-SCCM .....	46
4. STATISTICAL DATA ANALYSIS .....	47
5. CONCLUSIONS.....	49
ACKNOWLEDGMENTS .....	65
REFERENCES .....	65
II. SHEAR BEHAVIOR OF FULL-SCALE HIGH VOLUME FLY ASH-SELF CONSOLIDATING CONCRETE (HVFA-SCC) BEAMS .....	67
ABSTRACT.....	67
1. INTRODUCTION .....	68
2. RESEARCH SIGNIFICANT.....	70
3. EXPERIMENTAL WORK.....	70
3.1. MIX DESIGN.....	70
3.2. TEST BEAM DETAILS AND MATRIX.....	72
3.3. CASTING PROCEDURE AND CURING.....	72
3.4. INSTRUMENTATION AND TEST SETUP .....	73
3.5. TESTING PROCEDURE.....	73
4. EXPERIMENTAL RESULTS AND DISCUSSION .....	74
4.1. HVFA-SCC PROPERTY TEST RESULTS.....	74
4.2. COMPARISON TO CONVENTIONAL CONCRETE BEAMS .....	76
4.3. SHEAR DUCTILITY AND POST-DIAGONAL CRACKNG PERFORMANCE .....	77
4.4. LONGITUDINAL REINFORCEMENT STRAINS AND CRACK ANGLES .....	78
4.5. MODLING COMPARISON.....	79
4.6. COMPARISON WITH DATABASE.....	80
5. CONCLUSIONS AND RECOMMENDATIONS .....	80
ACKNOWLEDGEMENTS.....	94
REFERENCES .....	94



III. BOND PERFORMANCE OF HIGH VOLUME FLY ASH SELF- CONSOLIDATING CONCRETE (HVFA-SCC) IN FULL-SCALE BEAMS .....	97
ABSTRACT.....	97
1. INTRODUCTION .....	98
2. RESEARCH SIGNIFICANT.....	100
3. EXPERIMENTAL WORK.....	101
3.1 MIX DESIGN.....	101
3.2. BEAM SPLICE SPECIMEN DESIGN.....	103
3.3. CASTING PROCEDURE AND CURING.....	104
3.4. INSTRUMENTATION AND TEST SETUP .....	105
3.5. TESTING PROCEDURE.....	105
4. EXPERIMENTAL RESULTS AND DISCUSSION .....	106
4.1. GENERAL BEHAVIOR.....	106
4.2. CRACKING PATTERN AND MODE OF FAILURE.....	108
4.3. STRAIN AND STRESS BEHAVIOR OF STEEL REINFORCEMENT.....	108
4.4. STRENGTH INDEX AND DUCTILITY INDEX .....	109
4.5. COMPARISON HVFA-SCC TEST RESULTS WITH COLLECTED DATABASE .....	110
5. CONCLUSIONS AND RECOMMENDATIONS .....	111
ACKNOWLEDGMENTS .....	123
REFERENCES .....	123
IV. TIME-DEPENDENT PRESTRESS LOSS BEHAVIOR OF GIRDERS IN MISSOURI BRIDGE A7957 COMPARED WITH A U.S. DATA SET OF HIGH-PERFORMANCE CONCRETE BRIDGE .....	126
ABSTRACT .....	126
1. INTRODUCTION .....	127
2. BRIDGE DESCRIPTION.....	130
3. MONITORING SYSTEM.....	132
3.1. VIBRATING WIRE STRAIN GAUGES .....	132
3.2. DATA ACQUISITION SYSTEM .....	132
4. MATERIAL PROPERTIES .....	133
5. PRESTRESS LOSSES .....	133

5.1. ELASTIC SHORTENING LOSSES.....	133
5.2. COMPARISON FOR TOTAL PRESTRESS LOSSES .....	136
5.3. COMPARISON WITH PREVIOUSLY COLLECTED DATA .....	138
6. CONCLUSION.....	140
ACKNOWLEDGEMENTS.....	153
REFERENCES .....	153
V. UNIFORM THERMAL BEHAVIORS OF HIGH STRENGTH-SELF CONSOLIDATING CONCRETE BRIDGE GIRDERS (FIELD STUDY) .....	157
ABSTRACT.....	157
1. INTRODUCTION .....	158
2. BRIDGE DETAILS .....	160
3. MONITORING SYSTEM.....	161
4. RESULTS AND DISCUSSIONS.....	163
5. CONCLUSIONS.....	165
ACKNOWLEDGEMENTS.....	176
REFERENCES .....	177
VI. THERMAL GRADIENTS AND THEIR EFFECTS ON HIGH STRENGTH-SELF CONSOLIDATING CONCRETE BRIDGE GIRDERS.....	179
ABSTRACT.....	179
1. INTRODUCTION .....	180
2. BRIDGE DESCRIPTION.....	182
3. MONITORING SYSTEM.....	184
3.1 MEASUREMENTS .....	184
3.2. VIBRIATING WIRE STRAIN GAUGES (VWSGS) .....	185
3.3. DATA ACQUISITION SYSTEM .....	185
4. RESULTS AND DISCUSSION .....	185
5. CONCLUSIONS.....	189
ACKNOWLEDGEMENT .....	197
REFERENCES .....	198
SECTION	
4. GENERAL CONCLUSIONS .....	200
4.1. PART 1.....	200

4.2. PART 2..... 203

APPENDICES

A. HARDENED PROPERTIES OF HVFA-SCC MIXES.....205

B. ADDITIONAL DETAILS OF SHEAR BEHAVIOR STUDY.....217

C. SHEAR DATABASE..... 231

D. ADDITIONAL DETAILS OF BOND BEHAVIOR STUDY.....249

E. PRESTRESS LOSSES DATABASE.....263

F. HEALTH MONITORING SYSTEM (PCI BIG BEAM).....270

REFERENCES ..... 281

VITA .....284

## LIST OF ILLUSTRATIONS

Figure	Page
1.1. Pozzolanic Reaction of Fly Ash .....	3
1.2. Components of Internal Shear Resistance .....	7
1.3. Proportions of Internal Shear Resistance Components .....	8
1.4. Forces Transfer Between Steel and Concrete .....	9
1.5. Pullout Test Specimen .....	10
1.6. Beam-End Specimen .....	11
1.7. Anchorage Beam Specimen .....	11
1.8. Splice Beam Specimen .....	12
1.9. Bridge A7957 Side View .....	14
1.10. Aerial View of the A7957 Bridge .....	14
1.11. Cross Section View of Bridge A 7957 .....	16
1.12. NU Bridge Girder Cross Section .....	17
1.13. Strand Layout of Spans 1 and 3 Girders .....	17
1.14. Strand Layout of Span 2 Girders .....	18
1.15. Bridge A7957 Numbering System .....	18
1.16. Stress vs. Time for PC/PS Bridge Girder .....	20
1.17. Contour Maps for $T_{MaxDesign}$ for Concrete Bridges .....	25
1.18. Contour Maps for $T_{MinDesign}$ for Concrete Bridges .....	25
1.19. Design Thermal Gradients Suggested by NCHRP Report 276 .....	29
1.20. Design Thermal Gradients Adopted by AASHTO LRFD-2012 Specifications .....	30
3.1. Organization of the Dissertation .....	34
PAPER I	
1. Day 3 compressive strength versus peak hydration temperature .....	54
2. Relation between compressive strength and surface resistivity .....	55
3. Compressive strength versus replacement levels .....	55
4. Drying shrinkage at different replacement levels .....	57
5. Comparison of surface resistivity of the three phases at different replacement levels .....	58
6. Relation between peak hydration temperatures under different replacement levels .....	59

7. Effect of hydrated lime dosages on compressive strength for different replacement levels .....	59
8. Effect of hydrated lime dosages on drying shrinkage for different replacement levels .....	61
9. Effect of hydrated lime dosages on surface resistivity for different replacement levels .....	62
10. Desirability-function graphs for the optimization of the Eco-SCCM within the design ranges: (a) Phase I; (b) Phase II; (c) Phase III .....	64

## PAPER II

1. Fine and coarse aggregates physical properties .....	87
2. Typical beam details without shear reinforcement at the test region and cross sections with different longitudinal reinforcement layouts .....	88
3. Test setup, instrumentation, and testing and failure mode of a beam specimen.....	88
4. Development of compressive strength with time of HVFA-SCC mixes beam test results.....	89
5. Crack profile at the ultimate shear force of test beams.....	90
6. Comparison of ultimate shear test results with conventional concrete.....	91
7. Comparison of normalized shear stresses of HVFA-SCC test results with CC .....	91
8. Shear force versus mid-span deflection .....	92
9. Comparison of shear ductility of the HVFA-SCC with CC .....	92
10. Comparison of PDCR of the HVFA-SCC with CC test results.....	93
11. Load-deflection responses of the beams (test and FEM).....	93
12. Normalized shear strength versus longitudinal reinforcement ratios; CC data from Ortega study .....	94

## PAPER III

1. Test beam details of HVFC-SCC specimens.....	118
2. Test setup, instrumentation, and testing and failure mode of a beam specimen.....	119
3. Crack pattern of the HVFA-SCC beams at bond failure. ....	120
4. Load vs. strain of the longitudinal reinforcement of HVFA-SCC beams.....	121
5. Comparison and proposed equation for bond strength for splice beam specimens with different concrete types. ....	122

## PAPER IV

1. Front and side views of bridge A7957 located on Highway 50 near Linn, MO.....	148
2. Cross-section view of Nebraska University 53 girder. ....	149
3. Comparison of total prestress losses. ....	150
4. Average total prestress losses... ..	151
5. Total measured prestress losses as a percentage of the nominal jacking stress versus various parameters. ....	151

## PAPER V

1. Bridge A7957 Cross Section.....	170
2. Bridge A7957 during the summer.....	171
3. VWSGs installation. ....	171
4. Equavelant layers with sensor locations. ....	172
5. Maximum daily temperature of interior girder (S2-G3). ....	172
6. Maximum daily temperature of exterior girder (S2-G4). ....	173
7. Minimum daily temperature of interior girder (S2-G3).....	173
8. Minimum daily temperature of exterior girder (S2-G4). ....	174
9. Average maximum and minimum monthly temperatures of interior girder (S2-G3). ....	174
10. Average maximum and minimum monthly temperatures of exterior girder (S2-G4). ....	175
11. Maximum ABT vs. average maximum ambient temperature in July.....	175
12. Minimum ABT vs. average minimum ambient temperature in January.....	176

## PAPER VI

1. Bridge A7957 cross section .....	191
2. Cross section view of NU 53 girder.....	191
3. The maximum and minimum ambient temperature.....	192
4. Bridge A 7957 during the summer.....	192
5. VWSGs installation .....	193
6. Typical heating behavior in interior girder (S2-G3) on a sunny summer day .....	193
7. Typical cooling behavior in interior girder (S2-G3) on a cloudy winter day .....	194

8. Typical heating behavior in exterior girder (S2-G4) on a sunny summer day .....	194
9. Typical cooling behavior in exterior girder (S2-G4) on a cloudy winter day .....	195
10. Positive and negative daily thermal gradients of interior girder (S2-G3).....	195
11. Positive and negative daily thermal gradients of exterior girder (S2-G4) .....	196
12. Design positive gradients and maximum measured positive gradients .....	196
13. Design negative gradients and maximum measured negative gradients .....	197

## LIST OF TABLES

Table	Page
1.1. Recommended Workability Values of SCC Used in PC/PS Applications .....	6
1.2. Summary of the Code Equations Used in the Prediction of Total Prestress Losses by Components (Pretensioned Member) .....	23
1.3. Temperature Ranges from AASHTO LRFD 2012, Procedure A .....	24
1.4. Correlation Between Concrete Bridge Temperatures and Normal Daily Temperatures.....	26
 PAPER I	
1. Mixture Proportion Combinations .....	51
2. Effect of Overall Replacement Levels on the Performance of Eco-SCCM.....	52
3. Effect of Hydrated Lime Dosages on Peak Hydration Temperature for Different Replacement Levels .....	53
4. Range of Key Factors and Responses for Desirability Function .....	53
 PAPER II	
1. Chemical and Physical Properties of Cementitious Materials .....	83
2. Materials Proportions of HVFA-SCC Beams.....	83
3. Test Matrix of HVFA-SCC Beams.....	84
4. Fresh Properties of HVFA-SCC Mixes .....	84
5. Summary of Experimental Results of the HVFA-SCC Beams .....	85
6. Ortega Test Results of Conventional Concrete .....	85
7. Comparison of Test Results with AASHTO LRFD Equations .....	86
8. Comparison of Measured and Predicted Shear Strength and Deflection.....	86
 PAPER III	
1. Chemical and physical properties of cementitious materials.....	113
2. Materials proportions of HVFA-SCC beams.....	114
3. Fresh properties of HVFA-SCC mixes.....	114
4. Geometrical and mechanical properties of reinforcing bars .....	115
5. Test matrix of HVFA-SCC beams .....	115



6. Specimen properties and test results .....	116
7. Longitudinal reinforcement strain and stress of HVFA-SCC beams.....	117
8. Strength and ductility indices of HVFA-SCC beams .....	117

#### PAPER IV

1. Concrete mixture proportions .....	142
2. Summary of fresh properties, tests, and results .....	143
3. Summary of mechanical properties, tests, and results .....	144
4. Elastic shortening losses of high-strength concrete .....	145
5. Elastic shortening losses of high-strength self-consolidating concrete .....	146
6. Elastic shortening losses of normal-strength self-consolidating concrete .....	147

#### PAPER V

1. HS-SCC Mixture Proportions.....	167
2. Weighted Values Implemented to Calculate ABTs .....	167
3. Maximum Temperature Values Recorded for Monitored Girders .....	168
4. Minimum Temperature Values Recorded for Monitored Girders .....	169
5. Comparison of Measured Temperatures and Design Temperatures .....	170

#### PAPER VI

1. HS-SCC mixture proportions.....	190
2. Maximum and minimum thermal gradients.....	190

## **1. INTRODUCTION**

Self-consolidating concrete (SCC) can offer several economic long-term benefits for the design and construction of highway bridge structures. SCC is a highly workable, non-segregating concrete that can spread and fill formworks under its own weight without external vibration. SCC's unique properties make it an attractive choice for optimizing site manpower by reducing labor and possibly skill level, equipment job noise, and time of construction (Daczko 2009). SCC was proposed in Japan in the early 1980s by Okamura and Colleagues at Tokyo University (Ozawa et al. 1989). The engineers at that time desired to achieve a durable concrete structure independent of the quality of construction work after a gradual reduction in the number of skilled workers in Japan's construction industry.

The use of SCC in the design and construction of bridge structures is anticipated to lead to both short-term and long-term cost savings. SCC allows construction workers to produce a concrete structure with a high degree of homogeneity and uniformity. These attractive benefits of using SCC are anticipated to result in lower life cycle costs due to longer structure service lives and reduced maintenance requirements. To produce SCC, adjustments to traditional mixes have to be conducted, specifically using higher paste contents, higher fines contents, and the use of smaller rounded aggregates. These modifications can alter and raise concerns regarding the structural implications of SCC in bridge structures.

### **1.1. PART 1: DEVELOPMENT AND INVESTIGATION THE OVERALL PERFORMANCE OF HVFA-SCC**

Cement is often considered an essential input into the production of concrete, which is a primary building material for the construction industry. Large demand for the

use of concrete to construct infrastructure buildings, roads, bridges, and dams has increased tremendously. Cement production is growing by 2.5% annually, and cement consumption is expected to reach 3.7-4.4 billion tons by 2050 (Benhelal et al. 2013, Rubenstein 2012). Cement production is also a key source of CO<sub>2</sub> emissions, due to the extreme heat required to produce it. Each ton of cement requires 4.7 million BTU (1,377 kwh) of energy and generates nearly 1 ton of CO<sub>2</sub>, which accounts for 5-7% of global CO<sub>2</sub> emissions (Damtoft et al. 2008). With growing demand of cement in use of new concrete infrastructure projects, the sustainability of concrete is a very real concern in the coming decades. One of the solutions for this concern is the use of supplementary cementitious materials, such as fly ash, as a replacement for cement.

**1.1.1. Fly Ash.** It is a by-product of the combustion of pulverized coal in electric power-generation plants. Fly ash exhibits pozzolanic properties and has the capacity to create cementitious components when combined with water. The source of fly ash and the design of coal-fired boilers could significantly affect the chemical composition of fly ash. ASTM C 618-17, “Standard Specification for Coal Fly Ash and Raw or Calcined Natural Pozzolan for Use in Concrete,” categorizes fly ash by the chemical composition. There are two classes of fly ash, low calcium fly ash (Class F) and high calcium fly ash (Class C). Class F fly ash is normally produced from the combustion of anthracite or bituminous coal. However, Class C fly ash is derived from sub-bituminous or lignitic coals. Fly ash can exhibit only pozzolanic properties such as Class F or pozzolanic and cementitious properties such as Class C fly ash (ACI 232-2R, 2003). Even though the Class C fly ash exhibits some cementitious properties, the main contribution to the hardened concrete properties results from the pozzolanic reaction of

fly ash with calcium hydroxide ( $\text{Ca}(\text{OH})_2$ ) as a result of the cement hydration. The fly ash pozzolanic reaction is summarized in Figure 1.1.

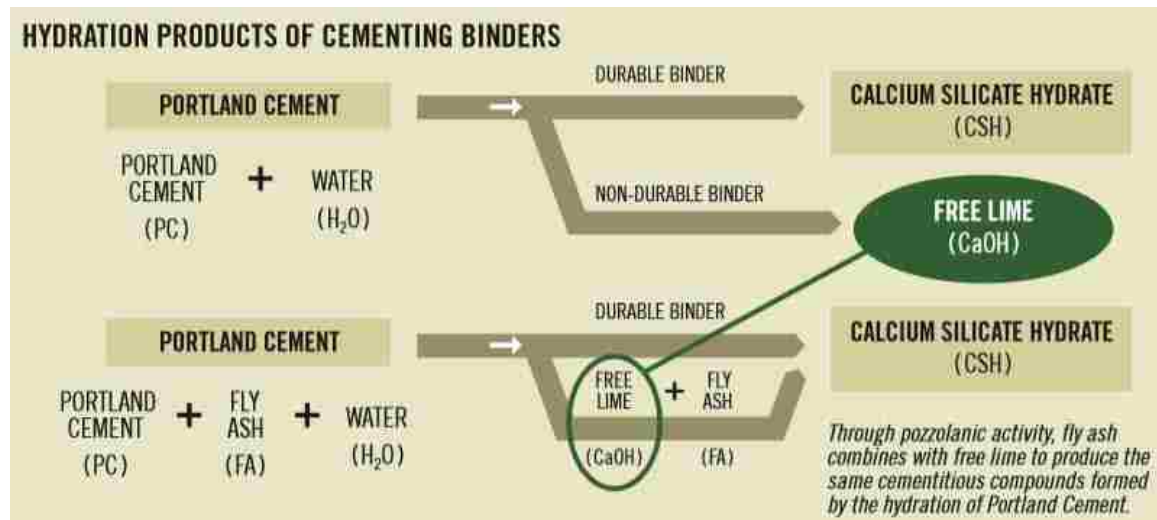


Figure 1.1. Pozzolanic Reaction of Fly Ash (Headwater Resources Tech Bulletin, 2017)

Currently, fly ash is used in some capacity in more than 50% of all ready-mixed concrete placed in the United States (Wilson and Kosmatka, 2011). When fly ash was originally used in concrete in the 1970s, there were some basic restrictions regarding its use. Typically, fly ash is added to structural concrete at 15-35% of the weight of the cement. Concrete with 50% or more of fly ash is generally considered to be high volume fly ash (ACI 232-2R, 2003). High volume fly ash (HVFA) concretes have been proposed as one potential method for reducing cement usage. This type of concrete offers a viable alternative to conventional concrete (concrete with 100% cement) and is significantly more sustainable. However, high fly ash content in concrete typically results in slow strength gains at an early age, delayed setting time, flash set, and sometimes the ultimate strength is reduced (Richardson et al. 2015, Headwater Resources Tech Bulletin, 2017). Consequently, current studies on HVFA concretes focus on increasing the limit of

substitution levels at which issues associated with high-level replacement can be successfully mitigated.

### **1.1.2. High Volume Fly Ash-Self Consolidating Concrete (HVFA-SCC).**

HVFA-SCC can be produced by combining HVFA up to 70% and self-consolidating rheology properties. The term HVFA-SCC may be defined as a new type of SCC developed within this research program that consists of carefully selected and proportioned materials, including a high amount of fly ash (up to 70% of the total cementitious materials) to produce durable, strong, and environmentally-friendly concrete. The HVFA-SCC should satisfy the following requirements:

- No evidence of segregation or settlement.
- Minimum 3-day compressive strength of 2,500 psi (17.5 MPa).
- Minimum 28-day compressive strength of 6,000 psi (42 MPa).
- Minimum durability factor of 75% based on Freeze-thaw test.

The target slump flow should be selected first in the mix design procedure. The table found in ACI 237R-11 can help with the selection of an appropriate slump flow target. For precast/prestressed applications, Table 1.1 Table 1 presents some slump flow test values as well as slump flow minus J-ring flow test values recommended by NCHRP 628 that are based on the intended application of SCC (Khayat and Mitchell 2009). HVFA-SCC was proposed to be used for highway bridge structures (superstructure and substructure) such as short-to-medium span girders, precast panels, columns, bents, walls, barriers, and abutments.

The modifications required in the mix design to produce a flowable, nonsegregating self-consolidating concrete raised concerns on the approach used to develop the particular mix design. A reduction in the coarse aggregate size and proportions combined with an increase in paste content can lead to increased creep and shrinkage, decreased bond strength and an interface shear transfer contribution to the concrete's shear strength. This leads to additional concerns when incorporating high content fly ash.

**1.1.3. Shear Behavior.** Typically, shear strength in reinforced concrete (RC) beams are affected by the tensile strength of concrete, longitudinal reinforcement, shear span to depth ratio ( $a/d$ ), axial forces, and the presence of transverse reinforcement. Two main concerns have been raised by engineers and designers regarding the SCC's shear strength. These concerns are the size, and content of coarse aggregates, which significantly affect the resistance to shear slip on the crack face. The aggregate size affects the amount of shear stress transferred across the crack's surface. Large diameter aggregates increase the roughness of the crack surface which allows higher shear stress to be transferred (Wight and MacGregor 2009). The cracks in SCC are likely to be smoother and more widely spaced than in conventional concrete, which could lead to decreased shear slip capacity and, thus, a smaller concrete contribution to shear strength. The inclined cracking load is considered to be equal to the inclined cracking shear. After propagating of inclined cracking, the shear strength of beams drops below the flexural capacity. Therefore, the web reinforcement is used to ensure that the full flexural capacity can be developed. In design practice, the concrete contribution to shear resistance is taken as the estimated shear force at inclined cracking for member without

Table 1.1. Recommended Workability Values of SCC Used in PC/PS Applications

Relative Values		Slump flow, in.			Slump flow –J-ring flow, in.		
		23.5-25	25-27.5	27.5-29	3-4	2-3	≤2
Low	Reinforcement density						
Medium							
High							
Small	Shape intricacy						
Moderate							
Congested							
Shallow	Depth						
Moderate							
Deep							
Short	Length						
Moderate							
Long							
Thin	Thickness						
Moderate							
Thick							
Low	Coarse Aggregate						
Medium							
High							

transverse. However, for members with transverse reinforcement, the nominal shear capacity has been taken as the sum of inclined cracking strength and the resistance provided by the web reinforcement (NCHRP-Report 579, 2007).

After inclined cracking occurs, the shear is resisted by several components: shear force carried by the uncracked concrete in the compression zone, interface shear transfer, the dowel action of the longitudinal reinforcement, and when applicable transverse reinforcement (stirrups) crossing the crack. These components are illustrated in Figure 1.2, with their average proportions in Figure 1.3.

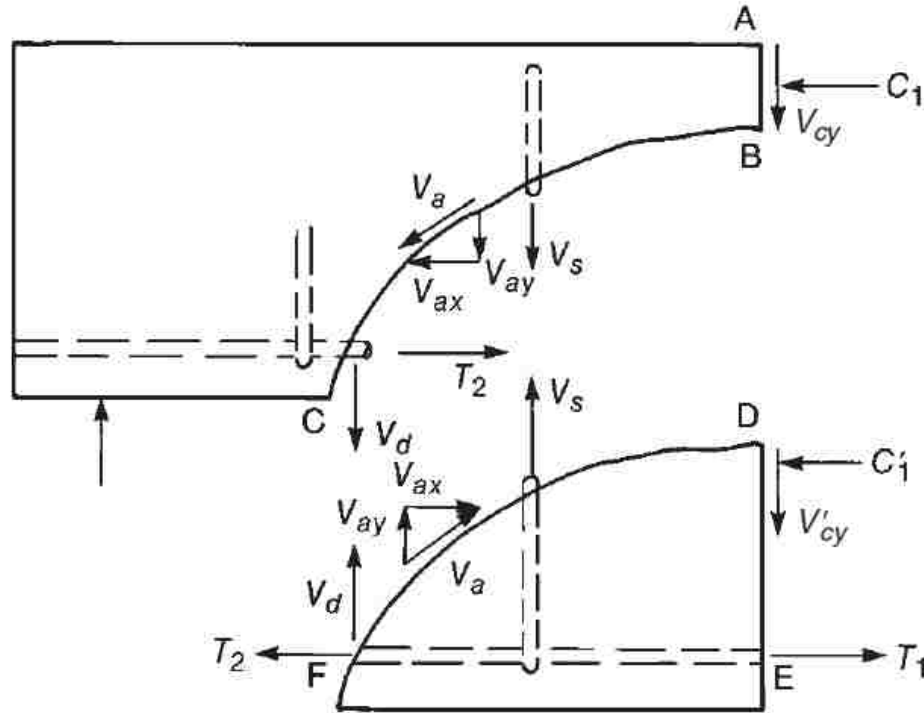


Figure 1.2. Components of Internal Shear Resistance (Wight and MacGregor 2009)



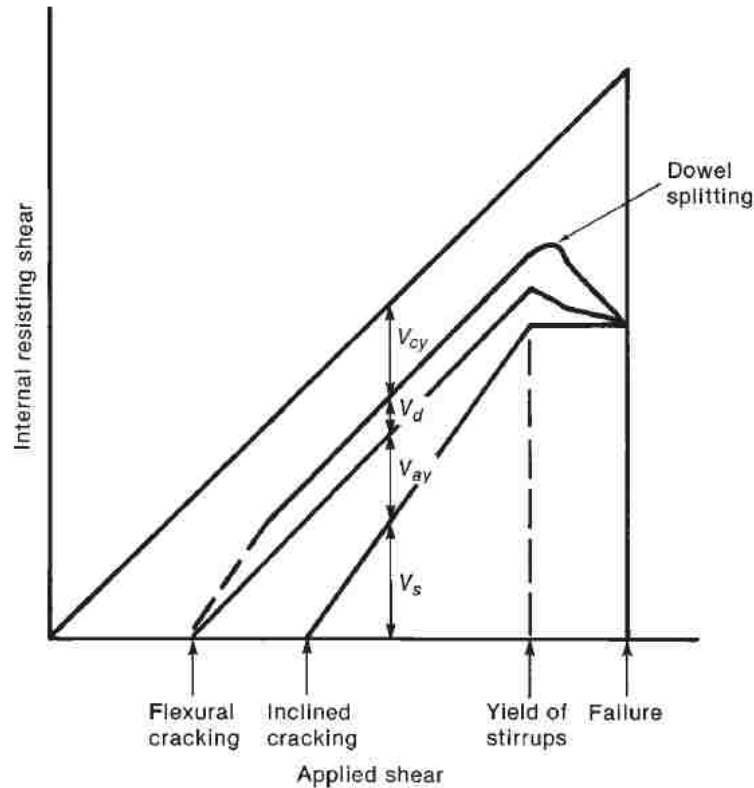


Figure 1.3. Proportions of Internal Shear Resistance Components (Wight and MacGregor 2009)

**1.1.4. Bond Behavior.** The force or stress between the reinforcement and the surrounding concrete is transferred through two mechanisms: physiochemical (adhesive) and mechanical (friction and bearing). The adhesive is a bond between the concrete and the steel. Friction is caused by the bar deformation, or ribs, slipping along the concrete, and the bearing is caused by the ribs bearing against the concrete (Swenty 2003). Figure 1.4. displays bond-transfer mechanisms. After the initial slip of the deformed bar, the adhesive is lost while the bearing of ribs against the surrounding concrete surface and frictional forces transfer forces. As the slip increases, the frictional forces along the surface of the bar become small compared to the bearing forces, and the bearing forces on the ribs resist the biggest part of force. To attain equilibrium, the forces

on the bar surfaces are balanced by compressive and shear stresses in the contacting concrete surface, which develop into tensile stresses that can lead to cracking in plans that are both perpendicular and parallel to the reinforcement (ACI 408R, 2003).

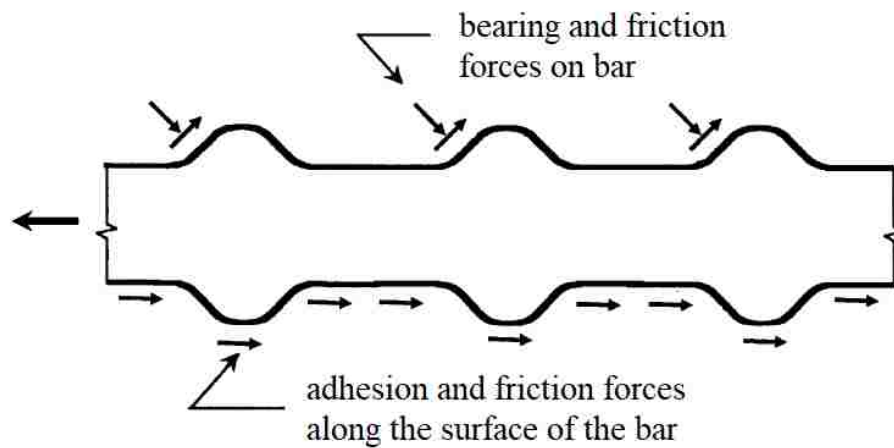


Figure 1.4. Forces Transfer Between Steel and Concrete (ACI 408R, 2003)

ACI 318-14 requires that steel reinforcement must be embedded into the concrete for a distance referred to as the development length in order to obtain complete composite behavior between the reinforcing steel and the concrete, which prevents bond failure from being the control mode of failure. The development length of reinforcing steel is dependent on the bar diameter, yield stress of the reinforcing steel, the coefficient of friction on the steel/concrete interface, the mechanical properties of the surrounding concrete, concrete cover and bar spacing, presence or absence of confinement, and bar geometry (ACI 408R, 2003).

Various bond tests have been suggested to study the bond between reinforcing bars and concrete. There are four common methods of bond testing. The details of each test method have an important role in the bond strength and the nature of the bond response. Two methods with small-scale configurations are the pullout specimen and

beam-end specimen tests. Two methods with large-scale configurations are the beam anchorage and splice beam tests.

The pullout test, shown in Figure 1.5, is the most common test because of its ease of fabrication and performing the test. This test does not reflect the real loading conditions of the structure because the bar in the specimens is under tension while the surrounding concrete is under compression. The most practical loading condition of the reinforced concrete structure is that both the bar and surrounding concrete experience tension. Therefore, this test is not accurate to predict the actual bond strength and it is recommended to use for the purpose of comparison.

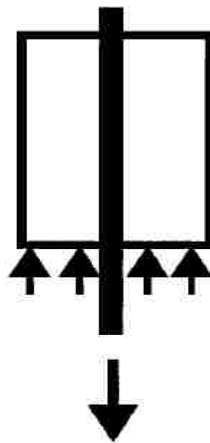


Figure 1.5. Pullout Test Specimen (ACI 408R, 2003)

The beam-end specimen test is a relatively simple test that gives an accurate means of testing bond strength. The reinforcing steel and the surrounding concrete are simultaneously placed in tension. The bar in the beam-end specimen is cast near the top end of the concrete block and pulling force is applied to the bar while a compressive force is applied at a distance approximately equal to the embedded length of the bar away from the end of the bar. Figure 1.6 outlines the loading setup and configuration of a beam-end specimen.

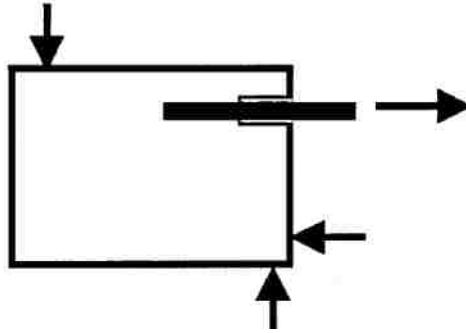


Figure 1.6. Beam-End Specimen (ACI 408R, 2003)

The beam anchorage specimen, which represents a large-scale specimen, is designed to simulate members with flexural cracks and a known bonded length. To achieve this, a beam anchorage specimen involves two points of exposed rebar on the bottom of the beam, as shown in Figure 1.7. The specimen is tested under a four-point load condition until failure. This method provides a realistic bond response, but it can be challenging to fabricate (ACI 408R, 2003).

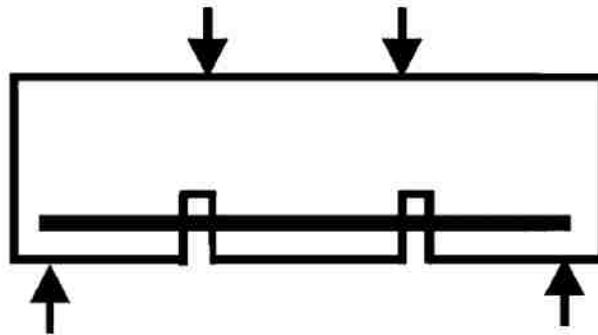


Figure 1.7. Anchorage Beam Specimen (ACI 408R, 2003)

The beam splice test specimen is another form of large scale-beam testing. It is normally fabricated with a splice in a constant moment region. This test can be run with or without confinement (transverse reinforcement) in the splice zone. This test is considered to be a realistic and accurate representation of structural conditions. It has provided a data base that was used to establish the formulation of the development

length, as well as the splice length in ACI 318 code (ACI 408R, 2003). A graphic of the beam splice test is shown in Figure 1.8.

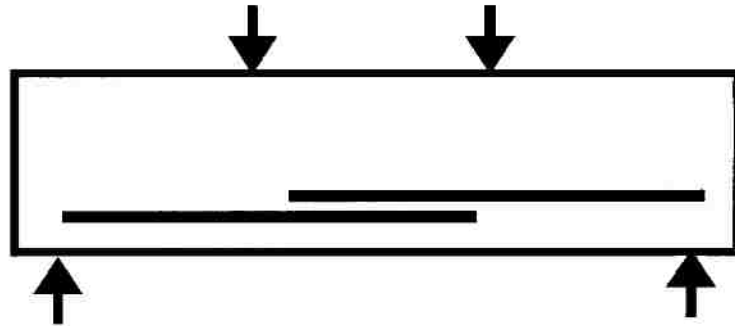


Figure 1.8. Splice Beam Specimen (ACI 408R, 2003)

The application of SCC is expected to enhance the bond between reinforcing steel and concrete due to its filling ability. However, the modified composition of SCC compared to the conventional concrete may influence the properties of the hardened concrete. Also, including a high amount of fly ash can influence the quality of the concrete bond. In other words, changing the mix design will affect the mechanical properties and as a result will influence the bond between steel and concrete (Aslani and Nejadi 2012, Pandurangan et al. 2010).

## **1.2. PART 2: TIME-DEPENDENT FIELD-BASED BEHAVIOR OF HS-SCC IN MISSOURI BRIDGE A7957 MO, USA**

Infrastructure is the backbone of the nation's economy and a necessary part of every nation's daily activities. Infrastructure elements including buildings, highways structures, ports, and dams play an important role in a county's development and productivity. Highway structures, particularly bridges, are vital to the transportation system. However, millions of trips are taken across structurally deficient bridges each day. The United States has 614,387 bridges and almost 40% of them are 50 years or

older. The average age of America's bridges is 43 years old. This number is going up as many bridges are approaching the end of their design life. In 2016, the ASCE Foundation released a report that 56,007 (9.1%) of U.S. bridges were structurally deficient and action needs to be taken (Infrastructure Report Card, 2017)

Recent deficiencies in the United States' aging infrastructure have created a desire to develop sustainable concrete mix designs with advanced concrete technology for bridge structures that will extend the service life beyond the current 50-years' service life. In infrastructure, the use of advanced and high-performance materials can extend bridge service life. HS-SCC is proposed here as an innovative concrete that merges attributes between self-consolidating rheology and high strength concrete properties. In other words, HS-SCC has all the benefits of SCC, such as flowability and stability, with the added benefit of increased strength. HS-SCC can be a potential alternative to conventional high strength concrete (HSC). The beneficial rheological, mechanical, and durability aspects of HS-SCC will lead to several advantages:

- Increased productivity, cost saving, and improved work environments.
- More efficient bridge designs, allowing for larger spans and fewer or smaller girders.
- Lower life cycle cost, longer service life, and lower maintenance requirements.

However, HS-SCC is not without its problems. The specific combination and modification of HS-SCC will affect the properties relevant to engineering projects such as creep, shrinkage, bond, shear, and thermal behavior.

**1.2.1. Bridge A7957.** The A7957 bridge, shown in Figure 1.9, is a highway bridge located on State Highway 50 in southeast Jefferson City, Missouri. The bridge is a part of 8.5 mi (14 km) two-lane expansion of Highway 50, and the bridge was constructed adjacent to bridge A3425. A more general location is given by latitude 38.494306 and longitude -91.987123. Figure 1.10 shows an aerial view of Highway 50. The A7957 bridge was designed to carry two lanes of traffic. The overall length of the bridge is 320 ft (97.5 m) with span lengths of 100 ft, 120 ft, and 100 ft (30.5 m, 36.6 m, 30.5 m) along the centerline of the Highway 50, and it is built on an 30° skew.



Figure 1.9. Bridge A7957 Side View



Figure 1.10. Aerial View of the A7957 Bridge

The bridge was designed to be simply supported for dead load and continuous for live load via a cast-in-place (CIP) composite concrete deck. Each span consists of four precast/prestressed concrete Nebraska University (NU) 53 girders. At the ends, the bridge is supported with reinforced concrete open-ended hinged diaphragm abutments. Figure 1.11 and Figure 1.12 show a cross section view of the bridge and girder details, respectively. The cross section of the NU53 girder provides several advantages during construction, giving designers more flexibility to increase strand capacity and reduce stress concentration in the edges by curved fillets (see Figure 1.12). The beams for span 1 and span 3 were prestressed by 30 Grade 270 (1860 MPa) steel tendons: 20 straight and 10 harped at double harping points. The 0.6 in. (15 mm) diameter tendons were seven-wire, low-relaxation strands. Four additional 3/8 in. (9.5 mm) diameter prestressing strands were added within the top flange of each girder for crack control (Figure 1.13). Span two girders were prestressed with the same type of strands; however, 28 straight strands and ten strands were harped at double points, as shown in Figure 1.14. D20 (MD 130) welded wire reinforcement was provided for shear resistance at spacing intervals of 4, 8, and 12 in. (100, 200, and 300 mm) along the length of the girder. The jacking force per strand was 44 kip (196 kN), but was slightly overstressed to 45 kip (200 kN) to compensate for anchorage losses. To produce a high early strength, a steam-curing regime was used to accelerate the hydration process of all the precast/prestressed concrete girders. The maximum steam regime temperature did not exceed 120°F (49°C). The maximum temperatures were held for a period sufficient to develop the required strength (14 to 38 hours).



Stay-in-place precast concrete deck panels with a target compressive strength of 8000 psi (55.2 MPa) span between the girder's top flange underneath the CIP concrete deck in the transverse direction. The stay-in-place precast panel provides a relatively inexpensive and easily erected option and a safe working area for the placement of CIP concrete deck. The precast concrete girders and deck panels were fabricated in August 2013 in Bonne Terre, Mo. Erection began in September 2013. The deck slab was cast from the east to the west sides of the girder after the erection of girders at the site in October 2013. The bridge entered service (opened to traffic) in mid-2014 after the roadway was completed.

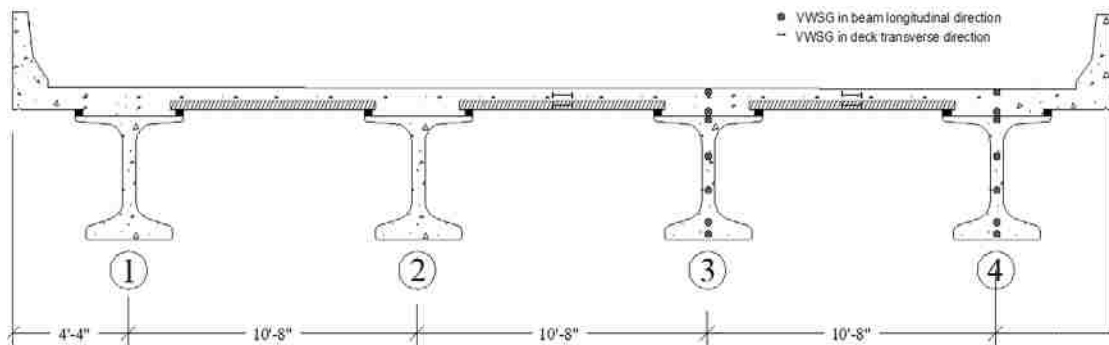
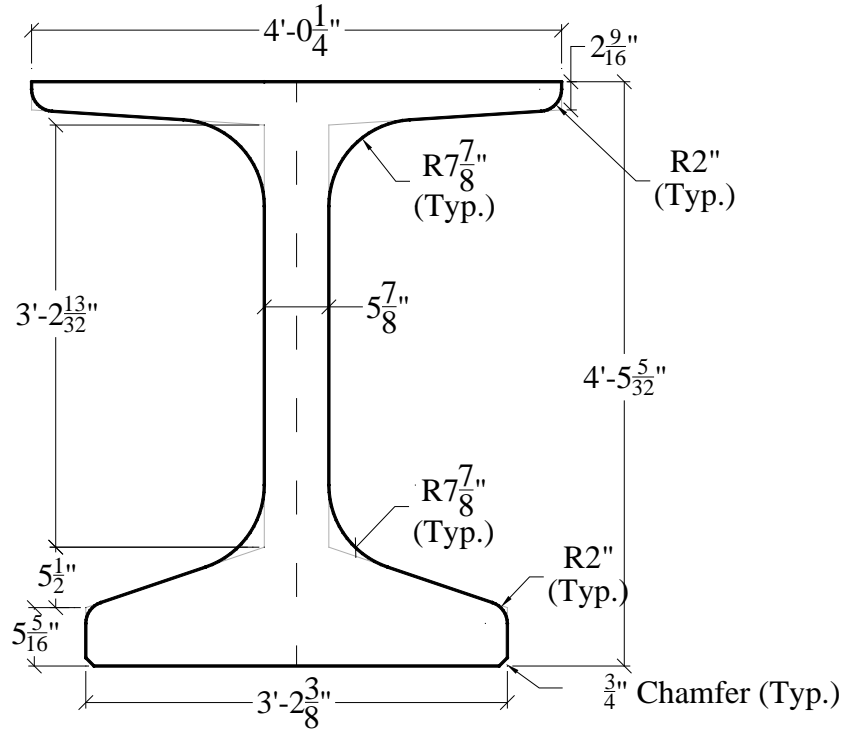


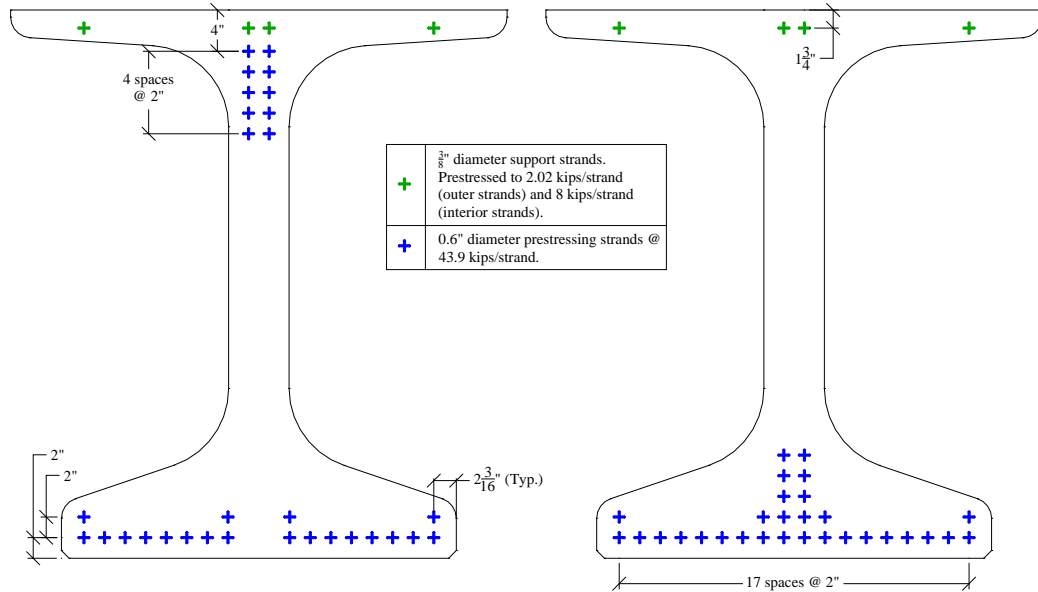
Figure 1.11. Cross Section View of Bridge A 7957

The superstructure elements of Bridge A7957 were identified for consistency during the research program. Spans were labeled S1 through S3 from west to east, and girders were labeled G1 through G4 from north to south. Each girder had a unique abbreviation identifying the span number and girder number (i.e., S1-G3 for span 1-2, girder 3). Only girder lines 3 and 4 included instrumentation within the member. The numbering sequence is shown in Figure 1.15.



Conversion: 1 in. = 25.4 mm

Figure 1.12. NU Bridge Girder Cross Section



Conversion: 1 in. = 25.4 mm

a) Ends

b) Mid-span

Figure 1.13. Strand Layout of Spans 1 and 3 Girders

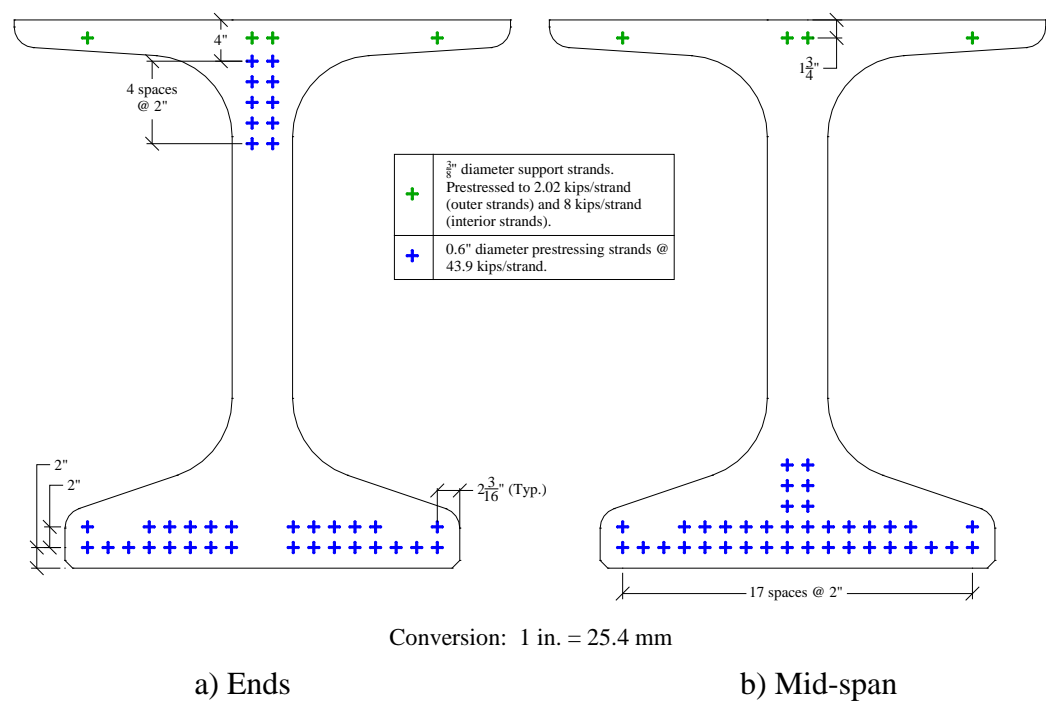


Figure 1.14. Strand Layout of Span 2 Girders

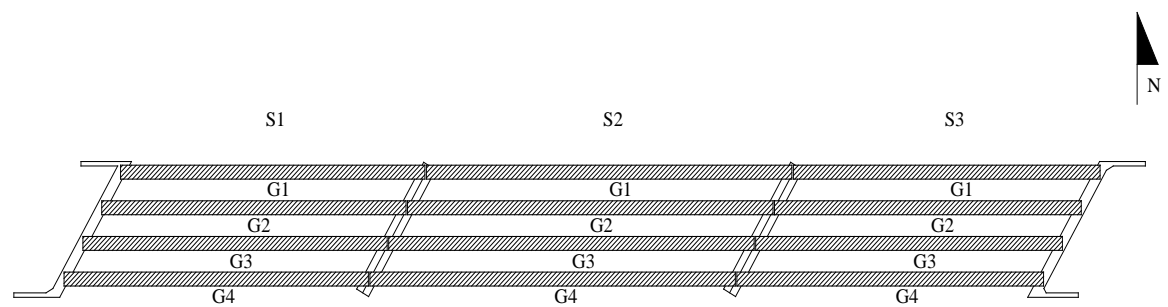


Figure 1.15. Bridge A7957 Numbering System

**1.2.2. Total Prestress Losses.** Prestress losses are the losses in tensile stress of prestress steel that affect the performance of prestressed concrete sections. Understanding and predicting the prestress losses is essential in the design of concrete beams. If care is not taken to determine the prestress losses, the designer can potentially over-stress the structural members during serviceability states. A poor estimate of prestress losses can result in a structure where allowable stresses are exceeded, or where camber and

deflection behavior is poorly predicted such that the serviceability of a structure may be adversely impacted.

Prestress losses in PS/PC members are influenced by several factors. External factors such as temperature and relative humidity and internal factors such as compressive strength, modulus of elastic, creep, and shrinkage play important roles with the amount of prestress losses in the bridge girder. The components of prestress losses over a girder's life cycle are illustrated in Figure 1.16. The losses can be classified into two categories: immediate and long-term (or time-dependent) losses. Immediate losses take place during prestressing of the tendon and transfer the prestress to the concrete member. The elastic shortening ( $\Delta f_{ES}$ ) and slip of the anchorage are immediate losses. Losses due to creep of the concrete ( $\Delta f_{CR}$ ), shrinkage of the concrete ( $\Delta f_{SH}$ ), and relaxation of the tendon ( $\Delta f_{RE}$ ) are considered time-dependent losses (Alghazali and Myers 2015). Anchorage seating losses are considered negligible for large prestressing beds like the one used in this study of almost 300 ft (91.4 m) (AASHTO LRFD, 2012).

Elastic shortening is the loss of prestress force that takes place when a strand becomes shorter. The forms are stripped, and the prestressing strands are released after adequate strength is added to the casting bed. As a result, the concrete and strands shorten under the load. Elastic shortening loss represents a significant portion of the total prestress loss.

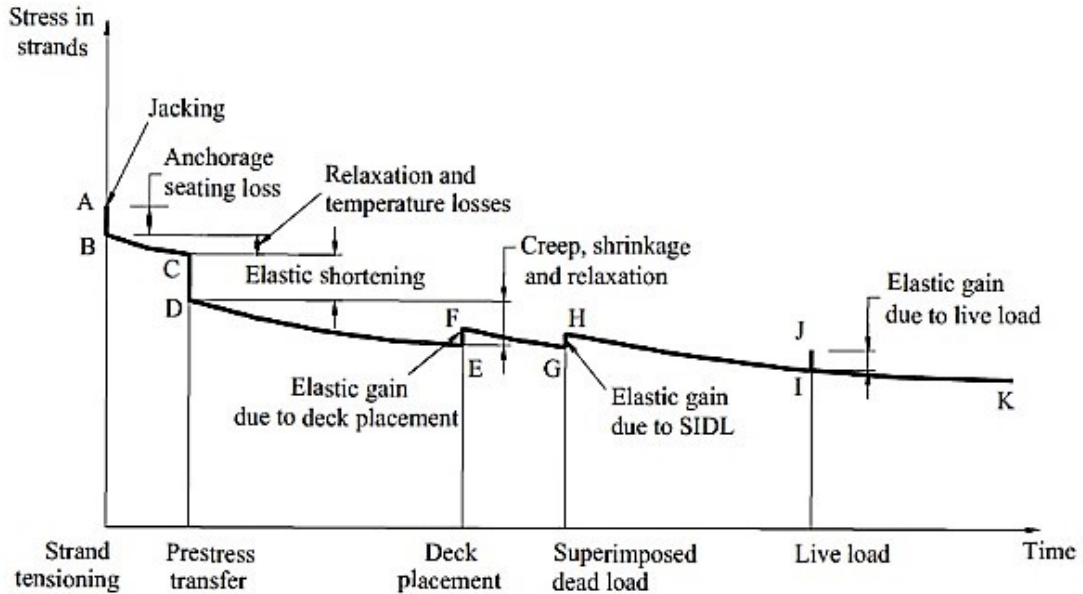


Figure 1.16. Stress vs. Time for PC/PS Bridge Girder (Tadros et al., 2003)

The time-dependent losses are constantly varying throughout the life cycle of the girder. The creep of concrete causes a time-dependent change in strain throughout the depth of the girder. Creep is the continual straining of concrete under sustained loading for a given time period. There are several factors that contribute to the creep, including the amount and duration of sustained load, concrete age at the time of loading, aggregate modulus of elasticity, water-to-binder ratio, aggregate-to-paste ratio, member size, and the amount of steel reinforcement. Shrinkage is another time-dependent loss and causes a loss of tension in the strand. Shrinkage is the time-varying loss of excess water in a concrete girder. Shrinkage causes the member to shorten and as a result leads to a loss of some stress in the prestressing tendons. Many factors influence shrinkage, including water-to-binder ratio, moisture, relative humidity and temperature of the environment, aggregate modulus of elasticity, aggregate-to-paste ratio, and the size and shape of the member. Intrinsic relaxation loss is the phenomenon in which the stress in the tendon

decreases while the length remains relatively constant. This type of loss is larger with larger initial stress and higher temperature. Steel relaxation loss is influenced by the amount of prestress applied to steel tendons, type and length of the tendons, and the method of prestressing used to tension the member. Low-relaxation prestressing strands type, which is almost exclusively used today, undergo considerably less relaxation than stress-relieved strands (Onyemelukwe and Kunnath 1997, Tadros et al. 2003).

Many specifications have allowed researchers to compute each loss individually and add them to determine the total loss, as shown in Equation 1. This equation allows for the lump-sum estimation of losses due to elastic shortening, creep, shrinkage, and relaxation:

$$\Delta f_{Total} = \Delta f_{ES} + \Delta f_{CR} + \Delta f_{SH} + \Delta f_{RE}. \quad (1)$$

With each method, relaxation losses are computed using an empirical method. Relaxation losses can be obtained for the tendons stressed beyond 55% based on the measured prestressing force using the relaxation model in Equation 2 (Nawy 2009):

$$\Delta f_{RE} = f_{pi}' \frac{\log_{10} t}{45} \left( \frac{f_{pi}'}{f_{py}} - 0.55 \right), \quad (2)$$

where  $f_{pi}'$  = the initial stress of prestressing tendons,  $t$  = time after prestressing, and  $f_{py}$  = specified yield strength of prestressing tendons.

The design of pretensioned concrete girders required accurate estimates of prestress losses. However, the current provisions that have been developed for computing prestress losses in conventional concrete may not provide reliable estimates for HS-SCC because the creep and shrinkage of HS-SCC are expected to be somewhat higher than

that of conventional concrete because typical SCC mixtures contain smaller percentages of coarse aggregate, smaller coarse aggregate size, and higher binder content than conventional concrete. Thus, research is needed to evaluate the applicability of the current models adopted by specifications such as AASHTO LRFD Bridge Design Specification (AASHTO LRFD, 2012) and the PCI Design Handbook (PCI, 2010) for estimating prestress losses in HS-SCC. This study was conducted to address this need. A summary of the AASHTO LRFD and the PCI methods to estimate elastic shortening (ES), creep (CR), shrinkage (SH), and strand relaxation (RE) is illustrated in Table 1.2.

**1.2.3. Uniform Temperature.** Concrete bridge structures are subjected to thermal effects due to the seasonal cycle. Concrete expands slightly as the temperature rises and contracts as the temperature falls, which causes axial movement in the bridge. Bridge structures must be designed to accommodate this axial movement associated with seasonal cycles (Elbadry and Ghali 1986, Myers and Bloch 2010). Designers realize that the average bridge temperature (ABT) is essential for the prediction of axial bridge movement. The evaluation of accurate values of extreme ABT is important for structural engineers during the design and construction phases of concrete bridges. If the temperatures are not considered within the design, thermal stress and thermal strain may result from restricting bridge component deformation, causing thermal cracking. Thus, the serviceability of the concrete structure will be compromised because of thermal cracking.

Table 1.2. Summary of the Code Equations Used in the Prediction of Total Prestress Losses by Components (Pretensioned Member)

Source of Losses	AASHTO LRFD – 2012 (ksi)	PCI – 2010 (ksi)
Elastic Shortening ( $\Delta f_{ES}$ )	$\frac{E_p}{E_{ct}} f_{cgp}$	$K_{es} \frac{E_{ps}}{E_{ci}} f_{cir}$
Creep ( $\Delta f_{CR}$ )	$\frac{E_{ps}}{E_{ci}} f_{cgp} \psi_b(t_d, t_i) K_{id}$ (Before deck placement)  $\frac{E_{ps}}{E_{ci}} f_{cgp} [\psi_b(t_f, t_i) - \psi_b(t_d, t_i)] K_{df}$ $+ \frac{E_{ps}}{E_c} \Delta f_{cd} \psi_b(t_f, t_d) K_{df}$ (After deck placement)	$K_{cr} \left( \frac{E_{ps}}{E_c} \right) (f_{cir} - f_{cds})$
Shrinkage ( $\Delta f_{SH}$ )	$\varepsilon_{bid} E_p K_{id}$ (Before deck placement)  $\varepsilon_{bdf} E_p K_{df}$ (After deck placement)	$(8.2 \times 10^{-6}) K_{sh} E_{ps} \left( 1 - 0.06 \frac{V}{S} \right) (100 - RH)$
Relaxation ( $\Delta f_{RE}$ )	$\frac{f_{pt}}{K_L} \left( \frac{f_{pt}}{f_{py}} - 0.55 \right)$	$[K_{re} - J(SH + CR_{ES})C]$
<p>1 ksi= 6.895 MPa 1 in=25.4 mm</p> <p><math>f_{cgp}</math>= stress in concrete at c.g. of pretensioned strands at release (due to prestress and self-weight);  <math>f_{cir}</math> = net compressive stress in concrete at c.g. at release; <math>f_{cds}</math>= stress in concrete at c.g. of prestressing force due to all superimposed, permanent dead loads that are applied to the member after it has been prestressed; <math>E_p=E_{ps}</math>=modulus of elasticity of prestressing steel, <math>E_{ct}=E_{ci}</math>= modulus of elasticity of concrete at release; <math>E_c</math>= modulus of elasticity of concrete at 28 days; <math>\psi_b(t_d, t_i)</math>= girder creep coefficient at time of deck placement due to loading introduced at transfer; <math>\psi_b(t_f, t_i)</math> = girder creep coefficient at final time due to loading introduced at transfer; <math>\psi_b(t_f, t_d)</math>= girder creep coefficient at final time due to loading at deck placement.</p>		



The current AASHTO LRFD specifications address designs for uniform bridge temperature (average bridge temperature) changes. Two methods were defined in these specifications, Procedure A and Procedure B, to determine the design uniform bridge temperatures. Procedure A presents a simplified method by linking between bridge materials and the climate zone as shown in Table 1.3. However, Procedure B determines the maximum and minimum design bridge temperatures for either concrete girder or steel girder bridges with concrete decks. The design temperatures are based on contour maps, shown in Figure 1.17 and Figure 1.18. Procedure B is a calibrated procedure and does not cover all bridge types. The temperatures provided in the contour maps are extreme bridge design temperatures for an average history of 70 years with a minimum of 60 years of data for locations throughout the United States. The design values for locations between contours should be determined by linear interpolation. As an alternative method, the largest adjacent contour may be selected to define  $T_{MaxDesign}$  and the smallest adjacent contour may be used to define  $T_{MinDesign}$ .

Table 1.3. Temperature Ranges from AASHTO LRFD 2012, Procedure A

Climate	Steel or Aluminum	Concrete	Wood
Moderate	0° to 120°F	10° to 80°F	10° to 75°F
Cold	-30° to 120°F	0° to 80°F	0° to 75°F

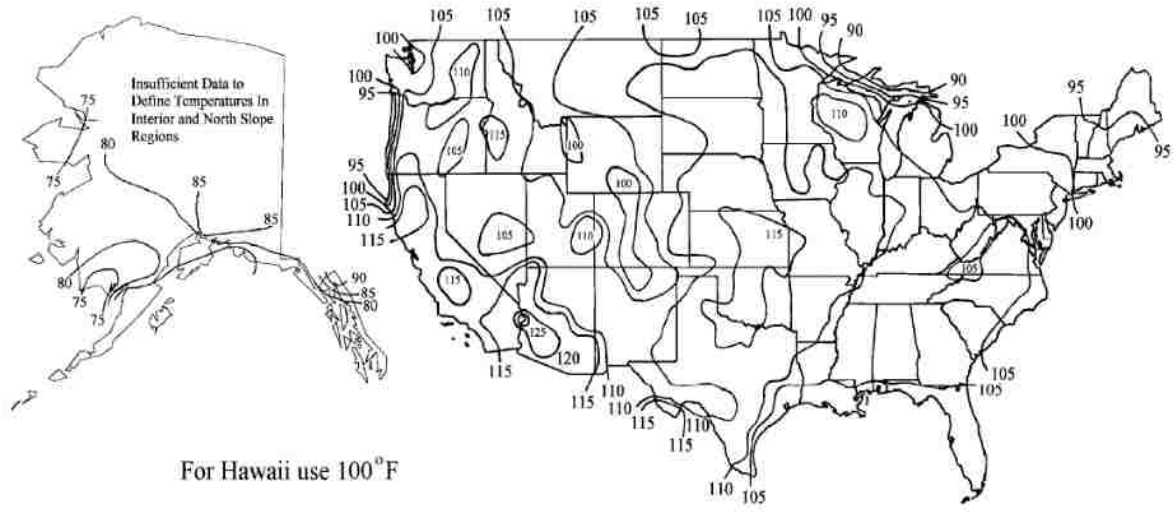


Figure 1.17. Contour Maps for  $T_{MaxDesign}$  for Concrete Bridges

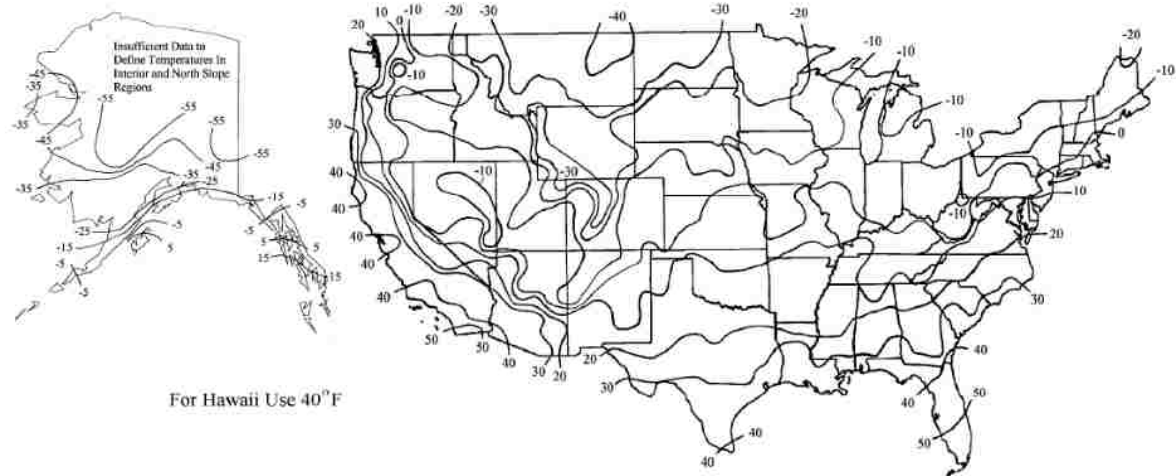


Figure 1.18. Contour Maps for  $T_{MinDesign}$  for Concrete Bridges

The National Cooperative Highway Research Program's (NCHRP) Report 276 (Imbsen et al. 1985) examined the effects of temperature changes in concrete bridge superstructures. In this report, the uniform bridge temperatures (effective bridge temperatures) were correlated with ambient temperatures. Table 1.4 shows the relationship between the normal daily extreme temperature and extreme effective temperatures.

Table 1.4. Correlation Between Concrete Bridge Temperatures and Normal Daily Temperatures

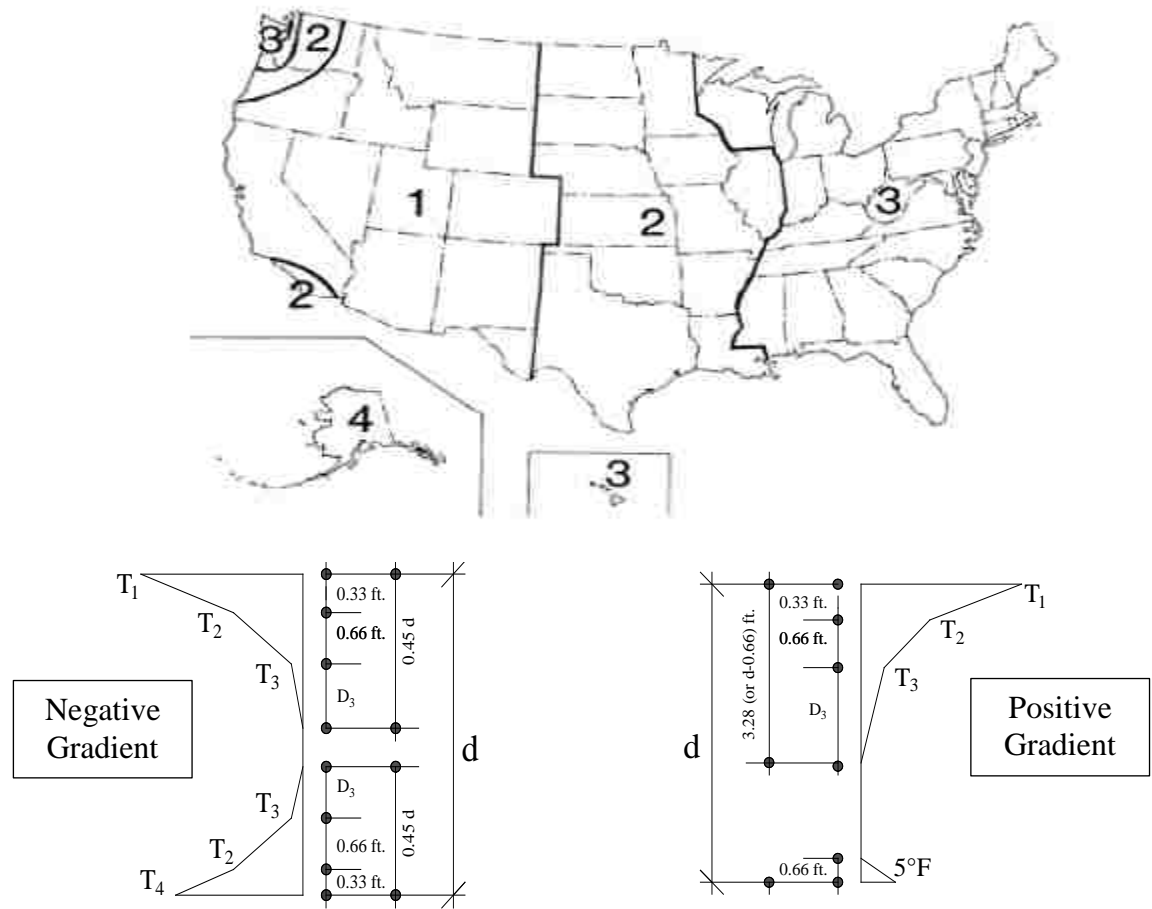
Normal Daily Minimum Temperature (°F)	Minimum Effective Temperature (°F)	Normal Daily Maximum Temperature (°F)	Maximum Effective Temperature (°F)
-30	-3	55	66
-25	0	60	69
-20	3	65	73
-15	5	70	77
-10	8	75	80
-5	11	80	84
0	13	85	88
5	16	90	92
10	19	95	95
15	22	100	98
25	29	105	101
30	32	110	105
35	35	---	---
40	38	---	---

**1.2.4. Thermal Gradients.** The daily temperature cycle leads to variations in the temperature distribution along the depth of the superstructure, which is generally a nonlinear variation. This leads to the development of thermal gradients in a structure (Abid et al. 2016). Thermal gradients produce a combination of axial and flexural stresses and strains through the depth of the structure (Barr et al. 2005). Although these stresses and strains are temporary in nature, their magnitude can exceed those resulting from live loads in certain cases. Therefore, thermal stresses and strains may result in thermal cracking. Thermal cracking does not generally affect the ultimate strength of the bridge

components. However, the serviceability of the structure may be significantly affected because thermal cracking causes corrosion of reinforcing steel, which reduces the service life of the structure (Myers and Yang 2004).

The diurnal variation of air temperature and solar radiation leads to thermal gradients in a structure. Concrete expands and contracts when subjected to temperature increases and decreases, respectively. During a sunny day, the exposed bridge deck heats up more quickly than the underside of the bridge since the underside is shaded from direct sunlight. As a result, a positive thermal gradient will occur (Imbsen et al. 1985). The magnitude of this gradient depends on the amount of radiation absorbed by the deck. In the summer, the positive gradients are typically significant, ranging from 38 to 55°F (21 to 31°C) when the amount of solar radiation is at a maximum (Imbsen et al. 1985). These gradients appear to be the largest when longer periods of cooler ambient temperature are followed by the larger solar radiation days (Larsson and Thelandersson, 2011). A bridge experiences a negative thermal gradient when the deck slab of the bridge is subjected to larger downward temperature swings than the underside of the bridge. Because the surface area of the bridge deck is typically much larger than the rest of the superstructure, the deck dissipates heat more rapidly than the bottom during the night. The peak negative thermal gradient tends to occur in the fall through spring when downward temperature cycles are largest. The negative thermal gradient magnitude is highly variable because it is dependent on the temperature distribution in the structure at the time when cooling begins and the difference between concrete and ambient temperatures (Imbsen et al. 1985).

NCHRP Report 276 proposed a design guideline for both positive and negative thermal gradients, as shown in Figure 1.19. For the purpose of design, the United States is subdivided into four zones based on maximum solar radiation. AASHTO LRFD 2012 specifications have modified the design thermal gradients specified by NCHRP Report 276. Figure 1.20 shows the modified positive NCHRP gradient by AASHTO LRFD specifications.



Positive Gradient

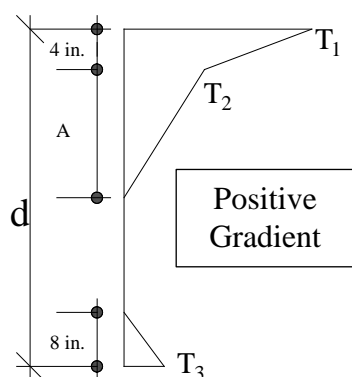
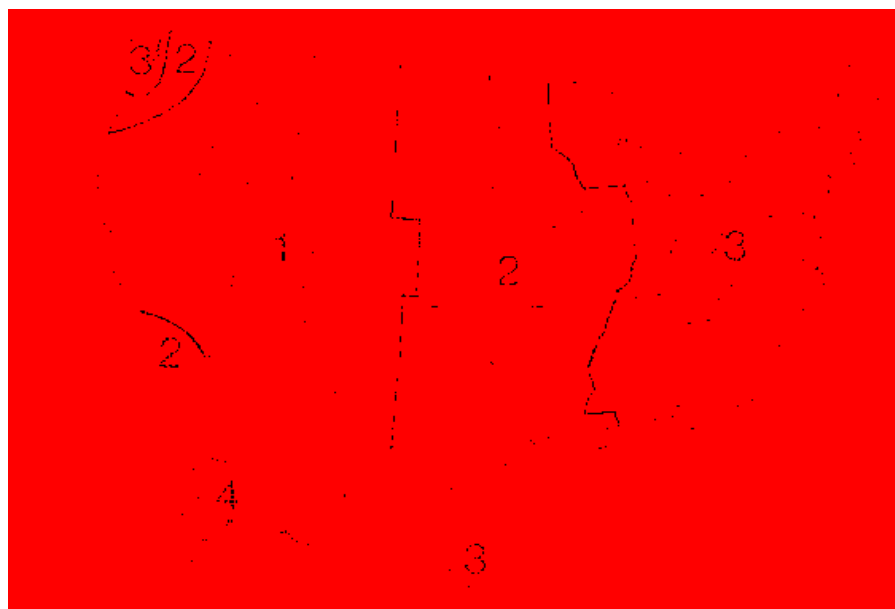
Zone	Plain Concrete Surface			2 in. Blacktop			4 in. Blacktop		
	T <sub>1</sub>	T <sub>2</sub>	T <sub>3</sub>	T <sub>1</sub>	T <sub>2</sub>	T <sub>3</sub>	T <sub>1</sub>	T <sub>2</sub>	T <sub>3</sub>
1	54	14	5	43	14	4	31	9	3
2	46	12	4	36	12	4	25	10	3
3	41	11	4	33	11	3	23	11	2
4	38	9	3	29	9	2	22	11	2

**Note:** All temperatures are in degree Fahrenheit.

Negative Gradient

Zone	Plain Concrete Surface				2 in. Blacktop				4 in. Blacktop			
	T <sub>1</sub>	T <sub>2</sub>	T <sub>3</sub>	T <sub>4</sub>	T <sub>1</sub>	T <sub>2</sub>	T <sub>3</sub>	T <sub>4</sub>	T <sub>1</sub>	T <sub>2</sub>	T <sub>3</sub>	T <sub>4</sub>
1	27	7	2	14	22	7	2	15	16	5	1	12
2	23	6	2	10	18	6	2	11	13	5	1	9
3	21	6	2	8	17	6	2	10	12	6	1	8
4	19	5	2	8	15	5	1	8	11	6	1	8

Figure 1.19. Design Thermal Gradients Suggested by NCHRP Report 276



Zone	T <sub>1</sub> (°F)	T <sub>2</sub> (°F)
1	54	14
2	46	12
3	41	11
4	38	9

**Notes:**

- Dimension “A” shall be taken as:
  - 12 in. for concrete superstructure that are 16 in. or more in depth
  - (d-4) in. for concrete superstructure that are less than 16 in. in depth
- Temperature value T<sub>3</sub> shall be taken as 0.0 °F, unless a site-specific study is made to determine an appropriate value, but shall not exceed 5 °F.
- Negative gradient values may be obtained by multiplying positive gradients values by -0.3 for plain concrete decks and -0.2 for deck with an asphalt overlay.
- All temperatures are in degree Fahrenheit.

Figure 1.20. Design Thermal Gradients Adopted by AASHTO LRFD-2012 Specifications

## 2. RESEARCH OBJECTIVES

The overall objective of this study was to investigate the performance of sustainable self-consolidating concrete targeted for highway bridge structures. To perform this study, the research for this project took two major tracks to establish the sustainable self-consolidating concretes. One involved extending the supplementary cementitious materials (SCM) with replacement levels up to 70%. All related drawbacks were mitigated with high replacement levels with SCMs, such as setting time, early age strength, and durability. The second track was by enhancing the compressive strength of SCC mix with 100% Portland cement to produce high strength-self consolidating concrete and monitoring the long-term performance of this type of concrete.

An extensive study involving laboratory material performance evaluation was carried out to explore the effects of substituting large amounts of SCM, as well as analyzing the interaction between concrete material's constitution to develop strong and durable concrete mixtures and validate the structural performance of these new developed concrete mixtures. In another side, a large program was carried out on a bridge in Missouri constructed with HS-SCC to monitor the long-term structural performance using health monitoring system (non-distractive test).

The objectives of this study can generally be classified into laboratory study-related issues and issues related to the practical field application. The specific objectives and responsibilities related to each sub-study are described as follows:

1. Examine different techniques to mitigate the harmful effects of high volume fly ash in the binder system. Different curing regimes and cement types were suggested in this objective to overcome the drawback related to using high amount of fly ash.



2. Perform a statistical approach to optimize the overall performance of a high amount of fly ash self-consolidating binder system based on mechanical properties, flow characteristics, cost, and durability properties in the mortar level to produce ecologically-friendly self-consolidating binder systems and scale up to a concrete level.
3. Optimize the particle size distribution of the aggregate skeleton based on the packing density approach to achieve dense particle packing, and as a result, the paste volume needed to fill voids between aggregate particles can be minimized.
4. Design and develop high volume fly ash-self consolidating concrete (HVFA-SCC) mixtures targeted for highway bridge structures using the results and knowledge obtained from objectives 2 and 3.
5. Evaluate the shear behavior of HVFA-SCC under reinforced full-scale beams. This objective included a study and evaluation of current analytical models to predict the shear behavior and response of HVFA-SCC, as well as to compare the shear test results to previous study results and the shear test database of conventional concrete.
6. Explore the bond strength behavior between HVFA-SCC and steel reinforcement using full-scale beam splice test specimens subjected to a four-point loading until failure of the splice, as well as to compare the bond test results with the splice beam test results reported in the literature.
7. Employ a health monitoring system on Bridge A7957 MO, USA using vibrating wire strain gauges and data acquisition system to monitor the

long-term deformations of PC/PS bridge girders constructed with HS-SCC.

8. Obtain and analyze strain data from the instrumented bridge girders to quantify prestress losses in HS-SCC bridge girders, as well as assess the conservatism and accuracy of the current prestress losses provisions (introduced in AASHTO LRFD 2012 and PCI 2010) and determine whether these provisions are adequate for HS-SCC girders.
9. Collect and analyze temperature data from the instrumented HS-SCC bridge girders to evaluate the thermal behavior (uniform bridge temperature and thermal gradients) and compare the findings of this study to the current provisions presented in AASHTO LRFD 2012 and NCHRP Report 276.

### 3. ORGANIZATION OF DISSERTATION

The outcomes of the research efforts reported in this dissertation have been disseminated to through several technical journal publications and conference proceedings. General conclusions based on the entire work are summarized at the end of the dissertation. A flow chart in Figure 3.1 illustrates the structure of the dissertation.

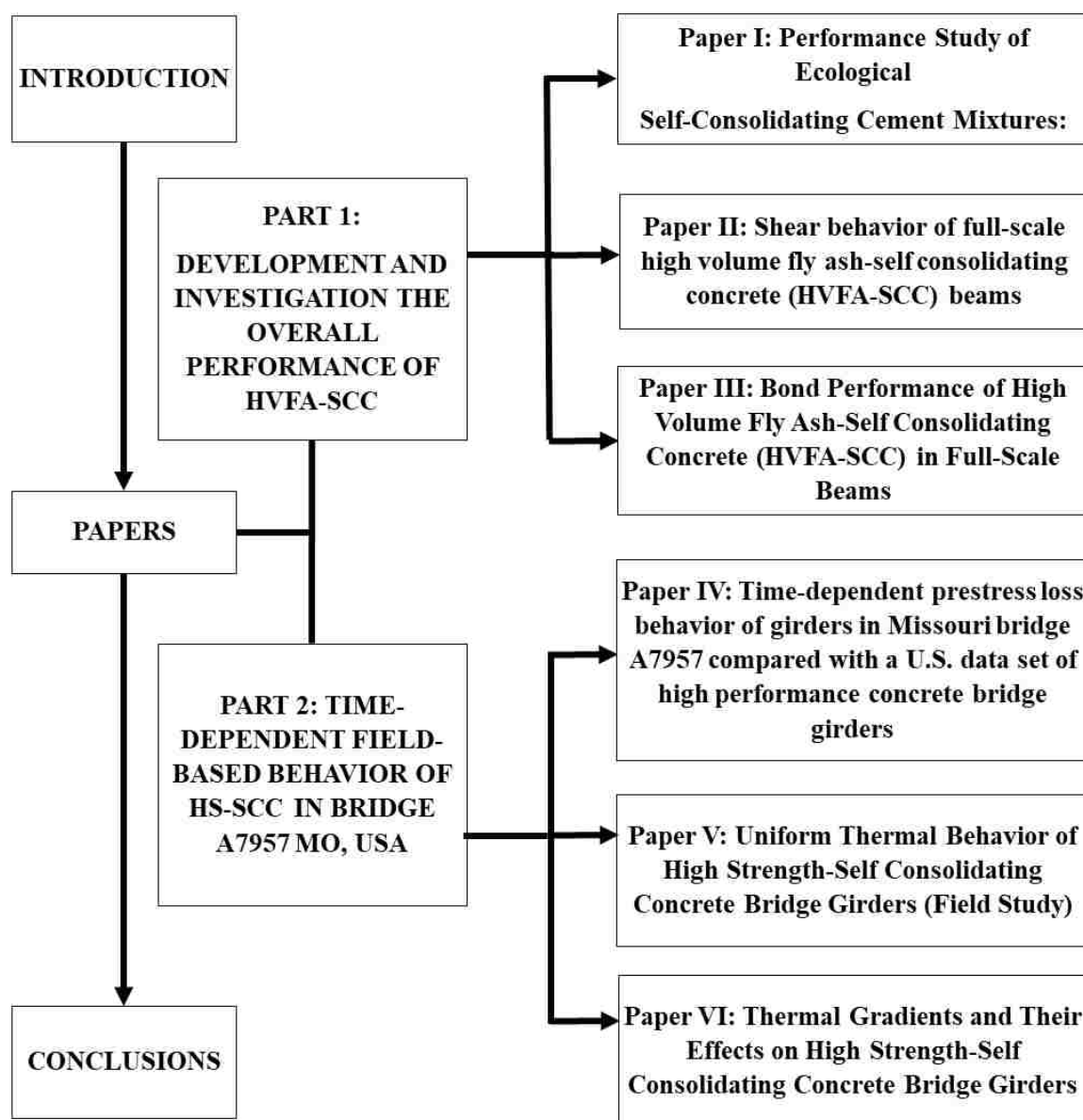


Figure 3.1. Organization of the Dissertation

## PAPER

### I. PERFORMANCE STUDY OF ECOLOGICAL SELF-CONSOLIDATING CEMENT MIXTURES

Hayder H. Alghazali and John J. Myers

#### ABSTRACT

This study presents a useful analytical method based on a statistical approach for optimizing the performance of Eco-SCCM (mortar component). Eco-SCCM is a new class of concrete mixtures which satisfies engineering design requirements (mechanical and rheological properties) and environmental concerns. Three different phases with a total of 43 mixtures were generated using Design Expert software to study the effect of using high volume fly ash on the performance of cement mixtures. Hydrated lime was added as the third component to increase the hydration activity of fly ash. Two different curing regimes were investigated. Fresh properties were measured, and hardened properties such as compressive strength, drying shrinkage, and surface resistivity were also monitored. The results of the phases were compared to track the effect of supplemental levels of fly ash levels and hydrated lime dosages as part. To optimize the performance of Eco-SCCM, the desirability function approach was successfully applied. Results showed that mixtures with 37% Portland cement type I/II and 63% fly ash under a moist curing regime yielded the highest performance level.

#### Keywords:

Eco-SCCM, Fly Ash, Hydrated Lime, Desirability Function Approach.

## 1. INTRODUCTION

Conserving the environment by reducing CO<sub>2</sub> emissions and energy consumption associated with cement manufacturing is a key to designing ecological concretes (more environmental- friendly concretes). Concrete is the most widely used material in the world to construct infrastructure buildings, roads, bridges, and dams. Cement is the primary component and most expensive component of concrete. Cement manufacture is highly energy and emissions intensive because of the extreme heat required to produce it. Each ton of cement requires 4.7 million BTU (1377 kW hr.) of energy and generates nearly a ton of CO<sub>2</sub>. Cement production is growing by 2.5% annually, and cement consumption is expected to reach 3.7 - 4.4 billion tons by 2050 (Benhelal et al. 2013; Rubenstein 2012). This gives the cement an obvious place to look to reduce greenhouse gas emissions.

Eco-SCCM is a new class of concrete mixtures which satisfies engineering design requirements (mechanical and rheological properties) and environmental concerns. Incorporating supplementary cementitious materials such as fly ash to constitute concrete binders is the most straightforward way to minimize the amount of Portland cement. Furthermore, using supplementary cementitious materials (SCMs) provide a means for the economic and ecological disposal of millions of tons of industrial by-product that could be safely incorporated as a cementitious material in concrete. After reducing the environmental impact of Portland cement production and providing a means of recycling industrial waste, SCM and concrete will stand strong together as a good solution to these issues.

Fly ash is a by-product of the combustion of pulverized coal in electric power generation plants. Currently, fly ash is used in some capacity in more than 50% of all

ready-mixed concrete placed in the United States (Wilson and Kosmatka 2011). When fly ash was originally used in concrete in the 1970s, there were some basic restrictions regarding its use. Typically, fly ash is added to structural concrete at 15 -35% of the weight of the cement. Concrete with 50% or more of fly ash is generally considered to be high volume fly ash (ACI Committee 232 2003). High volume fly ash (HVFA) concretes have been proposed as one potential method for reducing cement usage. However, high fly ash content in concrete typically results in slow strength gain at early ages, delayed setting times, and flash sets, and sometimes reduces ultimate strength (Richardson et al. 2015). Consequently, current studies in HVFA concretes focus on increasing the limit of substitution levels at which issues associated with high-level replacement can be successfully mitigated. Mitigation of high volume fly ash problems is an interesting area under investigation. The objective of this research is to optimize the overall performance of various cementitious material combinations under different curing regimes and Portland cement types. Furthermore, this study aims to evaluate the interaction of certain combinations of cementitious materials and the effect of powder additive on the performance of Eco-SCCM.

## **2. EXPERIMENTAL PROGRAM**

The experimental program was undertaken to evaluate the performance of mixtures made with high volume fly ash. This study was divided into three phases. Phase I was carried out using combinations of Type I/II Portland cement, Class C fly ash, and Type S hydrated lime. The samples of this phase were moist cured in a room maintained at a relative humidity (RH) of 95% or greater until the test day. Type III cement was used in Phase II instead of Type I/II to investigate the activity levels with a high amount of fly

ash. Curing concrete plays a major role in developing the concrete microstructure and pore structure and thus improves the concrete performance (Fantilli and Chiaia 2013). Most of the studies on strength development and pore size distribution were performed under a moist curing regime. Thus, Phase III in this study was developed to evaluate the combination mixtures' performance under an accelerated curing regime using hot water. Mixture combinations similar to Phase I were examined in Phase III.

Each mixture had a water-cementitious material ratio (w/cm) of 0.35. Binary and ternary combinations of cementitious materials were investigated for each phase proportioned with Portland cement, fly ash, and hydrated lime substitutions, by the total mass of cementitious materials. A polycarboxylate-based high range water reducer (HRWR) was employed to enhance the workability. The HRWR has a solid mass content of 23% and specific gravity of 1.05. The HRWR dosage was adjusted for all mixtures to secure initial flow table consistency of  $9 \pm 1$  in. ( $220 \pm 25$  mm). The water present in the HRWR was included as part of the mixing water to maintain constant w/cm. Well-graded locally available natural sand passing through sieve #4 (4.75 mm) was used for this program. The mix ratio of cementitious materials and sand was 1:2.75. The mortar properties of interest were rheological, mechanical, and durability.

## **2.1. EXPERIMENTAL DESIGN**

The cementitious material combinations in this program were generated using the Design-Expert® software program (version 10) (Vaughn and Polnaszek 2010) based on constraints imposed on the proportion limits of each individual component, and the literature and practical considerations to design a mixture with high volumes of fly ash. For the cement, proportion limits were chosen to be 25 - 50%. Fly ash design limits were

chosen to be 40 - 75%; however, the design limits of hydrated lime were chosen to be 0 - 15%. Control mixes with 100% cement were also prepared for each phase. In total, 43 binder combinations (including 9 replicated mixtures) were evaluated using different types of replacement, cement, and curing regimes, as illustrated in Table 1.

All mortar mixtures were prepared and tested at room temperature,  $23\pm 2$  °C ( $73\pm 4$  °F). A high shear mixer [Hobart mixer with 0.0142 m<sup>3</sup> (0.5 ft<sup>3</sup>) capacity] was used to prepare Eco-SCCM. The mixing sequence consisted of placing all water and HRWR in the mixing bowl followed by gradually adding the binder materials. The materials were mixed for 30 - 60 second at slow speed (1 rps). The entire quantity of sand was added slowly over a period of 30 seconds while mixing at slow speed. The cement mortar was mixed for additional 30 seconds at medium speed (2 rps). Finally, after resting 90 seconds, the mixing was resumed for additional 60 seconds at medium speed (2 rps). As needed, the HRWR was adjusted to secure an initial flow table consistency of  $220\pm 25$  mm ( $9\pm 1$  in.). For each mix of mortar, the duration of mixing time was about 4 - 5 min.

Two curing conditions were employed in this study to investigate the effect of curing regimes (Bentz 2007; Sajedi et al. 2012). For accelerated curing, a hot water system was used to simulate steam curing of precast applications. The maximum temperature of concrete did not exceed 70 °C (158 °F) in order to prevent the risk of delayed ettringite formation. The temperature rise during accelerated curing was limited to 20 °C/hr. (68 °F/hr.) and also the rate of cooling was limited to 20 °C/hr. (68 °F/hr.) in compliance with AASHTO LRFD 2007 (AASHTO LRFD 2010; Hwang et al. 2012). A preset period of at least four hours was allowed before the accelerated curing was applied. After the accelerated regime had been completed, the specimens were demolded



and stored at room temperature at 21 °C (70 °F) until the time of tests. Moist curing specimens were covered with wet burlap as soon as the mortar had set sufficiently so that no distortion or marring occurred. After 24 hours, the specimens were demolded and then stored in a room maintained at a relative humidity of 95% or greater until the testing day.

## **2.2. TESTS PROCEDURES**

Testing fresh properties and preparing samples of the Eco-SCCM was completed 5 - 30 min. following the initial contact of cement with water. The mortar temperature was determined first followed by the evaluation of fluidity. The fluidity characteristics of the mortars were measured at 6 min. and 30 min. after contact of water with cement, which corresponds to time zero. The investigated fluidity properties included the mini-slump and flow table tests. ASTM C1437 was followed to perform the fluidity tests (ASTM C1437 2015). The initial fluidity was performed immediately using a brass cone. The flow mold was first filled with mortar and rodded as necessary to eliminate any entrapped air, and then the mold was lifted away and mortar collapsed on the flow table. Two readings were recorded, and the average of both records was calculated as mini-slump flow in inches. Following that, both the table and the mortar were dropped 25 times in 15 seconds. The average of two perpendicular readings was calculated as flow table, also in inches. Both tests (mini-slump and flow table) were repeated after 30 min.

The wet unit weight was measured using a brass cylinder mold with a volume of 400 ml (24.4 in<sup>3</sup>), filled with mortar and consolidated using a micro-vibration table for 40 sec. before measuring the weight. A micro-vibration table was utilized to eliminate any largely entrapped air bubbles during mixing. The wet unit weight was calculated using Eq. (1):

$$\rho_{wet} = \frac{M_{sample}}{V_{mold}} \quad (1)$$

where  $\rho_{wet}$ ,  $M_{sample}$ , and  $V_{mold}$  represent the wet unit weight, the mass of the sample, and volume of mold, respectively.

Three 50 mm (2 in.) cubic specimens were used to determine the compressive strength for each age. The compressive strength test was performed according to ASTM C109 (ASTM C 109 2015). For each phase of this study, the compressive strength of mortar was determined at day 3, 7, 28, 56, and 90. For moist curing phases, the cubes were demolded after 24 hours and stored in a moist room until the testing day.

Accelerated curing phase specimens were demolded after 24 hours and stored under lab conditions. The compressive strength measurements were carried out using a Tinius-Olsen universal machine with a capacity of 890 kN (200 kips). The results for compressive strength represent the average values of the three specimens.

ASTM C 596 was followed to monitor drying shrinkage of the Eco-SCCM (ASTM C 596 2009). A digital extensometer was used to measure a change in length of prismatic specimens measuring 25.4 x 25.4 x 286 mm (1 x 1 x 11.25 in.). Specimens of Phase I and II were demolded after 24 hours and cured in a moist room for 7 days. Phase III specimens were demolded after 24 hours. The drying shrinkage measurements were taken after curing was completed for each phase and continued for 90 days.

The durability of Eco-SCCM was assessed by measuring surface electric resistivity. Electric resistivity is one of the intrinsic specifications of concrete that relates to its permeability (Ramezani-pour et al 2013). The electric resistivity meter was used to measure the surface resistivity of specimens at day 28, 56, and 90 for Phase I and II; however, the surface resistivity measurements were taken on day 1, 28, 56, and 90 for

Phase III. Two saturated 100 x 200 mm (4 x 8 in.) cylinders were tested. The result of surface resistivity reading for each cylinder represented the average of 24 readings (12 readings on each cylinder). The test was conducted according to AASHTO TP 95 (AASHTO TP 95 2011).

The semi-adiabatic method measured the temperature rising of hydration process. The semi-adiabatic calorimeter consisted of four receptacles in an insulated box with thermistors at the bottom of each receptacle. Two specimens were inserted for each mixture. Typically, data logging continued for approximately 48 hours after contact of cement with water. The curves of two specimens were averaged, resulting in a single hydration curve for each mixture.

### **3. EXPERIMENTAL RESULTS AND DISCUSSION**

#### **3.1. EFFECT OF OVERALL REPLACEMENT LEVELS ON THE PERFORMANCE OF ECO-SCCM**

This section highlights the combination effect of Class C fly ash and Type S hydrated lime on the performance of Eco-SCCM as shown in Table 2. All phases show a decrease in the compressive strength with increasing levels of replacement. At day 3, both Phases I and II exhibited very low strength when 75% replacement was utilized. However, phase III exhibited reasonable compressive strength at day 3. Compressive strength developed significantly after 28 days; the increase in compressive strength was more than 50% for mixtures with a replacement rate of 65% or more. This contributed to the pozzolanic reaction of fly ash with calcium hydroxide created by hydration of cement and water to produce the same cementitious compounds by the hydration of Portland cement (Islam and Islam 2010). The Late compressive strength of Phase I mixtures with

all replacement levels resulted in higher developing strength than Phase II and Phase III mixtures.

The peak hydration temperature decreased with increased cement replacement levels. The substitution of cement with 50% fly ash and hydrated lime decreased the peak hydration temperature by 9 °C (15 °F) and 17 °C (31 °F) for Phase I and Phase II hydration temperature, respectively. At the 75% replacement level, both Phase I and Phase II exhibited a substantial reduction in the peak hydration temperature. In summary, each 15% cement replacement with fly ash decreases the peak hydration temperature by approximately 3.5 and 4.2 °C (6.3 and 7.5 °F) in Phase I and Phase II, respectively.

Surface resistivity was selected to provide a rapid indication of the concrete resistance to penetration of chloride ions. Surface resistivity at 90 days was measured for each phase and results were compared. There was no obvious trend between replacement levels and surface resistivity for Phase I and II. However, a substantial increase in surface resistivity with increasing substitution of cement was observed in Phase III. The 75% cement replacement mixture had a 275% increase in surface resistivity when compared to the 100% cement mixture (Mix M1) and with the same curing regime. This may be due to ions redistributing under elevated temperature during curing. Further research must be undertaken to evaluate why this occurs.

Phase I mixtures with fly ash exhibited a considerable reduction in drying shrinkage values. More than 40% and 55% reduction of drying shrinkage was observed for 50% and 75% cement replacement mixtures, respectively. Phase II results showed a good reduction trend in the correlation between the cement replacement levels and drying

shrinkage value. Accelerated curing did not show any improvement in the drying shrinkage measurements in Phase II mixtures.

Figure 1 illustrates the correlation between the compressive strength at 3 days with peak hydration temperature of Phase I and II mixtures. It can be inferred from this figure that high generated temperature refers to high developed compressive strength at an early age. In other words, a higher peak is associated with greater reactivity. Using Type I/II cement with different fly ash proportions leads to a fair correlation ( $R^2=0.8$ ) between hydration temperature and early compressive strength. The same mixtures with Type III cement was  $R^2=0.69$ .

Data points of measured surface resistivity at different ages were plotted against the compressive strength of the same mixtures. A correlation was found between these properties, as shown in Figure 2. The relation is linear, which suggests that a predictor model is possible. The relation is given by Eq. (2). Even though it is not a strong relation, it can be used as a good point to predict the surface resistivity that relies on compressive strength or vice versa.

$$\text{Compressive strength} = 0.67 \text{ surface resistivity} + 32.3 \quad (2)$$

### **3.2. EFFECT OF FLY ASH REPLACEMENT LEVELS ON THE PERFORMANCE OF ECO-SCCM**

The effect of cement substitution with Class C fly ash is presented in this section. Hydrated lime was kept constant for all mixtures. A level of 10% hydrated lime was used to compare phase results. Compressive strength was observed at different ages. Figure 3 plots the compressive strength vs. replacement levels at 3, 28, and 90 days. At 3 days' age, Phase III mixtures exhibited higher compressive strength than both Phases I and II,

especially at 55% and or more replacement levels. This is because the curing type of Phase III accelerated the compressive strength at an early age. As apparent, Phase II mixture with 75% did not develop sufficient strength to meet any application requirements. Compressive strength increased gradually after 3 days. In general, Phase II mixture (mixtures with Type III cement) exhibited a higher developing strength rate than Phase I and III because Type III cement has higher fineness than Type I/II cement, thereby increasing the reactivity of Portland cement to produce more calcium hydroxide, which reacts with fly ash. As expected, accelerated curing affected late compressive strength compared to moist curing compressive strength results. Almost all mixtures of Phase I experienced higher compressive strength at 90 days than Phase III mixtures.

The effect of fly ash on drying shrinkage of Eco-SCCM is presented in Figure 4. As expected, increasing the fly ash substitution minimized drying shrinkage in all phases. Mixtures with 63% replacement exhibited the lesser amount of drying shrinkage than mixtures with 0%, 55%, and 75% replacement. In general, mixtures with moist curing (Phases I and II) had lower drying shrinkage than mixtures with an accelerated curing regime. High-level cement replacement levels (63% and 75%) showed a lower amount of drying shrinkage than other levels (0% and 55%). For 0% fly ash mixtures, accelerated curing did not improve the drying shrinkage property. Regarding the rate of drying shrinkage, the rates were balanced after 28 days for all three phases.

The results for the typical effect of fly ash on surface resistivity are shown in Figure 5. Phase I surface resistivity results followed a descending trend with fly ash replacement level. However, a considerable ascending trend in correlation was observed in Phase III surface resistivity results. As mentioned in the previous section, further

research needs to be undertaken to explain the significant increase in surface resistivity of Eco-SCCM when cured under an accelerated regime. Using Type III cement slightly improved the surface resistivity, especially with 55% replacement.

Typically, the activity of hydration reaction during the first days can be estimated by the peak hydration temperature. A correlation between peak hydration temperature and fly ash replacement level was explored in Figure 6. A strong correlation was found for both Phase I and II ( $R^2=0.99$  and  $R^2=0.98$ ). As expected, increasing the fly ash replacement level delays cementitious material reactivity since the rate of strength gain for fly ash is relatively slower at earlier ages.

### **3.3 EFFECT OF ADDING HYDRATED LIME TO ECO-SCCM**

The addition of hydrated lime provided additional calcium to the system to aid in complete hydration of the fly ash with low content of cement in the mixture (Holland et al. 2012). Two different dosages were used in each mixture of the same replacement level (high and low dosages). Figure 7-a displays the compressive strength results of Phase I for different cement replacements with two dosages of hydrated lime. Increasing the hydrated lime dosage from 5% to 7% slightly improved the compressive strength for 75% cement replacement at all ages. The 15% hydrated lime with 65% cement replacement did not show any considerable improvement compared to 10% dosage. There was no improvement for the 50% cement replacement and even a small decrease in compressive strength compared to 0% hydrated lime dosage. Phase II compressive strength results are illustrated in Figure 7-b. The same behaviors of Phase I with 65% and 75% cement replacements were observed in Phase II with the same replacement levels. However, the 50% cement replacement showed a considerable increase when adding hydrated lime by

7% by weight. The increase was observed with all ages of 50% cement replacement mixture. Figure 7-c displays the compressive strength results of Phase III. Almost the same observations in Phase I were found in Phase III when adding hydrated lime to the Eco-SCCM.

The effect of hydrated lime on drying shrinkage of Eco-SCCM is displayed in Figure 8. Each cement replacement level was studied under two dosages of hydrated lime. In the case of Phase I and Phase II, drying shrinkage decreased with increasing the hydrated lime dosage for replacement levels of 50%, 63%, and 65%. However, an increase was observed with 75% replacement mixtures of both phases. A slight reduction in drying shrinkage was observed in Phase III mixtures of 50% and 75% replacement level. However, mixtures of 65% replacement level showed an increase in drying shrinkage with increased hydrated lime.

The typical effect of hydrated lime on surface resistivity is shown in Figure 9. Different behavior was observed in each phase. In all phases, increasing hydrated lime from 5% to 15% decreased the surface resistivity. However, increasing hydrated lime dosage improved surface resistivity in 50% cement replacement. There is an ascending trend in correlation in surface resistivity with decreasing hydrated lime dosages only in Type III cement. As hydrated lime levels increased, peak hydration temperature also increased, except for mixtures of 65% replacement with 15% hydrated lime, as can be seen in Table 3.

#### **4. STATISTICAL DATA ANALYSIS**

A statistical approach was used in this study to optimize the binder compositions. Based on the analysis of the data through a statistically planned experimental program,



different combinations of key factors (Portland cement, fly ash, and hydrated lime) were varied, and several responses were selected to evaluate the performance of Eco-SCCM. Selected responses were a compressive strength, drying shrinkage, cost, surface resistivity, and fresh unit weight of Eco-SCCM (Ghafari et al. 2015).

A desirability function approach (DFA) was selected as a powerful approach to conducting the statistical analysis of this study. DFA is used to optimize multiple quality characteristic problems. In DFA, the estimated responses are transformed into a scale-free value called desirability ( $d_i$ ) that ranges from 0 to 1 and depends only on the closeness to lower and upper limits. A desirability value of 1 represents a completely desirable or ideal response value while 0 represents an undesirable value (one or more responses are outside their acceptance limit) (Nehdi and Summer 2002; Sengottuvel et al. 2013; Sengottuvel et al. 2012; ChittaranjanDas 2016).

The use of various desirability functions depends on whether a partial response is to be maximized, minimized, or assigned to a target value. The current study used a class of desirability function proposed by Derringer and Suich (Derringer and Suich 1980) as presented in Eq. 3:

$$D = (d_1^{k_1} * d_2^{k_2} * d_3^{k_3} \dots \dots \dots d_n^{k_n})^{-\sum k_i} \quad (3)$$

where  $n$  denotes the number of responses included in optimization and  $k_i$  is the relative importance of each individual function's  $d_i$ . Importance ( $k_i$ ) varies from 1 to 5, with 1 being least important and 5 being most important. There are multiple ways to determine the desirability function depending on the goal desired. A response can be one of the following: maximum, minimum, target, or in range. In this study, the desired responses (compressive strength, surface resistivity, and fresh unit weight) were

maximized and drying shrinkage and cost were minimized. Both responses and variables with their maximum and minimum limits required for performing numerical optimization are tabulated in Table 4.

To obtain the overall desirability, the data of each phase was analyzed by Design Expert software (version 10). Figure 10 displays the desirability results of each phase separately. Based on input data and desirability analysis, different optimum solutions were suggested depending on optimum performance. A high performance of Eco-SCCM was found with the proportion of 37% Portland cement, 63% fly ash, and 0% hydrated lime. These proportions gave 0.408 desirability function. Phase I mixtures expressed higher desirability functions than both Phase II and Phase III.

## **5. CONCLUSIONS**

The performance of cement-based mixtures with high amounts of fly ash (more than 50%) is presented in this study. To increase the hydration activity of the cement-based mixtures with high volume fly ash, two curing regimes and two Portland cement types were investigated.

The desirability function approach for optimizing of several responses revealed that it was possible to optimize the performance of Eco-SCCM with a high amount of fly ash. This approach can be applied and simultaneously maximizing the compressive strength and the surface resistivity, and minimizing the drying shrinkage and the cost of concrete mixtures. Results also indicate that incorporating hydrated lime with Eco-SCCM did not significantly improve the overall performance of Eco-SCCM.

The best overall performance was found for a binary system containing 37% Type I/II cement and 63% fly ash under a moist curing regime. These compositions can ensure

higher compressive strength and surface resistivity and lower drying shrinkage and cost. Adopting such binder in concrete applications can enhance the sustainability of cement-based materials.

Based on the results of this study, the substitution level of the fly ash can be increased to more than 50%. Such increase of the substitution level can ensure lower consumption of Portland cement and as a result, lower CO<sub>2</sub> emission and energy consumption associated with cement manufacturing. In addition, optimized self-consolidating concrete mixture with a high cement replacement and with a target compressive strength of 41-48 MPa (6-7 ksi) can be successfully achieved in the laboratory for application to the field. This type of concrete can be used for most of the bridge components (column, wall, cap, and deck slab) and precast applications.

Table 1. Mixture Proportion Combinations

Phase	Mix ID	Cementitious Materials, by weight (%)			Cement Type	Curing Regime
		PC	CFA	HL		
Phase I	1-M	100	0	0	Type I/II	Moist Curing
	2-M	25	68	7	Type I/II	Moist Curing
	3-M	40	45	15	Type I/II	Moist Curing
	4-M	37	59	4	Type I/II	Moist Curing
	5-M	50	43	7	Type I/II	Moist Curing
	6-M	35	50	15	Type I/II	Moist Curing
	7-M	37	56	7	Type I/II	Moist Curing
	8-M	37	53	10	Type I/II	Moist Curing
	9-M*	35	60	5	Type I/II	Moist Curing
	10-M*	45	45	10	Type I/II	Moist Curing
	11-M	25	65	10	Type I/II	Moist Curing
	12-M*	50	50	0	Type I/II	Moist Curing
Phase II	1-III	100	0	0	Type III	Moist Curing
	2-III*	45	45	10	Type III	Moist Curing
	3-III	50	50	0	Type III	Moist Curing
	4-III	37	53	10	Type III	Moist Curing
	5-III	25	68	7	Type III	Moist Curing
	6-III*	25	65	10	Type III	Moist Curing
	7-III*	35	60	5	Type III	Moist Curing
	8-III	50	43	7	Type III	Moist Curing
	9-III	35	50	15	Type III	Moist Curing
	10-III	40	45	15	Type III	Moist Curing
Phase III	1-A	100	0	0	Type I/II	Accelerated Curing
	2-A	25	68	7	Type I/II	Accelerated Curing
	3-A	40	45	15	Type I/II	Accelerated Curing
	4-A	37	59	4	Type I/II	Accelerated Curing
	5-A	50	43	7	Type I/II	Accelerated Curing
	6-A	35	50	15	Type I/II	Accelerated Curing
	7-A	37	56	7	Type I/II	Accelerated Curing
	8-A	37	53	10	Type I/II	Accelerated Curing
	9-A*	35	60	5	Type I/II	Accelerated Curing
	10-A*	45	45	10	Type I/II	Accelerated Curing
	11-A	25	65	10	Type I/II	Accelerated Curing
	12-A*	50	50	0	Type I/II	Accelerated Curing

Notes: PC is Portland cement; CFA is Class C fly ash; HL is Type S hydrated lime; \* Mix was replicated.

Table 2. Effect of Overall Replacement Levels on the Performance of Eco-SCCM

Property	Phase I					Phase II					Phase III				
	0	50	55	65	75	0	50	55	65	75	0	50	55	65	75
Mix ID	1-M	12-M	10-M	9-M	2-M	1-III	3-III	2-III	7-III	6-III	1-A	12-A	10-A	9-A	2-A
Compressive Strength (3 days)	40.4	22.0	30.1	19.6	5.4	62.6	30.9	36.1	21.8	0.8	44.7	31.0	38.1	31.9	22.5
Compressive Strength (28 days)	58.5	48.5	51.9	49.1	28.5	83.8	53.0	61.2	41.0	30.0	70.9	55.6	51.0	46.8	39.2
Compressive Strength (90 days)	80.9	64.1	63.7	64.6	43.7	87.7	63.0	68.7	53.7	34.8	71.7	59.3	58.1	52.9	47.5
Peak Hydration Temperature	41.23	32.43	32.08	29.29	23.82	47.35	30.22	31.13	30.67	23.26	41.23	32.43	32.08	29.29	23.82
Surface Resistivity (90 days)	56.57	48.00	54.57	48.93	34.45	51.18	43.10	65.71	44.16	53.30	60.16	75.54	88.16	114.23	168.15
Drying Shrinkage (90 days)	790	468	507	420	356	790	678	522	493	468	717	820	678	707	615

Table 3. Effect of Hydrated Lime Dosages on Peak Hydration Temperature for Different Replacement Levels

Replacement Level, %	Hydrated Lime, %	Peak Hydration Temperature, °F Phase I	Peak Hydration Temperature, °F Phase II
75	7	23.8	26.5
	10	26.9	28
65	5	29.3	28.2
	15	28.8	24.2
63	4	29.2	---
	10	29.5	---
50	0	32.9	30.2
	7	33.4	34.4

Table 4. Range of Key Factors and Responses for Desirability Function

Parameter	Limit		Criteria		
	Low	High	Goal	Weight	Importance
Cement (%)	25	50	Minimize	1	+++
Fly Ash (%)	40	75	In range	n.a.	n.a.
Hydrated Lime (%)	0	15	In range	n.a.	n.a.
Compressive	28	55	Maximize	4	++++
Drying Shrinkage	288	507	Minimize	2	++
Surface resistivity	35	55	Maximize	3	+++
Fresh Unit Weight	2114	2211	Maximize	1	+
Mini Slump (mm)	108	170	maximize	1	++++
Cost* (\$/kg)	0.045	0.057	Minimize	1	+

\*Based on local material cost, the total cost of each mix was calculated. For example, cement cost equals to \$11.5 per bag of 43 kg (94 lb), fly ash cost equals 40% of cement cost, hydrated lime has the same cement cost, and the HRWR cost about \$13.5 per 3.78 liters (1 gallon).

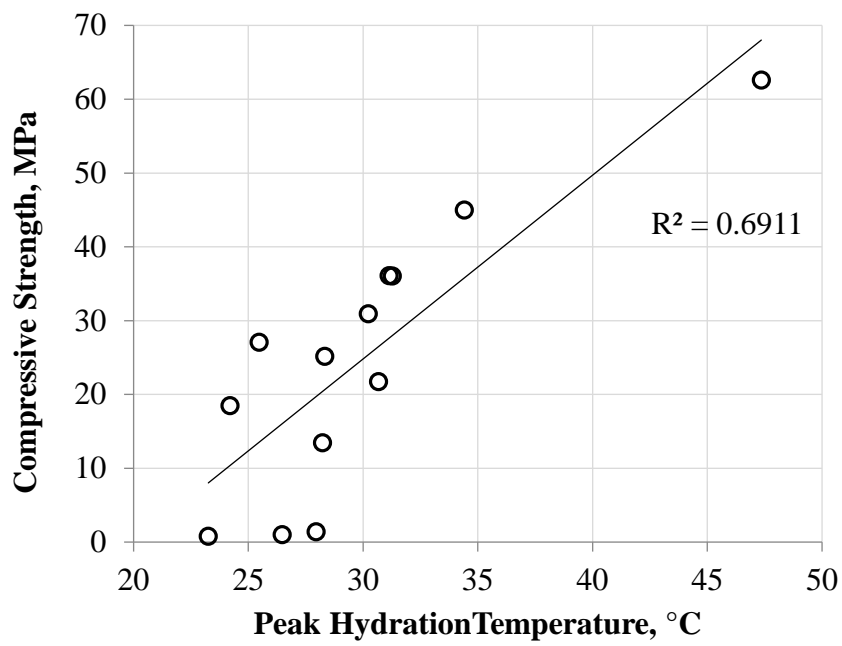
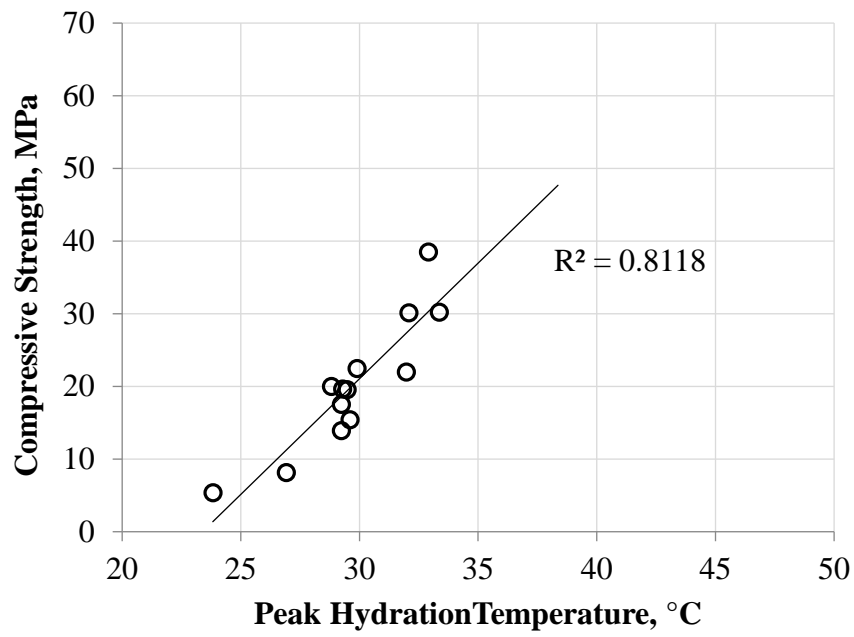


Figure 1. Day 3 compressive strength versus peak hydration temperature: (a) Phase I; (b) Phase II

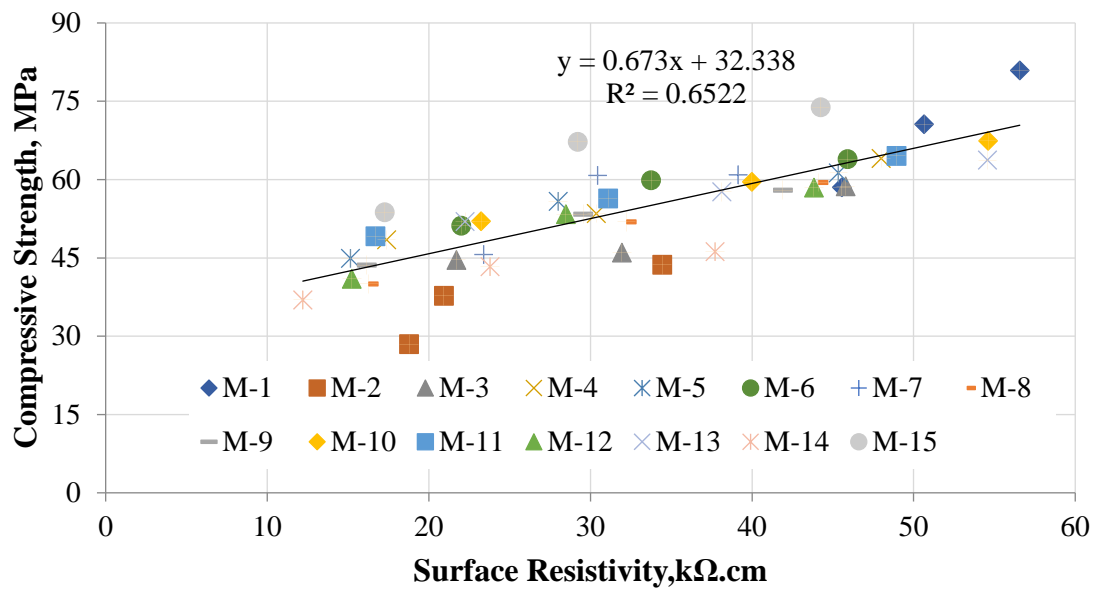
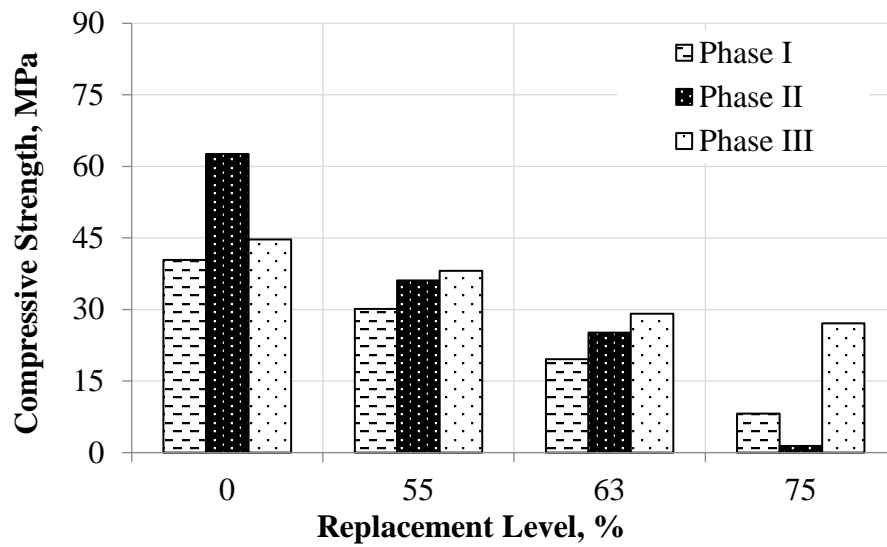


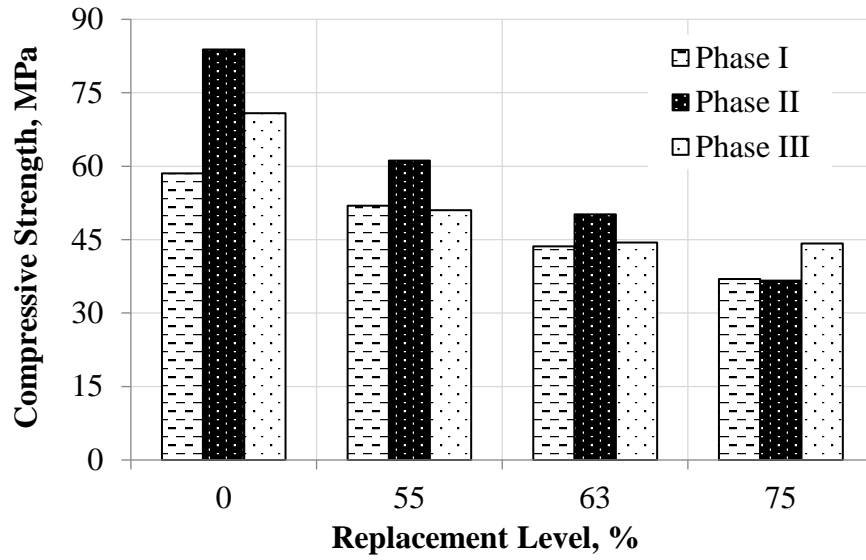
Figure 2. Relation between compressive strength and surface resistivity



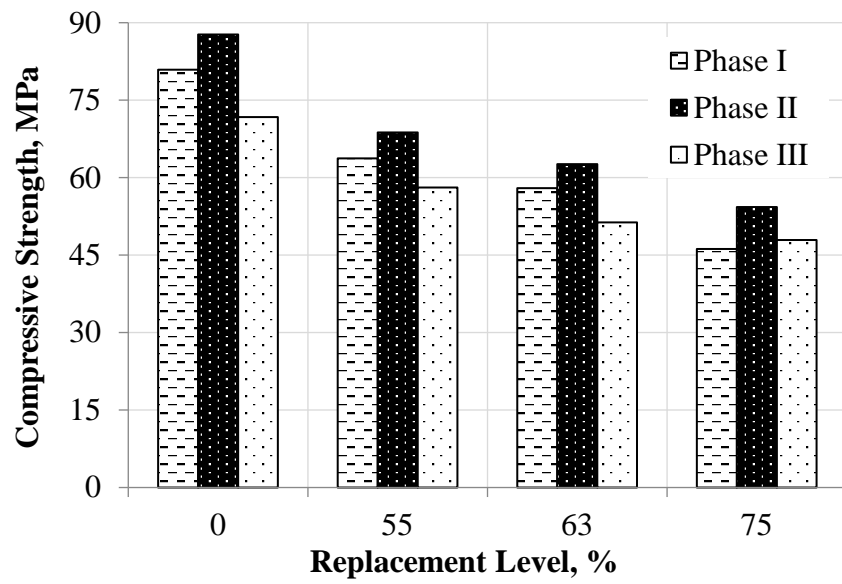
(a) Day 3 compressive strength

Figure 3. Compressive strength versus replacement levels



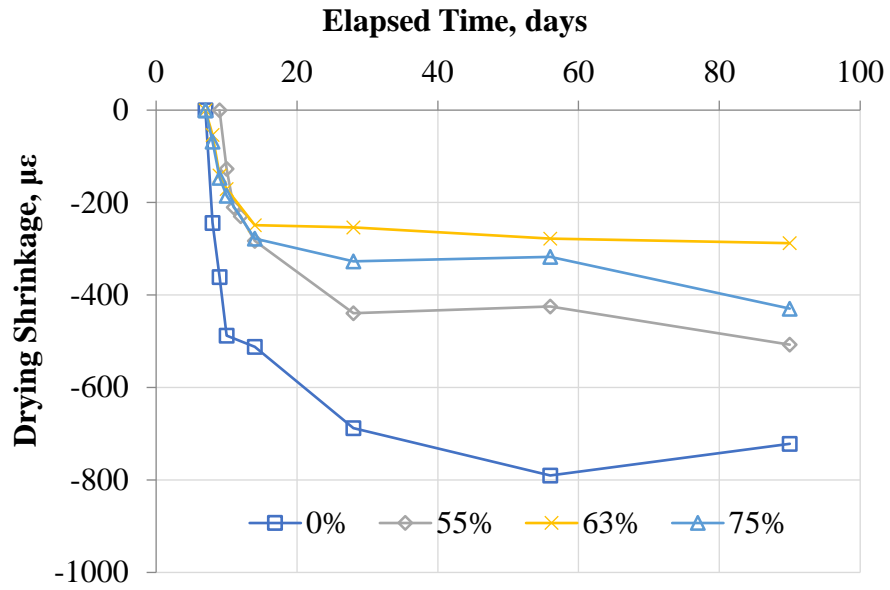


(b) Day 28 compressive strength

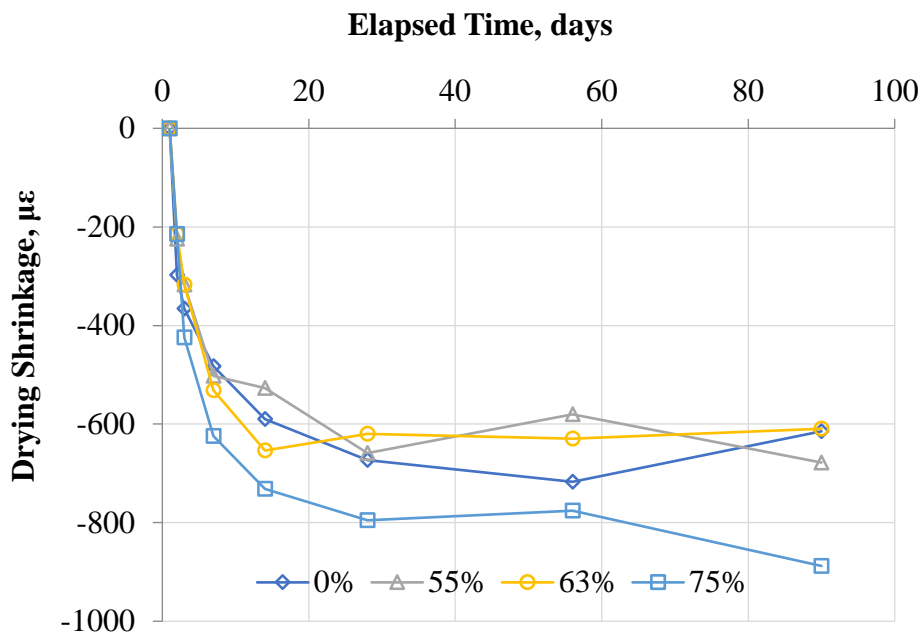


(c) Day 90 compressive strength

Figure 3. Compressive strength versus replacement levels (cont.)

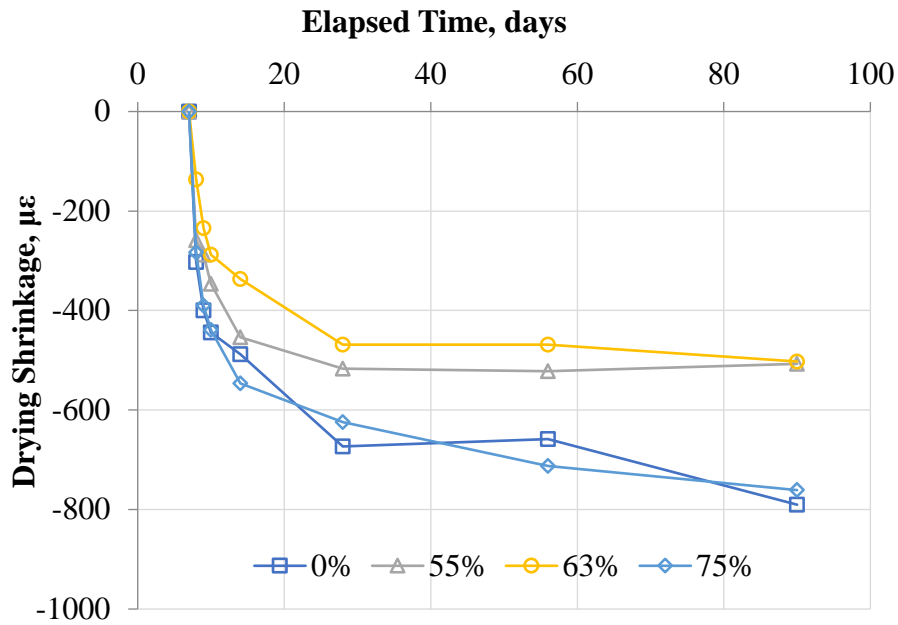


a) Phase I



b) Phase II

Figure 4. Drying shrinkage at different replacement levels



c) Phase III

Figure 4. Drying shrinkage at different replacement levels (cont.)

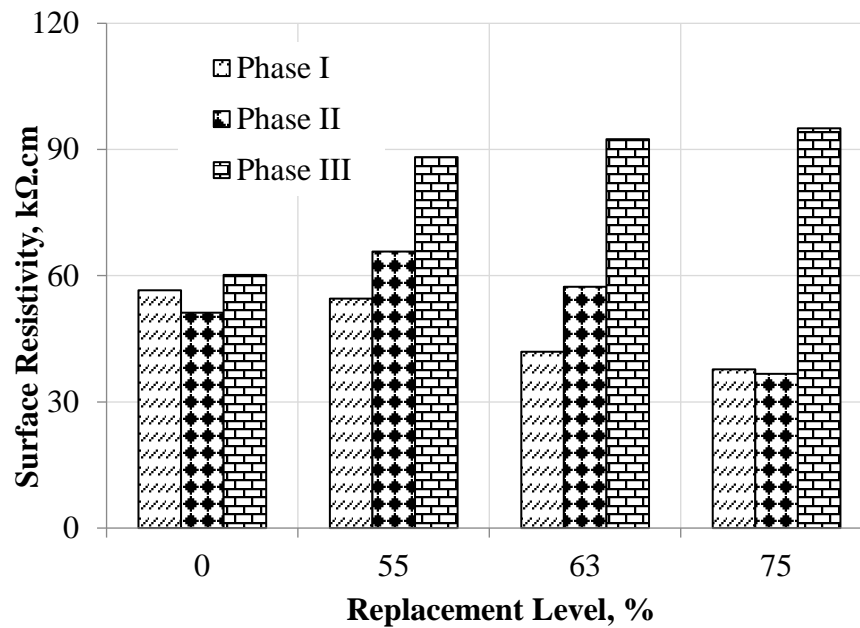


Figure 5. Comparison of surface resistivity of the three phases at different replacement levels

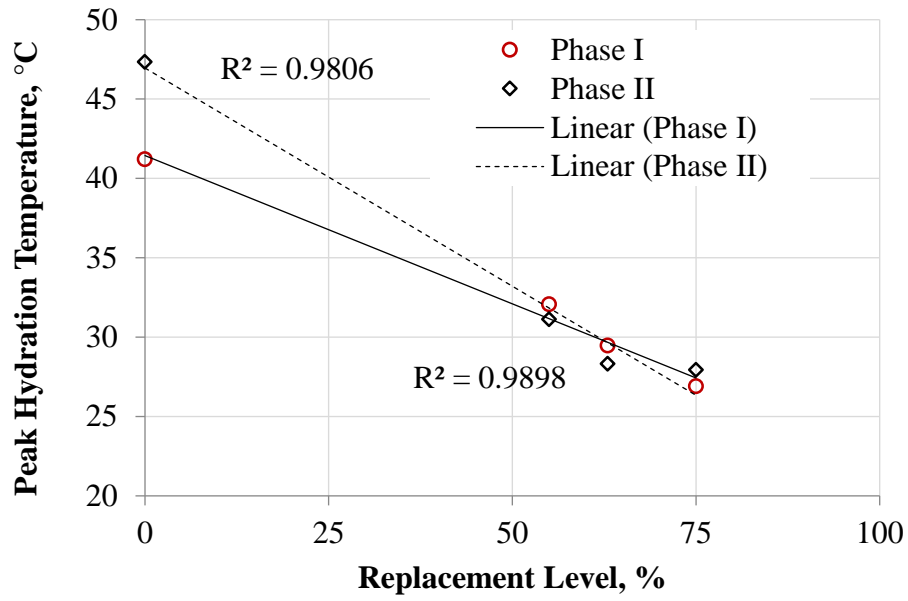


Figure 6. Relation between peak hydration temperatures under different replacement levels

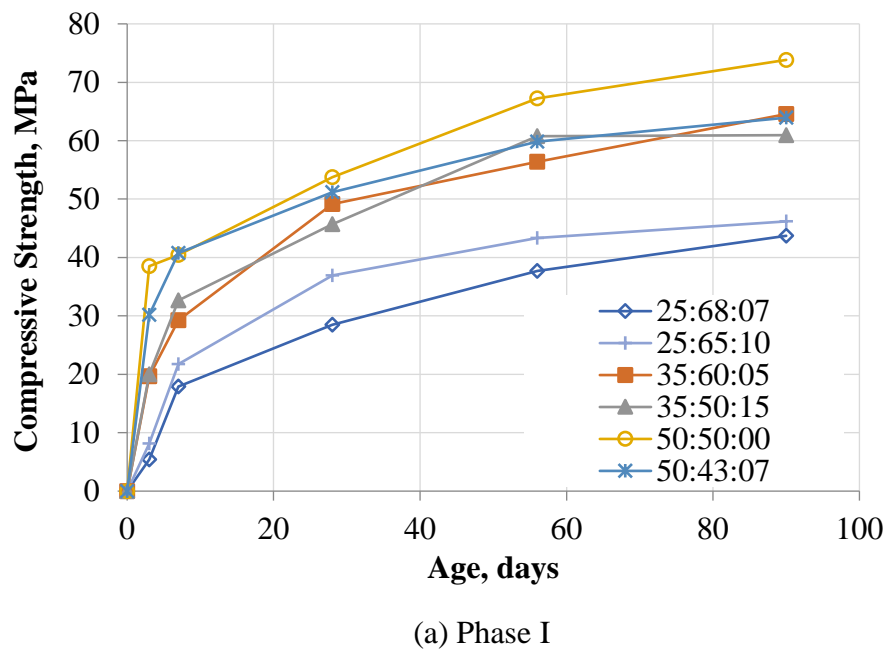
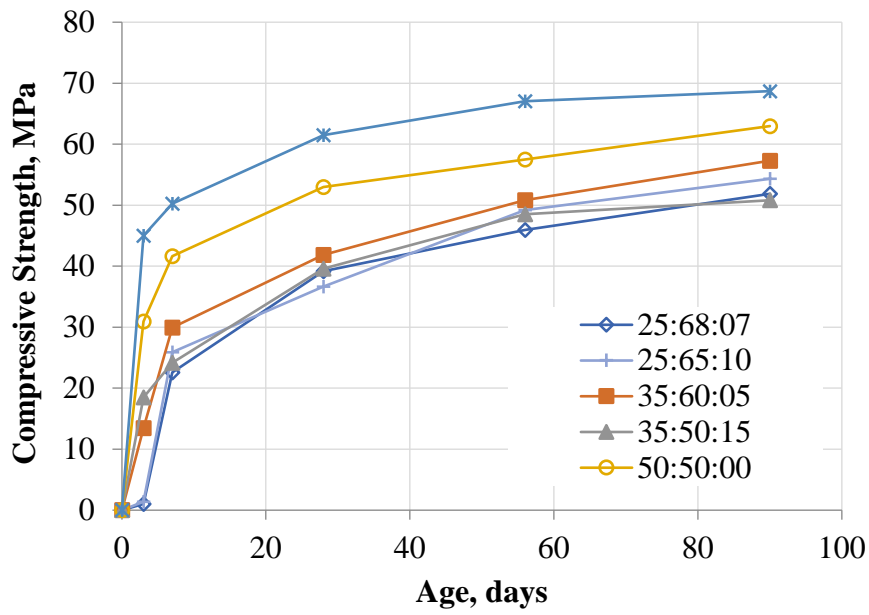
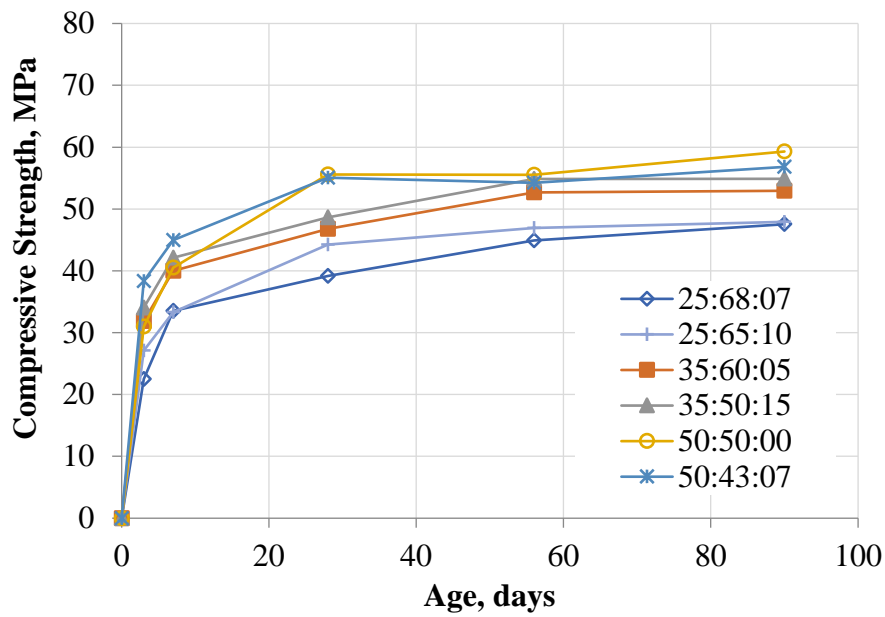


Figure 7. Effect of hydrated lime dosages on compressive strength for different replacement levels

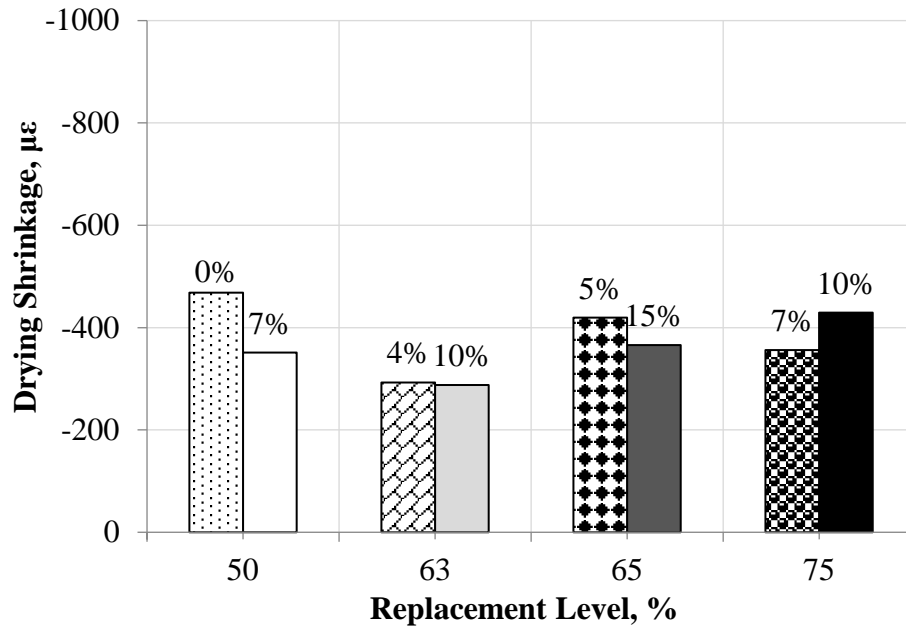


(b) Phase II

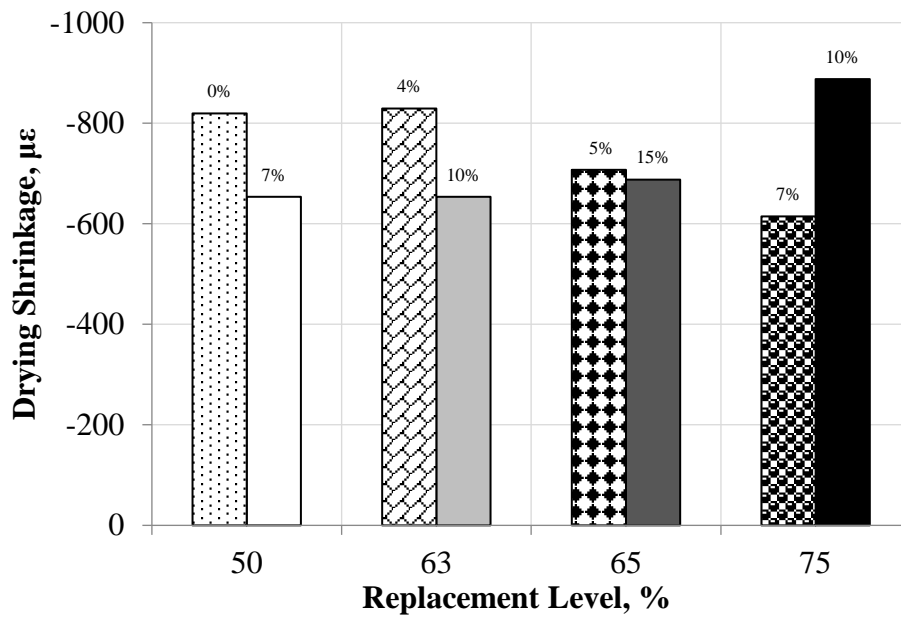


(c) Phase III

Figure 7. Effect of hydrated lime dosages on compressive strength for different replacement levels (cont.)

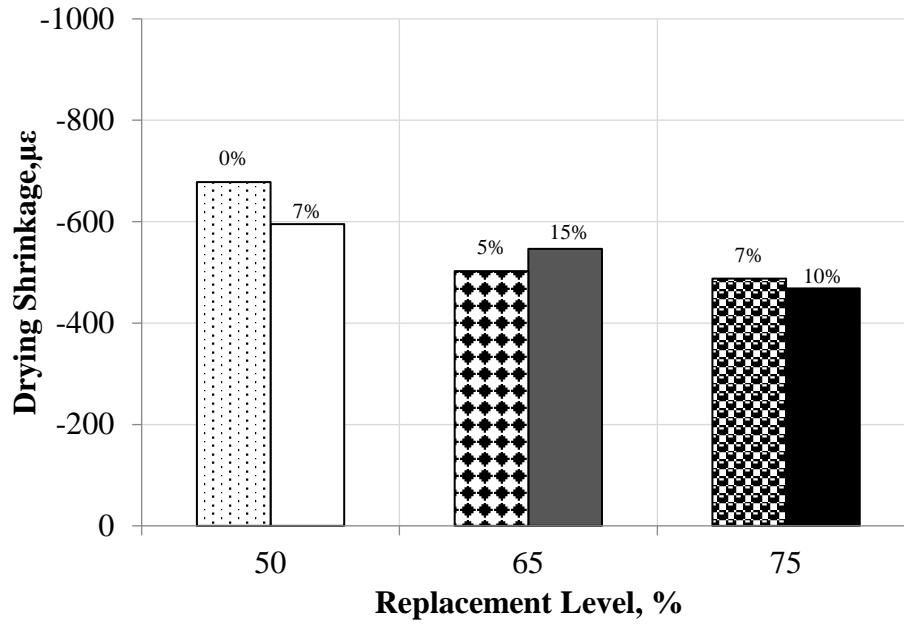


(a) Phase I



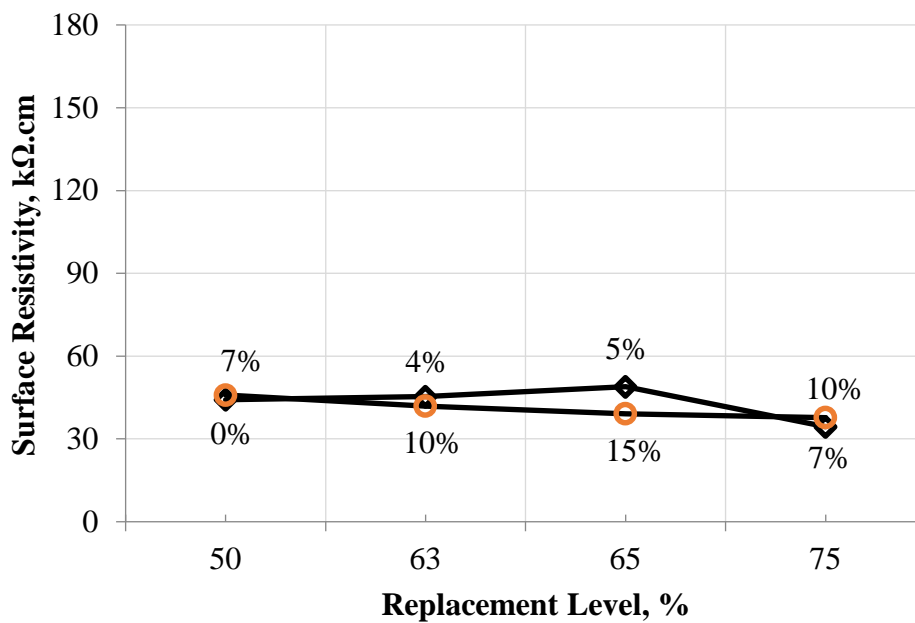
(b) Phase II

Figure 8. Effect of hydrated lime dosages on drying shrinkage for different replacement levels



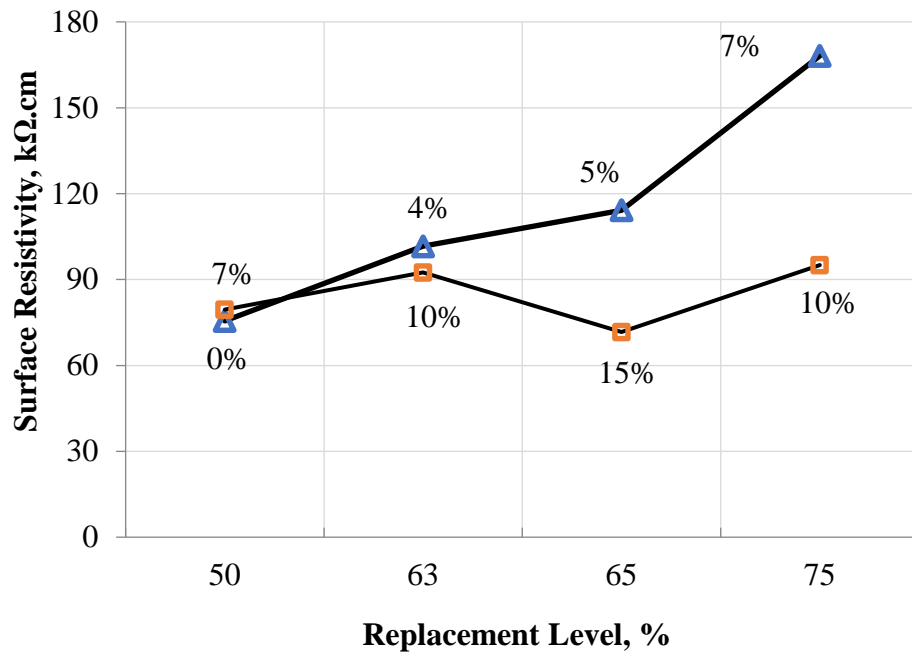
(c) Phase III

Figure 8. Effect of hydrated lime dosages on drying shrinkage for different replacement levels (cont.)

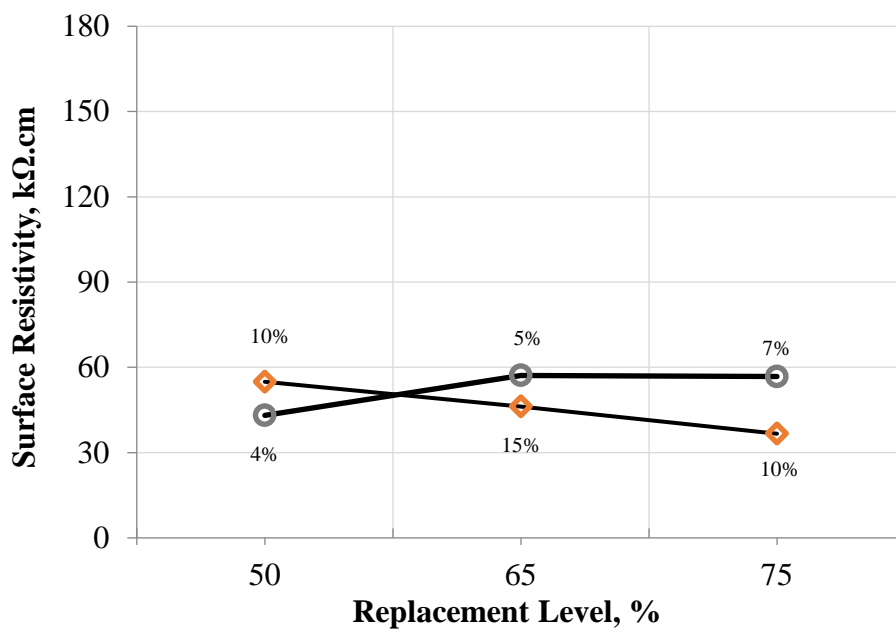


(a) Phase I

Figure 9. Effect of hydrated lime dosages on surface resistivity for different replacement levels



(b) Phase II



(d) Phase III

Figure 9. Effect of hydrated lime dosages on surface resistivity for different replacement levels (cont.)



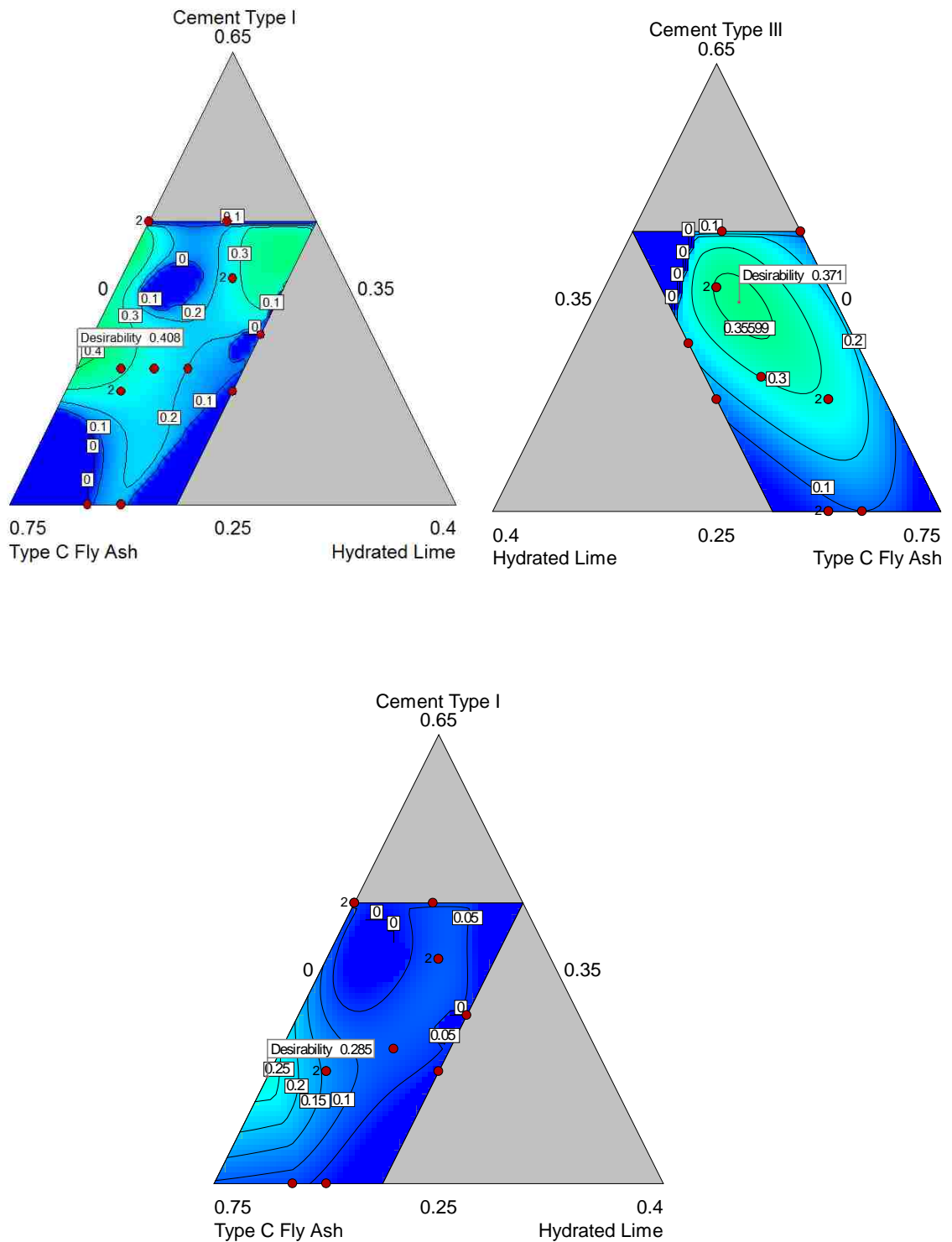


Figure 10. Desirability-function graphs for the optimization of the Eco-SCCM within the design ranges: (a) Phase I; (b) Phase II; (c) Phase III

## ACKNOWLEDGMENTS

The writers gratefully wish to acknowledge the financial support provided by the Missouri Department of Transportation (MoDOT) and the National University Transportation Center (NUTC) at the Missouri University of Science and Technology (Missouri S&T). The authors also wish to thank the Department of Civil, Architectural, and Environmental Engineering and the Center for Infrastructure Engineering Studies at Missouri S&T for their support. The conclusions and opinions expressed in this study are those of the authors and do not necessarily reflect the official views or policies of the funding institutions.

## REFERENCES

- AASHTO (2011). "Standard Method of Test for Surface Resistivity Indication of Concrete's Ability to Resist Chloride Ion Penetration." TP 95, Washington, DC.
- AASHTO. (2010). AASHTO LRFD bridge design specifications, 4th Ed., Washington, DC.
- ACI (American Concrete Institute) (2003). "Use of Fly Ash in Concrete." ACI Committee 232, Farmington Hills, MI.
- ASTM (2009). "Standard Test Method for Drying Shrinkage of Mortar Containing Hydraulic Cement." C596, West Conshohocken, Pa.
- ASTM (2015). "Standard Test Method for Compressive Strength of Hydraulic Cement Mortars (Using 2-in. or [50-mm] Cube Specimens)." C109/C109M, West Conshohocken, Pa.
- ASTM (2015). "Standard Test Method for Flow of Hydraulic Cement Mortar." C1437/C1437M, West Conshohocken, PA.
- Benhelal, E., Zahedi, G., Shamsaei, E., Bahadori, A. (2013). "Global strategies and potentials to curb CO<sub>2</sub> emissions in cement industry." *Journal of Cleaner Production*, Vol. 51, 142-161.
- Bentz, D.P. (2007). "Internal curing of high-performance blended cement mortars." *ACI Materials Journal*, 104(4), 408.
- ChittaranjanDas, V. (2016). "Response surface methodology and desirability approach to optimize EDM parameters." *International Journal of Hybrid Information Technology*, Vol. 9(4), 393-406.
- Derringer, G. and Suich, R. (1980). "Simultaneous optimization of several response variables." *Journal of Quality Technology*, Vol. 12(4), 214-219.

Fantilli, A.P. and Chiaia, B. (2013). "Eco-mechanical performances of cement-based materials: An application to self-consolidating concrete." *Construction and Building Materials Journal*, Vol. 40, 189-196.

Ghafari, E., Costa, H., and Júlio, E. (2015). "Statistical mixture design approach for eco-efficient UHPC." *Cement and Concrete Composites Journal*, Vol. 55, 17-25.

Holland, N., Nichols, A. and Nichols, J. (2012). "The use of hydrated lime in concrete as a cement replacement: effect on compressive strength." ASTM Committee C07.

Hwang, S. D., Khatib, R., Lee, H. K., Lee, S., and Khayat, K. (2012). "Optimization of steam-curing regime for high-strength, self-consolidating concrete for precast, prestressed concrete applications." *PCI journal*, 57(3), 48-62.

Islam, M.M. and Islam, M.S. (2010). "Strength behavior of mortar using fly ash as partial replacement of cement." *Concrete Research Letters*, Vol. 1(3), 98-106.

Nehdi, M. L. and Summer, J. (2002). "Optimization of ternary cementitious mortar blends using factorial experimental plans." *Materials and Structures Journal*, Vol. 35(8), 495-503.

Ramezani pour, A., Khazali, M. and Vosoughi, P. (2013). "Effect of steam curing cycles on strength and durability of SCC: A case study in precast concrete." *Construction and Building Materials Journal*, Vol. 49, 807-813.

Richardson, D. N., Beckemeier, K. W., and Volz, J. S. (2015). "Effects of powder additive on high volume fly ash mixtures." *ACI Materials Journal*. 112(4).

Rubenstein, M. (2012). "Emissions from the cement industry." The Earth Institute of Columbia University. <<http://blogs.ei.columbia.edu>>

Sajedi, F., Razak, H. A., Bin Mahmud, H., and Shafiq, P. (2012). "Relationships between compressive strength of cement-slag mortars under air and water curing regimes." *Construction and Building Materials Journal*, Vol. 31, 188-196.

Sengottuvel, P., Satishkumar, S. and Dinakaran, D. (2013). "Optimization of multiple characteristics of EDM parameters based on desirability approach and fuzzy modeling." *Procedia Engineering*, Vol. 64, 1069-1078.

Sengottuvel, P., SatishKumar, S. and Dinakaran, D. (2012). "Optimization of electrical discharge machining process parameters using desirability approach." *Applied Mechanics and Materials*, Vol. 159, 176-180.

Vaughn, N., and Polnaszek, C., (2010). "Design-Expert® software version 10- Stat-Ease." Minneapolis, MN.

Wilson, M. L., Kosmatka, S. H., (2011). "Design and control of concrete mixtures." Portland Cement Association, 15<sup>th</sup> edition. Washington, DC.

## II. SHEAR BEHAVIOR OF FULL-SCALE HIGH VOLUME FLY ASH-SELF CONSOLIDATING CONCRETE (HVFA-SCC) BEAMS

Hayder H. Alghazali and John J. Myers

### ABSTRACT

An experimental test was carried out to investigate the shear behavior of full-scale beams constructed with high volume fly ash self-consolidating concrete (HVFA-SCC). HVFA-SCC is a new concrete grade of HVFA concrete with the rheology of self-consolidating concrete that satisfies the quality of construction work, environment aspects, and concrete sustainability. Mixes with different cement replacement levels of fly ash and hydrated lime [50%, 60%, and 70% (by weight)] were used. Twelve full-scale reinforced concrete beams were cast and tested using a four-point load test setup. This study focused on observing the effect of factors such as cement replacement level, longitudinal reinforcement ratio, and shear reinforcement ratio on the beam shear behavior. All beams were 4000 mm (13 ft) in length, 457 mm (18 in.) in thickness, and 305 mm (12 in.) in width. Rheological and mechanical properties of the mixes were monitored. During testing, cracking and ultimate shear, deflection, crack pattern, and mode of failure were recorded. Furthermore, test results were compared to conventional concrete study, finite element modeling, and database of conventional concrete and self-consolidating concrete.

### Highlights

- Concrete mixtures with different cement replacement levels were developed.
- Full-scale beams were constructed with HVFA-SCC and tested under shear.
- Behavior was investigated in terms of cracking and ultimate shear, deflection,

crack pattern, and mode of failure.

- Analytical prediction was compared with the experimental results.
- Experimental results were compared to conventional concrete test results study and database.

**Keywords:**

High volume fly ash concrete, self-consolidating concrete, shear strength, fly ash, hydrated lime, rheology, sustainability.

**1. INTRODUCTION**

High volume fly ash self-consolidating concrete (HVFA-SCC) is the latest version of self-consolidating concrete (SCC) and one of the new innovations in concrete technology. It can be defined as a new type of SCC that consists of carefully selected and proportioned materials, including a high amount of fly ash (50% of the total cementitious materials or more) to produce durable, strong, and environment-friendly concrete. Fly ash is a by-product material of thermal power generating stations [1]. Just in the United States, there is 50 million tons of fly ash produced each year. Only 23 million tons are used in different categories such as concrete products, soil stabilization, and agriculture; the rest is disposed of. Making an application for fly ash in concrete can provide a mean for the economical and ecological disposal of million of tons [2].

As mentioned above, HVFA-SCC is considered a new concrete type; therefore, there is no available data or conducted studies on the structural performance of HVFA-SCC. Available literature either focuses on the structural performance of high volume fly ash concrete (HVFAC) or self-consolidating concrete (SCC). Concrete with a high amount of fly ash might not perform as well concrete with 100%

cement. Several studies have been conducted to address this concern. Ortega (2012) [3] investigated the shear performance of reinforced concrete beams constructed with HVFA concrete to determine its potential use in the field. A 70% fly ash replacement of cement mixture and a 100% portland cement mixture were utilized to construct the beams. The results were compared with different design approaches common to North America and Europe. He concluded that existing design code provisions for conventional concrete were acceptable for the design of HVFAC. In this work, it was noted that rather than a very brittle abrupt failure mode with significant release of energy (i.e. a loud noise, which is commonly observed in conventional concrete), the shear failure mode of HVFAC did not demonstrate a loud brittle failure with similar significant energy release.

Arezoumandi et al. (2013a) [4] conducted an experimental study on the shear strength of full-scale beams constructed with two different fly ash content (50% and 70% by weight) and compared their results with conventional concrete (CC). A total of 12 tests were performed without stirrups and with three different longitudinal reinforcement ratios. They concluded that the HVFAC beams have comparable shear strength to the CC beams.

Regarding the use of SCC in structural members, designers are still hesitant to implement SCC in the field. There is concern among designers that SCC may not resistance strongly in shear due to the comparatively smaller amount of coarse aggregates compared to conventional concrete, which leads to relatively smooth fractured surfaces and affects the aggregate interlock mechanism, thereby reducing the shear resistance. Lin and Chen (2012) [5] studied the SCC shear behavior with two content levels of coarse aggregate (CA) (lower and higher amounts of CA) to address the issue above. A total of 24 SCC beams were tested with a rectangular

cross-section. It was found that the shear strength of beams with a higher amount of CA exhibited comparable shear strength compared to the CC beams. However, SCC beams that contained less CA experienced lower ultimate shear strength than CC beams.

In the present study of beams constructed with HVFA-SCC, two concerning issues are examined regarding the shear behavior: the high amount of fly ash and self-consolidating behavior.

## **2. RESEARCH SIGNIFICANT**

To the authors' knowledge, this is the first study that investigated the shear strength behavior of full-scale beams constructed with HVFA-SCC. This study was developed to create a basis for safely implementing of HVFA-SCC in the bridge and precast applications. In practice, this study focused on the effect of cement replacement levels (50% to 70%), longitudinal reinforcement ratio (1.62 to 2.71), and shear reinforcement ratio (with and without stirrups) regarding the shear strength contributed to the concrete.

## **3. EXPERIMENTAL WORK**

This work represents the second phase conducted on HVFA-SCC. The shear test program was similar to that described in prior work by Ortega (2012) [3] and Arezoumandi et al. (2013b) [6] for consistent benchmarking. The following sections describe the experimental work details.

### **3.1. MIX DESIGN**

The HVFA-SCC mixes were developed through an optimizing process of both the binder composition and the aggregates. The HVFA-SCC mixes were proportioned with portland cement, fly ash, and hydrated lime [7]. Table 1 illustrates the properties of the cement and fly ash. To obtain the optimum performance of the three materials,

an investigation was conducted [8]. Because of this investigation, three different cement replacement levels (50%, 60%, and 70%) were selected by weight as binder compositions. The selected binder combination represented the best performance that can enhance the sustainability of cement-based materials. In addition, fine-to-coarse aggregate ratio was also investigated to optimize the particle size distribution of the aggregates. An experimental method (gyratory compaction) was utilized to maximize the packing density of the aggregates [9]. By maximizing the packing density of the aggregates, paste volume needed to fill the voids between aggregate particles could be minimized. Figure 1 displays the relation between the packing density ( $\phi$ ) and sand-to-crushed stone ratio.

For all mixtures, portland cement Type I/II, ASTM Type C fly ash, and Type S hydrated lime were used. The specific gravity of these materials is 3.15, 2.62, and 2.4, respectively. Natural siliceous riverbed sand with specific gravity 2.61 and absorption of 1.0 was used as fine aggregate. High-quality crushed stone dolomite with a maximum aggregate size of 10 mm (3/8 in.), specific gravity of 2.68, and absorption of 1.56 was used. Polycarboxylate-base high range water reducer (HRWR) admixture was employed to enhance the workability. The HRWR had a solid mass content of 23% and specific gravity of 1.05. The HRWR dosage was adjusted for the all mixtures to achieve a minimum slump flow of 660 mm (26 in.). The hydrated lime was used to enhance the early age strength development and the internal curing [10-12]. The final design of the HVFA-SCC mixes is illustrated in Table 2. A local ready-mix concrete company provided concrete. While batching the mixtures, the dry materials (cement, fly ash, sand, and crushed stone) and three-quarter water amount were added and mixed first in the ready-mix plant. After the truck mixer arrived at the lab, the hydrated lime, the HRWR, and the rest of the water were added, and all the



materials were mixed thoroughly. The HRWR was added gradually until achieving the target flowability by vision.

### **3.2. TEST BEAM DETAILS AND MATRIX**

Twelve reinforced HVFA-SCC beams were designed in such a manner that shear failure would dominate, avoiding flexural failure. To prevent any anchorage failure within the shear failure mechanism, an optimal anchorage of the longitudinal reinforcement (bottom reinforcement) was provided using a 90° hook at the beam ends. Table 3 summarizes the test matrix of the HVFA-SCC beams. All beams were 305 mm (12 in.) wide (b) with a total depth (h) of 457 mm (18 in.). The shear span-to-depth ratio was 3.0 or greater to ensure shear failure rather than flexural failure [3]. For all beams, the longitudinal reinforcement ratio varied between 1.62 to 2.71. Number 22 (#7) bars with a yield strength of 458 MPa (66.5 ksi) were used for longitudinal reinforcement. However, number 10 (#3) bars with a yield strength of 324 MPa (47 ksi) were used as shear reinforcement (stirrups) to ensure shear failure happens first. The resultant member design for the shear beams can be seen in Figure 2. The beam designation included a combination of letters and numerics: N or S indicated to the presence of shear reinforcement (N: no stirrups, S: stirrups); 5, 6, and 8 indicated the number of 22 longitudinal reinforcement bar within the tensile area of the beam section; and 50, 60, and 70 designated the cement replacement ratio. For example, a 50% cement replacement level and no stirrups beams with five longitudinal reinforcement bars in the bottom is designated as 50-5N.

### **3.3. CASTING PROCEDURE AND CURING**

Beams were cast using tight wooden forms. The inside faces of the form were oiled to prevent water absorption, and silicon materials were used in the corner to prevent any leakage. The reinforcement was carefully placed inside the forms, and

concrete was cast from one side without any compaction and in one lift; the concrete was allowed to flow from one end to the other end. The HVFA-SCC filled the forms with ease movement around reinforcing bars in each reinforcement configuration. Immediately after concrete was delivered, the rheological properties (slump flow, T50, J-Ring, and L-Box) were measured. After five hours, the beams were covered with a wet burlap mat for three days. Then, the beams and companion specimens were stripped and stored in the laboratory atmosphere up to the age of testing. Before testing, the beams were painted white to facilitate detection of the cracks.

### **3.4. INSTRUMENTATION AND TEST SETUP**

The instrumentation was provided to measure the applied load, deflection in the beam, and strain in the reinforcement. A linear strain gauge adhered on stirrups and main reinforcement. For beams with stirrups, the strain gauges were positioned vertically on the stirrups and as close as possible to the anticipated crack path. However, the strain gauges on the longitudinal reinforcement were installed on the lower layers of the reinforcement. Linear variable displacement transducers (LVDTs) were attached to the beam well below the compression zone [125 mm (5 in.) from the top] to measure deflection during testing. Both strain gauges and LVDTs were connected to a data acquisition system where the strains in the reinforcement, beam deflection, and load information were recorded.

### **3.5. TESTING PROCEDURE**

All the beams were simply supported and tested in a four-point bending configuration as shown in Figure 3. Two 649 kN (146 kips) servo-hydraulic actuators applied the load. The actuators intended to apply the two-point loads to the beams. The load was applied using a displacement rate of 0.50 mm/min (0.02 in./min) and the automatic data acquisition system recorded data every second. After each 22 kN (5

kips) load increment, the propagating cracks were marked, and their current terminal length and the current load was specified.

## **4. EXPERIMENTAL RESULTS AND DISCUSSION**

### **4.1. HVFA-SCC PROPERTY TEST RESULTS**

The measured fresh properties of HVFA-SCC mixtures that were assessed included consistency, passing ability, filling ability, unit weight, and entrapped air content. ASTM procedures were followed to assess these properties [13-16]. The fresh concrete properties of the HVFA-SCC are presented in Table 4. HVFA-SCC mixtures exhibited excellent rheological properties that satisfy the requirements of most precast and bridge applications. The mix with a 70% cement replacement level exhibited comparable compressive strength compared to a mix of 50% replacement level because the increase in hydrated lime increased the hydration activity of the fly ash. Figure 4 displays the development of compressive strength with time. ASTM C39 [17] was followed to measure the concrete compressive strength. Table 5 summarizes cracking shear force (shear force at the first diagonal crack) ultimate shear, maximum mid-span deflection at failure, the angle of inclined crack, and at which side of the beam failure occurred. All of the tested beams failed in shear. In general, there was no major difference in the cracking and ultimate shear forces for the same reinforcement details with the increase of cement replacement levels.

Beams with shear reinforcement exhibited high shear resistance, and the shear reinforcement contributions were about two times the concrete shear resistance despite the cement replacement levels. In this study, the minimum shear reinforcements ( $s=d/2$ ) were used in the beam's design.

In terms of crack propagation, the fine vertical flexural crack started to propagate at an early stage of loading and appeared around the mid-span of the

beams. With the increase in load, flexural-shear cracks were also formed in the vertical direction. With further increase in load, those flexural-shear cracks started to incline and penetrate toward the compression zone of the beam near the loading point. More diagonal cracks began to form separately in an area close to the support.

For beams without stirrups, failure occurred after a little increase in the load that causes the formation of diagonal cracks. However, failure occurred in beams with stirrups in the test region after all measured strain of shear reinforcements crossing the critical diagonal crack exceeded the yielding limit.

The crack angle of the inclined shear cracks in the beams without shear reinforcements ranged between 21 to 26 degrees. It was observed that the crack angle increased with the presence of shear reinforcement between 12-22%. Figure 5 illustrates the cracks' profiles of the all HVFA-SCC beams at failure stage. It worth noting that beams with 60% and 70% cement replacement had more flexural and flexural-shear cracks than beams with 50% cement replacement. The reason behind this phenomenon can be attributed to the dosage of hydrated lime used in these mixes, which can help increase the bond between concrete and steel reinforcement.

Regarding the maximum mid-span deflection, beams with 70% cement replacement exhibited more deflection than other beams, which can be clearly observed from the number and distribution of the cracks in this type of beams

Although the longitudinal reinforcement ratios ( $\rho$ ) varied from 1.59 to 2.71, results did not conclusively show a relation or trend between ultimate shear force and longitudinal reinforcement ratios. This is attributed to a weaker aggregate interlock mechanism due to the presence of lower coarse aggregate content and size. In contrast, longitudinal reinforcement ratios had an obvious effect on cracking shear

and the maximum mid-span deflection. Increasing the  $\rho$  led to increased cracking shear and decreased maximum deflection.

#### 4.2. COMPARISON TO CONVENTIONAL CONCRETE BEAMS

To provide further verification to the results of the HVFA-SCC shear study, the results of the present study were compared to a shear behavior study conducted by Ortega [3]. Ortega constructed the beams with fly ash concrete and conventional concrete (CC). The CC beams of Ortega's study were selected as a reference to compare with results of HVFA-SCC study. Ortega's beams were constructed, cast, cured, and tested in the same conditions of HVFA-SCC beams, so the variations were minimized. Table 6 summarizes the CC test results of Ortega study. It should be mentioned that these four beams are identical to those used in the present study in design, differing only in concrete type. The CC mix design consisted of 448 kg/m<sup>3</sup> (755 lb/yd<sup>3</sup>) cement, 1038 kg/m<sup>3</sup> (1750 lb/yd<sup>3</sup>) crushed stone [19 mm (0.75 in.) limestone], 659 kg/m<sup>3</sup> (1111 lb/yd<sup>3</sup>) natural sand, and w/c equal to 0.45.

Based on the comparison of the ultimate shear force presented in Figure 6, there is no major difference between the shear strength of HVFA-SCC and CC regardless of concrete compressive strength. The only difference that can be observed is the effect of longitudinal reinforcement ratios. As it is approved in normal concrete, a section with higher longitudinal reinforcement ratio has a higher shear capacity, which can be attributed to a combination of additional dowel action [19].

To account for the difference in compressive strength between the HVFA-SCC and the CC, the ultimate shear force is normalized. Since the shear resistance is proportional to the square root of the compressive strength, the normalized shear stress was determined as follows:

$$v_{test} = \frac{V_{ultimate}}{\sqrt{f'_c} b_w d} \quad (1)$$

The normalized shear stresses of HVFA-SCC and CC beams are displayed in Figure 7. As it appears in the Figure 7, the normalized values for both concrete types are exceeded or around the limit of the ACI code value of 0.167 [19].

### 4.3. SHEAR DUCTILITY AND POST-DIAGONAL CRACKING PERFORMANCE

Ductility is a desirable structural property for the concrete member. It allows for redistribution of stresses and provides warning of impending failure prior to collapse [5], [20]. Shear ductility is defined herein as the beam ability to withstand load after onset yielding in the shear reinforcement of the test region. To quantify the shear ductility of the beams with shear reinforcement in the test region, the shear ductility index was obtained by dividing the area under the load-deflection curve up to ultimate shear load ( $a_u$ ) by the area under the load-deflection curve to the first yield of the shear reinforcement ( $a_y$ ) as follows:

$$\text{Shear ductility index} = \frac{a_u}{a_y} \quad (2)$$

Based on this definition, the shear ductility indexes were determined from the test results presented in Figure 8 of the beams with shear reinforcement. As shown in Figure 9, the shear ductility increases with the increasing of cement replacement levels. Increasing replacement levels from 50% to 70% led to increased shear ductility by 35%. Beam with 70% replacement exhibited the highest shear ductility of the tested beams and even more than the CC beam.

The post-diagonal cracking performance can be defined as the ability of the beam to withstand load after the observation of first diagonal crack. For beams without shear reinforcement, post-diagonal cracking resistance (PDCR) was calculated as follows:

$$PDCR = \left( \frac{\text{Ultimate shear load} - \text{Cracking shear load}}{\text{Ultimate shear load}} \right) * 100\% \quad (3)$$

Figure 10 illustrates the calculated PDCR of the beams without shear reinforcement. Obviously, no trend was found between cement replacement level and PDCR. However, the CC beams showed an increase in PDCR with the increasing of longitudinal reinforcement ratio that can be attributed to the coarse aggregate size (19 mm) and the dowel action.

#### 4.4. LONGITUDINAL REINFORCEMENT STRAINS AND CRACK ANGLES

The crack angle and strain in the longitudinal reinforcement at the center of the shear test region were predicted using AASHTO LRFD equations shown below [21]. These equations were rewritten to consider into account non-prestressed members that were subjected to bending and shear only.

$$\text{For members without stirrups} \quad \varepsilon_s = \frac{\left( \frac{|M_u|}{d_v} + |V_u| \right)}{E_s A_s} \quad (4)$$

$$\text{For members with stirrups} \quad \varepsilon_s = \frac{\left( \frac{|M_u|}{d_v} + |V_u| \right)}{2E_s A_s} \quad (5)$$

$$\theta = 29 + 3500\varepsilon_s \quad (6)$$

The measured strains and crack angles were compared to those predicted values. The objective of this comparison was to establish if the AASHTO LRFD approach to predict strains and crack angles in conventional concrete beams is applicable to beams constructed with HVFA-SCC. Table 7 summarizes the experimentally measured values and the predicted values using AASHTO LRFD 10 as well. As shown in Table 7, the AASHTO LRFD equation to predict strain in longitudinal reinforcement is not always conservative in predicting strain of HVFA-SCC beams comparing to CC beams.

Regarding crack angles, the AASHTO LRFD equation overestimates the crack angle of HVFA-SCC beams, but is slightly better in predicting the CC beams' crack angles.

#### **4.5. MODELING COMPARISON**

A finite element modeling software is employed in this study to investigate the behavior up to the failure of HVFA-SCC beams [22]. A sectional analysis tool derived from modified compression field theory to predict the response of reinforced and prestressed concrete beams was adopted [23]. The measured concrete and steel properties, cross section dimensions, and reinforcement details of each beam were used to predict the shear behavior. This accounted for differences in the w/c ratios,  $f'_c$ , longitudinal reinforcement ratios, and tensile strength of the different concrete mixtures. Table 8 presents the ratios of  $V_{test}/V_{FEM}$  and  $\Delta_{test}/\Delta_{FEM}$  for all HVFA-SCC beams. The  $V_{test}/V_{FEM}$  values range from 0.88 to 1.36 with an average of 1.09 for beams without shear reinforcement and from 1.27 to 1.36 with an average of 1.31 for beams with shear reinforcement. The comparison, much like a benchmarking to conventional concrete specimens or a comparison to empirical code equations for conventional concrete, provides some sense of context to the results. The FEM results are found to be conservative for beams with shear reinforcement. On the other hand, FEM results for maximum mid-span deflection are found to over predict compare to experimental results. Figure 11 compares the load-deflection behavior between the experimental and the FEM methods of the beams with 70% cement replacement level. As displayed in the figure, curves based on the FEM method are shallow than experimental curves.



#### **4.6. COMPARISON WITH DATABASE**

Experimental data of measured shear strength reported in the literature were plotted against the results of the present study. The main objective of this effort was to compare the shear behavior of HVFA-SCC beams with collected data reported in the literature and check whether results of the present study fall between the collected data range. The collected data represent two types of concrete without shear reinforcement. Much of the data represent studies conducted on CC beams [3], and the rest are on self-consolidating concrete beams. The collected data is limited to compressive strength ranges between 75-20 MPa (10,878-2900 psi) and longitudinal reinforcement ratio varies between 4.5-0.58. Figure 12 displays the shear strength ratio as a function of compressive strength, beam effective depth, and beam width versus longitudinal reinforcement ratio. The implications of the results of the assembled database exhibits the following: first, the tests conducted in this study involving high volume fly ash self-consolidating concrete (HVFA-SCC) fall at or above the ACI 318-14 eq. 11-3 limit (ACI committee 318, 2014) [20] suggesting that the limited eco-concrete HVFA-SCC data satisfied the ACI limits with a reduced spread of data and thereby factor of safety; secondly, the HVFA-SCC test results fall down the nonlinear regression curve fit of the CC database; thirdly, the HVFA-SCC appears to fall below much of the CC and SCC data suggesting that as more HVFA-SCC data is collected calibration factors may need to be developed to yield a similar factor of over strength compared to the other concrete types relative to ACI limits.

#### **5. CONCLUSIONS AND RECOMMENDATIONS**

The test plan was developed to evaluate shear strength behavior of new innovation self-consolidating concrete type called HVFA-SCC. The concrete mixes basically consist of portland cement, Class C fly ash, and hydrated lime. Twelve full-

scale beams were constructed with three different cement replacement levels concrete (50%, 60%, and 70% by weight). The studied variables were the cement replacement levels, longitudinal reinforcement ratio, and shear reinforcement ratio. During testing, different responses such as shear force at first diagonal crack and at failure, load-deflection response, crack pattern, and mode of failure were recorded. Based on the results presented in this paper, the following conclusions are warranted:

- All HVFA-SCC mixes developed excellent rheological and mechanical properties (all test results exceeded the minimum target values specified by NCHRP report 628 for precast applications [24]) and are considered to be practical for most of the precast and some bridge applications. HVFA-SCC mixes developed early compressive strength greater than 35 MPa (5000 psi) after 3 days of age.
- HVFA-SCC beams with low longitudinal reinforcement ratio ( $\rho=1.59\%$ ) possess comparable shear strength capacity compared to CC beams. However, increasing the longitudinal reinforcement ratio does not show any obvious increasing trend on the ultimate shear capacity. This is because the coarse aggregate size (10 mm) affects the amount of shear transferred across cracks. Small diameter aggregate decreases the roughness of the crack surface and the effect of longitudinal reinforcement to prevent slippage is minimized [25].
- For beams with shear reinforcement, the shear ductility increases with the increasing of cement replacement levels. Increasing replacement levels from 50% to 70% led to increasing shear ductility by 35%. Beam with 70% replacement exhibited the higher shear ductility of the tested beams and even more than the CC beam (between 7-35% higher).

- In general, increasing the longitudinal reinforcement ratio only led to delaying the formation and propagation of a diagonal shear crack in the HVFA-SCC beams. An increase from 1.59% to 2.71% reinforcement ratio led to delaying the formation and propagation of diagonal cracks between 10 to 24 %.
- It was also observed that the HVFA-SCC beams with 70% cement replacement level experienced increased deflection, more cracks, and distribution over the 50% and 60% replacement levels. The improved deflection and crack pattern of 70% beams are hypothesized to be explained by dosage of hydrated lime used with 70% mixture. The hypothetical increase of hydrated lime dosage was believed to improve the bond between concrete and steel and help with the internal curing performance [12].
- Based on the collected database from the literature for CC and SCC beams, the shear strength ratios of HVFA-SCC test beams fell down the nonlinear regression curve fit of the CC database and at the lower bound of SCC data. This can be attributed to the lower aggregate fraction and aggregate size used in the HVFA-SCC, which can affect the aggregate interlocking mechanism.

Since this study was limited to three variables, the authors recommend investigating the long-term behavior of HVFA-SCC and the shear behavior with more variables such as aggregate size, type, and content; beam size; span-to-depth ratio; and compressive strength to come up with more reliable test results.

Table 1. Chemical and Physical Properties of Cementitious Materials

Properties	Unit	Cement	Fly Ash
SiO <sub>2</sub>	%	19.4	35.17
Al <sub>2</sub> O <sub>3</sub>		4.58	21.07
Fe <sub>2</sub> O <sub>3</sub>		3.2	6.58
CaO		62.7	26.46
MgO		3.27	6.22
SO <sub>3</sub>		3.19	1.43
Na <sub>2</sub> O		---	1.91
K <sub>2</sub> O		---	0.44
Na <sub>2</sub> O eq.		0.5	1.31
Loss of ignition		2.31	0.12
Fineness (+325 Mesh)		98.4	15.2
C <sub>3</sub> S		58	---
C <sub>2</sub> S		---	---
C <sub>3</sub> A		7	---
C <sub>4</sub> AF		---	---
Vicat set time, initial		minutes	90
Vicat set time, final	195		---
Specific gravity	---	3.15	2.68

Table 2. Materials Proportions of HVFA-SCC Beams

Mixture compositions (kg/m <sup>3</sup> )					
Composition	Type	Unit	Mixtures		
			HVFA-SCC 50	HVFA-SCC 60	HVFA-SCC 70
Cement	Type I	kg/m <sup>3</sup>	223	178	133
Fly Ash	Type C	kg/m <sup>3</sup>	191	223	254
Hydrated Lime	Type S	kg/m <sup>3</sup>	31	44	58
Sand	River Sand	kg/m <sup>3</sup>	824	820	817
Coarse Aggregate	3/8 in. Crushed Stone	kg/m <sup>3</sup>	916	912	908
w/cm		---	0.35	0.35	0.35
HRWR	Master Glenium 7500	mL/100 kg CM	737	815	802
% of Replacement		---	50	60	70

Table 3. Test Matrix of HVFA-SCC Beams

Mix ID	Beam ID	Bottom Reinforcement	Top Reinforcement	$\rho$	s, mm	Test Age, days
HVFA-SCC 50	50-5N	5#22	2#13	1.69	----	28
	50-6N	6#22	2#13	2.03	----	28
	50-8N	8#22	3#13	2.71	----	29
	50-8S	8#22	3#13	2.71	#10@178	29
HVFA-SCC 60	60-5N	5#22	2#13	1.69	----	28
	60-6N	6#22	2#13	2.03	----	28
	60-8N	8#22	3#13	2.71	----	29
	60-8S	8#22	3#13	2.71	#10@178	29
HVFA-SCC 70	70-5N	5#22	2#13	1.69	----	28
	70-6N	6#22	2#13	2.03	----	28
	70-8N	8#22	3#13	2.71	----	29
	70-8S	8#22	3#13	2.71	#10@178	29

Table 4. Fresh Properties of HVFA-SCC Mixes

Property	Specification	Mix ID			Target Value
		HVFA-SCC 50	HVFA-SCC 60	HVFA-SCC 70	
Slump flow (mm)	ASTM C1611	660	660	673	600 - 740
T50 (sec)		1.9	1.3	1.05	< 6.0
J-Ring (mm)	ASTM C1621	635	660	635	560 - 660
L-Box (%)		0.8	1	0.8	0.6 - 1.0
Unit weight (kg/m <sup>3</sup> )	ASTM C138	2313	2303	2252	---
Visual stability index (VSI)	ASTM 1611	0	0	0	0 - 1.0
Entrapped Air content (%)	ASTM C231	5	5	4.1	---

Table 5. Summary of Experimental Results of the HVFA-SCC Beams

Beam ID	$f'_c$ , MPa	Cracking Shear (Diagonal Crack), kN	Ultimate Shear $V_c$ (Failure), kN	Maximum Deflection ( $\Delta_{max}$ ), mm	Angle of Critical Crack, ( $\phi$ ), deg.	Failure Side
50-5N	53.5	124.4	149.2	9.0	21	E
50-6N	53.5	142.2	143.8	6.0	24	W
50-8N	53.5	140.0	144.0	6.4	23	E
50-8S	53.5	151.1	330.5	15.3	27	E
60-5N	45.9	117.7	142.5	14.4	22	W
60-6N	45.9	128.8	175.7	11.6	26	W
60-8N	45.9	146.6	150.6	6.9	23	E
60-8S	45.9	162.2	327.3	8.4	28	W
70-5N	52.9	128.8	146.6	12.9	24	W
70-6N	52.9	140.0	162.2	12.1	24	E
70-8N	52.9	142.2	154.7	10.7	25	E
70-8S	52.9	162.2	354.1	19.9	28	E

Table 6. Ortega Test Results of Conventional Concrete [3]

Beam ID*	$f'_c$ , MPa	Cracking Shear (Diagonal Crack), kN	Ultimate Shear $V_c$ (Failure), kN	Angle of Critical Crack, ( $\phi$ ), deg.	Failure Side
CC-5N	34.5	124.6	130.3	35	E
CC-6N	34.5	131.2	165.6	26	W
CC-8N	34.5	135.7	211.2	27	E
CC-8S	34.6	177.9	359.4	34	E

\* Beam IDs were renamed to be consistent with the present study.

Table 7. Comparison of Test Results with AASHTO LRFD Equations

Concrete Type	Beam ID	Longitudinal Strain		M/P	Angle of Critical Crack
		Measured	Predicted		Measured - Predicted
HVFA-SCC 50	5N	1845	1579	+	-14
	6N	733	1269	-	-8
	8N	799	1789	-	-9
	8S	2106	2215	-	-9
HVFA-SCC 60	5N	789	1509	-	-10
	6N	966	1551	-	-6
	8N	798	1009	-	-9
	8S	2220	2194	+	-9
HVFA-SCC 70	5N	1063	1553	-	-9
	6N	2533	1432	+	-14
	8N	1641	1037	+	-10
	8S	2851	2374	+	-11
CC [3]	5N	790	1367	-	3
	6N	910	1498	-	-6
	8N	1410	1432	-	-7
	8S	1920	2438	-	-2

\* (+) and (-) refer to underestimate and overestimate values, respectively.

Table 8. Comparison of Measured and Predicted Shear Strength and Deflection

Beam ID		$f_i$ , MPa	Finite Element Modeling		$V_{test}/V_{FEM}$	$\Delta_{test}/\Delta_{FEM}$
			$V_{ult}$ , kN	$\Delta_{max}$ , mm		
50	5N	3.75	133.8	16.3	1.11	0.55
	6N		147.1	16.6	0.98	0.36
	8N		163.9	15.6	0.88	0.41
	8S		260.8	44.6	1.27	0.34
60	5N	2.98	118	14.9	1.21	0.97
	6N		129.1	15.1	1.36	0.77
	8N		143.5	14.2	1.05	0.49
	8S		252.9	41.6	1.29	0.20
70	5N	3.65	131.4	16.1	1.12	0.80
	6N		145.5	16.5	1.11	0.73
	8N		162.6	15.5	0.95	0.69
	8S		260.2	44.6	1.36	0.45





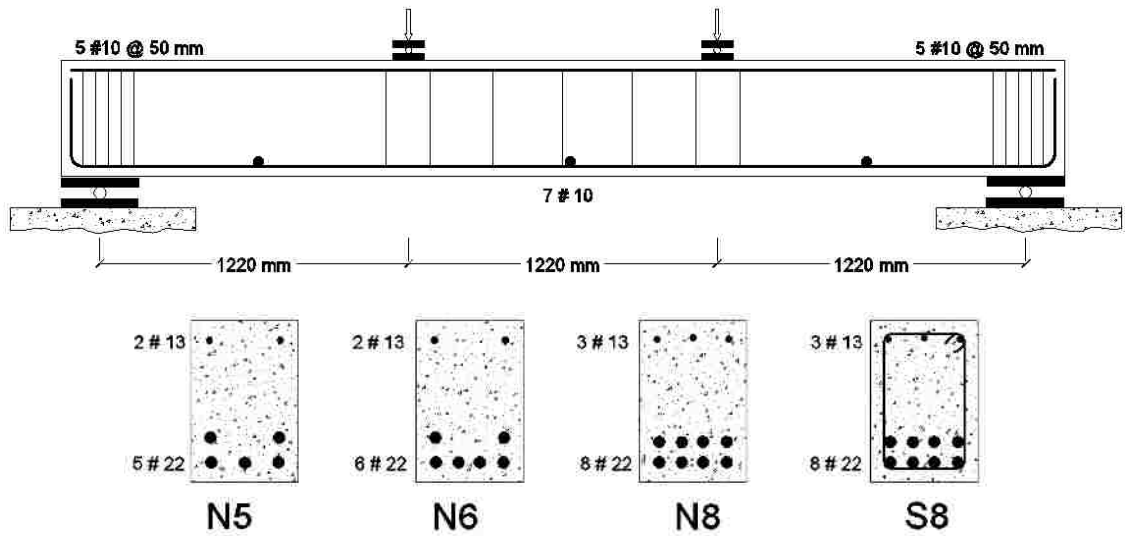


Figure 2. Typical beam details without shear reinforcement at the test region and cross sections with different longitudinal reinforcement layouts



Figure 3. Test setup, instrumentation, and testing and failure mode of a beam specimen

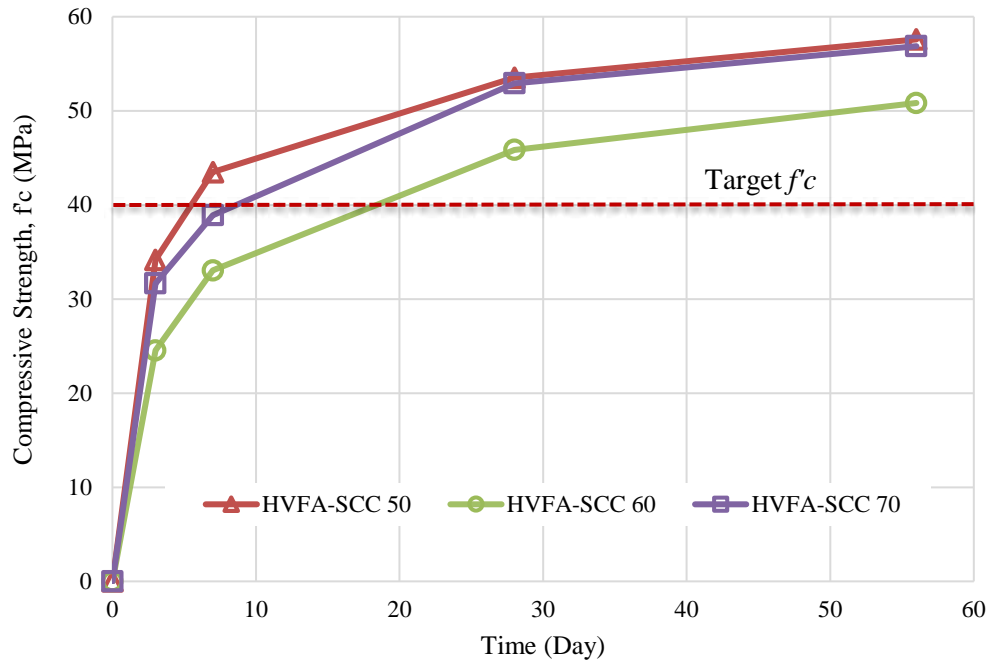


Figure 4. Development of compressive strength with time of HVFA-SCC mixes beam test results

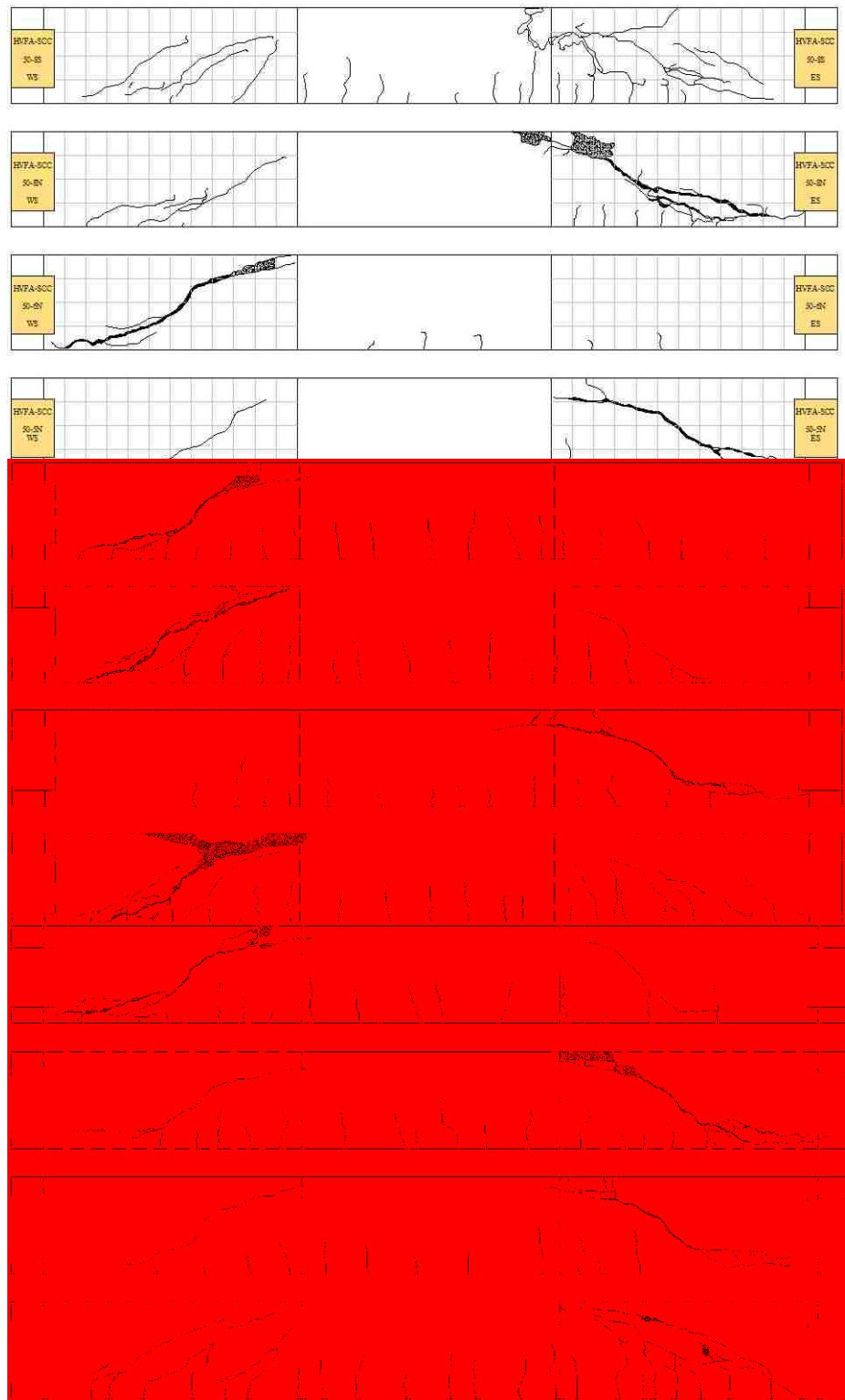


Figure 5. Crack profile at the ultimate shear force of test beams

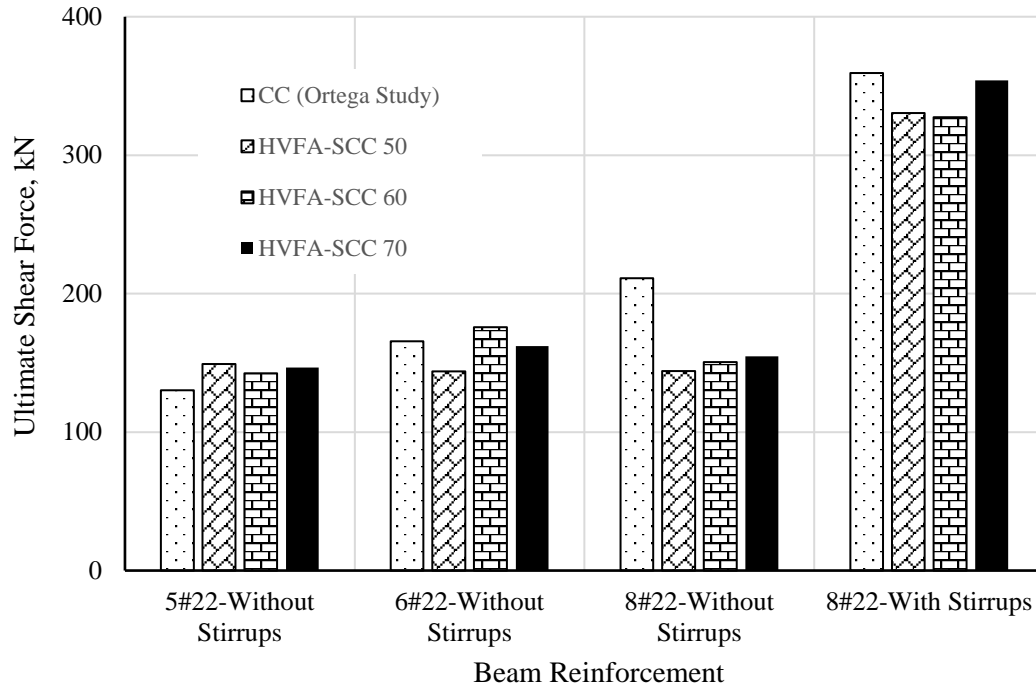


Figure 6. Comparison of ultimate shear test results with conventional concrete

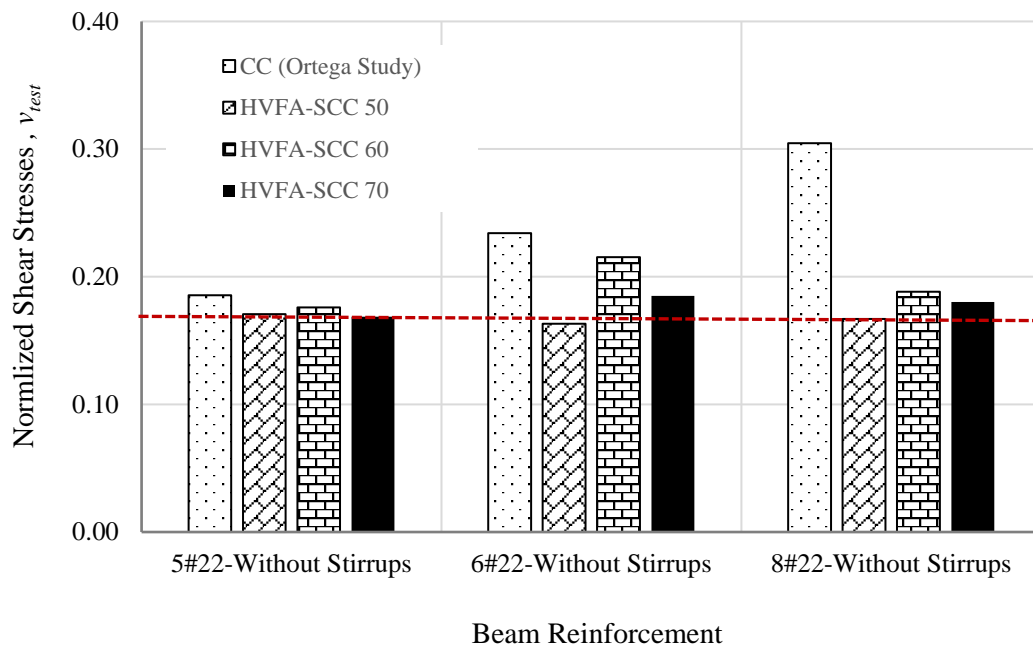


Figure 7. Comparison of normalized shear stresses of HVFA-SCC test results with CC

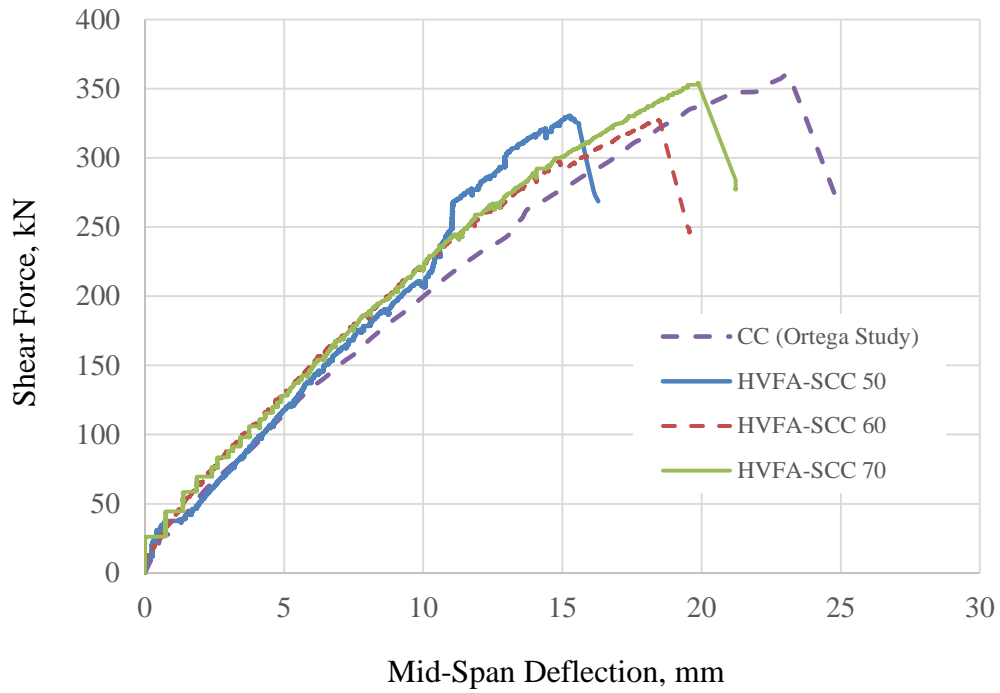


Figure 8. Shear force versus mid-span deflection

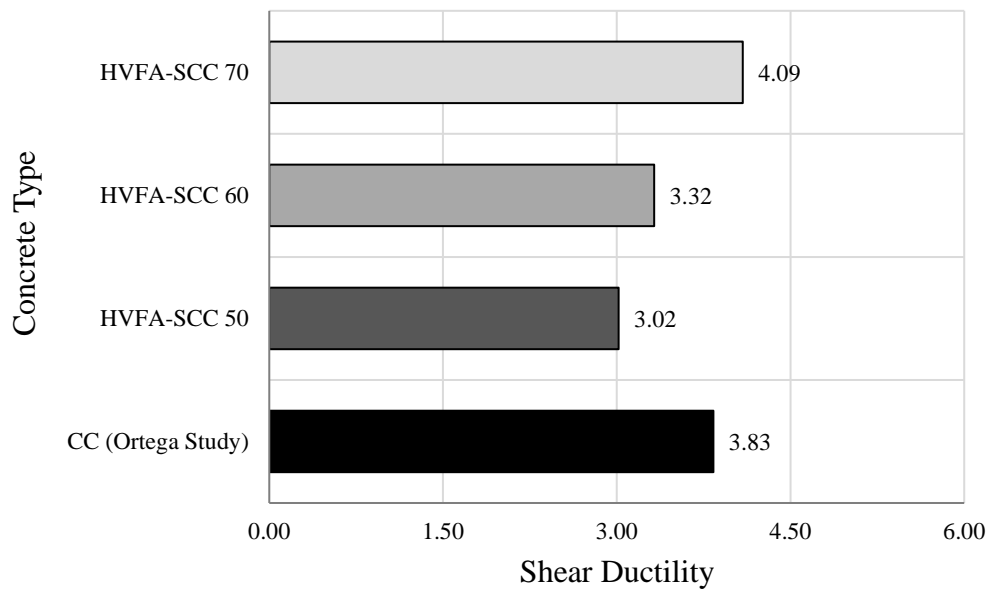


Figure 9. Comparison of shear ductility of the HVFA-SCC with CC

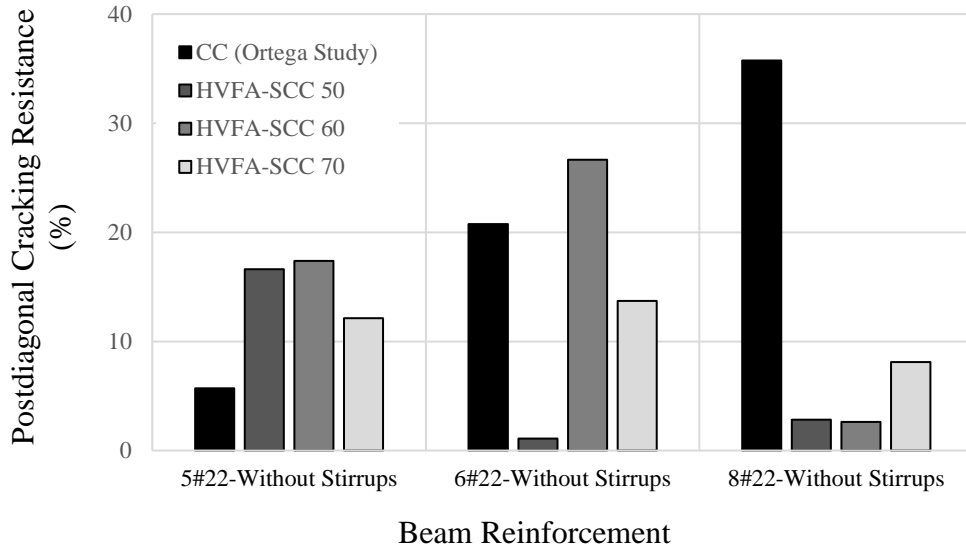


Figure 10. Comparison of PDCR of the HVFA-SCC with CC test results

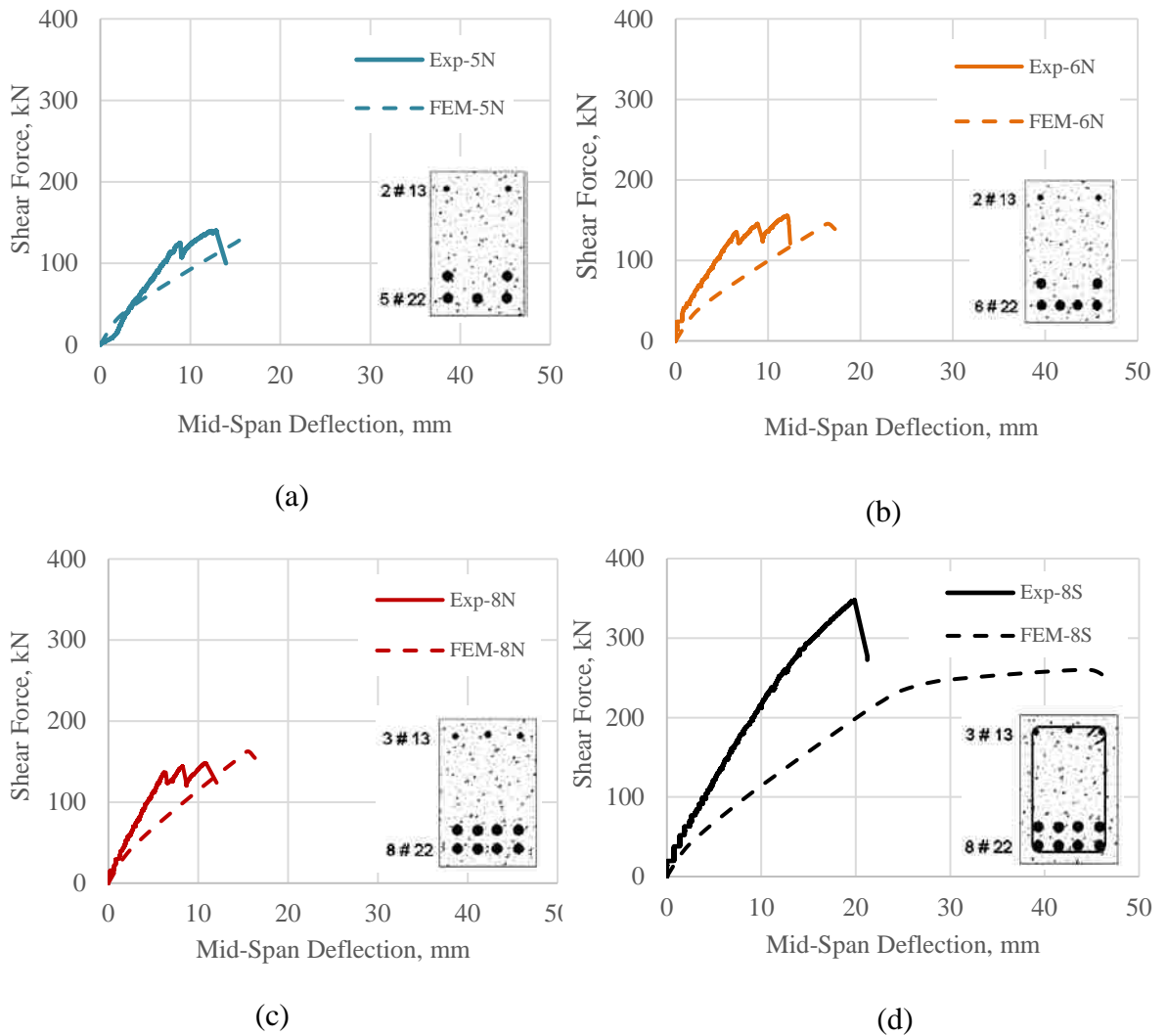


Figure 11. Load-deflection responses of the beams (test and FEM)

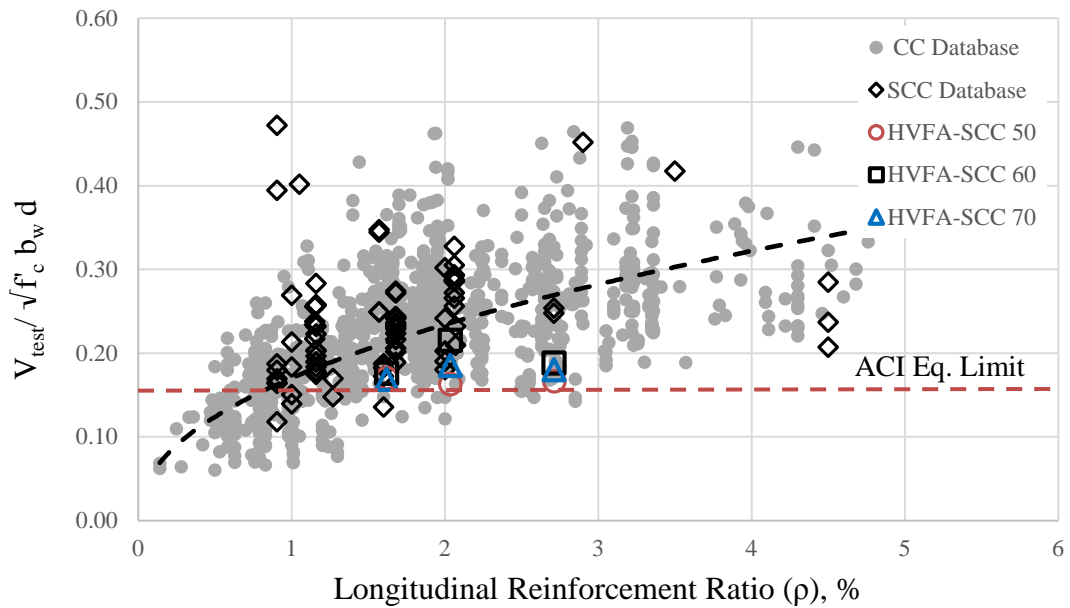


Figure 12. Normalized shear strength versus longitudinal reinforcement ratios; CC data from Ortega study (Ortega, 2012)

## ACKNOWLEDGEMENTS

The writers gratefully wish to acknowledge the financial support provided by the Missouri Department of Transportation (MoDOT), the National University Transportation Center (NUTC) at the Missouri University of Science and Technology (Missouri S&T), and the Center for Infrastructure Engineering. The authors also want to thank the Department of Civil, Architectural, and Environmental Engineering at Missouri S&T and HCED Iraq sponsor for their support. The opinions expressed in this study are those of the authors and do not necessarily reflect the views of sponsoring agencies.

## REFERENCES

- [1] ACI (American Concrete Institute) (2003). "Use of fly ash in concrete." ACI Committee 232, Farmington Hills, MI.

- [2] American Coal Ash Association. (2016) “Coal ash recycling reaches 52 percent as production and use trends shift.” <[www.aaa-usa.org](http://www.aaa-usa.org)> (4/1/2015).
- [3] Ortega C. A., (2012), "Shear and fracture behavior of high-volume fly ash reinforced concrete for sustainable construction". *Doctoral Dissertations*. Missouri University of Science and Technology. Paper 2259.
- [4] Arezoumandi, M., Volz, J.S., Myers, J.J. (2013a). “Shear behavior of high-volume fly ash concrete versus conventional concrete” American Society of Civil Engineering – Journal of Structural Engineering, 25(10), 1506-1513.
- [5] Lin C. and Chen J. (2012). “Shear behavior of self-consolidating concrete beams.” *ACI structural journal*, V. 109, No. 3, 307-315.
- [6] Arezoumandi, M., Volz, J.S., Ortega, C.O., Myers, J.J., (2013b) “Effect of total cementitious content on shear strength of high-volume fly ash concrete” Elsevier – Materials and Design Journal, Vol. 46, 301-309.
- [7] ACI (American Concrete Institute) (1993). “Guide for selecting proportions for high-strength concrete with portland cement and fly ash.” *ACI Mater. J.*, 90(3), 272–283.
- [8] Alghazali, H. and Myers, J., (2017). “Performance study of ecological self-consolidating cement mixtures (Eco-SCCM),” American Society of Civil Engineering – Journal of Materials in Civil Engineering, Vol. 29, Issue 12, pp. 1-11.
- [9] Khayat, K.H. and Mehdipour, I. (2014) “Design and performance of crack-free environmentally friendly concrete “crack-free eco-crete””. National University Transportation Center (NUTC), Missouri University of Science and Technology, Rolla, MO, USA (NUTC R322).
- [10] Richardson, D.N., Beckemeier, K.W., and Volz, J.S. (2015), “Effects of powder additive on high volume fly ash mixtures.” *ACI Materials Journal*. 112(4).
- [11] British Lime Association. (2015) “High performance mortars for a sustainable future.” <[www.britishlime.org](http://www.britishlime.org)> (May 20, 2015).
- [12] Volz, J.S., Myers, J.J., Richardson, D.N., Arezoumandi, M., Beckemeier, K., Davis, D., Holman, K., Looney, T., Tucker, B., (2012) “Design and evaluation of high-volume fly ash (HVFA) concrete mixes: Report A – Evaluation of HVFA Cementitious Paste and Concrete Mixtures,” Final Report A MoDOT TRyy1110, Missouri Department of Transportation, Jefferson City, Missouri, 262 pp.
- [13] ASTM (2014) “Standard Test Method for Slump Flow of Self-Consolidating Concrete.” C1611/C1611M, West Conshohocken, PA.



- [14] ASTM (2014) “Standard Test Method for Passing Ability of Self-Consolidating Concrete by J-Ring.” C1621/C1621M, West Conshohocken, PA.
- [15] ASTM (2014) “Standard Test Method for Density (Unit Weight), Yield, and Air Content (Gravimetric) of Concrete.” C138/C138M, West Conshohocken, PA.
- [16] ASTM (2014) “Standard Test Method for Air Content of Freshly Mixed Concrete by the Pressure Method.” C231/C231M, West Conshohocken, PA.
- [17] ASTM (2014) “Standard Test Method for Compressive Strength of Cylindrical Concrete Specimens.” C39/C39M, West Conshohocken, PA.
- [18] Taylor, H. P. J. (1972). “Shear strength of large beams.” *J. Struct. Div.*, 98 (ST11), 2473-2489.
- [19] ACI (American Concrete Institute) (2014). “Building code requirements for structural concrete.” ACI 318 and commentary 318R, Farmington Hills, MI.
- [20] Xie, Y., Ahmed, S., Yu, T., Hino, S., and Chung, W., (1994), “Shear ductility of reinforced concrete beams of normal and high strength concrete.” *ACI Structural Journal*. V. 91, No. 2.
- [21] AASHTO. (2010). AASHTO LRFD bridge design specifications, 4th Ed., Washington, DC.
- [22] Bentz, E. and Collins, M. (2000). Response 2000 [Software]. Available from: [www.ecf.utoronto.ca/~bentz/r2k.htm](http://www.ecf.utoronto.ca/~bentz/r2k.htm).
- [23] Bentz, E. (2000). Sectional analysis of reinforced concrete members. Ph.D. thesis, University of Toronto, Toronto, Canada.
- [24] Khayat, K., and Mitchell, D. (2009). “Self-consolidating concrete for precast, prestressed concrete bridge elements (NCHRP 628).” Transportation Research Board, Washington, D.C.
- [25] Wight, J.K., and MacGregor, J.G., (2009). “Reinforced concrete mechanics and design (6<sup>th</sup> Ed.). Pearson-Prentice Hall.

### III. BOND PERFORMANCE OF HIGH VOLUME FLY ASH SELF-CONSOLIDATING CONCRETE (HVFA-SCC) IN FULL-SCALE BEAMS

Hayder H. Alghazali and John J. Myers

#### ABSTRACT

This paper presents an experimental study on bond behavior between steel reinforcement and high volume fly ash self-consolidating concrete (HVFA-SCC). HVFA-SCC is a new concrete grade of HVFA concrete with the rheology of self-consolidating concrete that satisfies the quality of construction work, environment aspects, and concrete sustainability. Mixes with different cement replacement levels of fly ash and hydrated lime [50%, 60%, and 70% (by weight)] were used. Twelve full-scale reinforced concrete beams were cast and tested using a four-point load test setup. This study focused on observing the effect of factors such as cement replacement level, confinement conditions, and casting position on the beam flexural behavior. All beams were 10 ft (3,050 mm) in length, 18 in. (457 mm) in thickness, and 12 in. (305 mm) in width. Rheological and mechanical properties of the mixes were monitored. During testing, cracking and ultimate load, deflection, crack pattern, and mode of failure were recorded. Furthermore, test results were compared to a database of different concrete types such as conventional concrete and self-consolidating concrete. The findings of this study show that HVFA-SCC mix with 70% replacement is not only feasible in terms of acceptable bond behavior, but also is superior in other certain attributes.

#### Keywords:

High volume fly ash concrete, self-consolidating concrete, bond behavior, fly ash, hydrated lime, rheology, sustainability.

## 1. INTRODUCTION

In recent years, the desirability of producing more sustainable concrete has increased significantly, especially with growing cement production. Cement consumption is expected to reach 3.7-4.4 billion tons by 2050 with a demand rate of 2.5% annually<sup>1,2</sup>. This growth in cement demand raises an environmental concern. More ecological alternative solutions are needed to reduce cement consumption, and as a result, reduce CO<sub>2</sub> emission and the energy consumption associated with cement manufacturing<sup>3</sup>. Replacing cement with more sustainable materials such as fly ash has been proposed as the most straightforward way to minimize the amount of Portland cement used in concrete<sup>4</sup>. From an environmental perspective, replacing cement with fly ash reduces the concrete's overall carbon footprint and diverts an industrial by-product from the solid waste stream. Fly ash is a by-product material of thermal-power-generating stations<sup>5</sup>. Just in the United States alone, 50 million tons of fly ash are produced each year. Only 23 million tons are used in different applications; the rest is disposed of. Greatly increasing fly ash use in concrete can provide a means for the economical and ecological usage of millions of tons<sup>6</sup>.

Concrete sustainability can be enhanced by adopting concrete with self-consolidating rheological behavior<sup>7</sup>. Self-consolidating concrete decreases construction time and the man power needed on site<sup>8</sup> because SCC can flow into place without segregation, fill formwork, and encapsulate even very congested reinforcement without any mechanical vibration<sup>9</sup>. From a sustainability perspective, merging concrete with a high volume fly ash and the self-consolidating rheological behavior can lead to producing a more environment-friendly concrete. Therefore, high volume fly ash self-consolidating concrete (HVFA-SCC) is investigated in this study.

HVFA-SCC is the latest version of self-consolidating concrete (SCC) and one of the new innovations in concrete technology. It can be defined as a new type of SCC that consists of carefully selected and proportioned materials, including a high amount of fly ash (50% of the total cementitious materials or more) to produce durable, strong, and environment-friendly concrete. As mentioned above, HVFA-SCC is considered a new concrete type; therefore, there is no available data or conducted studies on the structural performance of HVFA-SCC.

In reinforced concrete construction, efficient and reliable force transfer between reinforcement and concrete is required for the optimal design. Stress transfers from concrete to deformed steel reinforcement through three modes: chemical adhesion, friction along the steel-concrete interface, and bearing resistance of the ribs on the steel against the surrounding concrete<sup>10</sup>. Numerous test methods have been created to determine the bond strength between concrete and steel reinforcing bars. The common four methods are the pull-out test, beam-end pullout test, beam anchorage test, and beam splice test. The current ACI 318-14 design provisions<sup>11</sup> for development length and splice length are based primarily on data collected from beam splice tests. It is considered a more realistic test compared to the other test methods.

Available literature either focuses on the structural performance of high volume fly ash concrete (HVFAC) or self-consolidating concrete (SCC). Concrete with a high amount of fly ash might not perform as well as concrete with 100% cement. Several studies have been conducted to address this concern. Wolfe<sup>12</sup> studied the bond behavior of HVFA concrete. Pull-out and beam splice tests were carried out on specimens with a 70% fly ash replacement of cement and then compared to identical tests performed on control specimens cast from a 100% Portland cement

mix. The pull-out tests were conducted on specimens with different bar diameters (either No. 4 or No. 6), while the tensile splice beam tests were conducted with only No.6 bars with and without confinement along the splice zone. The author concluded that the use of high volume fly ash concrete as cement substitute is not only practical in terms of the bond, but also excellent in some cases.

El-Azab et al.<sup>13</sup> studied the bond between SCC and the spliced tension bars in beams. The investigated parameters were reinforcement bar diameter and ratio, splice length, and casting position on the beam flexural behavior. All beams had a 6 ft (1.8 m) span and 8 x 16 in. (203 x 406 mm) cross section. The investigators indicated that a splice length of 40 times the bar diameter is almost the minimum splice length. The use of a smaller bar diameter with the same reinforcement amount increases both the beam capacity and ductility. They also concluded that top casting decreased both beam capacity and ductility by about 22% and 35%, respectively.

In the present study of beams constructed with HVFA-SCC, two concerning issues are examined regarding the bond behavior: the high amount of fly ash and self-consolidating behavior.

## **2. RESEARCH SIGNIFICANT**

To the authors' knowledge, this is the first study that investigates the bond strength behavior of full-scale beams constructed with HVFA-SCC. This study was developed to create a basis for safely implementing HVFA-SCC in the bridge and precast applications. In practice, this study focused on the effect of cement replacement level, confinement conditions, and casting position on the beams flexural behavior.

### 3. EXPERIMENTAL WORK

This work represents the third phase conducted on HVFA-SCC. All tests in this study were carried out at Missouri S&T. The following sections describe the experimental work details.

#### 3.1 MIX DESIGN

This section describes the process that was carried out to develop a concrete mix design using a high volume of cement replacement. The HVFA-SCC mixes were developed through an optimizing process of both the binder composition and the aggregates. The HVFA-SCC mixes were proportioned with Portland cement, fly ash, and hydrated lime. Table 1 illustrates the properties of the cement and fly ash used in this study. To obtain the optimum performance of the three materials, an investigation was conducted<sup>14</sup>. Because of this investigation, three different cement replacement levels (50%, 60%, and 70%) were selected by weight as binder compositions. The selected binder combination represented the best performance that can enhance the sustainability of cement-based materials. In addition, the fine-to-coarse aggregate ratio was also investigated to optimize the particle size distribution of the aggregates. An experimental method (gyratory compaction) was utilized to maximize the packing density of the aggregates<sup>15</sup>. By maximizing the packing density of the aggregates, the volume of paste required to fill the voids between aggregate particles could be minimized.

For all mixtures, Type I Portland cement, ASTM Type C fly ash, and Type S hydrated lime were used. The specific gravity of these materials were 3.15, 2.62, and 2.4, respectively. Natural siliceous riverbed sand with a specific gravity of 2.61 and absorption of 1.0 was used as fine aggregate. High-quality crushed stone dolomite with a maximum aggregate size of 3/8 in. (10 mm), a specific gravity of 2.68, and

absorption of 1.56 was used. Polycarboxylate-based high range water reducer (HRWR) admixture was employed to enhance the workability. The HRWR had a solid mass content of 23% and specific gravity of 1.05. The HRWR dosage was adjusted for the all mixtures to achieve a minimum slump flow of 26 in. (660 mm). The hydrated lime was used to enhance the early-age strength development and the internal curing<sup>16,17</sup>. The final design of the HVFA-SCC mixes is illustrated in Table 2. A local ready-mix concrete company provided the different concrete mixes for specimen fabrication.

While batching the mixtures, the dry materials (cement, fly ash, sand, and crushed stone) were mixed with three-quarters water first in the ready-mix plant. Once the concrete truck arrived at the lab, the hydrated lime, the HRWR, and the rest of the water were added, and all the materials were mixed thoroughly. The HRWR was added gradually until achieving the target flowability by inspection.

The measured fresh properties of HVFA-SCC mixtures were assessed for consistency, passing ability, filling ability, unit weight, and entrapped air content using ASTM procedures<sup>18-21</sup>. The HVFA-SCC mixtures property test results are presented in Table 3. These HVFA-SCC mixtures exhibited excellent rheological properties that satisfy the requirements for most precast and bridge applications.

The reinforcement bars used in this study were from the same individual lot of steel production and had the same parallel deformation pattern. Tensile tests were performed to investigate material properties such as yield stress and strain of the different high-strength hot-rolled reinforcing bars used in the research. All reinforcement bars conformed to the requirement of ASTM A615 specifications<sup>22</sup>. Table 4 summarizes the geometric and mechanical properties of the tested reinforcing bars.

### 3.2. BEAM SPLICE SPECIMEN DESIGN

The HVFA-SCC beams were designed following a test procedure that is considered the most realistic test method for both development and splice length. Twelve full-scale reinforced beams were constructed and tested under four-point loading until failure of the splice. The splice is located in the region of the beam subjected to a constant moment, and thus constant stress. A minimum constant moment region equal to twice of the beam height was provided to ensure a negligible effect of concentrated loads on the pure flexural behavior of the beams<sup>23</sup>. The beams' test matrices are summarized in Table 5.

All beams were 12 in. (305 mm) wide (b), a total depth (h) of 18 in. (457 mm), and 10 ft. (3050 mm) in length. The spliced is centered at midspan. The steel cage was comprised of six #6 (No. 19) bars, lap spliced in the center and hooked at the end to form three total longitudinal reinforcing bars. The splice length was determined following the equation of development length design presented in the ACI 318 code (2014)<sup>11</sup>. The equation was solved using the specification of beam specimens. To ensure bond failure before yielding of the reinforced bar, 70% of the code required development length was selected in the test specimen. This value was selected based first on previous studies<sup>12, 24</sup> and second to develop a steel stress less than yield to ensure splitting or slippage mode failure in all beam specimens. A yielding mode of failure provides little to no information regarding the bond strength of the reinforcing bar, and the objective was to compare the relative bond behavior of lap splice and not the ductility of the splices<sup>25</sup>.

The transverse steel consisting of #3 (No. 10) closed stirrups were used for shear reinforcement. Shear reinforcement was designed to guarantee that the bond failure occurred prior to shear failure. The stirrups were terminated approximately 5



in. (127 mm) from each end of the splice to eliminate the effect of confinement within the splice region for beams without confinement. However, the stirrups were installed across the splice on the confinement specimens. The splices' reaction to confinement was tested due to ACI's inclusion of a confinement variable in the development length equation (Equation 25.4.2.3a from ACI 318-14). To ensure the bond strength was not affected in any way by the existence of rust and mill scale, the splice region of each bar was brushed using a wire brush cup attached to an electric grinder. The test beam details are shown in Figure 1.

The beam designation included a combination of letters and numerics: B or T denoted the bottom or top splice specimens; WC or WOC referred to the presence of confinement in the splice region; and 50, 60, and 70 designated the cement replacement ratio. For example, a 50% cement replacement level and bottom splice specimen without confinement in the spliced region is designated as BWOC-50.

### **3.3. CASTING PROCEDURE AND CURING**

Beams were cast using tight wooden forms. The inside faces of the form were oiled to prevent water absorption, and silicon materials were used in the corner to prevent any leakage. The reinforcement was carefully placed inside the forms. A 1.5 in. (38 mm) steel chairs were used on the bottom to maintain 1.5 in. (38 mm) clear cover to the outside edge of the stirrups for the specimens with a bottom splice. However, the top splice specimens were turned upside down and 1 in. (25 mm) chairs were attached to the bottom of the cage to maintain clear cover to the splice at the top of the beam.

The HVFA-SCC was cast from one side without any compaction and in one lift; the concrete was allowed to flow from one end to the other end. The concrete filled the forms with ease around reinforcing bars in each reinforcement

configuration. Immediately after concrete was delivered, the rheological properties (slump flow, T50, J-Ring, and column segregation) were measured. During casting, it was observed that the elevation of HVFA-SCC horizontal surface rose steadily as casting progressed. It was also observed that during the filling process of HVFA-SCC, it flowed along the vertical surface of the formwork and removed air bubbles. Once the HVFA-SCC reached initial set (after five hours), the beam specimens and companion material property specimens were covered with wet burlap and plastic. The specimens were allowed to cure until the concrete compressive strength reached a minimum of 2500 psi (17 MPa), at which point they were stripped and stored in the laboratory atmosphere up to the age of testing. Before testing, the beams were painted white to facilitate detection of the cracks.

### **3.4. INSTRUMENTATION AND TEST SETUP**

The HVFA-SCC beams were tested in the Structural Engineering Research Laboratory (SERL) at Missouri S&T. Instrumentation was provided to measure the applied load, deflection in the beam, and strain in the reinforcement. Linear strain gauges were adhered to the main reinforcement. Strain gauges were installed at the ends of each splice to monitor the strain in the rebar during testing. Linear variable displacement transducers (LVDTs) were attached to the beam well below the compression zone [5 in. (125 mm) from the top] to measure deflection during testing. Both strain gauges and LVDTs were connected to a data acquisition system where the strains in the reinforcement, beam deflection, and load information were recorded.

### **3.5. TESTING PROCEDURE**

All the beams were simply supported and tested in a four-point bending configuration as shown in Figure 2. The load was applied by two 146 kips (649 kN) servo-hydraulic actuators. The actuators applied two-point loads to the beams using a

displacement rate of 0.050 in./min (1.27 mm/min) with the automatic data acquisition system recording data every second. After each 5 kips (22 kN) load increment, the propagating cracks were marked and their current terminal length and the current load was specified.

## 4. EXPERIMENTAL RESULTS AND DISCUSSION

### 4.1. GENERAL BEHAVIOR

The twelve beam splice test specimens were constructed to evaluate the bond performance of HVFA-SCC. During the test, three parameters were recorded for each test specimen. These values included applied load, corresponding midspan deflection, and corresponding strain at the end of each bar splice. Table 6 summarized the compressive strength at the time of testing ( $f'_c$ ), cracking load ( $P_{cr}$ ), ultimate load ( $P_{ult}$ ), and steel stress ( $f_s$ ). The steel stress recorded at the failure of the specimen was determined by averaging the three strain readings from each strain gauge in a member and then multiplying by the modulus of elasticity of the steel determined from the tension test of reinforcement.

The average bond strength was calculated using Eq. (1) from the calculated stress in the rebar at failure as follows:

$$u_{ave} = \frac{A_s f_s}{\pi d_b l_d} = \frac{f_s d_b}{4 l_d} \quad (1)$$

where  $u_{ave}$  is the average bond stress along the splice length,  $f_s$  is the stress in single rebar,  $l_d$  is the splice length,  $A_s$  is the cross-sectional area of rebar, and  $d_b$  is the bar diameter. In order to facilitate a direct comparison of test results with different compressive strength, the average bond strength ( $U_{test}$ ) of each test was normalized using Eq. (2):

$$u_{ave, normalized} = u_{ave} * \left( \frac{Design\ Strength}{Strength\ at\ testing} \right)^{1/4} \quad (2)$$

The design compressive strength for the HVFA-SCC mixes was 6,000 psi (41.4 MPa). The strength at testing for each mix design is reported in Table 6. The  $\frac{1}{4}$  power used in Eq. (2) was based on the development equation in ACI 408R-0310. Both the original and normalized average bond strength are presented in Table 6.

All the splice beams failed in bond, experiencing either splitting or slippage failure. As presented in Table 6, the cracking load of 50%, 60%, and 70% cement replacement of HVFA-SCC beams were almost identical. By increasing the replacement level from 50% to 70%, the normalized average bond strength of beams without confinement and bottom bar increased by 10%. However, for the top bar, test results show the beam of 70% had 26% and 7% higher bond compared with 50% and 60% replacement level, respectively. Furthermore, the top splice beams (in general) experienced 1.7% increase (i.e. higher) peak load than the bottom splice beams. This observation indicates that HVFA-SCC mixes were stable due to the very low w/c ratio (0.35) and the use of a high amount of fly ash, which may have resulted in a decrease in the amount of bleeding water accumulated beneath the top bar. In addition, the three days curing may have helped to have a cover strength higher than that with bottom splice beams.

Beams with confined longitudinal rebar by transverse stirrups had slightly increase in peak load when the percentage of cement replacement increased. Also, note that in the results of each replacement level, the confinement did not improve the peak load except for 50% replacement level (~ 4% increase).

In general, splice beams with 70% cement replacement exhibited a higher peak load and normalized bond strength than beams with 50% and 60% replacement, which may have been due to the high amount of hydrated lime used with this mix.

The increase of hydrated lime dosage is believed to improve the chemical adhesion between the bar and the concrete<sup>17</sup>.

#### **4.2. CRACKING PATTERN AND MODE OF FAILURE**

Figure 3 shows the crack pattern at failure load for each specimen. For all beams, flexural cracks were initiated at various locations along the tension side and within the constant moment region of beams (between the two-point loads). By increasing the applied load, newer flexural cracks began to form separately in an area outside of the constant moment region. Upon further increasing the applied load, the propagated flexural cracks developed more toward the compression side and bond failure occurred for the splice beams. However, beams without splice reinforcement continued to take more load and failed after concrete crushing in the compression region. All splice beams displayed a horizontal splitting failure along the length of the horizontal splice except the beams with confinement. The crack patterns experienced by splice beams without confinement were essentially identical. Confined beams with transvers stirrups in the splice zone had a slightly different crack pattern than beams without confinement. No horizontal cracks were visible with a bond failure in the confined beams. Furthermore, these beams experienced a slippage mode failure (pull-out failure). It was also noted that behavior at the failure of beams with confinement was very quiet (gradual and ductile) in contrast to the extremely violent (sudden and brittle) behavior for beams without confinement.

#### **4.3. STRAIN AND STRESS BEHAVIOR OF STEEL REINFORCEMENT**

In order to investigate the effect of cement replacement on strain behavior, the recorded data for each group (BWOc, BwC, and TwOc specimens) were plotted in load vs. strain format, as shown in Figure 4 (a-c). For all the splice beams, Figure 4 (a-c) shows two different stages in relation to the load intensity. The first stage (O-A)

represents pre-flexural cracking behavior, and the second stage (B-C) represents post-flexural cracking behavior. According to the plots, each group of specimens displayed almost similar behavior during testing except pre-flexural cracking stages of 70% cement replacement. The 70% specimens had much higher cracking load than the others did.

The results of the measured strains indicated that each specimen ultimately failed due to the bond around the splice rebar. In other words, the reinforcing bar failed in bond before reaching the yield limit. This observation is true for all specimens except TWOC-70 specimen, where the measured strain achieved the yield limit.

Table 7 presents measured stress (derived from strain gauge values) and predicted stress for each beam. The predicted stress was calculated using the moment curvature program Response-2000<sup>26</sup>. The measured longitudinal bar stresses of 70% splice specimens were higher than the 50% and 60% specimens. Also, specimens with confinement experienced higher stress than specimens regardless of the cement replacement ratio. This indicates that confinement allowed more bar ribs in the splice region to participate in the stress transfer between the bar and surrounding concrete<sup>27</sup>.

The ratio of measured to predicted stress in the longitudinal reinforcement splice beams is presented in Table 7. This ratio was determined to validate results obtained based on the assumed stress-strain diagram. As shown in Table 7, the ratios range from 1.88-1.38. This range indicates that moment-curvature approach underestimated the longitudinal reinforcement stress for the HVFA-SCC specimens.

#### **4.4. STRENGTH INDEX AND DUCTILITY INDEX**

To examine the concrete bond efficiency of HVFA-SCC, the strength and ductility indices of each specimen was examined. The strength index is defined as the

ultimate load of the splice specimen to that for the reference specimen without splice (continuous longitudinal internal reinforcement). The ductility index is represented as the ratio of the central deflection at the maximum load of splice specimen to that of the specimen without splice. These definitions are similar to that adopted in Reference<sup>28</sup>. Based on these definitions, the strength and ductility indices were calculated and summarized in Table 8. It should be observed that an increase of cement replacement from 50% to 70% led to an increase in the strength index by 21%, 10%, and 23% for BWOC, BWC, and TWOC specimens, respectively. Concurrently, the ductility index shows an increase as well with the increasing of cement replacement from 50% to 70%. Specimens with 70% had an average ductility 39% higher than specimens with 50% cement replacement.

#### **4.5. COMPARISON HVFA-SCC TEST RESULTS WITH COLLECTED DATABASE**

Splice beam test results reported in the literature were collected for comparison purposes. The main objective of this effort was to investigate whether test results of the present study fall within the trend of collected data. To make the comparison easier for presentation, the normalized bond strength to the square root of compressive strength was plotted against splice length to bar diameter ratio. The collected data is limited to compressive strength ranges between 3000-10,000 psi (21-69 MPa); bar diameter of #5 (16), #6 (19), and #8 (25); and different concrete types including HVFAC, SCC, CC, in addition to HVFA-SCC (current study). For the test results,  $(u_{test} / \sqrt{f'_c})$  was plotted against  $(l_s / d_b)$  in Figure 5. A good agreement ( $R^2=0.7$ ) was found between the bond strength and other parameters ( $f'_c$ ,  $l_s$ , and  $d_b$ ). Furthermore, the bond test results of HVFA-SCC fall within the nonlinear regression

curve fit of collected data. It can be concluded that HVFA-SCC possesses bond strength comparable to other concrete types.

## 5. CONCLUSIONS AND RECOMMENDATIONS

The test plan was developed to evaluate bond strength behavior of a new innovative sustainable self-consolidating concrete type called HVFA-SCC. The concrete mixes mainly consist of Portland cement, type C fly ash, and hydrated lime. Twelve full-scale beams were constructed with three different cement replacement levels concrete (50%, 60%, and 70% by weight). The studied variables were the cement replacement levels, confinement conditions, and casting position. During testing, responses such as force at first crack and at failure, load-deflection response, crack pattern, and mode of failure were recorded. Based on the results presented in this paper, the following conclusions are warranted:

- All HVFA-SCC mixes developed excellent rheological and mechanical properties considered to be practical for most of the precast and some bridge applications. HVFA-SCC mixes developed early compressive strength greater than 3,000 psi (21 MPa) to allow precast specimens to be moved from casting beds at early-ages.
- All the splice beams failed in bond, experiencing either splitting or slippage failure. For a beam examining top bar affects, test results showed that the specimen of 70% had 26% and 7% higher bond compared with 50% and 60% replacement level, respectively. Furthermore, the top splice beams (in general) experienced 1.7% increase (i.e. higher) peak load than the bottom splice beams. This means that HVFA-SCC mixes were very stable mixes.



- In general, splice beams with 70% cement replacement exhibited a higher peak load and normalized bond strength than beams with 50% and 60% replacement, which may have been due to the high amount of hydrated lime used with this mix. The increase of hydrated lime dosage is believed to have improved the chemical adhesion between the bar and the concrete
- Adding transverse stirrups in the splice zone changed the mode of failure and crack pattern. Moreover, behavior at failure was very quiet (gradual and ductile) in contrast to the extremely violent (sudden and brittle) behavior for beams without confinement.
- The bond efficiency of HVFA-SCC represented by strength and ductility indices showed an increase with increases in cement replacement from 50% to 70%.
- Comparison with collected data revealed that the bond test results of HVFA-SCC fall within the nonlinear regression curve fit. It can be concluded that HVFA-SCC possesses bond strength comparable to other concrete types.

Since this study was limited to three variables, the authors recommend investigating the bond behavior with more variables, such as aggregate size, type, and content; beam size; span-to-depth ratio; and compressive strength, to augment these test results.

Table 1. Chemical and physical properties of cementitious materials

Properties	Unit	Cement	Fly Ash
SiO <sub>2</sub>	%	19.4	35.17
Al <sub>2</sub> O <sub>3</sub>		4.58	21.07
Fe <sub>2</sub> O <sub>3</sub>		3.2	6.58
CaO		62.7	26.46
MgO		3.27	6.22
SO <sub>3</sub>		3.19	1.43
Na <sub>2</sub> O		---	1.91
K <sub>2</sub> O		---	0.44
Na <sub>2</sub> O eq.		0.5	1.31
Loss on ignition		2.31	0.12
Fineness (+325 Mesh)		98.4	15.2
C <sub>3</sub> S		58	---
C <sub>2</sub> S			---
C <sub>3</sub> A		7	---
C <sub>4</sub> AF	---	---	
Vicat set time, initial	minutes	90	---
Vicat set time, final		195	---
Specific gravity	---	3.15	2.68

Table 2. Materials proportions of HVFA-SCC beams


Mixture compositions [lb/yd <sup>3</sup> (kg/m <sup>3</sup> )]				
Composition	Type	Mixtures		
		HVFA-SCC 50	HVFA-SCC 60	HVFA-SCC 70
Cement	Type I	375 (223)	300 (178)	225 (133)
Fly Ash	Type C	323 (191)	375 (223)	428 (254)
Hydrated Lime	Type S	52 (31)	75 (44)	97 (58)
Sand	River Sand	1389 (824)	1383 (820)	1377 (817)
Coarse Aggregate	3/8 in. Crushed Stone	1544 (916)	1537 (912)	1530 (908)
w/cm	---	0.35	0.35	0.35
HRWR (fl. oz./100 lb CM)	Master Glenium 7500	11.2	9.7	13.8
% of Replacement	---	50	60	70

Conversion: fl oz./100 lb CM = 65.19847 mL/100 kg CM.

Table 3. Fresh properties of HVFA-SCC mixes

Property	Specification	Mix ID		
		HVFA- SCC 50	HVFA- SCC 60	HVFA- SCC 70
Slump flow, in. (mm)	ASTM C1611	27 (686)	28 (711)	27 (686)
T50 (sec)		1.07	1.5	0.97
J-Ring, in. (mm)	ASTM C1621	26 (660)	27.5 (699)	26 (660)
Column Segregation, %	ASTM 1611	2.1	1.98	0
Unit weight, lb/yd <sup>3</sup> (kg/m <sup>3</sup> )	ASTM C138	3920 (2325)	3910 (2320)	3883 (2303)
Visual stability index (VSI)	ASTM 1611	0	1	0
Entrapped Air content, %	ASTM C231	2.5	2.4	3.2

Table 4. Geometrical and mechanical properties of reinforcing bars

Bar #	Ø, in. (mm)	$h_R$ , in.(mm)	$S_R$ , in.(mm)	$f_y$ , ksi, (MPa)	$f_u$ , ksi, (MPa)	Elongatio n (%)	
3	0.375 (10)	0.035 (0.89)	0.218 (5.54)	74 (510)	110 (759)	15	
4	0.5 (13)	0.025 (0.64)	0.262 (6.65)	77 (531)	111 (766)	13	
6	0.75 (19)	0.04 (1.02)	0.425 (10.80)	66 (455)	108 (745)	14	

Where: Ø = bar diameter,  $h_R$  = average height of deformation,  $S_R$  = average spacing of deformation,  $f_y$  = yielding stress, and  $f_u$  = ultimate stress.

Table 5. Test matrix of HVFA-SCC beams

Mix ID	Beam ID	Bottom Reinf.	Top Reinf.	$\rho$ , %	Stirrup	Splice Location	Splice Length, in.	Confinement
HVFA-SCC 50	REF-50	3 # 6	2 # 4	0.68	#3 @ 7"	N/A	0	No
	BWOC-50	3 # 6	2 # 4	0.68	#3 @ 7"	Bottom	10	No
	BWC-50	3 # 6	2 # 4	0.68	#3 @ 7"	Bottom	10	Yes, #3@7"
	TWOC-50	3 # 6	2 # 4	0.68	#3 @ 7"	Top	10	No
HVFA-SCC 60	REF-60	3 # 6	2 # 4	0.68	#3 @ 7"	N/A	0	No
	BWOC-60	3 # 6	2 # 4	0.68	#3 @ 7"	Bottom	10	No
	BWC-60	3 # 6	2 # 4	0.68	#3 @ 7"	Bottom	10	Yes, #3@7"
	TWOC-60	3 # 6	2 # 4	0.68	#3 @ 7"	Top	10	No
HVFA-SCC 70	REF-70	3 # 6	2 # 4	0.68	#3 @ 7"	N/A	0	No
	BWOC-70	3 # 6	2 # 4	0.68	#3 @ 7"	Bottom	10	No
	BWC-70	3 # 6	2 # 4	0.68	#3 @ 7"	Bottom	10	Yes, #3@7"
	TWOC-70	3 # 6	2 # 4	0.68	#3 @ 7"	Top	10	No

Conversion: 1 in = 25.4 mm; bar size of #3 = 10 mm, #4 = 13 mm, and #6 = 19 mm; N/A=not applicable

Table 6. Specimen properties and test results

Mix ID	Beam ID	$d_b$ , in.	$d_s$ , in.	$f'_c$ , psi	$l_{splice}$ , in.	$P_{cr}^2$ , kips	$P_{ult}$ , kips	$\Delta_{at\ ult\ load}$ , in.	$f_s$ , psi	$U_{test}$ , psi	$U_{test}$ , normalized psi	Failure Mode <sup>3</sup>
HVFA- SCC 50	REF-50	0.75	N/A	6370	0	23	110	1.8	66.0 <sup>1</sup>	---	---	Flexural
	BWOC-50	0.75	N/A		10	21	52	0.12	57.8	1083	1099	Splitting
	BWC-50	0.75	0.375		10	22	54	0.16	63.6	1193	1210	Pull out (Slippage)
	TWOC-50	0.75	N/A		10	17	53	0.122	52.2	979	994	Splitting
HVFA- SCC 60	REF-60	0.75	N/A	6490	0	19	103	1.93	66.0 <sup>1</sup>	---	---	Flexural
	BWOC-60	0.75	N/A		10	23	57	0.121	64.7	1213	1237	Splitting
	BWC-60	0.75	0.375		10	21	55	0.157	64.1	1201	1225	Pull out (Slippage)
	TWOC-60	0.75	N/A		10	15	57	0.145	61.2	1148	1171	Splitting
HVFA- SCC 70	REF-70	0.75	N/A	6250	0	22	107	1.57	66.0 <sup>1</sup>	---	---	Flexural
	BWOC-70	0.75	N/A		10	20	61	0.121	63.8	1196	1208	Splitting
	BWC-70	0.75	0.375		10	19	58	0.163	65.8	1233	1246	Pull out (Slippage)
	TWOC-70	0.75	N/A		10	20	63	0.215	66.0 <sup>1</sup>	1238	1250	Yielding

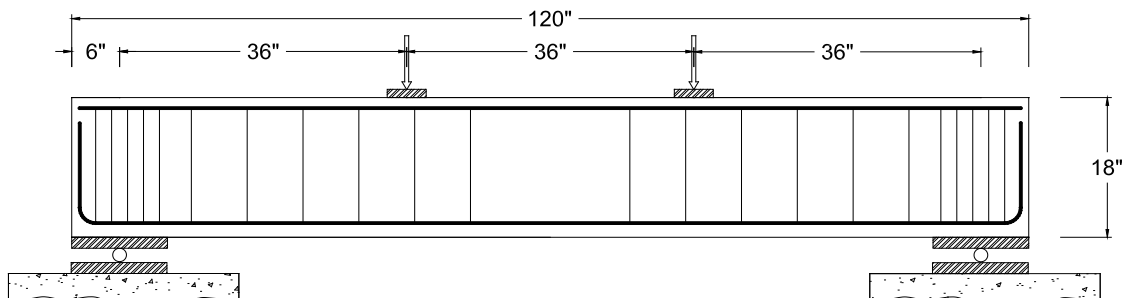
Note: <sup>1</sup>stress was limited to the yield stress of 66 ksi; <sup>2</sup>Cracking load ( $P_{cr}$ ) was recorded at the observation of the first crack; <sup>3</sup>Failure considers splitting when a small clear cover or small spacing between reinforced bars exists; however, pull out failure occurs when the reinforcing bar slips, and as a result, the concrete between the bar deformations is crushed, leading to a simple pulling out of the bar. Conversion: 1 in. = 25.4 mm; 1 psi = 0.006895 MPa; 1 kips = 4.45 kN.

Table 7. Longitudinal reinforcement strain and stress of HVFA-SCC beams

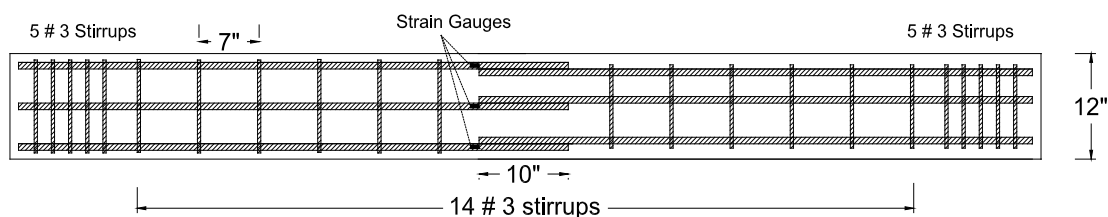
Mix ID	Beam ID	Measured Strain, $\mu\epsilon$	Steel Stress at Failure Load, ksi (MPa)		Measured/ Predicted Stress
			Measured	Predicted	
HVFA-SCC 50	REF-50	13635	---	---	---
	BWOC-50	1844	58 (340)	32 (220)	1.80
	BWC-50	2030	64 (441)	34 (234)	1.87
	TWOC-50	1666	52 (358)	33 (227)	1.58
HVFA-SCC 60	REF-60	18650	---	---	---
	BWOC-60	2065	65 (448)	37 (255)	1.75
	BWC-60	2046	64 (441)	34 (234)	1.88
	TWOC-60	1955	61 (420)	37 (255)	1.65
HVFA-SCC 70	REF-70	16065	---	---	---
	BWOC-70	2036	64 (441)	46 (317)	1.39
	BWC-70	2100	65 (448)	40 (276)	1.64
	TWOC-70	2215	66 (455)	48 (331)	1.38

Table 8. Strength and ductility indices of HVFA-SCC beams

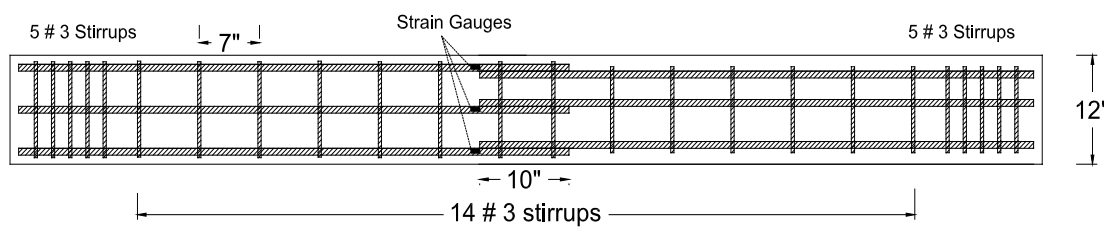
Mix ID	Beam ID	Strength	Ductility
HVFA-SCC 50	REF-50	1.00	1.00
	BWOC-50	0.47	0.07
	BWC-50	0.49	0.09
	TWOC-50	0.48	0.07
HVFA-SCC 60	REF-60	1.00	1.00
	BWOC-60	0.55	0.06
	BWC-60	0.53	0.08
	TWOC-60	0.55	0.08
HVFA-SCC 70	REF-70	1.00	1.00
	BWOC-70	0.57	0.08
	BWC-70	0.54	0.10
	TWOC-70	0.59	0.14



a) Typical beam details without transverse stirrups in splice zone.



b) Splice cage without confinement.



c) Splice cage with confinement.

Conversion: 1 in. = 25.4 mm

Figure 1. Test beam details of HVFC-SCC specimens.



Figure 2. Test setup, instrumentation, and testing and failure mode of a beam specimen.



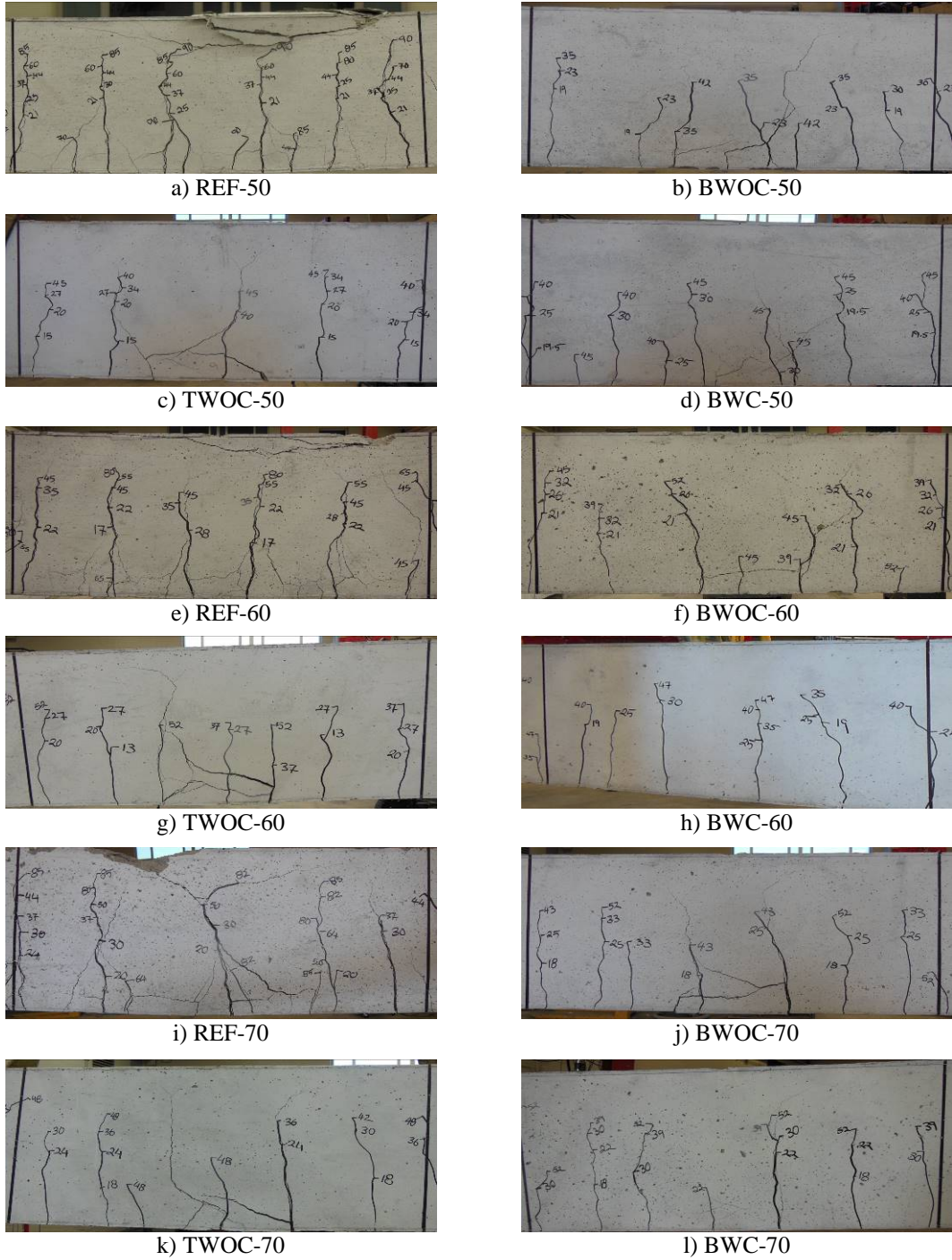
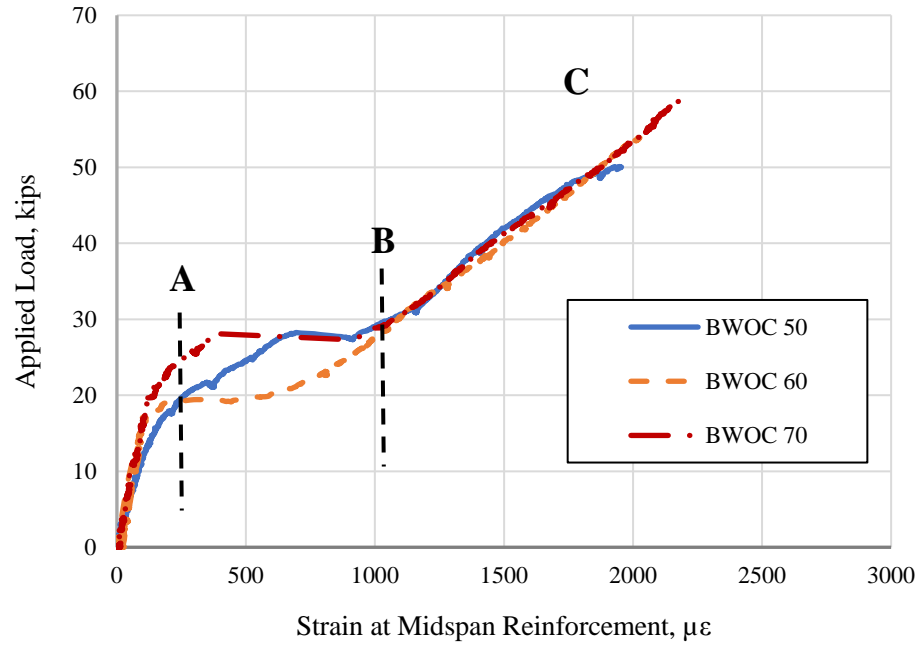
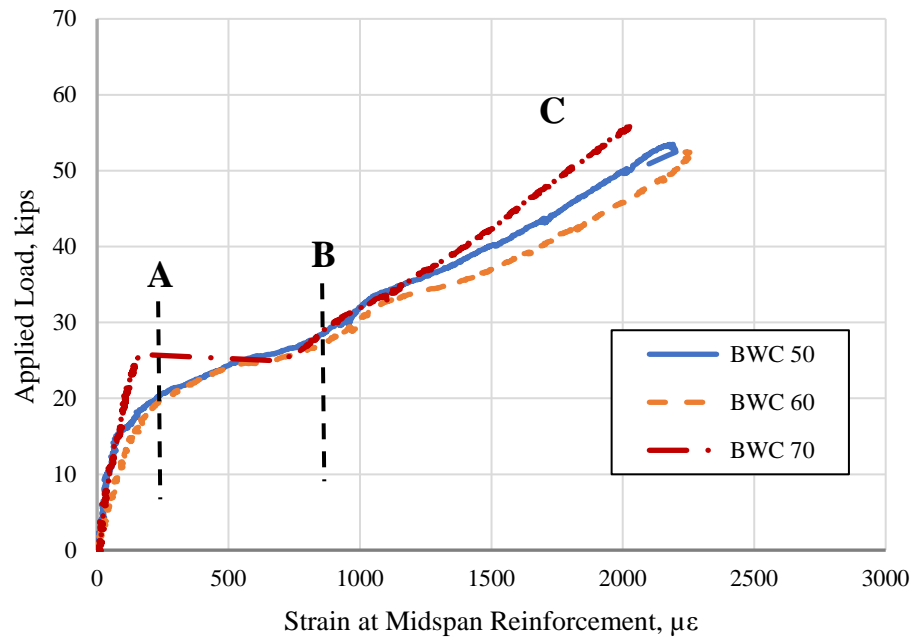


Figure 3. Crack pattern of the HVFA-SCC beams at bond failure.

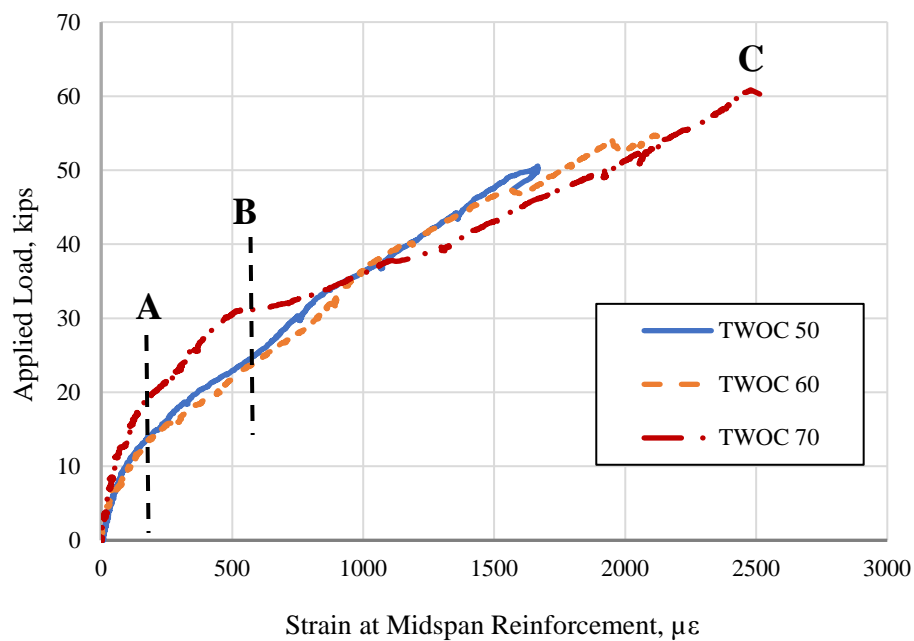


a) BWOC beams



b) BWC beams

Figure 4. Load vs. strain of the longitudinal reinforcement of HVFA-SCC beams.



c) TWOC beams

Conversion: 1 kips = 4.45 kN

Figure 4. Load vs. strain of the longitudinal reinforcement of HVFA-SCC beams (Cont.).

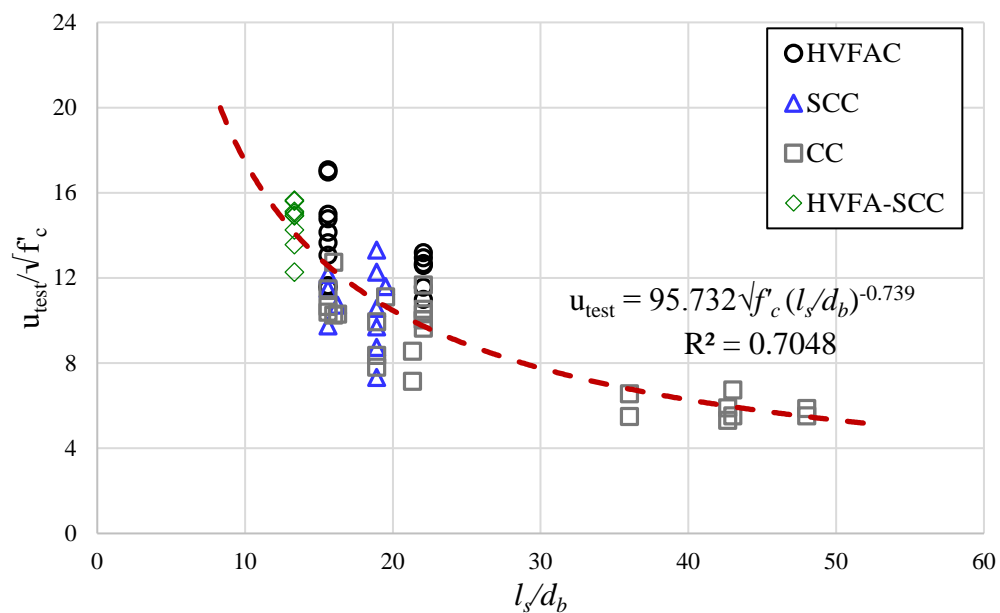


Figure 5. Comparison and proposed equation for bond strength for splice beam specimens with different concrete types.

## ACKNOWLEDGMENTS

The writers gratefully wish to acknowledge the financial support provided by the National University Transportation Center (NUTC) at Missouri University of Science and Technology (Missouri S&T). The authors also thank the Department of Civil, Architectural, and Environmental Engineering, the Center for Infrastructure Engineering Studies at Missouri S&T, and HCED Iraq sponsor for their support.

## REFERENCES

1. Benhelal, E., Zahedi, G., Shamsaei, E., and Bahadori, A., "Global strategies and potentials to curb CO<sub>2</sub> emissions in cement industry", *Journal of Cleaner Production*, V. 51, 2013, pp. 142-161.
2. Rubenstein, M., "Emissions from the cement industry". The Earth Institute of Columbia University, 2012.
3. Taylor, M., Tam, C., and Gielen, D., "Energy efficiency and CO<sub>2</sub> emissions from the global cement industry," *Korea*, V. 50 (2.2), 2006, pp. 61-72.
4. Gartner, E., "Industrially interesting approaches to "low-CO<sub>2</sub>" cements," *Cement and Concrete research*, V. 34(9), 2004, pp. 1489-1498.
5. ACI (American Concrete Institute), "Use of Fly Ash in Concrete." ACI Committee 232, Farmington Hills, MI, 2003.
6. American Coal Ash Association, "Coal ash recycling reaches 52 percent as production and use trends shift," <[www.aaa-usa.org](http://www.aaa-usa.org)>, 2016.
7. Ready Mixed Concrete Association of Ontario, "Best practices guidelines for self-consolidating concrete," <<https://www.rmcao.org>> Mississauga, ON, 2008.
8. Scrivener, K. L., and Kirkpatrick, R. J., "Innovation in use and research on cementitious material," *Cement and concrete research*, V. 38(2), 2008, pp. 128-136.
9. Daczko, J. A., "Self-consolidating concrete: applying what we know," CRC Press, 1 edition, 2012.

10. American Concrete Institute (ACI 408R-03), "Bond and Development of Straight Reinforcing Bars in Tension," American Concrete Institute, Detroit, Michigan, 2003.
11. American Concrete Institute (ACI 318-14), "Building Code Requirements for Structural Concrete and Commentary," American Concrete Institute. Detroit, Michigan, 2014.
12. Wolfe, M.H., "Bond strength of high-volume fly ash concrete," Master's thesis, Missouri University of Science and Technology, 2011.
13. El-Azab, M.A., Mohamed. H.M., and Farahat. A., "Effect of tension lap splice on the behavior of high strength self-compacted concrete beams," *Alexandria Engineering Journal*, V. 53(2), 2014, pp. 319-328.
14. Alghazali, H. and Myers, J., "performance study of ecological self-consolidating cement mixtures (Eco-SCCM)," American Society of Civil Engineering – Journal of Materials in Civil Engineering, Vol. 29, Issue 12, December 2017, pp. 1-11.
15. Khayat, K.H. and Mehdipour, I., "Design and performance of crack-free environmentally friendly concrete (crack-free eco-crete)," National University Transportation Center (NUTC), Missouri University of Science and Technology, Rolla, MO, USA (NUTC R322), 2014.
16. Richardson, D.N., Beckemeier, K.W., and Volz, J.S., "Effects of powder additive on high volume fly ash mixtures," *ACI Materials Journal*, V. 112(4), 2015.
17. British Lime Association, "High performance mortars for a sustainable future," <[www.britishlime.org](http://www.britishlime.org)>, 2015.
18. ASTM C1611/C1611M, "Standard Test Method for Slump Flow of Self-Consolidating Concrete.," West Conshohocken, PA, 2014.
19. ASTM C1621/C1621M, "Standard Test Method for Passing Ability of Self-Consolidating Concrete by J-Ring," West Conshohocken, PA, 2014.
20. ASTM C138/C138M, "Standard Test Method for Density (Unit Weight), Yield, and Air Content (Gravimetric) of Concrete," West Conshohocken, PA, 2014.

21. ASTM C231/C231M, "Standard Test Method for Air Content of Freshly Mixed Concrete by the Pressure Method," West Conshohocken, PA, 2014.
22. ASTM A615/A615M, "Deformed and Plain Carbon-Steel Bars for Concrete Reinforcement," West Conshohocken, PA, 2014.
23. Weiss, W. J., Guler, K., and Shah, S. P., "An experimental investigation to determine the influence of size on the flexural behavior of high strength reinforced concrete beams," *In 5<sup>th</sup> Int. Symp. on Utilization of HS/HP Concrete*, Sandefjord, Norway, Proceedings V. 2, 20–24 June 1999, pp. 709-718.
24. Looney, T. J., Arezoumandi, M., Volz, J. S., and Myers, J. J., "An experimental study on bond strength of reinforcing steel in self-consolidating concrete," *International journal of concrete structures and materials*, 2012, pp. 1-11.
25. Turk, K., Benli, A., and Calayir, Y., "Bond strength of tension lap-splices in full scale self-compacting concrete beams," *Turkish J. Eng. Env. Sci.*, V. 32, 2008, pp. 377-386.
26. Bentz, E. and Collins, M., "Response 2000 [Software]," Available from: [www.ecf.utoronto.ca/~bentz/r2k.htm](http://www.ecf.utoronto.ca/~bentz/r2k.htm), 2000.
27. Pandurangan, K., Kothandaraman, S., and Sreedaran, D., "A study on the bond strength of tension lap splices in self compacting concrete," *Materials and structures*, V. 43(8), 2010, pp. 1113-1121.
28. El-Azab, A. and Mohamed, H. M., "Effect of tension lap splice on the behavior of high strength concrete (HSC) beams," *HBRC Journal*, V. 10(3), 2014, pp. 287-297.

#### **IV. TIME-DEPENDENT PRESTRESS LOSS BEHAVIOR OF GIRDERS IN MISSOURI BRIDGE A7957 COMPARED WITH A U.S. DATA SET OF HIGH-PERFORMANCE CONCRETE BRIDGE**

Hayder H. Alghazali and John J. Myers

##### **ABSTRACT**

In this study, six precast, prestressed concrete girders were constructed and instrumented to measure prestress losses of bridge A7957 in Missouri. The concrete mixture for the bridge was designed with varying mechanical and rheological properties. High-strength concrete, high-strength self-consolidating concrete, and normal-strength self-consolidating concrete were used to construct the bridge girders. Vibrating wire strain gauges with integrated thermistors were embedded through the girders' cross sections to measure strains and temperatures. The measured short- and long-term prestress losses were compared with those obtained using different empirical models, specified in the AASHTO LRFD Bridge Design Specifications and in the PCI Design Handbook: Precast and Prestressed Concrete. This study also presents a comparison of measured prestress losses with data reported in the literature for different concrete types.

##### **Keywords:**

Bridge, girder, high-strength concrete, high-strength concrete, normal-strength concrete, prestressed, prestress loss, self-consolidating concrete, strain.

## 1. INTRODUCTION

Long service life and low maintenance costs for bridges are attainable with sustainable and durable advanced concrete materials. Constructing a bridge with these new types of concrete often requires monitoring to evaluate its performance and various aspects of its structural behavior. A comprehensive structure health monitoring system, including sensors that measure parameters related to performance and structural behavior, can be the most efficient way to obtain actionable data on bridge performance. In this study, high-strength concrete (HSC) and self-consolidating concrete (SCC) with two different performance levels were used in the construction of the superstructure of a bridge.

HSC gives bridge designers greater flexibility for the design of precast, prestressed concrete structures. It permits longer span structures that result from more compact sections. Using HSC can lower the initial project cost by allowing longer spans for a given girder cross section or by increasing the girder spacing and reducing the number of girders.<sup>1</sup> ACI 363R-10<sup>2</sup> defines HSC as a type of concrete with a specific 28-day strength of 8000 psi (55 MPa) or greater. The high strength is made possible by reducing porosity, inhomogeneity, and microcracks in the hydrated cement paste and the transition zone. HSC is considered to be more durable than conventional concrete. However, its production requires more attention to quality control than conventional concrete. Mixture designs for HSC require the use of strong, durable aggregate and often a high cementitious material content, which generally results in a lower water–cementitious materials ratio. An HSC mixture design can vary depending on locally available materials that allow the fresh concrete to be workable and ensure that the strength development is as specified by the designer. With the variety of constituent



materials and requirements, many performance-related issues require closer attention. Differences in the amount of time-dependent losses are one example of an area currently under investigation. Understanding and predicting prestress losses is essential in the design of a prestressed concrete beam. If care is not taken to determine the prestress losses at various stages, the design can result in poor serviceability state behavior.

SCC was developed in Japan in the 1980s and started to be used widely in the United States in the 1990s. It can be consolidated into every corner of a framework purely by means of its own weight and without the need for mechanical consolidation.<sup>3</sup> High-strength SCC is a recent innovation developed by civil engineers. It has all the benefits of self-consolidating concrete (such as flowability and stability) with the added benefit of increased strength. It is beneficial in cases that require a congested steel cross section because it can envelop and encapsulate the steel reinforcement, even in congested steel areas.<sup>4</sup> High-strength SCC is a type of material for which the material proportions can be modified (for example, reducing the content and size of the coarse aggregate or increasing the paste volume to enhance fluidity) compared with either HSC or SCC. A question is raised here regarding SCC's constituent make-up and effect of fluidity on the structural behavior of high-strength SCC. Differences in the engineering properties (such as time-dependent losses and the modulus of elasticity in concrete structure applications) are examples of an area under investigation. The efficient design of a prestressed concrete member needs to be well understood.

Prestress losses are the losses in tensile stress of prestress steel that affect the performance of a prestressed concrete section. The tensile force in the tendon does not stay constant according to the recorded value in the jacking gauge, but changes over time.

The losses are classified into two categories: immediate and long-term (or time-dependent) losses. Immediate losses take place during prestressing of the tendon and transfer the prestress to the concrete member. The elastic shortening and slip of the anchorage are immediate losses. Losses due to creep of the concrete, shrinkage of the concrete, and relaxation of the tendon are considered time-dependent losses.<sup>5</sup> There are numerous prestress loss estimation procedures that can be found in a variety of sources. The most commonly used approaches to determine the components of prestress losses are provided by the American Association of State Highway and Transportation Officials' AASHTO LRFD Bridge Design Specifications<sup>6</sup> and the PCI Design Handbook: Precast and Prestressed Concrete.<sup>7</sup>

A limited number of full-scale studies have been conducted to determine the long-term behavior of prestressed HSC and high-strength SCC beams. In a recent study by Myers et al.,<sup>1</sup> two precast, prestressed HSC and high-strength SCC bridges were instrumented. The HSC bridge spans a length of 48 ft (15 m) and has a width of 10 ft (3 m). The high-strength SCC bridge spans a length of 34 ft (10 m) and has a width of 10 ft. A total of 32 vibrating wire strain gauges with built-in thermistors were used in the beams and decks. Two data acquisition system boxes were used to monitor both bridges. The researchers incorporated two commonly used loss estimate models for calculating total prestress losses, from the AASHTO LRFD specifications and the PCI Design Handbook. The researchers reported that the losses in the HSC and high-strength SCC bridges were approximately 6.21% and 4.86%, respectively, of the nominal jacking stress. It was concluded that the AASHTO LRFD specifications model overestimated the prestress loss of HSC by 23% and high-strength SCC by 57% when the measured

modulus of elasticity of the material was used in the predicted model. The PCI Design Handbook model was not as accurate and overestimated the total prestress loss by 24% for HSC and 85% for high-strength SCC when the measured modulus of elasticity of the material was used in the predicted model.

In a study conducted by Roller et al.,<sup>8</sup> four 131 ft (39.9 m) long full-scale bridge girders were instrumented to evaluate the prestress losses in HSC bulb-tee girders for the Rigolets Pass Bridge in Louisiana. The total measured prestress losses derived from concrete strains corrected for temperature and load effects were found to be lower than corresponding values calculated using the AASHTO LRFD specifications.

Brewe and Myers<sup>9</sup> conducted a study on six reduced-scale high-strength SCC prestress girders. They used a demountable mechanical strain gauge to monitor prestress losses. The measured prestress losses were compared with various code models. The authors concluded that the PCI Design Handbook method overestimated the prestress losses by approximately 21%, the refined method in the 2007 AASHTO LRFD specifications underestimated the losses by approximately 18%, and the 2004 AASHTO LRFD specifications overestimated the losses by 10%. They also believed that the 2007 AASHTO LRFD specifications method would provide superior results for most projects because this method uses improved equations with fewer assumptions.

## **2. BRIDGE DESCRIPTION**

Bridge A7957 is located on Highway 50 in Osage County, MO. The bridge has three spans with precast, prestressed concrete girders. The bridge was designed to be simply supported for dead load and continuously for live load via a cast-in-place concrete deck (Figure 1). Each span was designed with concrete mixtures of varying compressive

strengths. The two exterior spans are 100 ft (30 m) long, and one interior span is 120 ft (37 m) long. Two intermediate bents and two abutments support the superstructure. The bridge has a superelevation of 2.0%.

Each span implemented four precast, prestressed Nebraska University (NU) 53 girders. The girder's cross section provides several advantages during construction, giving designers more flexibility to increase strand capacity and reduce stress concentration in the edges by curved fillets (Figure 2). The first and third span beams were prestressed by 30 Grade 270 (1860 MPa) steel tendons: 20 straight and 10 harped at double harping points. The 0.6 in. (15 mm) diameter tendons were seven-wire, low-relaxation strands. Four additional 3/8 in. (9.5 mm) diameter prestressing strands were added within the top flange of each girder for crack control. Span two girders were prestressed with the same type of strands; however, 28 straight strands and ten strands were harped at double points. D20 (MD 130) welded wire reinforcement was provided for shear resistance at spacing intervals of 4, 8, and 12 in. (100, 200, and 300 mm) along the length of the girder. The jacking force per strand was 44 kip (196 kN), slightly overstressed to 45 kip (200 kN) to compensate for anchorage losses. To produce a high early strength, steam-curing regime was used to accelerate the hydration process of all the precast, prestressed concrete girders. The maximum steam regime temperature did not exceed 120°F (49°C). The maximum temperatures were held for a period sufficient to develop the required strength (14 to 38 hours).

The target 28-day compressive strength of the HSC and normal-strength SCC was 8000 psi (55.2 MPa) and the specified release strength was 6500 psi (44.8 MPa). However, the high-strength SCC had a 10,000 psi (68.95 MPa) target 28-day

compressive strength and a release compressive strength of 8000 psi. Table 1 presents the mixture proportions of each type of concrete. The precast concrete girders and deck panels were fabricated in August 2013 in Bonne Terre, Mo. Erection began in September 2013. The deck slab was cast from the east to the west sides of the girder, after erection of girders at the site in October 2013. The bridge entered service (opened to traffic) in mid-2014 after the roadway was completed.

### **3. MONITORING SYSTEM**

High-strength concrete, high-strength SCC, and normal-strength SCC girders were produced for spans 1, 2, and 3 of Bridge A7957, respectively. They were instrumented to obtain data for the measured strain and temperature. Six instrumented girders (S1-G3, S1-G4, S2-G3, S2-G4, S3-G3, and S3-G4) were monitored from fabrication through service life.

#### **3.1. VIBRATING WIRE STRAIN GAUGES**

A total of 86 vibrating wire strain gauges with built-in thermistors were used to measure the strain and temperature of the precast, prestressed concrete girders. The standard pattern at the midspan consisted of five gauges over the height of the girder and two more in the slab above the girder. During construction, vibrating wire strain gauge readings were made before strand release, after strand release, during transportation and erection, and before and after casting the deck slab concrete. Monitoring of the bridge is ongoing.

#### **3.2. DATA ACQUISITION SYSTEM**

The data from the vibrating wire strain gauges were recorded by two wireless data acquisition system boxes. Following the erection of the girders, the data acquisition

system was anchored to the interior side of the intermediate bent pier caps for long-term monitoring. A cellular antenna, which was also anchored to the interior side of the bent 2 pier cap, was used to send the data from the data acquisition system in real time back to the researchers during fabrication of the precast, prestressed concrete girders and at the various stages of the bridge construction. Measurements were taken at five-minute intervals.

#### **4. MATERIAL PROPERTIES**

Material property tests were performed on specimens collected from the same batch of concrete as the girders to have adequate predictions for the prestress losses. All the tests follow standard ASTM guidelines.<sup>10-18</sup> Table 2 and Table 3 present a summary of the tests, test methods, and results.

#### **5. PRESTRESS LOSSES**

##### **5.1. ELASTIC SHORTENING LOSSES**

Elastic shortening is the loss of prestress force that takes place when a strand becomes shorter. The forms are stripped, and the prestressing strands are released after adequate strength is added to the casting bed. As a result, the concrete and strands shorten under the load. Elastic shortening loss represents a significant portion of the total prestress loss. The vibrating wire strain gauges embedded in the concrete girder were used to measure elastic shortening indirectly. These measurements were obtained by subtracting the strain reading immediately after release from the baseline strain measurement recorded just before release. Measurements were taken at the level of the strand's center of gravity of the steel. The measuring strain was corrected for thermal effect and multiplied by the modulus of elasticity of the prestressing strands  $E_{ps}$  (28,500

ksi [197 MPa]) to determine measured elastic shortening prestress losses (Eq. [1]). Equation (2) was used to calculate the change in stress from elastic shortening  $\Delta f_{ES}$  Calculated.

$$\Delta f_{ES, Measured} = E_{ps} \epsilon_{cgs} \quad (1)$$

where

$\Delta f_{ES, Measured}$  = measured change in stress from elastic shortening

$\epsilon_{cgs}$  = strain at the centroid of the prestressing steel

$$\Delta f_{ES, Calculated} = \frac{E_{ps}}{E_{ci}} f_{cgs} \quad (2)$$

where

$E_{ci}$  = modulus of elasticity of the concrete at release

$f_{cgs}$  = stress of the concrete at the centroid of the prestressing strands

Equation (3) was used to estimate the  $f_{cgs}$ .

$$f_{cgs} = \frac{P}{A} + \frac{Pe^2}{I_g} - \frac{Me}{I_g} \quad (3)$$

where

$P$  = estimated force immediately after release

$A$  = gross cross-sectional area

$e$  = eccentricity of the strand

$I_g$  = gross moment of inertia (uncracked section)

$M$  = moment applied to the beam

The measured elastic shortening losses were determined and compared with the empirical equations adopted by the 2012 AASHTO LRFD specifications and the 2007 PCI Design Handbook with the actual and approximate modulus of elasticity. The modulus of elasticity plays an important role in predicting elastic shortening losses. Coarse aggregate typically makes up the majority of a concrete mixture; therefore, the behavior of the final hardened concrete depends on the type and quantity of coarse aggregate. From this point, the expression specified in the American Concrete Institute's (ACI's) Building Code Requirements for Structural Concrete (ACI 318-14) and Commentary (ACI 318R-14)<sup>19</sup> was selected (Eq. [4])<sup>2</sup> to predict the modulus of elasticity. In addition, the expression adopted by ACI 363R-10<sup>2</sup> was also used to determine modulus of elasticity (Eq. [5]). Table 4 through Table 6 display the results of measured and predicted elastic shortening using the actual and approximate modulus of elasticity.

$$E_c = 33w_c^{1.5} \sqrt{f'_c} \quad (4)$$

where

$E_c$  = concrete modulus of elasticity

$w_c$  = concrete density

$f'_c$  = concrete compressive strength

$$E_c = 40,000 \sqrt{f'_c} + 10^6 \quad (5)$$

The measured elastic shortening values were typically higher than those predicted by the AASHTO LRFD specifications and the PCI Design Handbook. The method given in the AASHTO LRFD specifications underestimated the elastic shortening losses by



25%. However, the PCI Design Handbook method tended to underestimate the elastic shortening losses of HSC by 35%. As a result, the AASHTO LRFD specifications method was considered more accurate than the PCI Design Handbook method.

## 5.2. COMPARISON FOR TOTAL PRESTRESS LOSSES

The total prestress losses in precast, prestressed girders consist of elastic shortening loss, shrinkage of concrete, creep of concrete, and relaxation of strand, which are considered for serviceability cases.<sup>20,21</sup> Relaxation losses were obtained for the tendons stressed beyond 55% based on the measured prestressing force using the relaxation model (Eq. [6]).<sup>22</sup> These losses do not affect the ultimate strength of a girder, but they may lead to poor prediction of service camber and deflection.<sup>23</sup> Empirical models have been provided by AASHTO LRFD specifications and PCI Design Handbook to determine the components of prestress losses separately.

$$\Delta f_{RE} = f_{pi}' \frac{\log_{10} t}{45} \left( \frac{f_{pi}'}{f_{py}} - 0.55 \right) \quad (6)$$

where

$f_{pi}'$  = initial stress of prestressing tendons

t = time after prestressing

$f_{py}$  = specified yield strength of prestressing tendons

The strain readings at the center of gravity of the steel from the vibrating wire strain gauges were used to measure the total prestress loss in the concrete girder. These values were determined through strain compatibility using the portion of prestress loss due to elastic shortening, creep, and shrinkage. The relaxation losses were estimated

analytically. The measured prestress losses were compared with predicted losses calculated according to the AASHTO LRFD specifications and the PCI Design Handbook using the measured elastic modulus of concrete.

The total measured losses of the HSC girders averaged 38.6 ksi (266 MPa), or 19.4% of the nominal jacking stress of 199 ksi (1370 MPa). However, the total measured losses of the SCC girders (both high-strength SCC and normal-strength SCC) averaged 45.1 ksi (311 MPa), or 22.6% of the nominal jacking stress. In general, elastic shortening losses represented 44.4 % of the total losses. However, time-dependent losses due to creep and shrinkage were less than the elastic shortening losses for measured values in all monitored girders.

Predicted total prestress loss values according to the AASHTO LRFD specifications and the PCI Design Handbook underestimated the measured total strain. Surprisingly, the AASHTO LRFD specifications and PCI Design Handbook methods showed good agreement with measured losses for HSC girders. Losses computed using the PCI Design Handbook method with measured parameters resulted in under predictions of total prestress losses. However, the calculated losses using this method are closer in magnitude to the measured losses than the losses calculated using the AASHTO LRFD method with measured parameters (Figure 3).

Based on this analysis, for precast, prestress HSC, high-strength SCC, and normal-strength SCC, the PCI Design Handbook and AASHTO LRFD specifications methods are recommended for prestress loss estimation in the preliminary design stage. The average difference between the values calculated according to these methods and the measured values was less than 20%. However, for more accurate prediction, these

specifications require some modifications to accommodate the material composition of SCC.

Figure 4 displays the total measured prestress losses for HSC, high-strength SCC, and normal-strength SCC. The high-strength SCC girders had high total prestress loss overall. However, the data are not normalized to take differences in girder length into account. The normalized values indicate that the total loss over a unit length is about 6% less for high-strength SCC than for normal-strength SCC. Furthermore, as could be anticipated, HSC showed total prestress losses of lower magnitude than those of high-strength SCC and normal-strength SCC.

### **5.3. COMPARISON WITH PREVIOUSLY COLLECTED DATA**

Experimental data of measured prestress losses reported in the literature were utilized to make a comparison with measured prestress losses of the Bridge A7957 girders. The collected data<sup>7,21,23-28</sup> contain results that were monitored to evaluate prestress loss in pretensioned beams or girders. The data set contains a total of 58 girder members and includes bridge members located throughout the United States in a variety of environmental conditions and with varying concrete mechanical properties, curing regimes, and geometries. To understand each case study presented in the literature, the cross-sectional area, length, compressive strength, and modulus of elasticity of each specimen were also collected and reported as associated with elastic shortening and total prestress loss. These details provide a clear idea regarding the total prestress losses in each case study. Various prestress loss measurement techniques were used on the specimens; however, a vibrating wire strain gauge was used for most of the collected data. The main objective of this effort was to compare the prestress losses of the Bridge A7957 girders with the data reported in the literature and to check whether the total

prestress losses of Bridge A7957 fall within the collected data range and whether any trends appear.

The collected data were classified into three groups according to concrete type. The first group, with 17 pretensioned girders, was for HSC with a compressive strength greater than 8000 ksi (55 MPa). The second group comprised data for high performance concrete (HPC), with 33 cases included. The remaining set of 8 data points was for SCC. For the specific data set, reference 29 may be reviewed that has the data in tabular format or please contact the authors.

From the data set, the authors concluded that the total measured prestress losses, including elastic shortening, creep of concrete, shrinkage of concrete, and relaxation of the tendon for all the girders ranged from 10% to 35 % of the nominal jacking stress. Because the Bridge A7957 losses were 19.2% and 22.6% for HSC and SCC, respectively, these results fall within the range of the compiled data. Furthermore, the HSC data exhibit lesser variance than other classes of concrete.

After the results were inspected, an effort was made to examine the effects of various parameters, such as specimen length, concrete compressive strength, modulus of elasticity, and geometry, on the total prestress loss. The data were filtered to extract all the relevant information from each study and eliminate the results that were considered outliers. This resulted in 33 specimens to be analyzed for these effects. The total prestress losses decrease as the cross-sectional area increases, while increasing specimen length leads to an increase in the total prestress loss (Figure 5). In addition to geometry effects, the mechanical properties (compressive strength and modulus of elasticity) did not show any general trend with total prestress loss (Figure 5).

## 6. CONCLUSION

This full-scale study was conducted to determine the long-term behavior of prestressed HSC, high-strength SCC, and normal-strength SCC beams. Based on this research, the following conclusions can be drawn:

- A data acquisition system and vibrating wire strain gauges were successfully installed and are functioning adequately to collect strains and temperatures in the girders of Bridge A7957 during fabrication, erection, and service life.
- The measured elastic shortening losses for HSC, high-strength SCC, and normal-strength SCC averaged 19.13, 20.866, and 17.43 ksi (131.9, 143.87, and 120.18 MPa), respectively. For all the girders, the measured elastic shortening losses were higher than predicted using gross cross section and measured or predicted modulus of elasticity.
- The average ratios of measured to predicted elastic shortening according to the AASHTO LRFD specifications and the PCI Design Handbook were between 1.21 and 1.67 for HSC and between 1.35 and 1.43 for high-strength SCC. For normal-strength SCC, the ratios of measured to predicted losses were between 1.23 and 1.42. The difference between the measured and predicted values might be due to resistance to the shortening of the girders before the release, which could cause losses to appear artificially high. It might also be explained by the differences between the actual modulus of elasticity and the values determined from companion specimen tests.
- For all the girders, elastic shortening losses accounted for the largest component of the total measured loss.

- Both the AASHTO LRFD specifications and PCI Design Handbook empirical models underestimated the elastic shortening losses of HSC, high-strength SCC, and normal-strength SCC based on either the actual or predicted modulus of elasticity.
- The total prestress losses averaged 38.65, 48.85, and 43.24 ksi (266.5, 336.8, and 298.1 MPa) for the HSC, high-strength SCC, and normal-strength SCC girders, respectively.
- For most girders, the total measured prestress losses were greater than predicted using the AASHTO LRFD specifications and PCI Design Handbook methods.
- In general, the AASHTO LRFD specifications method tended to be more accurate than the PCI Design Handbook method in predicting HSC prestress losses.
- The total prestress losses in the compiled data included elastic shortening, creep of concrete, shrinkage of concrete, and relaxation of strand for all the girders ranged from 10% to 35% of the nominal jacking stress. Because the Bridge A7957 losses were 19.2% and 22.6% for HSC and SCC, respectively, these results fall within the range of the compiled data. Furthermore, the HSC results data exhibit lesser variance than other types of concrete.

Table 1. Concrete mixture proportions

Material	Type	Quantity		
		HSC	HS-SCC	NS-SCC
Coarse aggregate, lb/yd <sup>3</sup>	¾ in. crushed stone, grade E dolomite	1780	n/a	n/a
	½ in. crushed stone, grade E dolomite	n/a	1340	1476
Fine aggregate, lb/yd <sup>3</sup>	River sand	1085	1433	1433
Cement, lb/yd <sup>3</sup>	Portland cement, Type I	800	850	750
Water/cement	n/a	0.32	0.33	0.35
Chemical admixtures, fl. oz/yd <sup>3</sup>	Air entraining agent	8	17	17
	Type D water reducer and retard	9.2	76.5	67.5
	Type F high-range water reducer	17.2	25.5	25.5

Note: HSC = high-strength concrete; HS-SCC = high-strength self-consolidating concrete; n/a = not applicable; NS-SCC = normal-strength self-consolidating concrete. 1 in. = 25.4 mm; 1 lb/yd<sup>3</sup> = 0.593 kg/m<sup>3</sup>; 1 oz/yd<sup>3</sup> = 37 g/m<sup>3</sup>.

Table 2. Summary of fresh properties, tests, and results

Rheological properties	Test method	Member (span girder)					
		S1-G3	S1-G4	S2-G3	S2-G4	S3-G3	S3-G4
Air, %	ASTM C231 <sup>10</sup>	6.9	6.9	7.5	7.6	6	8.3
Slump or slump flow, in.	ASTM C1611 <sup>11</sup>	9	9	27	26	26.5	26.5
J-ring, in.	ASTM C1621 <sup>12</sup>	n/a	n/a	26.5	25	25.5	25.5
Local temperature, °F	n/a	n/a	n/a	78	76	74	78
Segregation column S, %	ASTM C1610 <sup>13</sup>	n/a	n/a.	0	0.56	n/a	0
Concrete temperature, °F	ASTM C1064 <sup>14</sup>	73	73	n/a	80	80	82

Note: n/a = not applicable. 1 in. = 25.4 mm; °C= (°F - 32)/1.8.



Table 3. Summary of mechanical properties, tests, and results

Tests	Test method	Specimens	Concrete age	Member (span girder)					
				S1-G3	S1-G4	S2-G3	S2-G4	S3-G3	S3-G4
Compressive strength, psi	ASTM C39 <sup>15</sup>	4 in. diameter × 8 in. long cylinder	Release	6896	7635	8516	8141	6924	6434
			28 days	10,774	9733	11,238	10,433	9966	9135
			365 days	10,236	10,642	11,121	11,551	9604	8642
Modulus of elasticity, ksi	ASTM C469 <sup>16</sup>		Release	4435	4717	5328	4697	4706	4212
			28 days	5223	5143	5710	5204	5256	4792
			365 days	5648	5604	5575	5800	5771	5452
Modulus of rupture, psi	ASTM C78 <sup>17</sup>	6 × 6 × 21/24 in. beams	28 days	587	653	691	633	817	640
Coefficient of thermal expansion, $\mu\epsilon/^\circ\text{F}$	ASTM C490 <sup>18</sup>	4 in. diameter × 24 in. long cylinder	180 days	4.97		5.51		6.28	

Note: 1 in. = 25.4 mm; 1 psi = 6.895 kPa; 1 ksi = 6.896 MPa;  $^\circ\text{C} = (^\circ\text{F} - 32)/1.8$ .

Table 4. Elastic shortening losses of high-strength concrete

High-strength concrete								
Result method	S1-G3				S1-G4			
	Microstrain	Stress, psi	Jacking <sup>‡</sup> , %	<i>m/p</i> ratio	Microstrain	Stress, psi	Jacking <sup>‡</sup> , %	<i>m/p</i> ratio
Measured	$632 \times 10^{-6}$	18,024	9.1	1	$710 \times 10^{-6}$	20,235	10.2	1
AASHTO <sup>*</sup>	$521 \times 10^{-6}$	14,855	7.5	1.21	$490 \times 10^{-6}$	13,968	7	1.45
AASHTO <sup>†</sup>	$483 \times 10^{-6}$	13,769	6.9	1.31	$459 \times 10^{-6}$	13,086	6.6	1.55
PCI <sup>*</sup>	$452 \times 10^{-6}$	12,869	6.5	1.4	$425 \times 10^{-6}$	12,100	6.1	1.67
PCI <sup>†</sup>	$476 \times 10^{-6}$	13,580	6.8	1.33	$461 \times 10^{-6}$	13,127	6.6	1.54

Note: AASHTO = AASHTO LRFD specifications; *m* = measured loss; n/a = not applicable; n/a = not applicable; n.d.= no data; *p* = predicted loss; PCI = PCI Design Handbook. 1 psi = 6.895 kPa.

\* Methods using measured modulus of elasticity.

† Methods using approximate modulus of elasticity (Eq. [4] for AASHTO and Eq. [5] for PCI).

‡ Percentage of total prestress loss stress to nominal jacking stress.

Table 5. Elastic shortening losses of high-strength self-consolidating concrete

High-strength self-consolidating concrete								
Result method	S2-G3				S2-G4			
	Microstrain	Stress, psi	Jacking <sup>‡</sup> , %	<i>m/p ratio</i>	Microstrain	Stress, psi	Jacking <sup>‡</sup> , %	<i>m/p ratio</i>
Measured	n.d.	n/a	n/a	n/a	$732 \times 10^{-6}$	20,866	10.5	1
AASHTO <sup>*</sup>	$524 \times 10^{-6}$	14,940	7.5	n/a	$524 \times 10^{-6}$	14,940	7.5	1.4
AASHTO <sup>†</sup>	$525 \times 10^{-6}$	14,971	7.5	n/a	$537 \times 10^{-6}$	15,312	7.7	1.36
PCI <sup>*</sup>	$452 \times 10^{-6}$	12,876	6.5	n/a	$511 \times 10^{-6}$	14,572	7.3	1.43
PCI <sup>†</sup>	$533 \times 10^{-6}$	15,179	7.6	n/a	$541 \times 10^{-6}$	15,409	7.7	1.35

Note: AASHTO = AASHTO LRFD specifications; *m* = measured loss; n/a = not applicable; n/a = not applicable; n.d.= no data; *p* = predicted loss; PCI = PCI Design Handbook. 1 psi = 6.895 kPa.

\* Methods using measured modulus of elasticity.

† Methods using approximate modulus of elasticity (Eq. [4] for AASHTO and Eq. [5] for PCI).

‡ Percentage of total prestress loss stress to nominal jacking stress.

Table 6. Elastic shortening losses of normal-strength self-consolidating concrete

Normal-strength self-consolidating concrete								
Result method	S3-G3				S3-G4			
	Microstrain	Stress, psi	Jacking, ‡ %	<i>m/p ratio</i>	Microstrain	Stress, psi	Jacking, ‡ %	<i>m/p ratio</i>
Measured	$605 \times 10^{-6}$	17,240	8.7	1	$618 \times 10^{-6}$	17,621	8.9	1
AASHTO*	$491 \times 10^{-6}$	13,998	7	1.23	$491 \times 10^{-6}$	13,998	7	1.26
AASHTO†	$482 \times 10^{-6}$	13,741	6.9	1.25	$500 \times 10^{-6}$	14,255	7.2	1.24
PCI*	$425 \times 10^{-6}$	12,126	6.1	1.42	$500 \times 10^{-6}$	14,255	7.2	1.24
PCI†	$476 \times 10^{-6}$	13,561	6.8	1.27	$488 \times 10^{-6}$	13,897	7	1.27

Note: AASHTO = AASHTO LRFD specifications; *m* = measured loss; n/a = not applicable; n/a = not applicable; n.d.= no data; *p* = predicted loss; PCI = PCI Design Handbook. 1 psi = 6.895 kPa.

\* Methods using measured modulus of elasticity.

† Methods using approximate modulus of elasticity (Eq. [4] for AASHTO and Eq. [5] for PCI).

‡ Percentage of total prestress loss stress to nominal jacking stress.

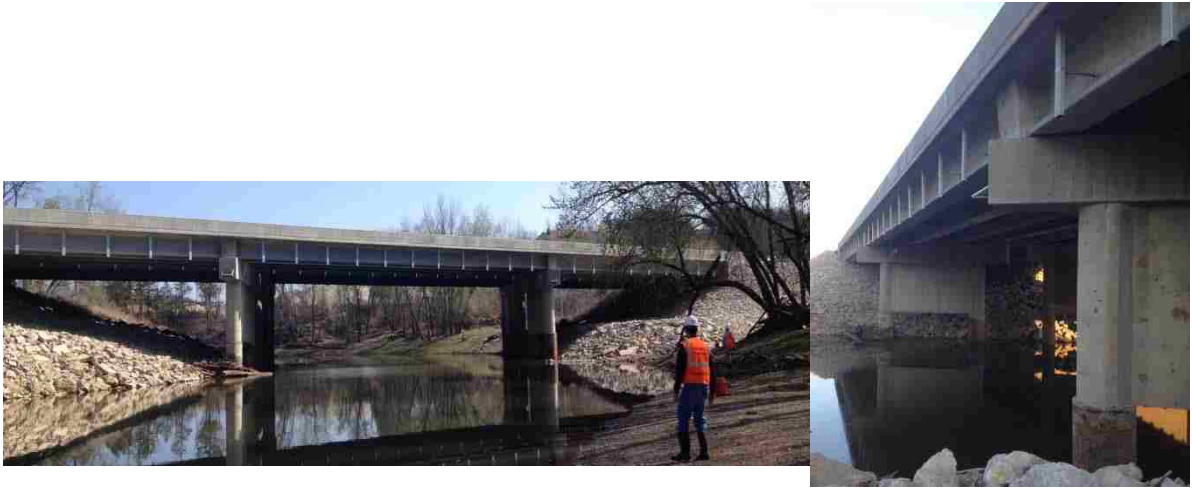


Figure 1. Front and side views of bridge A7957 located on Highway 50 near Linn, MO.

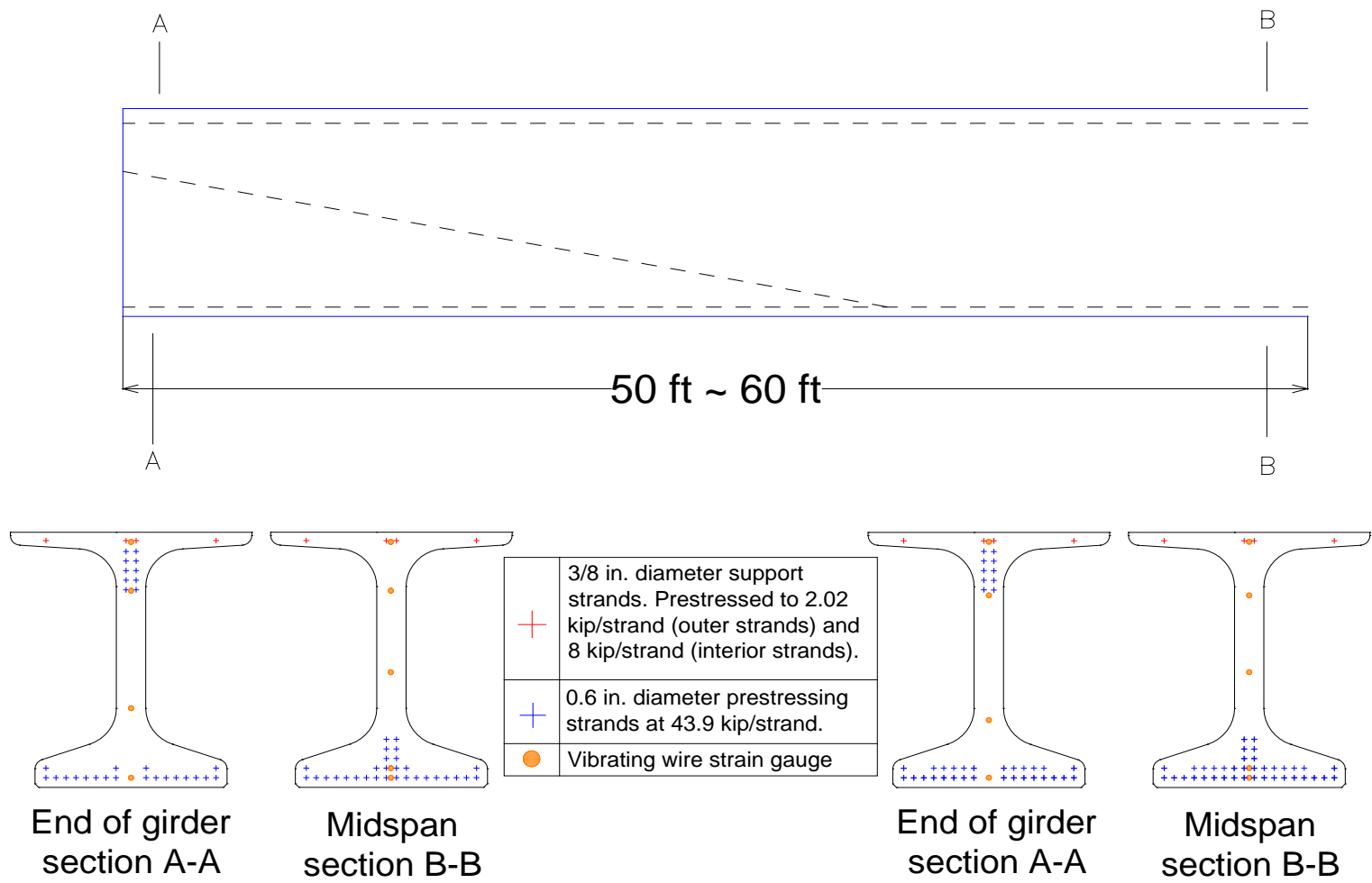


Figure 2. Cross-section view of Nebraska University 53 girder. Note: 1 in. = 25.4 mm; 1 ft = 0.305 m; 1 kip = 4.448 kN.

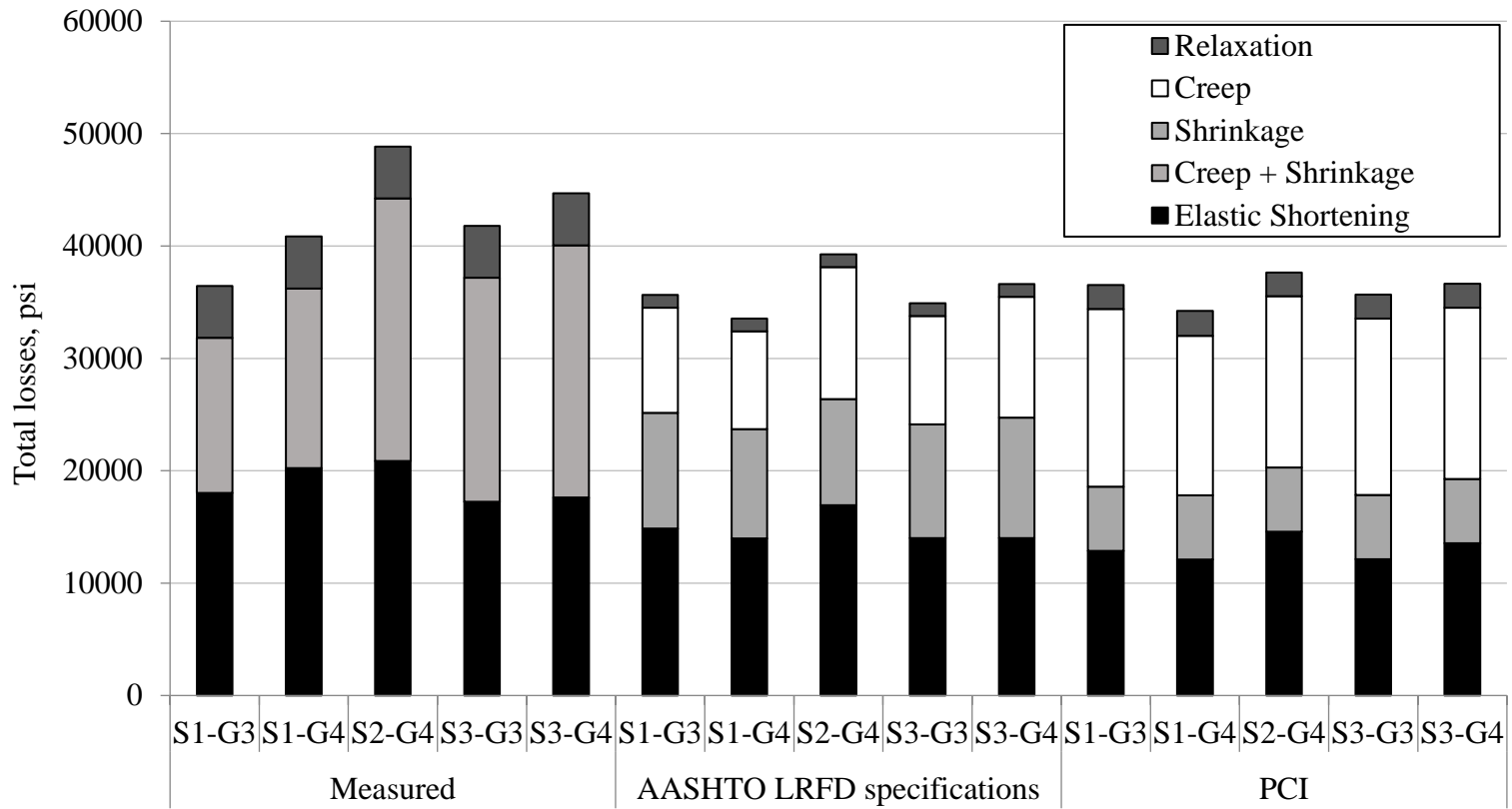


Figure 3. Comparison of total prestress losses. Note: 1 psi = 6.895 kPa.

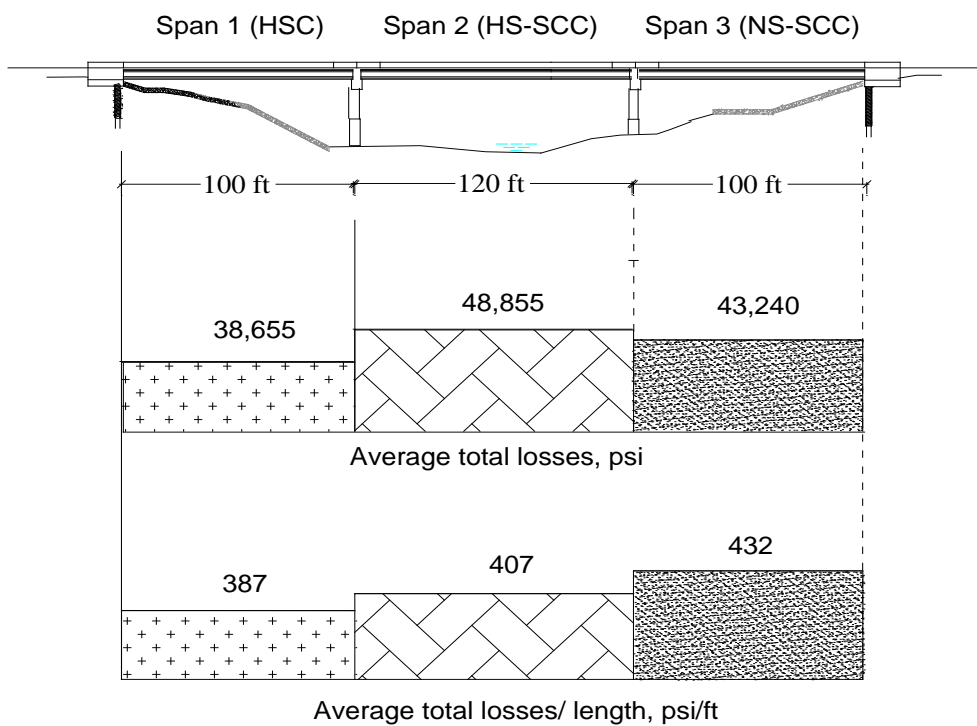


Figure 4. Average total prestress losses.

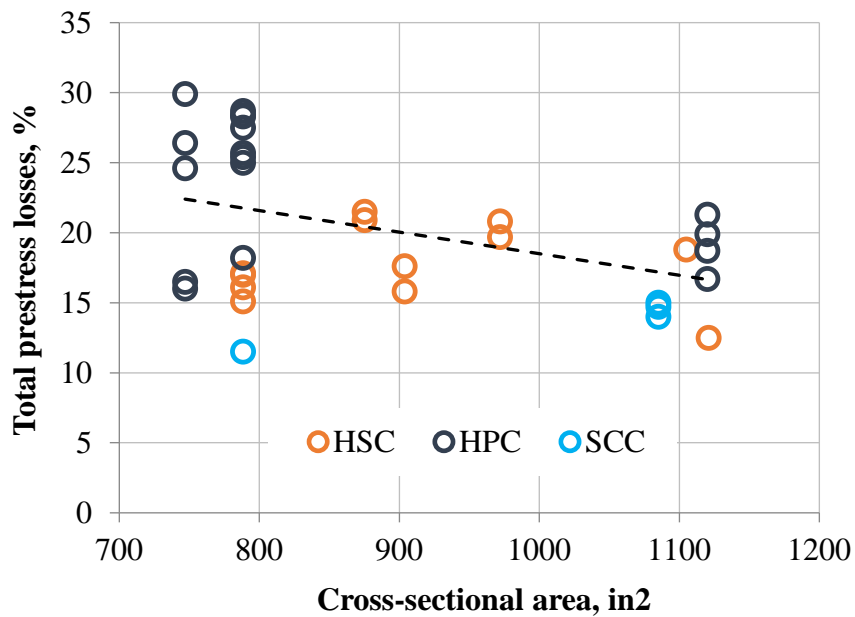


Figure 5. Total measured prestress losses as a percentage of the nominal jacking stress versus various parameters



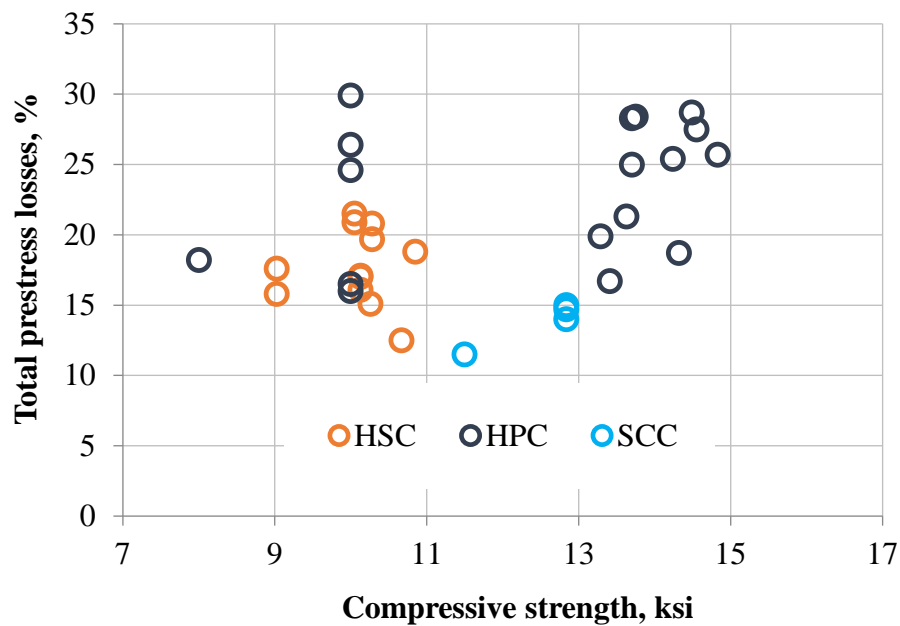
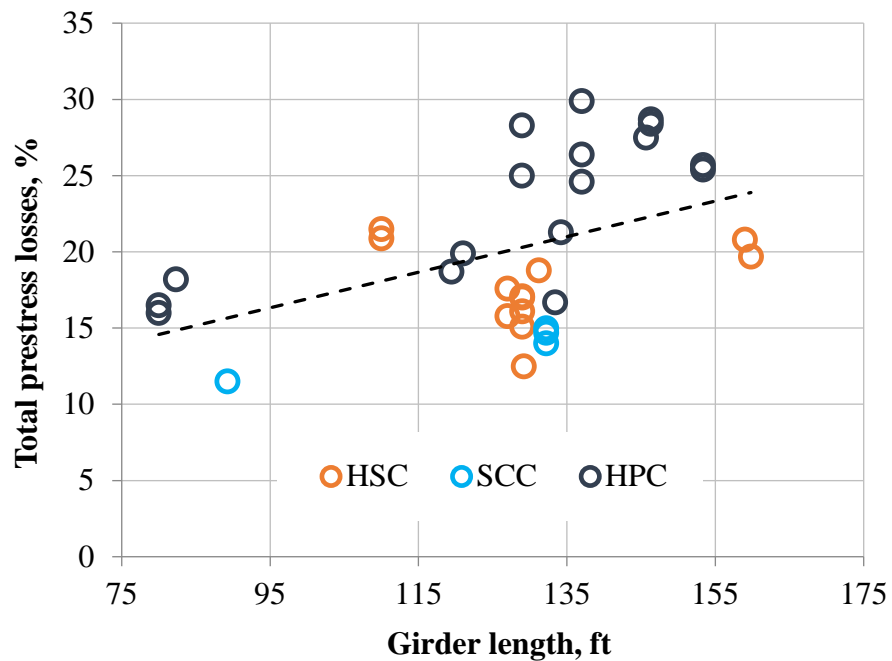


Figure 5. Total measured prestress losses as a percentage of the nominal jacking stress versus various parameters (cont.)

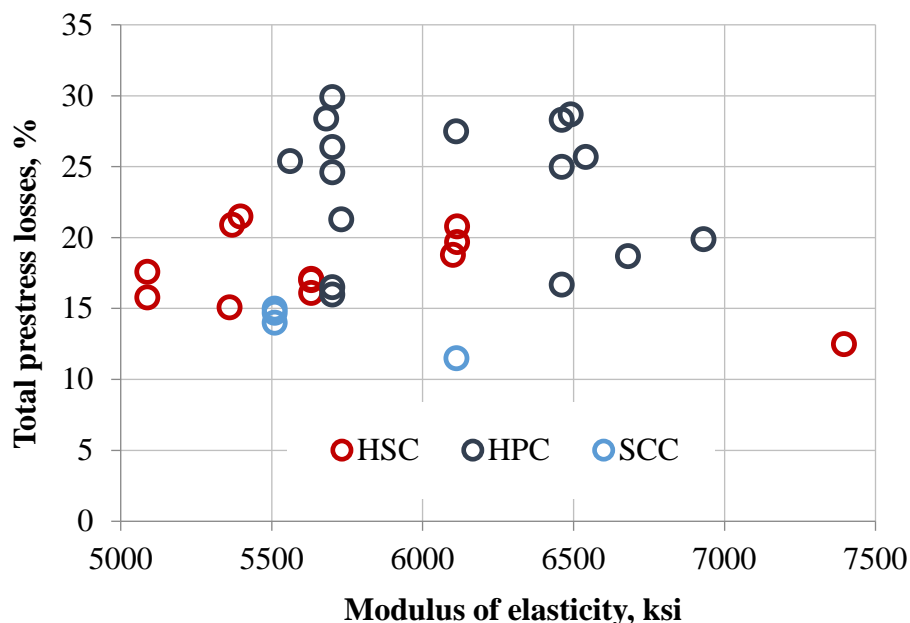


Figure 5. Total measured prestress losses as a percentage of the nominal jacking stress versus various parameters (cont.)

## ACKNOWLEDGEMENTS

The authors gratefully acknowledge the financial support provided by the Missouri Department of Transportation and the National University Transportation Center at the Missouri University of Science and Technology (Missouri S&T). They also wish to thank the support received from both the department of Civil, Architectural and Environmental Engineering and the Center for Infrastructure Engineering Studies at Missouri S&T.

## REFERENCES

1. Myers, J. J., and K.E. Bloch. 2013. *Innovative concrete bridging systems for pedestrian bridges: implementation and monitoring*. National University Transportation Center Report R250. Rolla, MO: Center for Transportation Infrastructure and Safety, Missouri University of Science and Technology.

2. ACI (American Concrete Institute) Committee 363. 2010. *Report on High-Strength Concrete (ACI 363R-10)*. Farmington Hills, MI: ACI.
3. Daczko, J. A. 2012. *Self-Consolidating Concrete: Applying What We Know*. Abingdon, U.K.: Spon Press.
4. ACI Committee 237. 2007. *Self-Consolidating Concrete*. ACI 237R-07. Farmington Hills, MI: ACI.
5. Alghazali, H. H., and J. J. Myers. 2015. "Creep and Shrinkage of Ecological Self-Consolidating Concrete". In *Second International Conference on Performance-based and Life-cycle Structural Engineering (PLSE 2015) Proceedings, December 9–11, 2015, Brisbane, Australia*. St. Lucia, Australia: University of Queensland.
6. AASHTO (American Association of State Highway and Transportation Officials). 2012. *AASHTO LRFD Bridge Design Specifications*. 6<sup>th</sup> ed., customary U.S. units. Washington, DC: AASHTO.
7. PCI Industry Handbook Committee. 2010. *PCI Design Handbook: Precast and Prestressed Concrete*. MNL-120. 7<sup>th</sup> ed. Chicago, IL: PCI.
8. Roller, J. J., H. G. Russell, R. N. Bruce, and W. R. Alaywan. 2011. "Evaluation of prestress losses in high-strength concrete bulb-tee girders for the Rigolets Pass Bridge." *PCI Journal* 56 (1): 110–134.
9. Brewe, J. E., and J. J. Myers. 2010. "High-strength self-consolidating concrete girders subjected to elevated fiber stresses, part 1: prestress loss and camber behavior." *PCI Journal* 55 (4): 59–77.
10. ASTM Subcommittee A09.60.2010. Standard Test Method for Air Content of Freshly Mixed Concrete by the Pressure Method. ASTM C231/C231M-10. West Conshohocken, PA: ASTM International.
11. ASTM Subcommittee A09.47.2009. Standard Test Method for Slump Flow of Self-Consolidating Concrete. ASTM C1611/C1611M-09. West Conshohocken, PA: ASTM International.
12. ASTM Subcommittee A09.47.2008. Standard Test Method for Passing Ability of Self-Consolidating Concrete by J-Ring. ASTM C1621/C1621M-08. West Conshohocken, PA: ASTM International.
13. ASTM Subcommittee A09.47.2010. Standard Test Method for Static Segregation of Self-Consolidating Concrete Using Column Technique. ASTM C1610/C1610M-10. West Conshohocken, PA: ASTM International.

14. ASTM Subcommittee A09.60.2012. Standard Test Method for Temperature of Freshly Mixed Hydraulic-Cement Concrete. ASTM C1064/C1064M-12. West Conshohocken, PA: ASTM International.
15. ASTM Subcommittee A09.61.2012. Standard Test Method for Compressive Strength of Cylindrical Concrete Specimens. ASTM C39/C39M-12a. West Conshohocken, PA: ASTM International.
16. ASTM Subcommittee A09.61.2010. Standard Test Method for Static Modulus of Elasticity and Poisson's Ratio of Concrete in Compression. ASTM C469/C469M-10. West Conshohocken, PA: ASTM International.
17. ASTM Subcommittee A09.61.2010. Standard Test Method for Flexural Strength of Concrete (Using Simple Beam with Third-Point Loading). ASTM C78/C78M-10. West Conshohocken, PA: ASTM International.
18. ASTM Subcommittee A01.95.2011. Standard Practice for Use of Apparatus for the Determination of Length Change of Hardened Cement Paste, Mortar, and Concrete. ASTM C490/C490M-11. West Conshohocken, PA: ASTM International.
19. ACI Committee 318. 2014. *Building Code Requirements for Structural Concrete (ACI 318-14) and Commentary (ACI 318R-14)*. Farmington Hills, MI: ACI.
20. Alghazali H. H., and J. J. Myers. 2015. "High Strength Self Consolidating Concrete Prestress Losses of Bridge A7957, MO, USA Compared to Code Models." In *Fifth International Conference on Construction Materials: Performance, Innovations and Structural Implications (ConMat'15) Proceedings, August 19–21, 2015, Whistler, BC, Canada*. Vancouver, Canada: University of British Columbia.
21. Gross, S. P. 1999. "Field performance of prestressed high performance concrete highway bridges in Texas." PhD diss., University of Texas at Austin.
22. Nawy, E. G. 2009. *Prestressed Concrete: A Fundamental Approach*. 5<sup>th</sup> ed. Upper Saddle River, NJ: Prentice Hall.
23. Tadros, M. K., N. Al-Omaishi, S. J. Seguirant, and J. G. Gallt. 2003. *Prestress Losses in Pretensioned High-Strength Concrete Bridge Girders*. National Cooperative Highway Research Program Report 496 (NCHRP Report 496). Washington, DC: Transportation Research Program.
24. Trejo, D., M. B. Hueste, Y. Kim, and H. Atahan. 2008. *Characterization of self-consolidating concrete for design of precast prestressed bridge girders*. Report 0-5134-2. College Station, TX: Texas Transportation Institute.

25. Ruiz, E. D., R. W. Floyd, B. W. Staton, N. H. Do, and W. M. Hale. 2008. *Prestress losses in prestressed bridge girders cast with self-consolidating concrete, MBTC-2071*. Fayetteville, AR: Mack-Blackwell Rural Transportation Center, University of Arkansas.
26. Myers, J. J., and Y. Yang. 2005. *High performance concrete for bridge A6130-Route 412 Pemiscot County, Missouri*. UTC R39. Rolla, MO: University of Missouri–Rolla.
27. Barr, P., M. Eberhard, J. Stanton, B. Khaleghi, and J. C. Hsieh. 2000. *High performance concrete in Washington State SR18/SR516 overcrossing: Final report on girder monitoring*. Seattle, WA: Washington State Transportation Center (TRAC).
28. Waldron, G. J. 2004. “Investigation of long-term prestress losses in pretensioned high performance concrete girders.” PhD diss., Virginia Polytechnic Institute and State University.
29. Alghazali, H.H., Myers, J.J., “A Study of Elastic Shortening Losses of High-Strength Self-Consolidating Concrete Prestress Girders,” *International Journal of Research in Engineering and Science (IJRES)*, Vol. 4, Issue 9, ISSN (Print) 2320-9356, September 2016, pp 06-16.

## **V. UNIFORM THERMAL BEHAVIORS OF HIGH STRENGTH-SELF CONSOLIDATING CONCRETE BRIDGE GIRDERS (FIELD STUDY)**

Hayder H. Alghazali and John J. Myers

### **ABSTRACT**

Thermal loadings are essential factors in highway bridge design. Knowledge of average bridge temperature (ABT) is important for the prediction of axial bridge deformations during the seasonal temperature cycle. In this study, an on-site instrumentation program to measure the uniform thermal behavior in precast prestressed (PC/PS) high strength-self consolidating concrete (HS-SCC) girders was conducted at the A7957 Bridge on HWY 50, in Missouri, USA. Thermistors integrated within vibration wire strain gauges (VWSG) to record concrete temperature were installed in the bridge girders and the deck slab at specific points of interest. Data concerning temperature were monitored and recorded for over two years. The measured ABT (maximum and minimum) were compared to the design uniform temperatures recommended in the National Cooperative Highway Research Program (NCHRP) Report 276 and American Association of State Highway and Transportation Officials (AASHTO LRFD 2012) methods. The test results showed that these methods did not accurately reflect the extreme temperature measured in this study. A new approach (site-specific basis) was developed by the authors to provide more realistic design temperatures than current methods.

### **Keywords:**

High strength-self consolidating concrete, Thermal Behavior, Health Monitoring, Precast Prestressed Girders, NCHRP Report 276

## 1. INTRODUCTION

Concrete bridge structures are subjected to thermal effects due to the seasonal cycle. Concrete expands slightly as temperature rises and contracts as the temperature falls which causes axial movement in the bridge. Bridge structures must be designed to accommodate this axial movement associated with seasonal cycles (1) (2). Designers realize that the ABT is essential for the prediction of axial bridge movement. The evaluation of accurate values of extreme ABT is important for structural engineers during the design and construction phases of concrete bridges. If the temperatures are not considered within the design, thermal stress and thermal strain may result from restricting bridge component deformation, causing thermal cracking. Thus, the serviceability of the concrete structure will be compromised because of thermal cracking.

High strength-self consolidating concrete (HS-SCC) is an innovation that has been developed by civil engineers to have all benefits of self-consolidating concrete (e.g., as flowability and stability) with the added benefit of increased strength (3) (4) (5). It is beneficial in cases that require a congested steel cross-section because it can pass and encapsulate the steel reinforcement, even in congested steel areas. The HS-SCC type has modifications on material proportions (e.g., reducing content and size of coarse aggregate, and increasing in the paste volume to enhance fluidity). Material properties are one of the several factors that can influence the heat of superstructure (6). A question is raised here regarding SCC's constituent makeup and effect of fluidity on the structural behavior of HS-SCC. Thermal behaviors are examples of an area under investigation. The efficient design of prestressed concrete member needs to be well understood.

A limited number of full-scale studies (field studies) have been conducted to monitor the long-term thermal behaviors of prestressed concrete beams and to see the effect of concrete type on beam thermal behavior. Myers and Yang studied the thermal behavior of high performance concrete bridge girders (7). The measurements were made in Missouri State. They found that the maximum ABTs ranged between 118 to 108 °F (45 to 42 °C) and minimum ABT ranged between 63 to 57 °F (17 to 14 °C) in the AASHTO Type IV girders. The maximum temperatures tended to occur during the summer, typically in July. However, the minimum temperature tended to occur during winter months from December through February. They examined different methods to estimate the effective bridge temperatures such as AASHTO LRFD 1994 specifications (procedure A and procedure B) (8) and NCHRP report 276 (9) methods and concluded that both methods are inappropriate for the bridge locations monitored

Rojas in 2014 conducted a field study on two bridges, I-girder and box girder concrete bridges, to measure the uniform bridge temperature (10). The I-girder bridge (called the California Bridge) was built in 1975. However, the box girder bridge (referred to as Utah Bridge) was built in 1976. The concrete used in the superstructure of the bridges was classified as normal concrete with compressive strength ranged between 3500 - 4000 psi (24 - 28 MPa). The investigator collected temperature data from these bridges using thermocouples. He found that the maximum measured ABT for the California Bridge occurred during June 2013 with a magnitude of 113 °F (45 °C), exceeding the AASHTO LRFD 2010 specifications (11) by 0.49°F (0.28 °C). For the Utah Bridge, the maximum measured ABT occurred during July 2013 with a magnitude



of 107°F (42 °C), exceeding the AASHTO LRFD 2010 specifications by 1.5 °F (0.83 °C).

The objectives of this study were to collect and analyze temperature data from the two instrumented HS-SCC girders, in order to quantify temperature changes in this bridge, and to evaluate the accuracy of the maximum and minimum uniform design temperature defined in the recommended design guidelines by comparing the predicted values to the measured values.

## **2. BRIDGE DETAILS**

The A7957 Bridge on Highway 50 is located in Osage County, Missouri. Latitude and longitude coordinates of the site are 38 29 39.11 N, 91 59 14.00 W. The bridge has three spans with PC/PS concrete girders. The bridge was designed to be simply supported for dead load and continuous for live load via a cast-in-place (CIP) deck (12). Each span was designed with concrete mixtures of different compressive strength. The two exterior spans are 100 ft (30.5 m) long and one interior is 120 ft (36.6 m) long. Two intermediate bents and two abutments support the superstructure. The concrete deck was the riding surface.

Each span used four PC/PS Nebraska University 53 (NU53) girders as shown in Figure 1. The NU 53 girder was developed by the University of Nebraska's Center for Infrastructure Research in cooperation with the Nebraska Department of Roads. The girder's cross section provides several advantages during construction, giving designers more flexibility to increase strand capacity and reduce stress concentration in the edges by curved fillets. Span two with HS-SCC was utilized for this study. The beams were prestressed by 38, Grade 270 steel strands: 28 straight and 10 harped at double harping

points. The 0.6 in. (15 mm) diameter strands were 7-wire, low-relaxation strands. Four additional 3/8 in. (9 mm) diameter prestressing strands were added within the top flange of each girder for crack control.

The design 28-day compressive strength of HS-SCC was 10,000 psi (68.9 MPa) and the specified release strength was 8,000 psi (55.2 MPa). The mixture proportion of HS-SCC mix design is presented in Table 1. Steam curing regime was employed to accelerate the hydration process of all PC/PS girders. The maximum temperature of steam regime did not exceed 120 °F (49 °C). The precast girders and deck panels were fabricated in August 2013 at County Materials Corporation, located in Bonne Terre, Missouri, USA. Erection began in September 2013. The deck slab was cast from the east side to the west of the girder, after the erection of girders at the site in October 2013. The bridge entered into service (i.e., opened to traffic) during the middle of 2014 after the roadway was completed.

### **3. MONITORING SYSTEM**

The structural monitoring system was installed on the bridge to measure strains and temperatures. This paper analyzes more than two years' worth of temperature data. The focus of the monitoring data analysis is on finding the maximum and minimum uniform temperatures that can develop in the bridge girders and compare those to the design code guidelines.

The bridge temperatures were measured using the thermistors integrated within VWSGs embedded in the concrete structure. Temperatures were recorded using an automated data acquisition system installed on the bridge. Since the bridge was not equipped with a weather station, temperature data from the closest weather station to the

bridge monitored by the National Climatic Data Center (NCDC) via the internet was used (13). The closest NCDC weather station is located at the Jefferson City Water Plant, MO, which was approximately 17 miles (28.5 km) from the A7957 Bridge. Image of the bridge during the summer is shown in Figure 2.

A total of 86 vibrating wire strain gauges with built-in thermistors (Type EM-5) were placed at the both ends (2 ft from the end) and mid-span of each of the instrumented girders (two girders for each span). The standard pattern in the mid-span consisted of five gauges over the height of the girder and two more in the slab above the girder. This paper is focused only on the HS-SCC girders produced for span 2. The instrumented girders (namely: S2-G3 and S2-G4) of span 2 were examined. Images of the VWSGs within the girder's height are shown in Figure 3. Data from these VWSGs was sampled at 5 mins intervals with the intention to measure static and slowly-varying response due to creep, shrinkage, and temperature variations. Communication with the DAS for data download was via a wireless modem over a cellular telephone network.

For each set of readings (readings from all VWSGs at the midspan or the ends), an ABT was calculated. The ABT can be defined as a weighted mean of the temperatures at different depths of the composite cross-section and is computed as the sum of the products of each measured temperature within the cross-section and its given weight (14). The weight of each area was computed using the proportion of that area to the total area of composite cross-section. Weights for each layer of the composite beam at mid-span are illustrated in Table 2 and Figure 4. It is worthy to mention here, this process didn't consider the variation in the coefficient of thermal expansion of concretes used in the CIP deck, precast panels, and the girders.

#### 4. RESULTS AND DISCUSSIONS

The ABT was considered in this study as the best representation of the temperature associated with uniform axial movements of the bridge. Temperatures in both beams and deck were used in the calculation of the ABT to reflect the interaction between the beams and composite deck with respect to axial movements.

Two and a half years of data for daily maximum and daily minimum average temperature of the bridge girders are presented in Figure 5 through Figure 8. Two girders were investigated [internal girder (S2-G3) and external girder (S2-G4)] to see the effect of shade and direct sunlight. In general, as can be seen in Figure 5 through Figure 8, the differences in bridge temperatures between the internal and external girders were not significant. The basic trends of the bridge temperatures essentially followed the seasonal ambient temperature fluctuation. The temperature curves partially overlap with each other, and the daily variations in temperature make some trends difficult to visualize, so the average daily maximum and minimum temperatures were calculated for each calendar month, as shown in Figure 9 and Figure 10. It can be noticed that maximum average temperatures tend to occur at the end of July and beginning of August, typically during the middle of the summer.

For both girders (S2-G3 and S2-G4), the maximum average ambient temperatures remained higher than the maximum ABTs. At most, the ambient temperature was 8 °F (4.5 °C) warmer than the ABTs (see Figure 9). The minimum ABTs generally happened in January. They tended to remain higher than the minimum ambient temperatures. On average, the difference was about 7.5 °F (4 °C) during the peak winter month of January, as can be seen in Figure 10.

Table 3 provides the maximum measured temperatures and ABTs recorded for each girder at both ends and midspan. The lowest values of the maximum average daily temperature are also included. The maximum ABTs were 90 °F (32 °C) and 92 °F (33 °C) for S2-G3 and S2-G4 girders at mid-span, respectively. The ABTs at midspan were higher than that at the ends because the end span had more surface area to dissipate heat than midspan. In other words, the addition of the interior bent and cast in place connection masses affect heat gain and loss. Table 4 lists the minimum measured temperature and ABTs. The minimum ABTs were -1 °F (-18 °C) and -2 °F (-20 °C) for S2-G3 and S2-G4 girders, respectively. Again, the minimum ABTs occurred at the midspan. In addition, the minimum ABT [-2 °F (-19 °C)] was higher than ambient temperature [-9 °F (-23 °C)] at the time of the minimum ABT. Unlike maximum temperatures, the lowest monthly average ambient temperature [13 °F (-11 °C) (see Table 4)] was higher than the minimum ABT [-2 °F (-19 °C)].

To determine the applicability of using the current design methods recommended by NCHRP report 276 (9) and AASHTO LRFD 2012 specifications (15), the measured and design maximum and minimum ABTs were compared. Design values are computed and summarized in Table 5. The design temperatures suggested in NCHRP report 276 were more accurate in predicting the maximum ABTs. However, the coldest extreme measured temperature was less than the temperature called for in NCHRP report 276.

The design temperatures calculated using the AASHTO LRFD 2012 specifications (procedure A and procedure B) were also clearly inappropriate for the bridge location monitored in this study. So even though these procedures are simple to

use (in the absence of more specific data), they are not general enough for use in warmer climates such as Missouri.

Based on collected data from different field studies presented in the literature (2) (7) (14), the authors developed a new approach to provide more realistic design temperatures than current methods (see Figure 11 and Figure 12). As can be seen in Eq. 1 and Eq. 2, this approach is more site specific. Eq. 1 and Eq. 2 were derived as a function of the average daily extreme temperature in January and July at the location of the given jobsite.

$$T_{design,max}(^{\circ}F) = -0.0465 T_{July,max}^2 + 10 T_{July,max} - 413 \quad (1)$$

$$T_{design,min}(^{\circ}F) = 0.025 T_{Jan,min}^2 - 0.17 T_{Jan,min} - 8.5 \quad (2)$$

where  $T_{July,max}$  ( $^{\circ}F$ ) is the average daily maximum ambient temperature in July at the bridge location, and  $T_{Jan,min}$  ( $^{\circ}F$ ) is the average daily minimum ambient temperature in January at the bridge location. Design temperatures computed for the bridge location in this study using Eq. 1 and Eq. 2 are presented in Table 5.

## 5. CONCLUSIONS

This full-scale study examined and analyzed more than two years' worth of field-based temperature data of a new class of SCC PS/PC girders in the field. The ABTs were monitored continuously at a 5-minute interval and compared to the design ABT recommended in the NCHRP report 276 and AASHTO LRFD 2012 specifications. Based on the findings, the following conclusions were established:

1. The maximum measured uniform bridge temperature of HS-SCC girders was 92 °F (33 °C) and the minimum uniform bridge temperature was -2 °F (-19 °C). These temperatures can be used for designing the expansion joints and predicting the thermal stresses in the girders.
2. The average maximum and minimum daily bridge temperatures followed the same pattern of seasonal ambient temperatures. These values fell between range of the maximum and minimum seasonal ambient temperatures.
3. The methods for effective bridge temperature suggested in the NCHRP report 276 and AASHTO LRFD 2012 specifications did not accurately reflect the extreme temperature measured in this study.
4. A new approach was developed by the authors to provide more realistic design temperatures. The calculated temperatures using this suggested approach correlate well with the extreme ABTs obtained in this study ( $R^2=0.9$ ). Due to the limit nature of the data set used to derive this approach, the authors recommend further experimental data (from bridges other than those used) is necessary to determine the validity of this approach.

Table 1. HS-SCC Mixture Proportions

Type	Material	HS-SCC
Coarse Aggregate, (lb/yd <sup>3</sup> )	(1/2") Grade E Dolomite	1340
Fine Aggregate, (lb/yd <sup>3</sup> )	Weber, Cristal City Sand/Class A Ledges 4-1	1433
Cement, (lb/yd <sup>3</sup> )	Portland Cement – Type I	850
w/c	---	0.33
Chemical Admixtures, fl. oz/yd <sup>3</sup>	Air Entraining Agent	17.0
	Water Reducer and Retardant	76.5
	High Range Water Reducer	25.5
Design Air Content (%)	---	5

Notes: 1 lb/yd<sup>3</sup>=0.593 kg/m<sup>3</sup>, 1 oz. /yd<sup>3</sup>=37 g/m<sup>3</sup>

Table 2. Weighted Values Implemented to Calculate ABTs

Layer No.	Weight, %
1	0.075
2	0.157
3	0.07
4	0.054
5	0.132
6	0.256
7	0.256



Table 3. Maximum Temperature Values Recorded for Monitored Girders

Description	Interior Beam (S2-G3)			Exterior Beam (S2-G4)		
	Support-W	Mid-Span	Support-E	Support-W	Mid-Span	Support-E
<b>Absolute Maximum Temperature</b>						
Measured	97	102	97	101	100	100
Average Temperature	90	90	90	89	92	89
Ambient Temperature	97	97	97	97	97	97
<b>Lowest Daily Maximum Temperature</b>						
Average Temperature	11	10	9	13	11	9
Ambient Temperature	1	1	1	1	1	1
<b>Highest Average Daily Maximum Temperature per Month</b>						
Average Temperature	81	81	81	81	82	80
Ambient Temperature	88	88	88	88	88	88
<b>Lowest Average Daily Maximum Temperature per Month</b>						
Average Temperature	25	25	24	25	26	24
Ambient Temperature	35	35	35	35	35	35

Note: All Temperature in °F ( $^{\circ}\text{F}=1.8^{\circ}\text{C}+32$ )

Table 4. Minimum Temperature Values Recorded for Monitored Girders

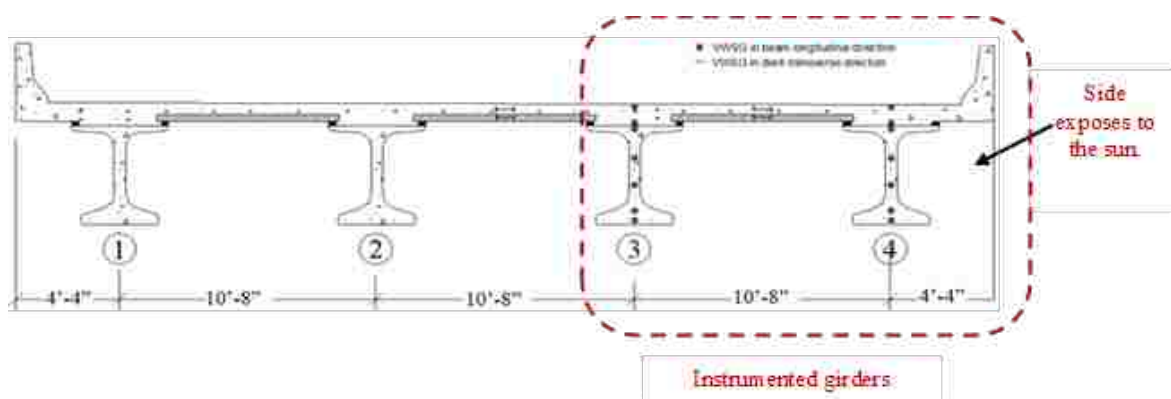
Description	Interior Beam(S2-G3)			Exterior Beam (S2-G4)		
	Support-W	Mid-Span	Support-E	Support-W	Mid-Span	Support-E
<b>Absolute Minimum Temperature</b>						
Measured	3	-2	3	2	-2	4
Average Temperature	7	-1	6	7	-2	5
Ambient Temperature	-9	-9	-9	-9	-9	-9
<b>Highest Daily Minimum Temperature</b>						
Average Temperature	82	81	83	82	81	83
Ambient Temperature	79	79	79	79	79	79
<b>Lowest Average Daily Minimum Temperature per Month</b>						
Average Temperature	19.71	18.52	19.34	20.86	18.50	20.02
Ambient Temperature	12.84	12.84	12.84	12.84	12.84	12.84
<b>Highest Average Daily Minimum Temperature per Month</b>						
Average Temperature	74	72	75	74	72	74
Ambient Temperature	69	69	69	69	69	69

Note: All Temperature in °F (°F=1.8°C+32)

Table 5. Comparison of Measured Temperatures and Design Temperatures

	Maximum		Minimum	
	Interior Beam	Exterior Beam	Interior Beam	Exterior Beam
<b>Ambient Temperature</b>				
Extreme Ambient Temp. Ever Recorded	111	111	-21	-21
Avg. Extreme Ambient Temp. for Peak Month (Jan/July)	86	86	12	12
<b>Measured Average Bridge Temperatures</b>				
Extreme Recorded Temperature on the Bridge	102	101	-2	-2
Extreme Average Bridge Temperature	90	92	-1	-2
Average Daily Bridge Temperature for Peak Month (Jan/July)	81	81	19	19
<b>Design Temperatures</b>				
NCHRP Report 276	96	96	9	9
AASHTO LRFD Specification (2012) Procedure A	81	81	0	0
AASHTO LRFD Specification (2012) Procedure B	113	113	-2	-2
Suggested by Authors	92	92	-3	-3

Note: All Temperature in °F ( $^{\circ}\text{F}=1.8^{\circ}\text{C}+32$ )



Notes: 1 in. = 25.4 mm

Figure 1. Bridge A7957 Cross Section.



Figure 2. Bridge A7957 during the summer.



a) VWSGs in the midspan



b) VWSG close up view



c) DAS attached to the pier bent cap

Figure 3. VWSGs installation.

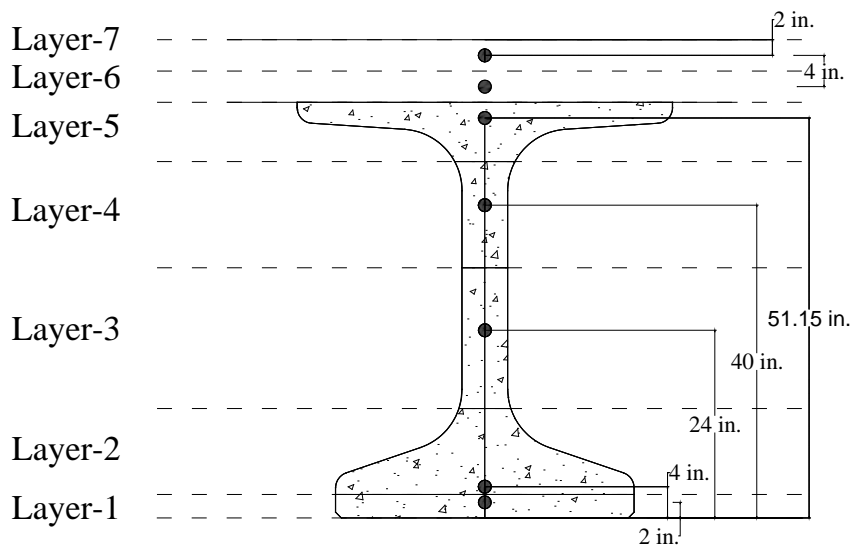


Figure 4. Equivelant layers with sensor locations.

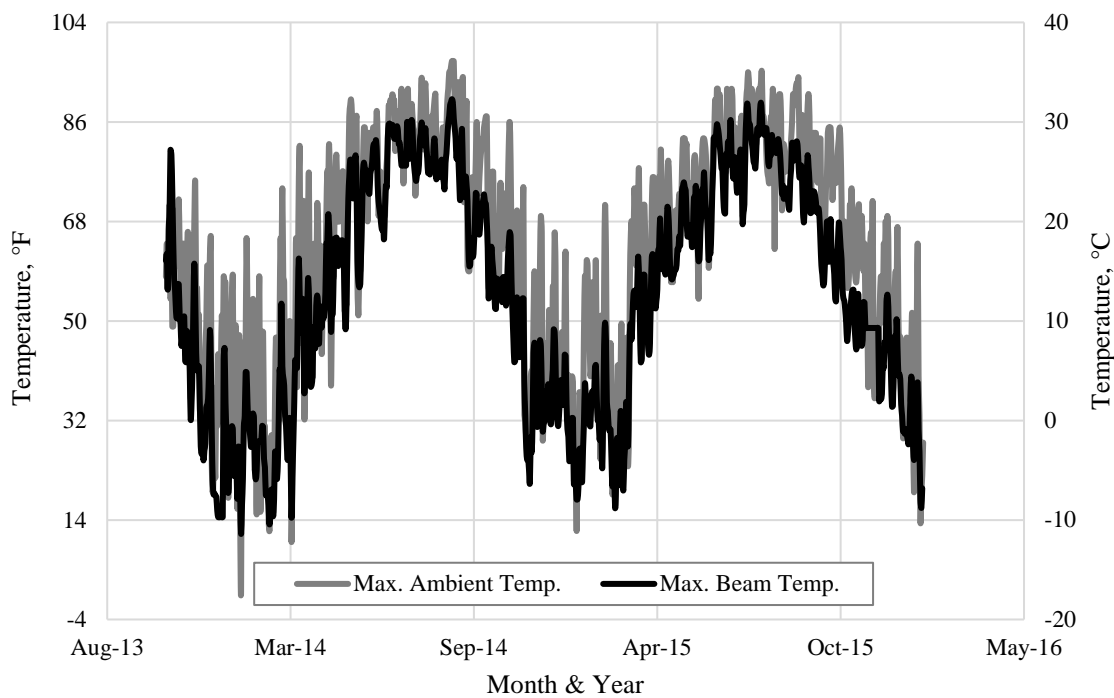


Figure 5. Maximum daily temperature of interior girder (S2-G3).

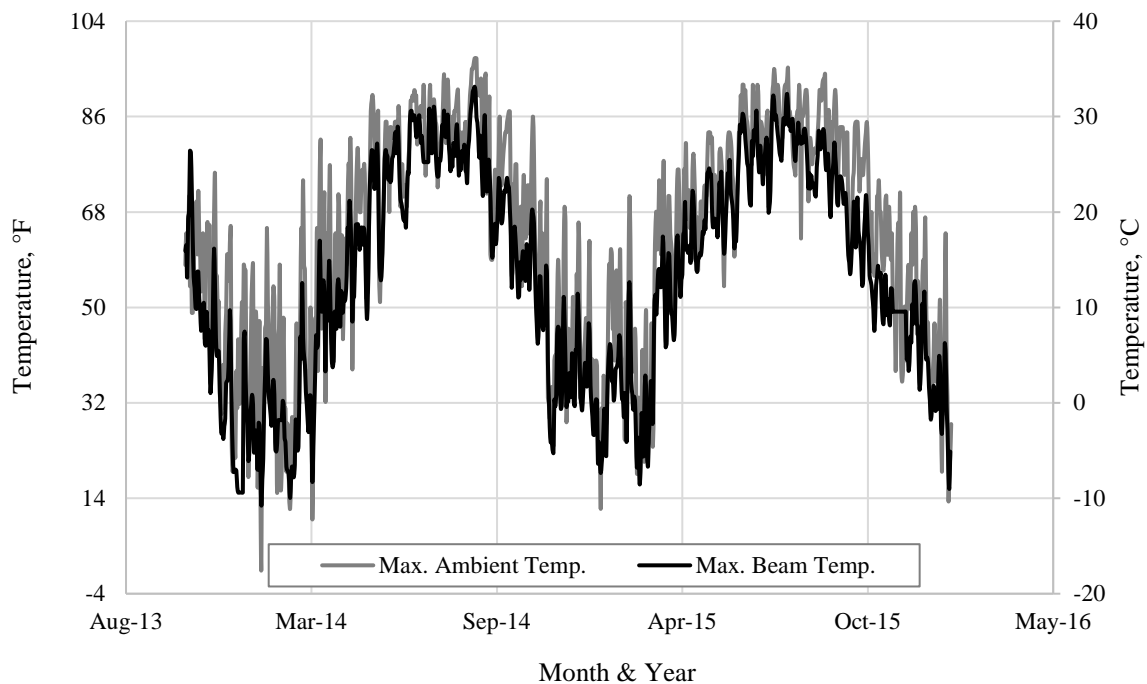


Figure 6. Maximum daily temperature of exterior girder (S2-G4).

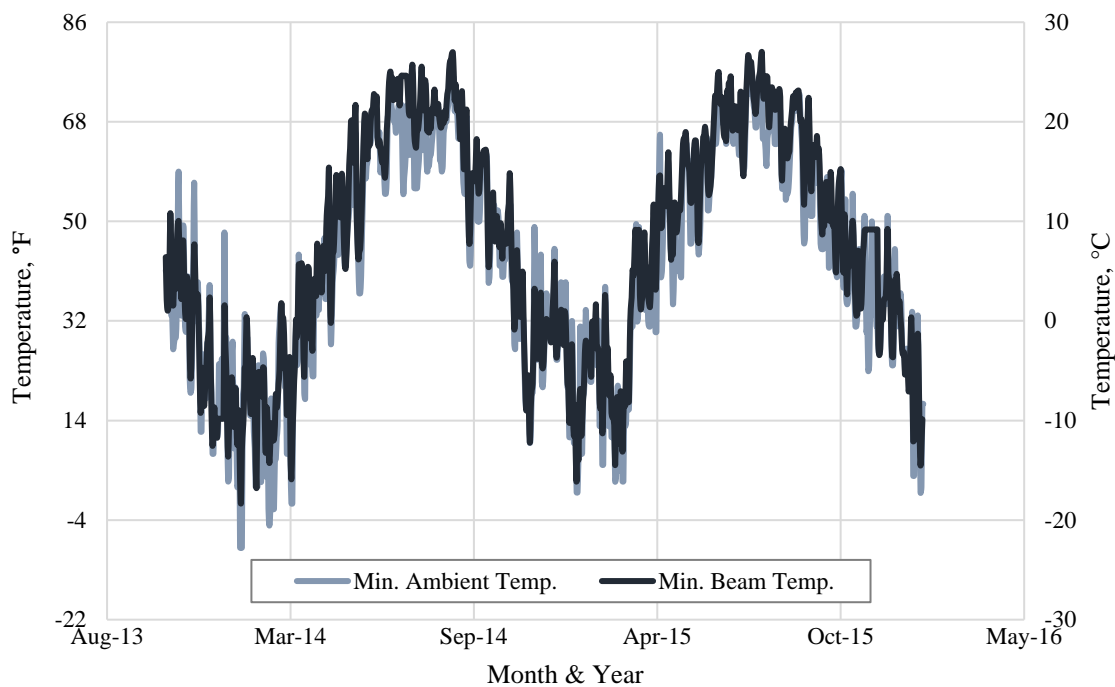


Figure 7. Minimum daily temperature of interior girder (S2-G3).

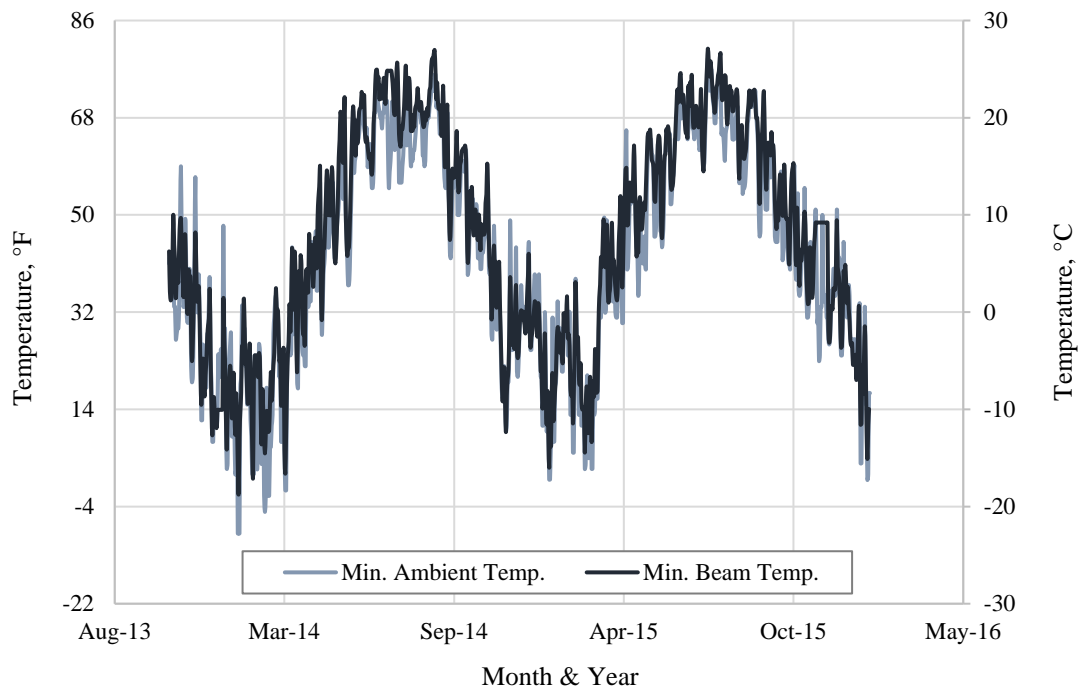


Figure 8. Minimum daily temperature of exterior girder (S2-G4).

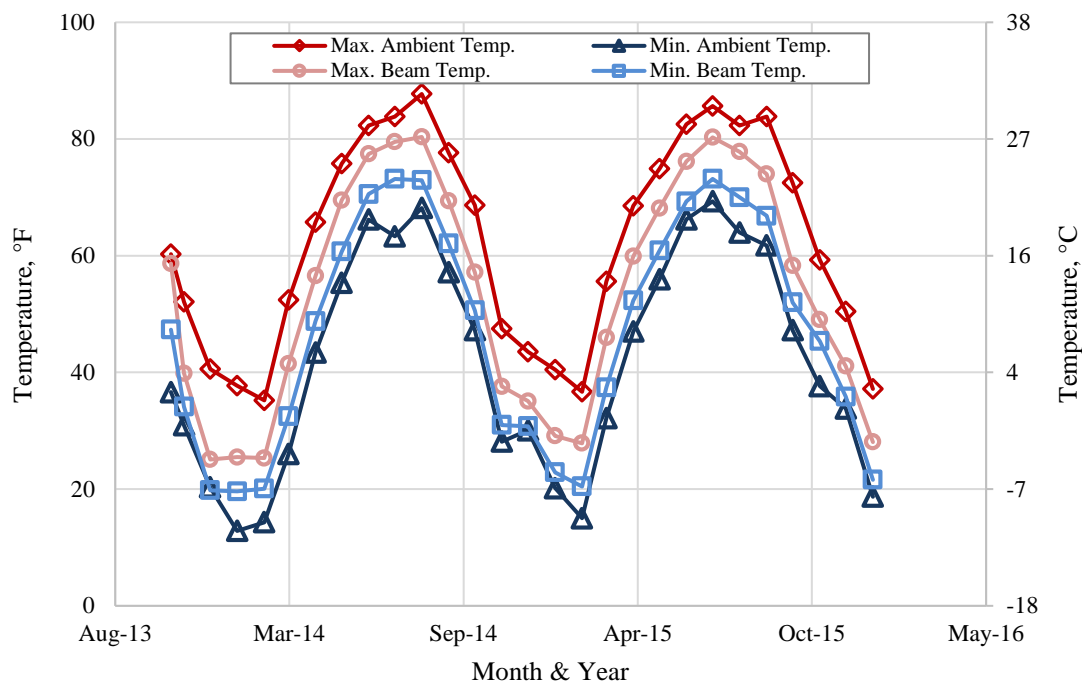


Figure 9. Average maximum and minimum monthly temperatures of interior girder (S2-G3).

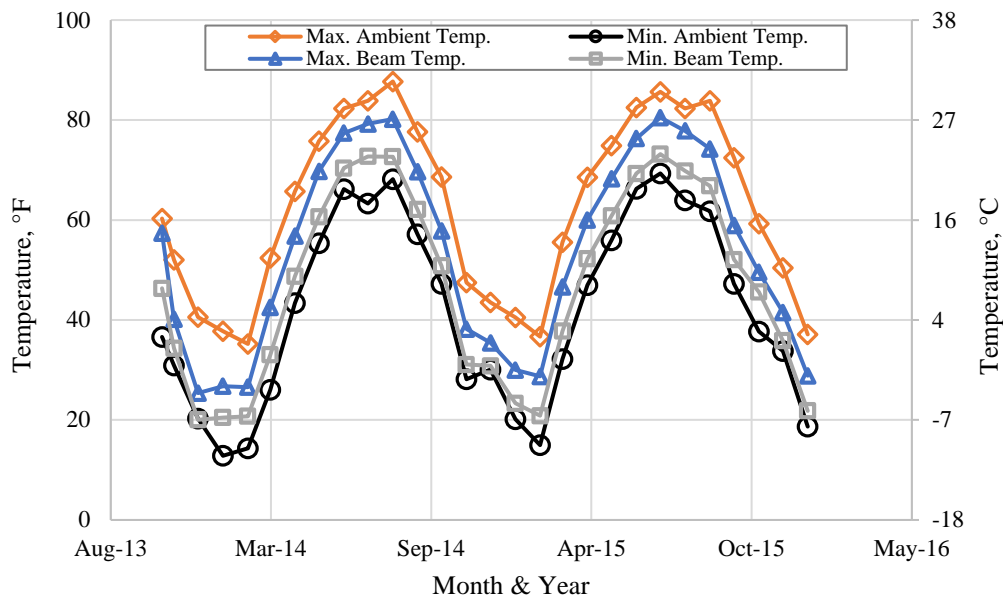


Figure 10. Average maximum and minimum monthly temperatures of exterior girder (S2-G4).

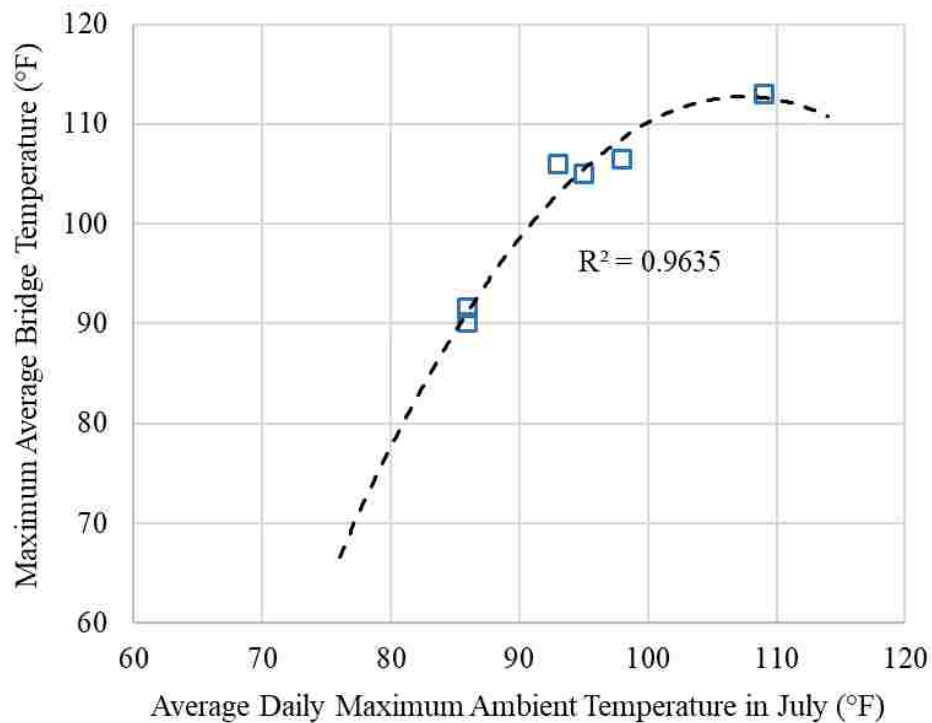


Figure 11. Maximum ABT vs. average maximum ambient temperature in July



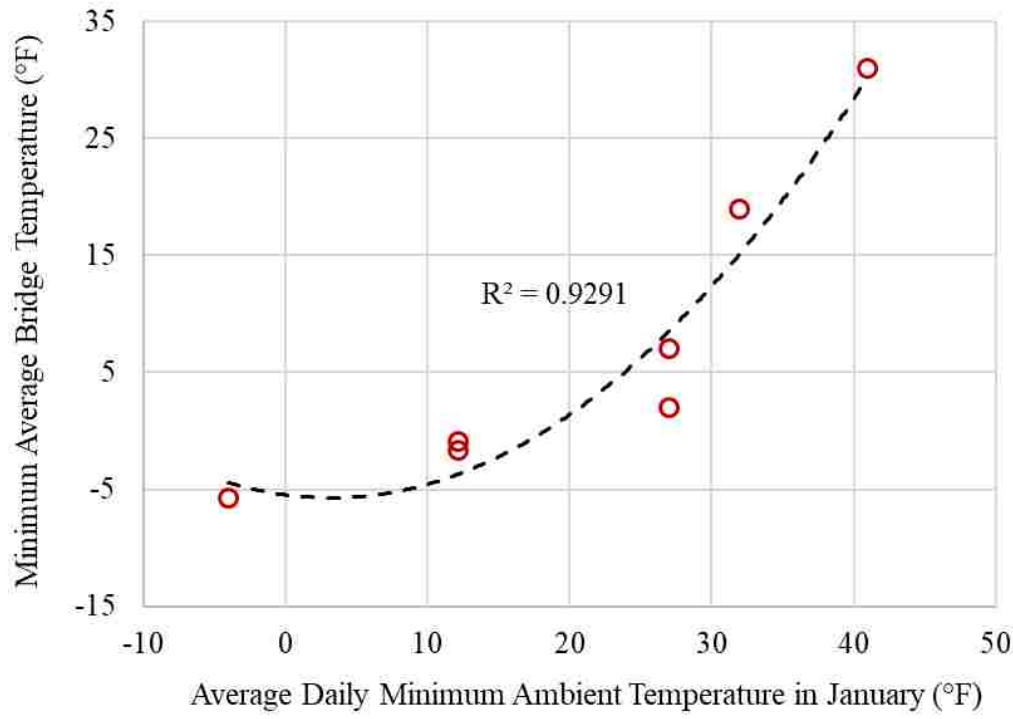


Figure 12. Minimum ABT vs. average minimum ambient temperature in January

**ACKNOWLEDGEMENTS**

The writers gratefully wish to acknowledge the financial support provided by the Missouri Department of Transportation (MoDOT), the National University Transportation Center (NUTC) at the Missouri University of Science and Technology (Missouri S&T), and the Center for Infrastructure Engineering. The authors also want to thank the Department of Civil, Architectural, and Environmental Engineering at Missouri S&T and HCED Iraq sponsor for their support.

## REFERENCES

1. Elbadry, M., and A. Ghali. Thermal Stresses and Cracking of Concrete Bridges. *ACI Journal (Technical Paper)*, Vol. 83, No. 6, pp. 1001-1009, November 1986.
2. Myers, J. J., and K. E. Bloch. *Innovative concrete bridging systems for pedestrian bridges: implementation and monitoring*. Missouri University of Science and Technology, National University Transportation Center (NUTC) Report R250, 2010.
3. ACI Committee 237R-07. *Self-Consolidating Concrete*. American Concrete Institute; Detroit, Michigan, 2007.
4. ACI Committee 363. *State of the Art Report on High Strength Concrete*. American Concrete Institute, Farmington Hills, Michigan, 2010.
5. Alghazali H. H. and J. J. Myers. *High Strength Self Consolidating Concrete Prestress Losses of Bridge A7957, MO, USA Compared to Code Models*. Proceedings of Fifteen ConMat'15 Conference, Vancouver, BC Canada, 2015.
6. Daczko J. A. *Self -Consolidation Concrete, Applying What We Know*. 1<sup>st</sup> edition Spon Press, Abingdon, Oxon, 2012.
7. Myers, J. J. and Y. Yang. *High performance concrete for bridge A6130-Route 412 Pemiscot County, MO*. UTC R39, 2005.
8. *AASHTO LRFD Bridge Design Specifications*. American Association of State Highway and Transportation Officials, Washington, DC, 1994.
9. Imbsen, R. A., D. E. Vandershof, R. A. Schamber, and R. V. Nutt. NCHRP Report No. 276. *Thermal Effects in Concrete Bridge Superstructures*. Transportation Research Record, Washington, DC. 1985.
10. Rojas, E. *Uniform temperature predictions and temperature gradient effects on I-girder and box girder concrete bridges*. Utah State University. 2014.
11. *AASHTO LRFD Bridge Design Specifications*. American Association of State Highway and Transportation Officials, Washington, DC, 2010.
12. Nawy, E. G. *Prestressed Concrete: A Fundamental Approach Fifth Edition*. Upper Saddle River; New Jersey, 2009.
13. NCDC. *Quality Controlled Local Climatological Data*. National Climatic Data Center; website:  
<http://www1.ncdc.noaa.gov/pub/orders/cdo/687365.csv>

14. Gross, S.P. “*Field performance of prestressed high performance concrete highway bridges in Texas;*” University of Texas at Austin, Ph.D. Dissertation, 1999.
15. *AASHTO LRFD Bridge Design Specifications*. American Association of State Highway and Transportation Officials, Washington, DC, 2012.

## **VI. THERMAL GRADIENTS AND THEIR EFFECTS ON HIGH STRENGTH- SELF CONSOLIDATING CONCRETE BRIDGE GIRDERS**

Hayder H. Alghazali and John J. Myers

### **ABSTRACT**

An on-site instrumentation program to measure the thermal gradients in precast prestressed high strength-self consolidating concrete (HS-SCC) was conducted Bridge A7957 located on Highway 50, near Linn, Missouri, USA. Vibration wire strain gauges (VWSG) with built in thermistor to record concrete temperature were installed in the bridge girders and the deck slab in specific points of interests. Data concerning temperature gradients and thermal induced strains through the HS-SCC girders were monitored over a two-year period. Comparisons were made between design thermal gradients (NCHRP Report 276 and AASHTO LRFD) and those measured in-situ within the HS-SCC girders and the cast-in-place deck.

### **Keywords:**

High strength-self consolidating concrete, thermal gradient, health monitoring, precast prestressed girders, NCHRP report 276

## 1. INTRODUCTION

High strength-self consolidating concrete (HS-SCC) is a new innovation that has been developed by civil engineers to have all benefits of self-consolidating concrete (e.g., as flowability and stability) with the added benefit of increased strength<sup>1,2,3</sup>. It is beneficial because it can pass through and encapsulate the reinforcing steel, even in congested steel areas. The HS-SCC type has modifications on material proportions (e.g., reducing content and size of coarse aggregate, and increasing in the paste volume to enhance fluidity). Material properties are one of the several factors that can influence the heat of superstructure<sup>4</sup>. A question is raised here regarding SCC's constituent make-up and effect of fluidity on the structural behavior of HS-SCC. Thermal behaviors are examples of an area under investigation. The efficient design of prestressed concrete (PC) member needs to be well understood.

The daily temperature cycle leads to variation in the temperature distribution along the depth of the superstructure, which is generally a nonlinear variation. This leads to the development of thermal gradients in a structure<sup>5</sup>. Thermal gradients produce a combination of axial and flexural stresses and strains through the depth of the structure<sup>6</sup>. Although these stresses and strains are temporary in nature, their magnitude can exceed those resulting from live loads in certain cases. Therefore, thermal stresses and strains may result in thermal cracking. Thermal cracking does not generally affect the ultimate strength of the bridge components. However, the serviceability of the structure may be significantly affected because thermal cracking causes corrosion of reinforcing steel and thus reduces the service life of the structure<sup>7</sup>.

The diurnal variation of air temperature and solar radiation leads to thermal gradients in a structure. Concrete expands and contracts when subject to temperature increase and decrease, respectively. During a sunny day, the exposed bridge deck heats up more quickly than the underside of the bridge since the underside is shaded from direct sunlight. As a result, a positive thermal gradient will occur<sup>8</sup>. The magnitude of this gradient depends on the amount of radiation absorbed by the deck. In the summer, the positive gradients are typically significant, ranging from 38 to 55 °F (21 to 31 °C), when the amount of solar radiation is at a maximum<sup>8</sup>. These gradients appear to be largest when longer periods of cooler ambient temperature are followed by the larger solar radiation days<sup>9</sup>. A bridge experiences a negative thermal gradient when the deck slab of the bridge subject to larger downward temperature swings than the underside of the bridge. Because the surface area of the bridge deck is typically much larger than the rest of the superstructure, the deck dissipates heat more rapidly than the bottom during the night. Peak negative thermal gradient tends to occur in the fall through spring when downward temperature cycles are largest. The negative thermal gradient magnitude is highly variable because it is dependent on the temperature distribution in the structure at the time when cooling begins and the difference between concrete and ambient temperatures<sup>8</sup>.

Myers and Yang studied the thermal behavior of high performance concrete bridge girders<sup>7</sup>. They found that the average maximum positive gradients were lowest during the winter months and highest during the summer months. Maximum daily negative gradients also varied from day to day. The time of the year did generally not affect negative gradients. They frequently occurred sometime during the early morning,

but the exact time varied substantially from day to day. The average maximum negative gradients remained relatively constant during the year. The maximum positive gradient ranged from 23 to 36 °F (13 to 20 °C), and the peak negative gradients ranged from 7 to 20 °F (4 to 11 °C).

Gross in his Ph.D. study<sup>9</sup> traced the thermal gradients of four different bridges constructed with high performance concrete and high strength concrete in the State of Texas. Thermal gradients were measured for a one-year period. He found that the maximum bridge positive thermal gradients ranged from 28 to 36 °F (16 to 20 °C) for all four bridges. However, he found that negative thermal gradients ranged from 11 to 13 °F (6 to 7°C). Furthermore, he concluded that the design positive gradients suggested by NCHRP 267 and AASHTO LRFD underestimated the temperature measured at two depths of the deck. Otherwise, the shapes of the measured and design positive gradients were similar. The measured negative thermal gradients correlated very well with those predicted by NCHRP 267 and AASHTO LRFD.

## **2. BRIDGE DESCRIPTION**

The A7957 Bridge on Highway 50 is located in Osage County, Missouri. The bridge has three spans with PC/PS concrete girders. The bridge was designed to be simply supported for dead load and continuous for live load via a CIP deck<sup>11, 12</sup>. Each span was designed with concrete mixtures of different compressive strength. The two exterior spans are 100 ft (30.5 m) long and one interior is 120 ft (36.6 m) long. The superstructure is supported by two intermediate bents and two abutments. The bridge has a superelevation of 2.0%.

Each span implemented four PC/PS Nebraska University 53 (NU53) girders as shown in Figure 1. The NU 53 girder was developed by the University of Nebraska's Center for Infrastructure Research in cooperation with the Nebraska Department of Roads. The girder's cross section provides several advantages during construction, giving designers more flexibility to increase strand capacity and reduce stress concentration in the edges by curved fillets (see Figure. 2). Span two with HS-SCC was utilized for this study. The beams were prestressed by 38, Grade 270 steel strands: 28 straight and 10 harped at double harping points. The 0.6 in. (15 mm) diameter strands were 7-wire, low-relaxation strands. Four additional 3/8 in. (9 mm) diameter prestressing strands were added within the top flange of each girder for crack control. The jacking force per strand was approximately 44 kips, slightly overstressed to 45 kips to compensate for chuck slippage losses.

The target 28-day compressive strength of HS-SCC was 10,000 psi (68.9 MPa) and the specified release strength was 8,000 psi (55.2 MPa). The mixture proportion of HS-SCC mix design is presented in Table 1. Steam curing regime was utilized to accelerate the hydration process of all PC/PS girders. The maximum temperature of steam regime did not exceed 120 °F (49 °C). The precast girders and deck panels were fabricated in August 2013 at County Materials Corporation, located in Bonne Terre, Missouri, USA. Erection began in September 2013. The deck slab was cast from the east side to the west of the girder, after the erection of girders at the site in October 2013. The bridge entered into service (i.e., opened to traffic) during the middle of 2014 after the roadway was completed.



### 3. MONITORING SYSTEM

The structural monitoring system was installed on the bridge to measure strains and temperatures. This paper analyzes more than two years' worth of temperature data. The focus of the monitoring data analysis is on finding the maximum positive and negative temperature gradients that can develop in the bridge girders and comparing those to design code guidelines.

#### 3.1 MEASUREMENTS

Thermistors within VWSGs were utilized to monitor the temperature gradient within the cross section of the girders. Temperatures were recorded using an automated data acquisition system installed on the bridge. Since the bridge was not equipped with a weather station, temperature data from the closest weather station to the bridge monitored by the National Climatic Data Center (NCDC) via the internet was used<sup>13</sup>. The closest NCDC weather station is located at the Jefferson City Water Plant, MO, which was approximately 17 miles (27.4 km) from the A 7957 Bridge. The ambient temperature was used as an indicator to predict the occurrence of maximum and minimum thermal gradients during the analysis. The daily maximum and minimum ambient temperatures are illustrated in Figure 3. Image of the bridge during the summer is shown in Figure 4.

The HS-SCC girders produced for span 2 of the A7957 Bridge were instrumented to obtain data for the measured strain and temperature. Two instrumented girders (namely: S2-G3 and S2-G4) of span 2 were monitored. The VWSGs locations within instrumented PC/PS girders are illustrated in Figure 1.

### **3.2. VIBRATING WIRE STRAIN GAUGES (VWSGS)**

A total of 86 vibrating wire strain gauges with built-in thermistors (type EM-5) were utilized to measure the strain and temperature for the PC/PS girders. The VWSGs were installed in the mid-span and ends of the girder. The standard pattern in the mid-span consisted of five gauges over the height of the girder and two more in the slab above the girder. Images of the VWSGs within the girder's height are shown in Figure 5.

### **3.3. DATA ACQUISITION SYSTEM**

The data from the VWSGs were recorded by a data acquisition system (DAS). The DAS used was Campbell Scientific CR800 box which works wirelessly. Following the erection of the girders, the CR800 DAS was anchored to the interior side of the intermediate bent pier caps for long-term monitoring. Data from these VWSGs was sampled at 5 mins intervals with the intention to measure static and slowly-varying response due to creep, shrinkage, and temperature variations. Communication with the DAS for data download was via a wireless modem over a cellular telephone network.

## **4. RESULTS AND DISCUSSION**

During the day, the cross section of a concrete girder can heat or cool non-uniformly due to the low thermal conductivity of the concrete. This produces gradients that typically significant through the depth of the cross section. For purpose of computation, a positive thermal gradient was defined as a gradient in which the maximum temperature occurred at a location higher than the location of the minimum temperature. The maximum temperature typically occurs in the deck. Similarly, a negative gradient was defined as a gradient in which the maximum temperature occurs at a location lower than the minimum temperature in the deck. The magnitude of either

gradient was defined as the difference between the maximum and the minimum temperatures through a cross section of a concrete girder. The positive thermal gradients are generally observed on hot, clear, and sunny afternoon with high solar radiation during the summer, typically between 2:00 and 4:00 pm. and negative thermal gradients occur in general between 1:00 and 8:00 pm during the cold, cloudy day throughout the year<sup>15</sup>.

For NU girders, typical heating and cooling behaviors on sunny summer days and cloudy winter days are shown in Figure 6 through Figure 9, respectively. A positive gradient exists when the deck heats up quicker than the beam. During the morning (8:00 am) the deck warms up more quickly from solar radiation than the underside of the superstructure (beams) which is shaded from direct sunlight, resulting in a positive gradient. The magnitude of this gradient is increased during the afternoon (12:00 pm – 2:00 pm) where the beam heats up somewhat uniformly, however; since the surface area of the deck is typically much larger than the beams, the deck heats up at a faster rate than the beam. During the late afternoon and early evening, the temperature toward the top of the deck begins to drop quickly, as the deck reradiates heat to the atmosphere. The beam temperatures fall down slowly and uniformly until the deck temperature drops below the beam temperature and results in a negative gradient.

Figure 10 and Figure 11 illustrate the time of maximum daily positive thermal gradients and negative thermal gradients occurrence for interior and exterior HS-SCC girders, respectively. The magnitude of the maximum positive gradient varied substantially from day to day. Maximum positive gradients trended to be higher during summer months and lower during the winter months because of the intense solar radiation and high ambient temperature. The average maximum negative gradients are

substantially smaller than the average maximum positive gradients. As visible in Figure 10 and Figure 11, thermal gradients in the interior (S2-G3) and exterior (S2-G4) girders had a slightly different distribution over the years. These differences can be attributed to the intensity of solar radiation on the top surface of the girders (deck slab). The interior girder was shadowed during the morning and the afternoon even though the solar attitude is the lowest during that time. In contrast, the exterior girder was exposed to direct sunlight on the south side from approximate sun rise to sun set because the deck overhang does not shade the beam surface. In other words, the differences were due to the shadow.

Magnitudes of the maximum measured thermal gradients for exterior and interior HS-SCC girders are summarized in Table 2. The peak positive gradients recorded at a time during measurement period ranged from 21.2 to 25.77 °F (11.78 to 14.32 °C), and the peak negative gradients ranged from -9.09 to -17.23 °F (-5.05 to -9.57 °C). It is important to mention here that these gradients are temperature differences between the beam and the location of the top deck gauge [2 in. (50 mm) below the deck surface], not the deck surface.

The positive thermal gradients for the supports of interior girder tended to be 3 to 5 °F (2 to 3 °C) higher than the mid-span, and the negative gradients tended to be 4 to 7 °F (2 to 4 °C) lower than the mid-span. However, the variation of positive gradients for the supports of exterior girder was minimal, and the negative gradients tended to be 1 to 4 °F (0.6 to 2 °C) higher than the mid-span. Possible considerations for the mid-span having a higher gradient can be attributed to the location of support which causes the girders to experience quite different temperatures due to shadow and solar attitude<sup>15</sup>.

Moreover, the addition of the interior bent and cast in place connection masses affect heat gain and loss. At this location, heat will enter and leave from the girder ends in a higher rate than the deck surface. This action will cause a higher thermal gradient section than sections where heat can enter and dissipate more freely at the girder ends and deck surface, such as at mid-span<sup>16</sup>.

To determine the applicability of HS-SCC girders to a current design standard, the results for the typical positive thermal gradients and negative thermal gradients were compared with the NCHRP report 2768 and AASHTO LRFD specification<sup>17</sup>. The NCHRP report 276 and the AASHTO LRFD specifications provide the engineer with temperature gradients over the depth of cross section to predict the vertical thermal behavior of a bridge. Figure 12 illustrates the theoretical positive gradient compared to the interior and exterior mid span girders. Figure 13 illustrates the theoretical negative gradient compared to the interior and exterior mid span girders. It can be clearly seen in Figure 12 that the maximum measured positive gradients are reasonably similar in shape to the design positive gradients specified by NCHRP and AASHTO. The main differences are that the temperatures at bottom gauge [located 6 in (150 mm)] below the deck surface and temperature in the beam web [located 20 in (1000 mm) or less] below the deck surface were both underestimated by the design gradients for all cases. The measured negative gradients had a shape approximately similar to the design negative gradients. The only clear differences are all temperatures in gauges located 40 in. (1000 mm) below the deck surface were underestimated by NCHRP and AASHTO specification. More in-depth results will appear in a full journal article to discuss the impact of these temperature gradients on bridge behaviors and/or design.

## 5. CONCLUSIONS

This study represents measured field-based thermal gradients of a new class of SCC PS/PC girders in the field. Thermal gradients were monitored for a two-and-a-half-year period in both girders. Maximum positive thermal gradients in the both girders ranged from 21.2 to 25.77 °F (11.78 to 14.32 °C). Maximum negative thermal gradients in the monitored girders ranged from -9.09 to -17.23 °F (-5.05 to -9.57 °C). These measured values are based on top deck gauges located 2 in. (50 mm) below the deck surface. The maximum positive thermal gradient typically occurred between 2:00 to 4:00 pm during the summer. However, the maximum negative thermal gradient typically occurred between 1:00 to 8:00 pm during the winter. The temperature profile of thermal gradient in exterior beams was observed to be quite different from those in interior beams under certain conditions. Differences in thermal gradients can be contributed to direct sun, shadow, and wind. The design positive thermal gradients suggested by NCHRP report 276 and AASHTO LRFD provided theoretical values that were close to the values of the top and the bottom of the beam. However, intermediate points appeared to be underestimated by the models. In both girders at 24 in (610 mm) from the bottom, there is a difference of 2.54 °F (1.41 °C) between measured data and theoretical ones. The design negative thermal gradients underestimated temperatures measured at certain depths within the beam.

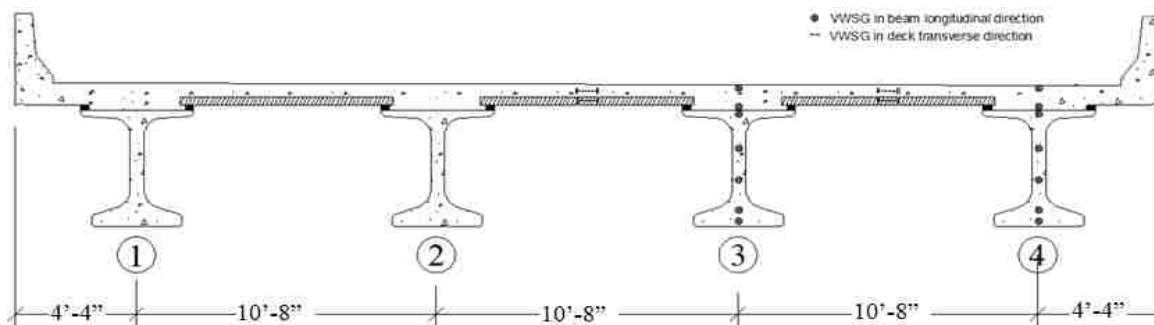
Table 1. HS-SCC mixture proportions

Type	Material	HS-SCC
Coarse Aggregate, (lb/yd <sup>3</sup> )	(1/2") Grade E Dolomite	1340
Fine Aggregate, (lb/yd <sup>3</sup> )	Weber, Cristal City Sand/Class A Ledges 4-1	1433
Cement, (lb/yd <sup>3</sup> )	Portland Cement – Type I	850
w/c	---	0.33
Chemical Admixtures, oz/yd <sup>3</sup>	Air Entraining Agent	17.0
	Water Reducer and Retardant	76.5
	High Range Water Reducer	25.5
Design Air Content (%)	---	5

Notes: 1 lb/yd<sup>3</sup>=0.593 kg/m<sup>3</sup>, 1 oz. /yd<sup>3</sup>=37 g/m<sup>3</sup>

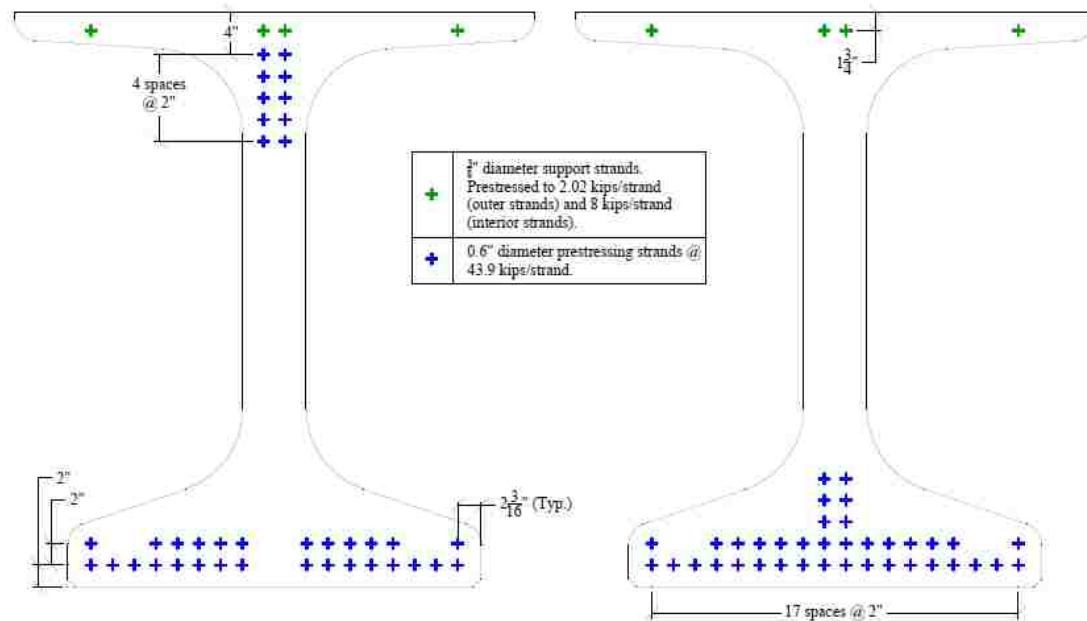
Table 2. Maximum and minimum thermal gradients

Girder ID	Support (West)		Mid-span		Support (East)	
	S2-G3	S2-G4	S2-G3	S2-G4	S2-G3	S2-G4
Positive Gradient, °F (°C)	25.77 (14.32)	22.89 (12.72)	21.20 (11.78)	22.26 (12.37)	23.90 (13.28)	22.57 (12.54)
Negative Gradient, °F (°C)	-15.60 (-8.67)	-16.22 (-9.01)	-9.09 (-5.05)	-17.23 (-9.57)	-13.16 (-7.31)	-13.14 (-7.30)



Notes: 1 in. = 25.4 mm

Figure 1. Bridge A7957 cross section



Conversion: 1 in. = 25.4 mm

a) End view

b) Mid-span view

Figure 2. Cross section views of NU 53 girder



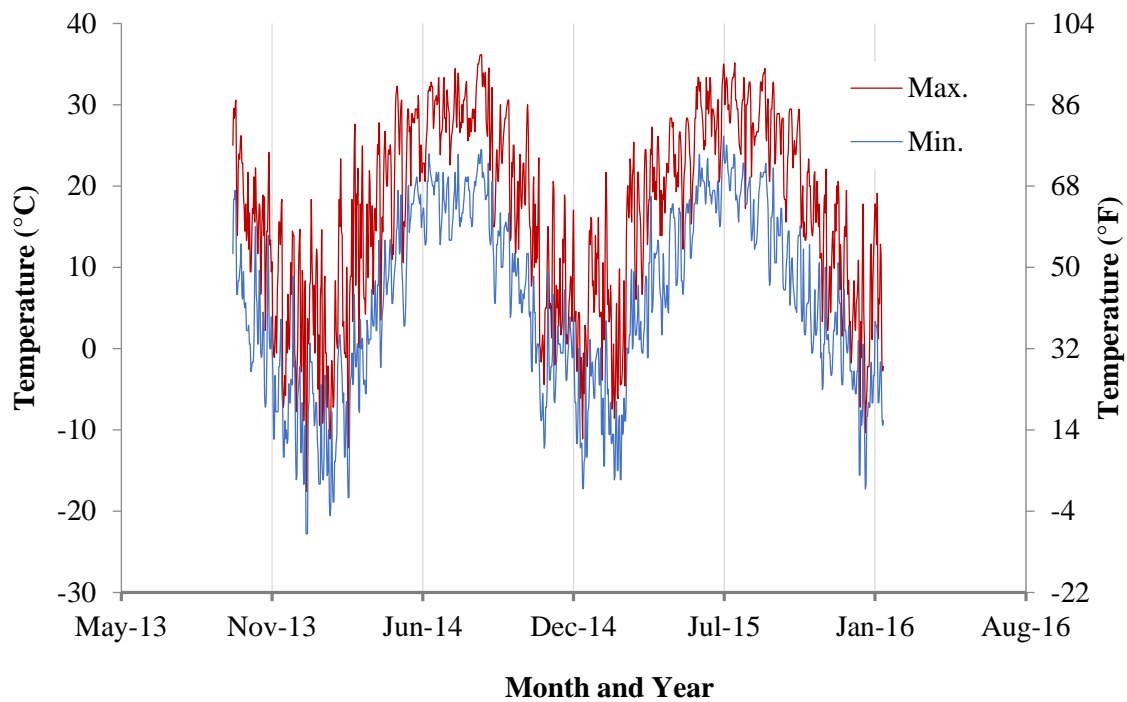


Figure 3. The maximum and minimum ambient temperature



Figure 4. Bridge A7957 during the summer

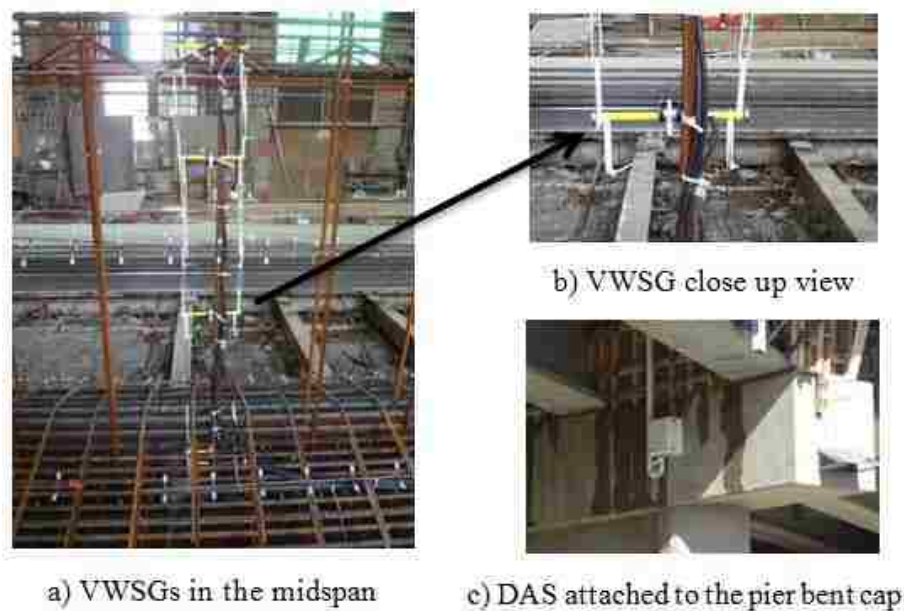


Figure 5. VWSGs installation

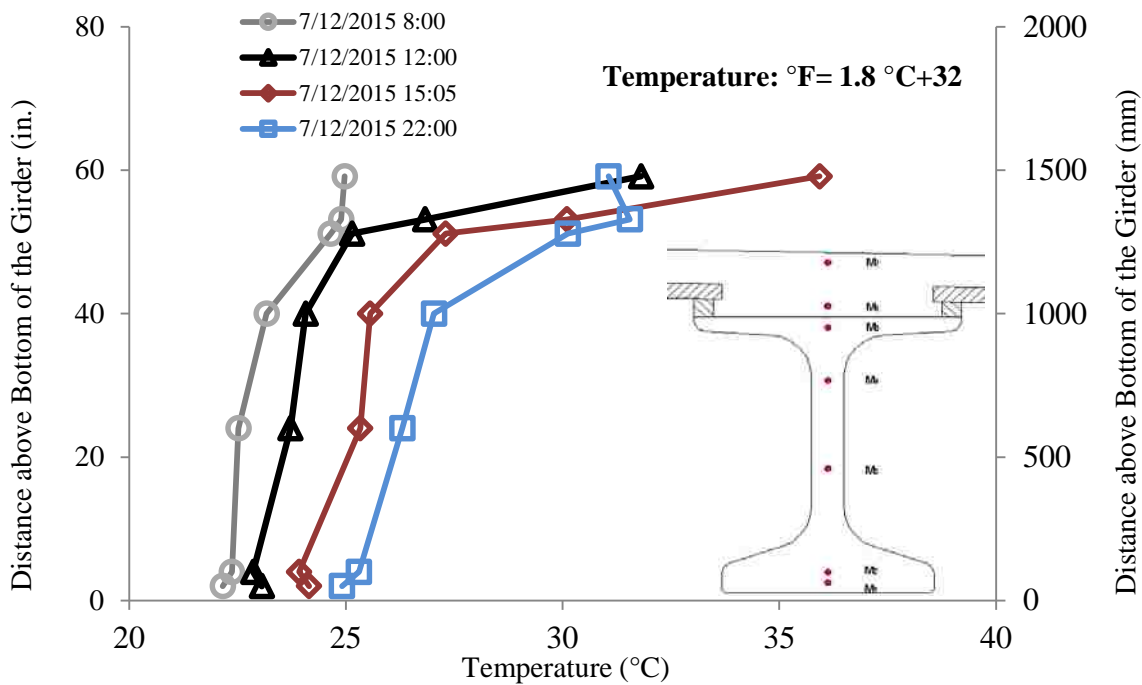


Figure 6. Typical heating behavior in interior girder (S2-G3) on a sunny summer day

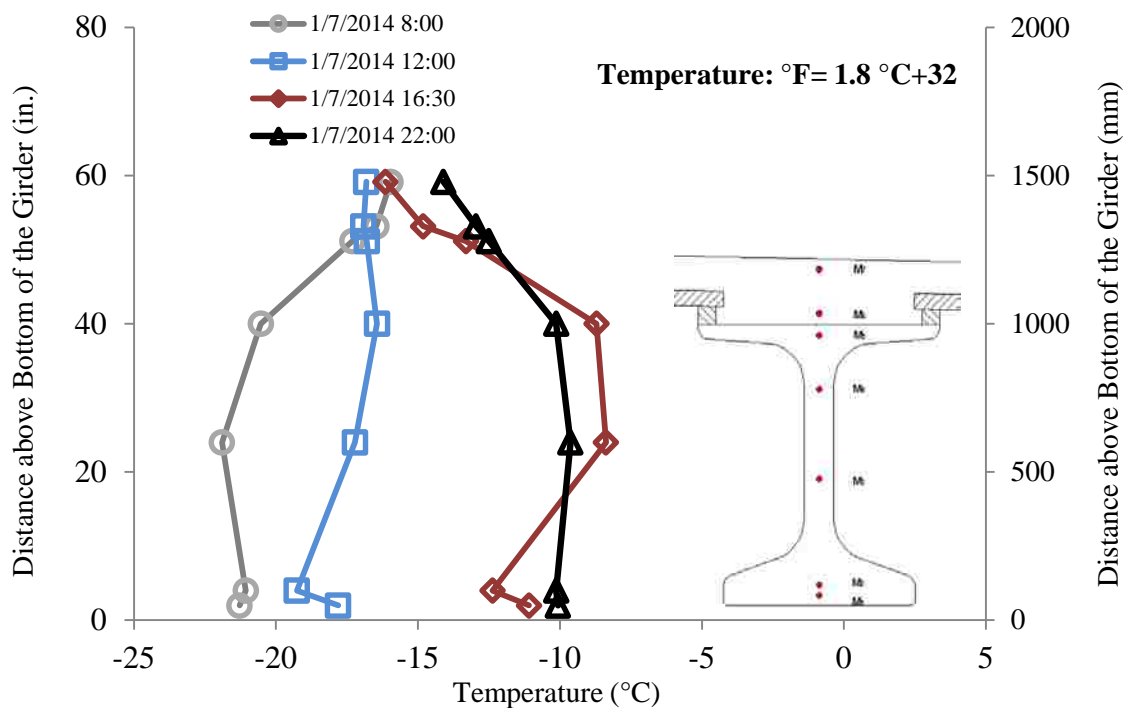


Figure 7. Typical cooling behavior in interior girder (S2-G3) on a cloudy winter day

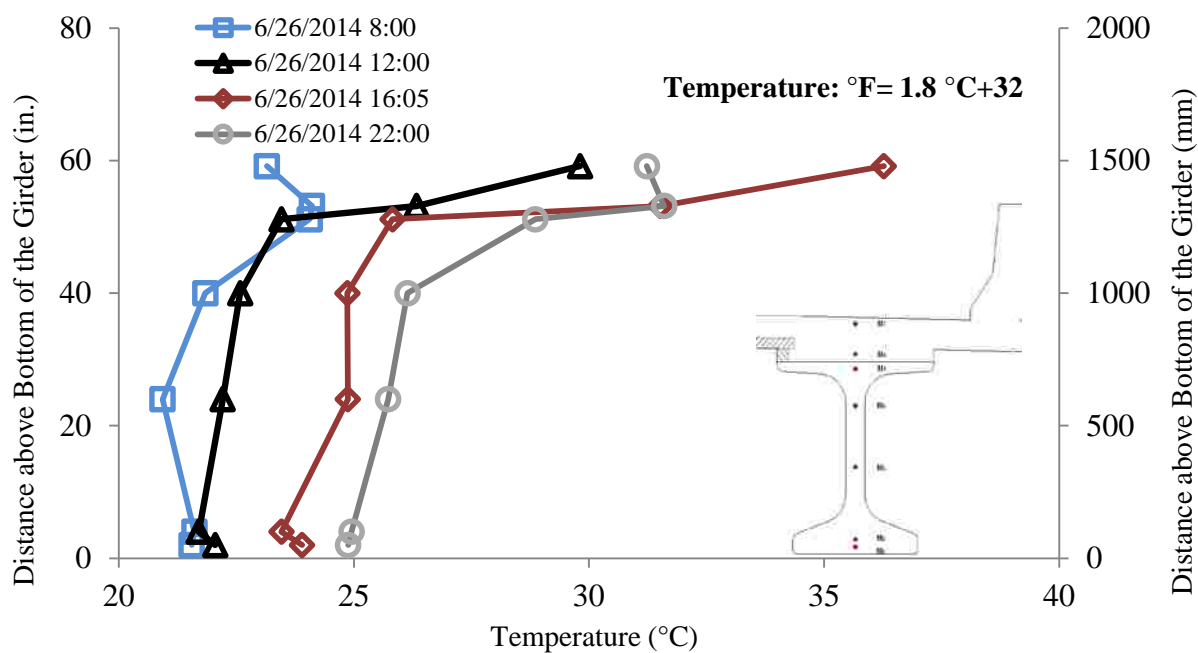


Figure 8. Typical heating behavior in exterior girder (S2-G4) on a sunny summer day

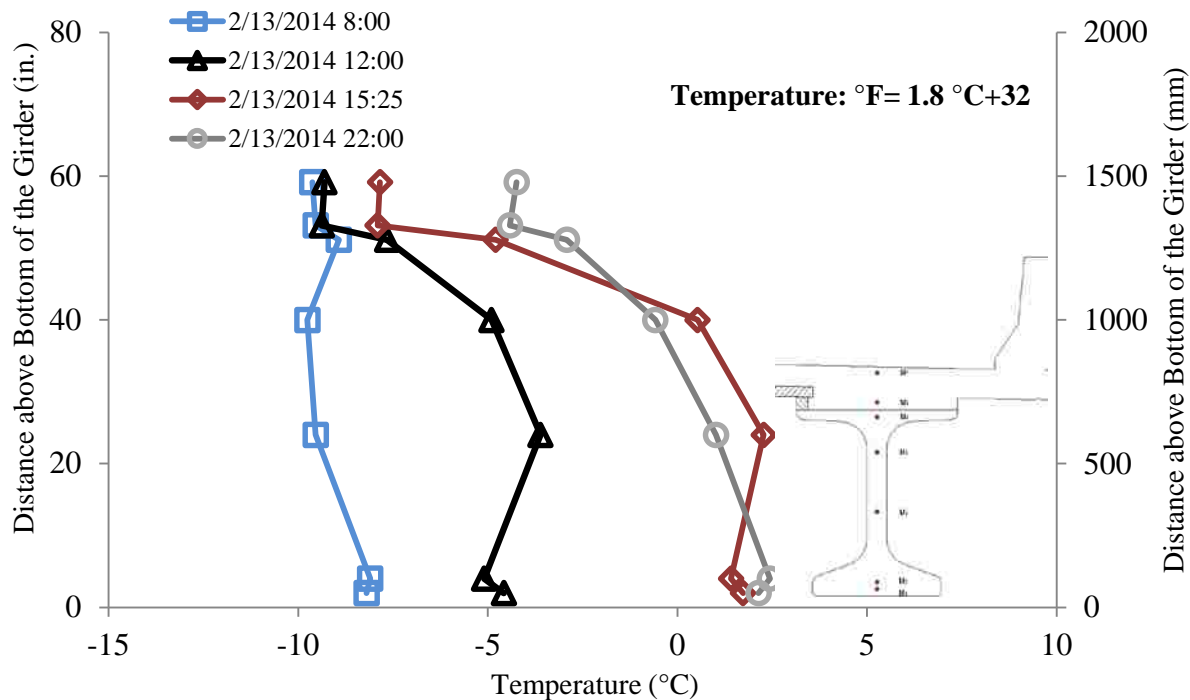


Figure 9. Typical cooling behavior in exterior girder (S2-G4) on a cloudy winter day

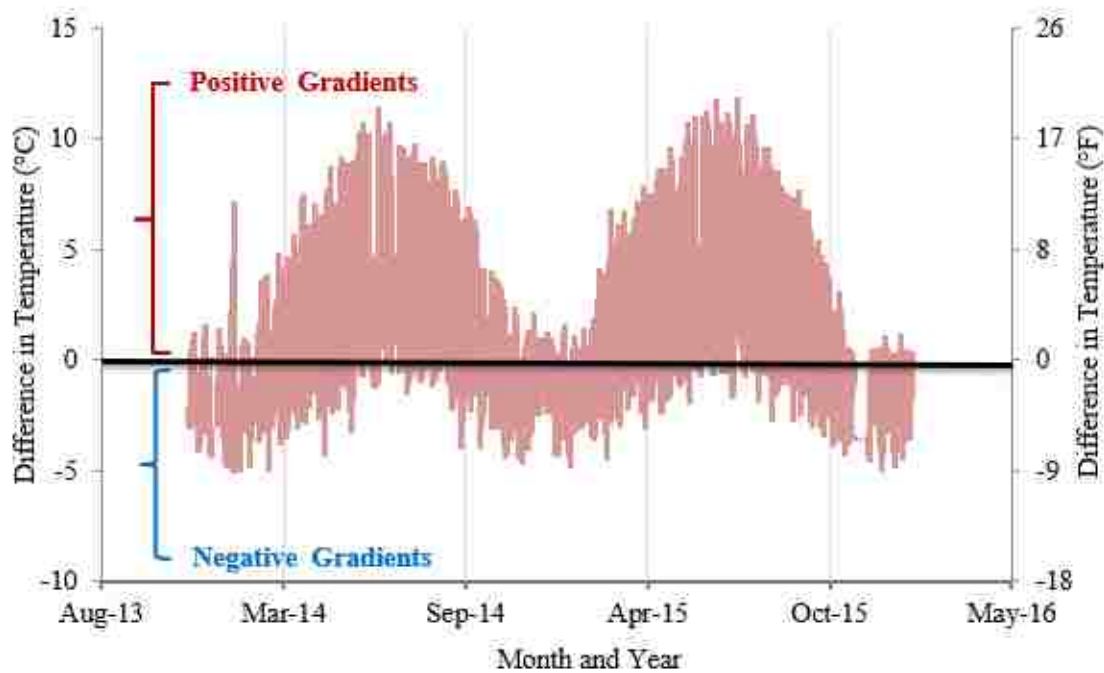


Figure 10. Positive and negative daily thermal gradients of interior girder (S2-G3)

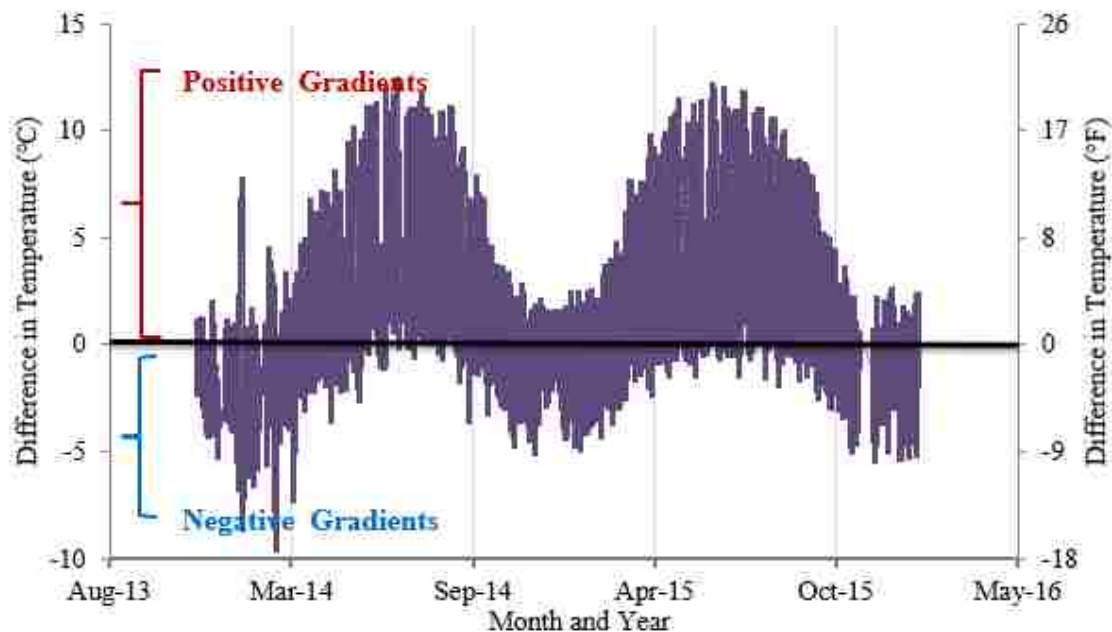


Figure 11. Positive and negative daily thermal gradients of exterior girder (S2-G4)

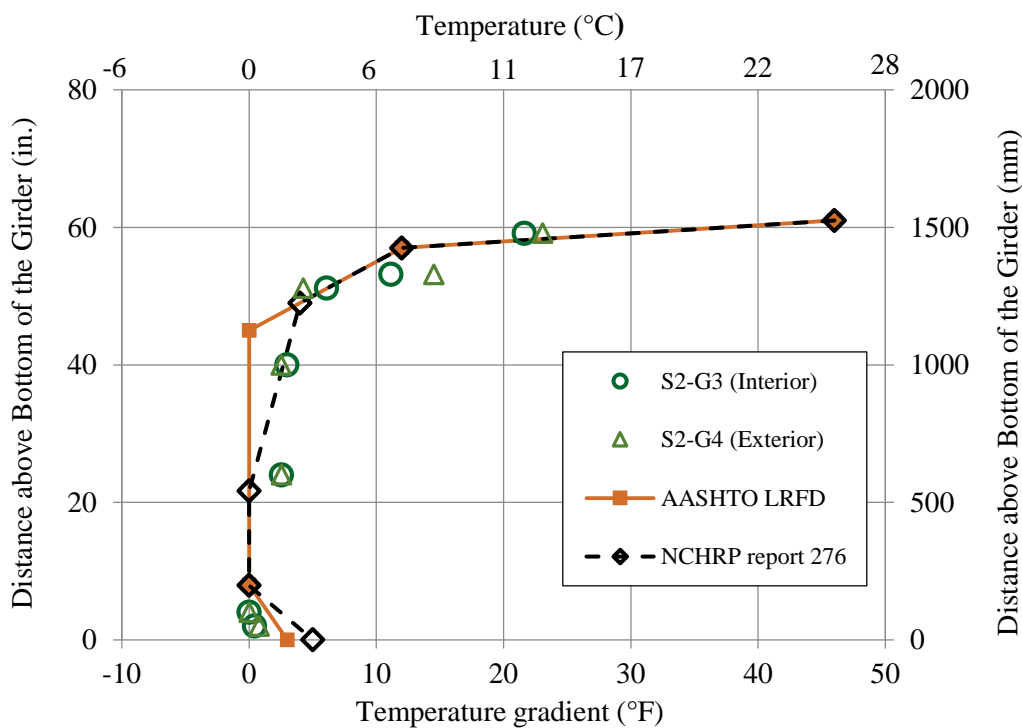


Figure 12. Design positive gradients and maximum measured positive gradients

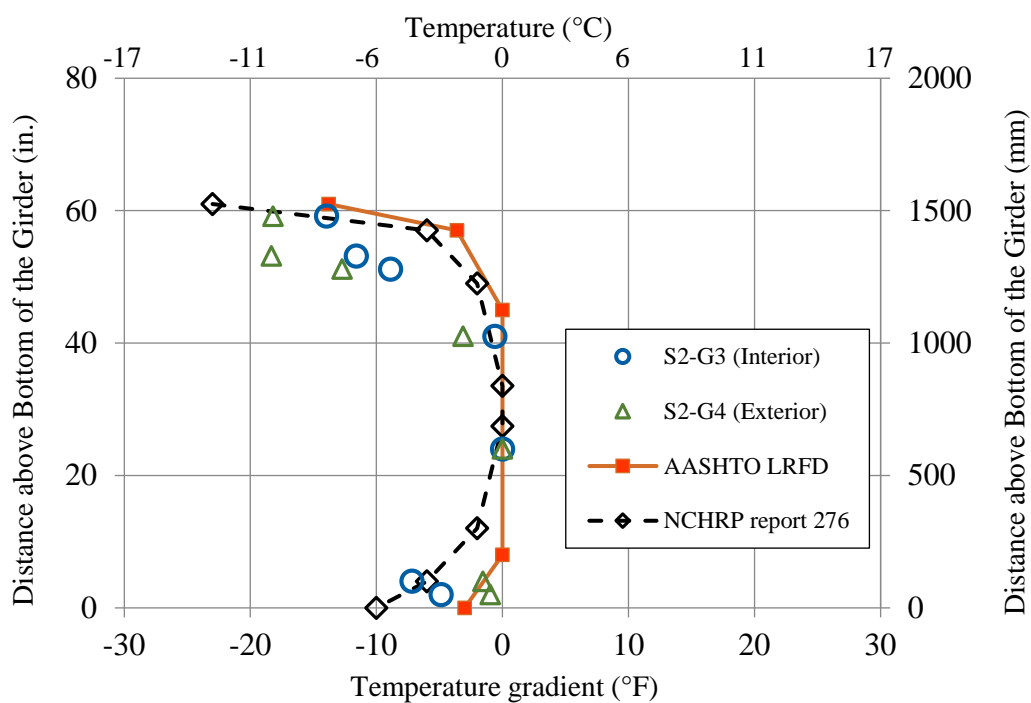


Figure 13. Design negative gradients and maximum measured negative gradients

## ACKNOWLEDGEMENT

The writers gratefully wish to acknowledge the financial support provided by the Missouri Department of Transportation (MoDOT), the National University Transportation Center (NUTC) at the Missouri University of Science and Technology (Missouri S&T), and the Center for Infrastructure Engineering. The authors also want to thank the Department of Civil, Architectural, and Environmental Engineering at Missouri S&T and HCED Iraq sponsor for their support.

**REFERENCES**

1. ACI Committee 237R, "Self-Consolidating Concrete," American Concrete Institute; Detroit, Michigan, 2007.
2. ACI Committee 363, "State of the Art Report on High Strength Concrete," American Concrete Institute, Farmington Hills, Michigan, 2010.
3. Alghazali H.H. and Myers J.J., "High Strength Self Consolidating Concrete Prestress Losses of Bridge A7957, MO, USA Compared to Code Models," *Proceedings of Fifteen ConMat'15 Conference*, Vancouver, BC Canada, 2015.
4. Priestly, M. J. N., "Design of Concrete Bridges for Temperature Gradients," *ACI Journal*, Vol. 75, No. 5, 1978, pp. 209-217.
5. Abid, S. R., Tayşi, N., and Özakça, M., "Experimental Analysis of Temperature Gradients in Concrete Box-Girders," *Construction and Building Materials*, V. 106, 2016, pp.523-532.
6. Barr, P. J., Stanton, J. F., and Eberhard, M. O., "Effects of Temperature Variations on Precast, Prestressed Concrete Bridge Girders," *Journal of Bridge Engineering*, V. 10(2), 2005, pp.186-194.
7. Myers, J.J. and Yang. Y., "High Performance Concrete for Bridge A6130-Route 412, Pemiscot County, MO," UTC R39, 2004.
8. Imbsen, R.A., Vandershof, D.E., Schamber, R.A., and Nutt, R.V., "Thermal Effects in Concrete Bridge Superstructures," *Transportation Research Record*, (NCHRP Report No. 276, Washington, DC.), 1985.
9. Larsson, O., and Thelandersson, S., "Estimating Extreme Values of Thermal Gradients in Concrete Structures," *Materials and Structures*, V. 44(8), 2011, pp. 1491-1500.
10. Gross, S.P., "Field Performance of Prestressed High Performance Concrete Highway Bridges in Texas," University of Texas at Austin, Ph.D. Dissertation, 1999.

11. Nawy, E. G., "Prestressed Concrete: A Fundamental Approach Fifth Edition," Upper Saddle River; New Jersey, 2009.
12. PCI Design Handbook. Precast/Prestressed Concrete Institute Seventh Edition, PCI. Chicago, Illinois, 2010.
13. NCDC, "Quality Controlled Local Climatological Data," National Climatic Data Center; website: <http://www1.ncdc.noaa.gov/pub/orders/cdo/687365.csv>.
14. Hedegaard, B. D., French, C. E., and Shield, C. K., "Investigation of Thermal Gradients Effects in the I-35W St. Anthony Falls Bridge," *Journal of Bridge Engineering*, 18(9), 2012, pp. 890-900.
15. Lee, J. H., "Investigation of Extreme Environmental Conditions and Design Thermal Gradients During Construction for Prestressed Concrete Bridge Girders," *Journal of Bridge Engineering*, V. 17(3), 2011, pp. 547-556.
16. Myers, J.J.; Bloch, K.E., "Innovative Concrete Bridging Systems for Pedestrian Bridges: Implementation and Monitoring," Missouri University of Science and Technology, National University Transportation Center (NUTC) Report R250, 2010.
17. AASHTO LRFD Bridge Design Specifications. American Association of State Highway and Transportation Officials; Washington, DC, 2012.



## SECTION

### 4. GENERAL CONCLUSIONS

This section summarizes the most important findings of this research program. In general, the detailed conclusions of this research were presented at the end of each paper. Only the major findings and contributions of the research program are presented here. These conclusions are broken down into the following major findings in each part.

#### 4.1. PART 1

1. Test results of high volume fly ash-self consolidating mortar show that both Type III cement and accelerated curing regime phases significantly improved the early age compressive strength of the mortar mixes with 50% cement replacement up to 65% for Type III and 75% for the accelerated curing regime.
2. The addition of Type S hydrated lime slightly improved the early-age compressive strength with replacement levels more than 50% and decreased the drying shrinkage mortar mixtures.
3. In general, increasing the cement replacement levels showed a considerable reduction in drying shrinkage. More than 40% reduction in drying shrinkage was observed for 50% and 75% cement replacement. However, a combined high amount of fly ash with accelerated curing did not show any improvement in the drying shrinkage.
4. Based on the test results of the mortar study, the fly ash replacement level can be increased to more than 50% while maintaining equivalent performance to the mixes with 100% ordinary Portland cement.

5. Based on the targeted fresh properties, all HVFA-SCC mixes exhibited excellent rheological properties in terms of flowability (slump flow  $\geq 27$  in.), passing ability [J-ring  $\geq 26$  in. (660 mm)], and the stability (column segregation  $\leq 2.1$ ).
6. The compressive strength of HVFA-SCC mixes with (50%, 60%, and 70% by weight) developed an early-age compressive strength greater than the target strength of 2500 psi (17.5 MPa) after three days of age.
7. All of the HVFA-SCC mixes with air entrainment exhibited excellent performance in the aspects of concrete freezing and thawing resistance. The durability factors of investigated mixes were 97% or greater.
8. In terms of crack patterns, the normalized ultimate shear strength in full-scale shear test results indicated that there was no major difference between the behavior of HVFA-SCC mixes studied and the CC beams. The only observed difference was the effect of the longitudinal reinforcement ratio. Increasing the longitudinal reinforcement ratio from 1.59 to 2.71 did not show any effect on the ultimate shear force. This may be due to the lower coarse aggregate content and size of HVFA-SCC mixes, which results in a weaker aggregate interlock mechanism.
9. Based on the shear database of experimental studies from literature for CC and SCC beams, the shear test results of HVFA-SCC beams follow the trend of the data and fell at or above the ACI 318-14 limits, suggesting that the limited HVFA-SCC data satisfies the ACI limits with a reduced spread of data and thereby factor of safety. The HVFA-SCC

test results fall below the non-linear regression curve fit of the CC database which suggests that as more HVFA-SCC data is collected, calibration factors may need to be developed to yield a similar factor of over strength compared to the other concrete types relative to the ACI limits.

10. The research results of bond studies of HVFA-SCC showed that all the splice beams failed in bond, experiencing either splitting or slippage failure.
11. In general, top splice beams exhibited a higher peak load compared to the beams cast with bottom splices. This gives an indication that HVFA-SCC mixes were very stable mixes.
12. In general, the bond test results of the HVFA-SCC beams with confinement in splice zone did not show any improvement in terms of the peak load. The presence of transverse reinforcement in the splice zone only changed the mode of failure and crack patterns.
13. Based on the splice beam experimental results from different concrete types (CC, SCC, and HVFAC), the bond test results of HVFA-SCC beams follow the same trend observed in the previous test results which gives a good indication that HVFA-SCC mixes are consistent with CC, SCC, and HVFAC mixes.

#### 4.2. PART 2

14. The health monitoring system was successfully installed on Bridge A7957 to collect the behavioral data (strain and temperature) of the in-service condition of the bridge on a real-time basis.
15. The VWSGs (Type ME-5) and the built-in data acquisition system worked perfectly for more than two years of continuous monitoring. The collected data of the long-term monitoring was consistent and realistic and gave a good indication of the reliability and durability of the types of instrumentation used in this study.
16. The total measured prestress losses averaged 39, 49, and 43 ksi (267, 337, 298 MPa) or 19%, 25%, and 22% of the nominal jacking stress for the HSC, HS-SCC, and NS-SCC girders, respectively. In general, the elastic shortening losses represent 44% of total prestress losses.
17. The AASHTO LRFD specification and the PCI Design Handbook underestimated the total prestress losses of HS-SCC girders by 24% and 30%, respectively.
18. Based on the collected data of total prestress losses from literature, the measured losses ranged from 10% to 35% of the nominal jacking stress. This range indicates that the prestress losses constructed with HSC and SCC fall within the range of the compiled data.
19. The maximum and minimum uniform bridge temperatures of HS-SCC bridge girders were 92 °F (33 °C) and -2 °F (-19 °C), respectively. The maximum average bridge temperature was found to be higher than the

maximum average ambient temperature by up to 6 °F (4 °C). However, the minimum average bridge temperature was observed to be up 14 °F (8 °F) lower than the minimum average ambient temperature.

20. The methods for effective bridge temperature proposed in the NCHRP report 276 and AASHTO LRFD specification did not accurately reflect the extreme temperature measured in this study.
21. The maximum measured positive gradients in the HS-SCC bridge girders ranged from 21 to 26 °F (12 to 14 °C) and the maximum measured negative gradients in the monitored girders ranged from -9 to -17 °F (-5 to -10 °C). These measured values were based on top deck gauges located 2 in (50 mm) below the deck surface.
22. The design positive and negative thermal gradients specified by NCHRP report 276 and the AASHTO LRFD specifications underestimated the temperatures measured at certain depths within the HS-SCC bridge girders.

## APPENDIX A.

### HARDENED PROPERTIES OF HVFA-SCC MIXES

## HARDENED PROPERTIES OF HVFA-SCC MIXES

This section presents the test results of freezing and thawing resistance, concrete surface resistivity, carbonation, and drying shrinkage of HVFA-SCC mixes. In this section, an SCC mix with 100% ordinary Portland cement was developed and tested in association with HVFA-SCC mixes for comparison purposes.

### Freeze and Thaw Resistance Test

This test was conducted according to a modified version of the ASTM C666-15 “Standard Test Method for Resistance of Concrete to Rapid Freezing and Thawing.” Procedure B was selected to determine the concrete resistance to rapidly repeated cycles of freezing and thawing in the laboratory. The specimens were 3 in. (75 mm) in width, 3 in. (75 mm) in height, and 16 in. (406 mm) in length in accordance to the standard requirements for specimen dimensions. Table A.1 presents the freezing and thawing test results in terms of durability factor and mass loss. Each data point represents the average of two replicated specimens. Each specimen was exposed to 300 cycles of freezing and thawing while submerged in water. After every 30 or 34 cycles, the transverse frequency and mass loss were measured.

Table A.1 - Freeze and Thaw Resistance Test Results

Mix ID*	Replacement Level (%)	Durability Factor	Mass Loss (%)
Mix-1	0	98	0.006
Mix-2	50	98	0.077
Mix-3	60	97	0.026
Mix-4	70	98	0.109

Note: All mixes with air entrainment admixture.

Based on the test results of the durability factor, all mixes passed the ASTM requirement of having a durability factor equal to or greater than 60, and the mixes, passed the Missouri department of transportation's durability factor of  $\geq 75$ . These results show the excellent durability performance of air entrainment HVFA-SCC mixes compared to the SCC mix with 100% ordinary Portland cement.

### Concrete Resistivity Test

The surface electric resistivity was selected to provide a rapid indication of the concrete's resistance to the penetration of chloride ions. The electric resistivity meter (shown in Figure A.1) was used as a tool to measure the surface resistivity of concrete specimens. For each mix, two saturated 4 in. x 8 in. (100 mm x 200 mm) cylinders were tested. Each surface resistivity measurement represents the average of 18 readings (9 readings on each cylinder). The test was conducted according to the AASHTO TP 95 "Method of Test for Surface Resistivity Indication of Concrete's Ability to Resist Chloride Ion Penetration." The surface resistivity test correlated well with the rapid chloride permeability (RCP) test. Table A.2 illustrates the numerical correlation between these two tests.



Figure A. 1- Surface Resistivity Meter



Table A.2 - The Correlation Between Surface Resistivity and RCP (Florida DOT 2004)

Chloride Ion Permeability	RCP Test, Charged Passed (Coulombs)	Surface Resistivity, 4 x 8 in. cylinder (k $\Omega$ . Cm)
High	> 4,000	< 12
Moderate	2,000 – 4,000	12 – 21
Low	1,000 – 2,000	21 – 37
Very Low	100 – 1,000	37 – 254
Negligible	< 100	> 254

The surface resistivity of the investigated mixes is presented in Figure A.2.

According to the suggested correlation, the mixes with 0% and 70% cement replacement exhibited very low ion permeability. Mixes made with 50% and 60% cement replacement can be considered as having negligible chloride ion permeability.

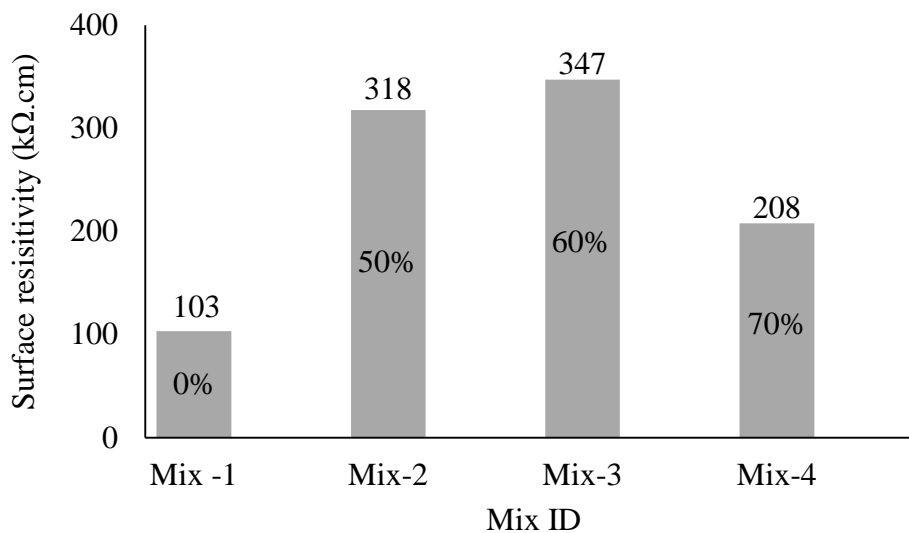


Figure A.2 - Surface Resistivity Test Results of Investigated Mixes

## **Accelerated Carbonation Test**

Carbonation is one source that can cause corrosion of reinforcement in concrete structures. The carbon dioxide in the atmosphere or water reacts with hydrated cement components in the concrete and leads to a reduction in the concrete alkalinity (reducing pH of pore solution), which causes deterioration of the reinforcement passivation layer. There are several factors that influence the carbonation rate, including temperature, ambient relative humidity, the concentration of carbon dioxide, concrete cover, water to cement ratio, and compressive strength and permeability of concrete. Carbonation was examined in this study following the RILEM CPC 18 recommendation “Measurement of Hardened Carbonation Depth.” At the age of 90 days, two 4 x 8 in. (100 x 200 mm) cylinder specimens from each mix were sliced for 2, 4, and 2 in. (50, 100, 50 mm) thickly sliced specimens using the concrete cutting machine. For the carbonation test, the 4 in. (100 mm) thick sliced specimens were coated with an epoxy resin to ensure that carbon dioxide could diffuse only into the specimens top and bottom faces (Sadati et al. 2015). Then, all the specimens were stored in a sealed carbonation chamber for 8 weeks. The conditions inside the chamber were 60% relative humidity,  $73 \pm 2$  °F ( $23 \pm 2$  °C), and 3% carbonation dioxide concentration. The carbonation depth measurements were conducted on a fresh specimen section that was recently obtained by fracturing the specimen perpendicularly to its axis by spraying a phenolphthalein pH indicator on the surface. The concrete surface color was examined. If the sprayed surface turns to pink, it means that the concrete pH is above 10 and the carbonation did not occur in that portion of the specimen. However, if the sprayed surface turns colorless on the edges, it indicates that the concrete pH value is below 8 (RILEM CPC 18, 1988). A digital caliper was used to

measure the thickness of the portion with no color change. An average of eight readings was reported as the carbonation depth of specimens. The accelerated carbonation test sequence is summarized in Figure A.3.



a) Slicing the cylinders



b) Specimens inside the chamber



c) Specimens after Spraying the phenolphthalein pH indicator

Figure A.3 - Carbonation Test Sequence

The measured carbonation depth of the investigated mixes is presented in Table A.3. Based on the obtained test results, the HVFA-SCC mixes exhibited a higher carbonation depth than the SCC mix with 100% cement.

Table A.3 - Measured Carbonation Depth Results

Mix ID	Replacement Level (%)	Carbonation Depth (in.)
Mix-1	0	0
Mix-2	50	0.34
Mix-3	60	0.36
Mix-4	70	0.34

### Drying Shrinkage Test

Drying shrinkage in this study was monitored using a 3 x 3 x 11.25 in. (75 x 75 x 285 mm) prism prepared according to the ASTM C157-08 “Standard Test Method for Length Change of Hardened Hydraulic-Cement Mortar and Concrete.” After casting, the specimens were covered with wet burlap for up to 24 hours. Then the specimens were demolded and stored in a moist room (relative humidity of 95% or greater and 73+2 °F (23+2 °C) temperature) for 6 days. A digital extensometer was used to measure the change in length after 7, 8, 9, 10, 14, 28, 56, 90, and 256 days. The drying shrinkage of the investigated mixes is illustrated in Figure A.4. Based on the obtained results, the HVFA-SCC mix with 70% cement replacement with fly ash and hydrated lime exhibited

a considerable reduction in drying shrinkage value. More than 40% reduction of the drying shrinkage was observed for the 70% mix compared to mix with the 100% Portland cement. This could be attributed to the high dosage of hydrated lime used with Mix-4 (British Lime Association, 2015).

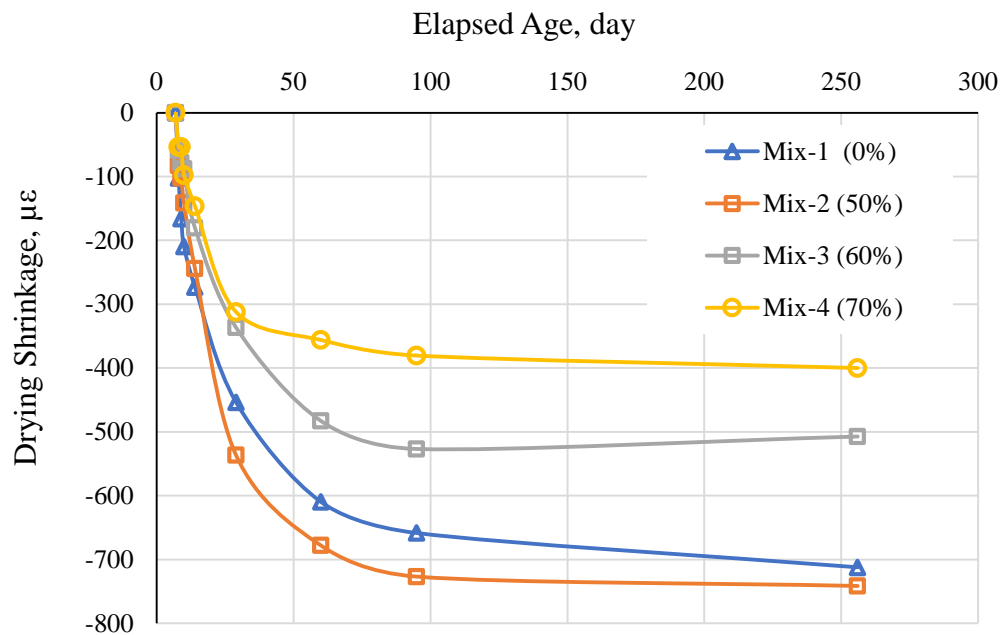


Figure A.4 - Drying Shrinkage Test Results

### Fracture Energy

Three-point bend tests were utilized on the notched beams to determine fracture energy in this study. In this method, recommended by technical committee RILEM 50-FMC, the fracture energy is defined as the work needed to create one-unit area of a crack. As the beam is broken in two halves, the fracture energy can be computed by dividing the total dissipated energy by the ligament area as shown in Eq. 1. It is worth noting that this method in fracture mechanic texts is also known as the work-of-fracture method (WFM) or Hillerborg's method.

$$G_F = \frac{W_f}{b(d-a_0)} \quad (1)$$

where the term  $W_f$  is the total energy dissipated in the test, and  $b$ ,  $d$ , and  $a_0$  are the width, height, and the initial notch depth of the beam cross section, respectively.

Moreover, the brittleness of a material in the work of fracture method can be described as the characteristic length, which is related to the fracture process zone length that was introduced by Hillerborg et al. (1976) as:

$$l_{ch} = \frac{E_c G_f}{f_t^2} \quad (2)$$

where  $E_c$  and  $f_t$  are the modulus of elasticity and the tensile strength, respectively.

The lower the value of  $l_{ch}$ , the more brittle the material.

In this study, the beam specimens measured 6 in. x 6 in. x 24 in. (150 mm x 150 mm x 600 mm) with a span equal to 18 in. (450 mm). A notch-to-depth ratio of 0.25 was introduced in the center of each beam with a Teflon plate cast into the concrete as opposed to being saw cut after the concrete hardened. The tests were displacement-controlled, and thus, a closed-loop servo electro-controlled MTS machine was used at a loading rate of 0.005 in/min (0.12 mm/min). Figure A-5 displays set up of the fracture energy specimens.

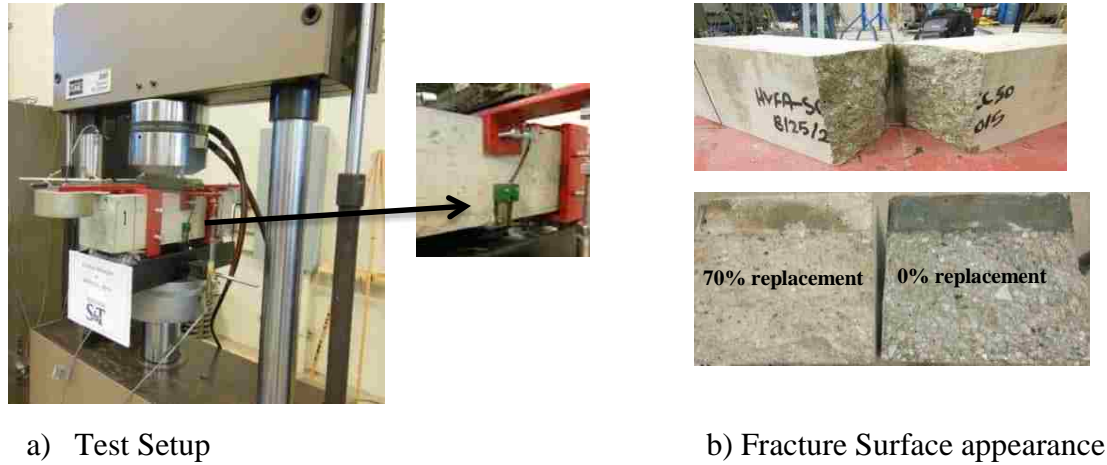


Figure A-5. Fracture Energy Test

Fracture energy is the energy required to create a crack with in a unit area. The total energy is determined by measuring the area under a load-displacement curve according to Eq. 1. The results of the fracture energy tests for HVFA-SCC are presented in Table 4 along with the compressive strength, tensile strength, and modulus of elasticity at the time of testing.

Table Value of Fracture Energy Measured from Beam Tested in All Mixes

Mix ID	$f'_c$ ksi	$f_t$ psi	E ksi	Average Peak load kips	$G_F$ (lb/in.)				Average $G_F$ (lb/in)	COV (%)	$l_{ch}$ in.
					Beam 1	Beam 2	Beam 3	Beam 4			
Control-SCC	8.3	624	4699	3.03	1.26	1.44	1.27	1.30	1.32	6.5	15.9
HVFA-SCC 50	7.8	545	5352	2.70	1.13	1.14	1.23	0.95	1.11	10.5	20.0
HVFA-SCC 60	6.7	431	5178	2.47	0.75	0.81	1.09	1.09	0.94	19.2	26.1
HVFA-SCC 70	7.7	529	5671	2.83	0.95	1.47	1.09	1.31	1.20	19.1	24.3



## REFERENCES

- ASTM C666/C666M, (2015). "Standard Test Method for Resistance of Concrete to Rapid Freezing and Thawing.", West Conshohocken, PA.
- MoDOT Section 1005, (2017) "Concrete," Missouri Department of Transportation Specifications and Engineering Policy Guide.
- AASHTO (2011). "Standard Method of Test for Surface Resistivity Indication of Concrete's Ability to Resist Chloride Ion Penetration." TP 95, Washington, DC.
- Florida Department of Transportation (2004). "Florida Method of Test for Concrete Resistivity as an Electrical Indicator of its Permeability," FM 5-578.
- RILEM Committee CPC-18. (1988). "Measurement of hardened concrete carbonation depth." TC14-CPC.
- Sadati, S., Arezoumandi, M., and Shekarchi, M. (2015). "Long-term performance of concrete surface coatings in soil exposure of marine environments." *Construction and Building Materials*, V. 94, pp. 656-663.
- ASTM C157/C157M, (2008). "Standard Test Method for Length Change of Hardened Hydraulic-Cement Mortar and Concrete." West Conshohocken, PA.
- British Lime Association, (2015). "High performance mortars for a sustainable future," <[www.britishlime.org](http://www.britishlime.org)>.
- RILEM FMC-50 (1985). "Determination of the fracture energy of mortar and concrete by means of three-point bend tests on notched beams." *Material Struct* 1985; 18(4):287–90.
- Hillerborg A., Modeer M., Petersson P.E. (1976). "Analysis of crack formation and crack growth in concrete by means of fracture mechanics and finite elements". *Cement Concrete Research* 1976;6: 773–82.

## APPENDIX B.

### ADDITIONAL DETAILS OF SHEAR BEHAVIOR STUDY

The material in Appendix B is additional details to demonstrate the first diagonal cracking and ultimate shear results presented in Paper II. In addition, the measured angle of the critical shear crack is presented in this appendix.

## 50-5N

Stage	Shear Force, kips
Cracking Shear (Diagonal Crack)	28
Ultimate Shear $V_c$ (Failure)	33.53
Angle of Critical Crack, ( $\phi$ ), deg.	21
Failure Side	East



Figure B-1. Cracking Shear in Specimen 50-5N



Figure B-2. Ultimate Shear in Specimen 50-5N

## 50-6N

Stage	Shear Force, kips
Cracking Shear (Diagonal Crack)	32
Ultimate Shear $V_c$ (Failure)	32.32
Angle of Critical Crack, ( $\phi$ ), deg.	24
Failure Side	West

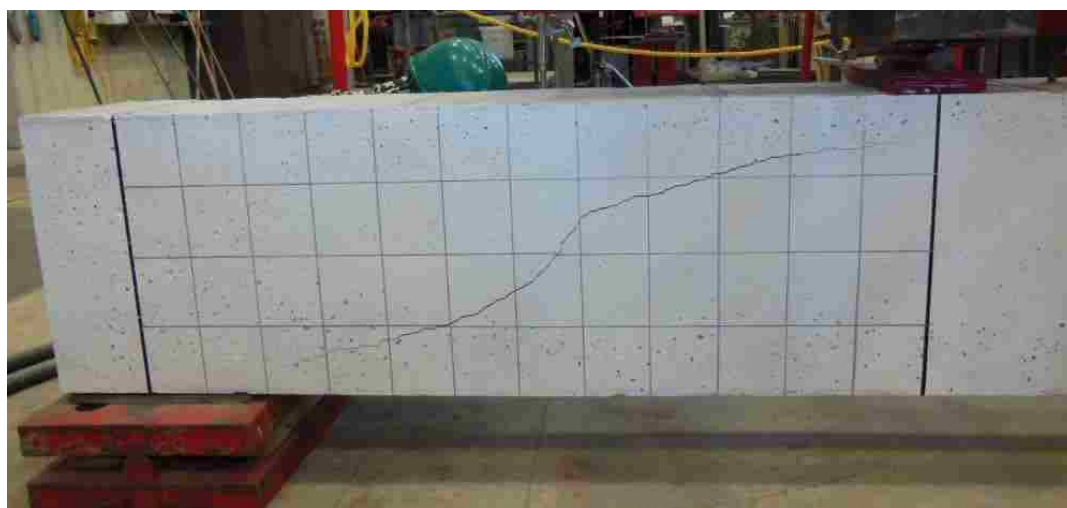


Figure B-3. Cracking Shear in Specimen 50-6N



Figure B-4. Ultimate Shear in Specimen 50-6N

**50-8N**

Stage	Shear Force, kips
Cracking Shear (Diagonal Crack)	31.5
Ultimate Shear $V_c$ (Failure)	32.38
Angle of Critical Crack, ( $\phi$ ), deg.	23
Failure Side	East



Figure B-5. Cracking Shear in Specimen 50-8N

50-8S

Stage	Shear Force, kips
Cracking Shear (Diagonal Crack)	34
Ultimate Shear $V_c$ (Failure)	74.29
Angle of Critical Crack, ( $\phi$ ), deg.	27
Failure Side	East

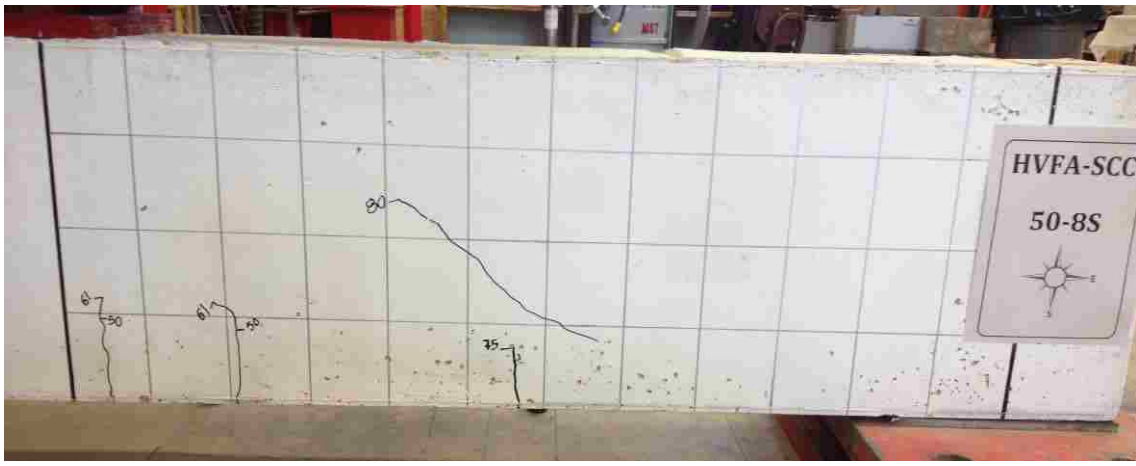


Figure B-6. Cracking Shear in Specimen 50-8S

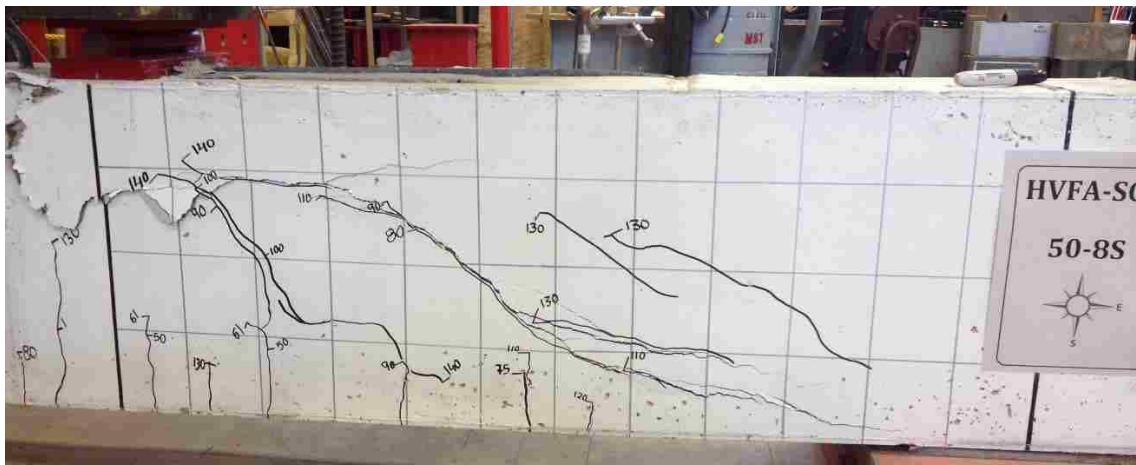


Figure B-7. Ultimate Shear in Specimen 50-8S

## 60-5N

Stage	Shear Force, kips
Cracking Shear (Diagonal Crack)	26.5
Ultimate Shear $V_c$ (Failure)	32.03
Angle of Critical Crack, ( $\phi$ ), deg.	22
Failure Side	West



Figure B-8. Cracking Shear in Specimen 60-5N

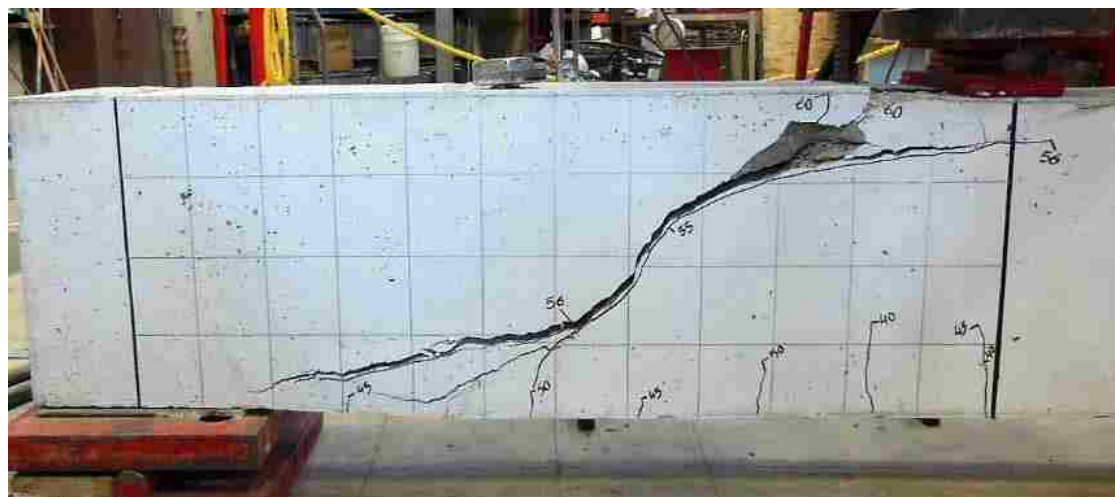


Figure B-9. Ultimate Shear in Specimen 60-5N



## 60-6N

Stage	Shear Force, kips
Cracking Shear (Diagonal Crack)	29
Ultimate Shear $V_c$ (Failure)	39.49
Angle of Critical Crack, ( $\phi$ ), deg.	26
Failure Side	West

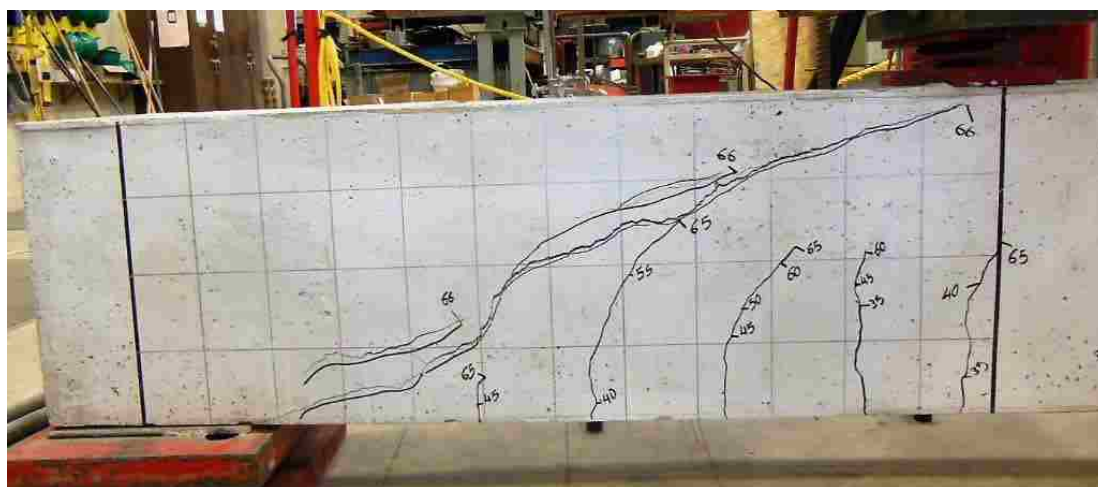


Figure B-10. Cracking Shear in Specimen 60-6N

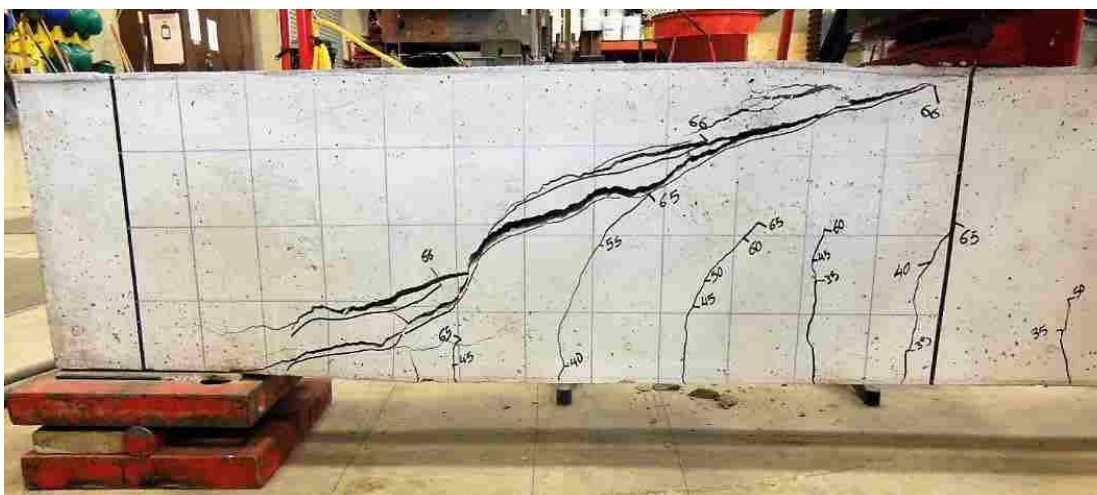


Figure B-11. Ultimate Shear in Specimen 60-6N

## 60-8N

Stage	Shear Force, kips
Cracking Shear (Diagonal Crack)	33
Ultimate Shear $V_c$ (Failure)	33.85
Angle of Critical Crack, ( $\phi$ ), deg.	23
Failure Side	East

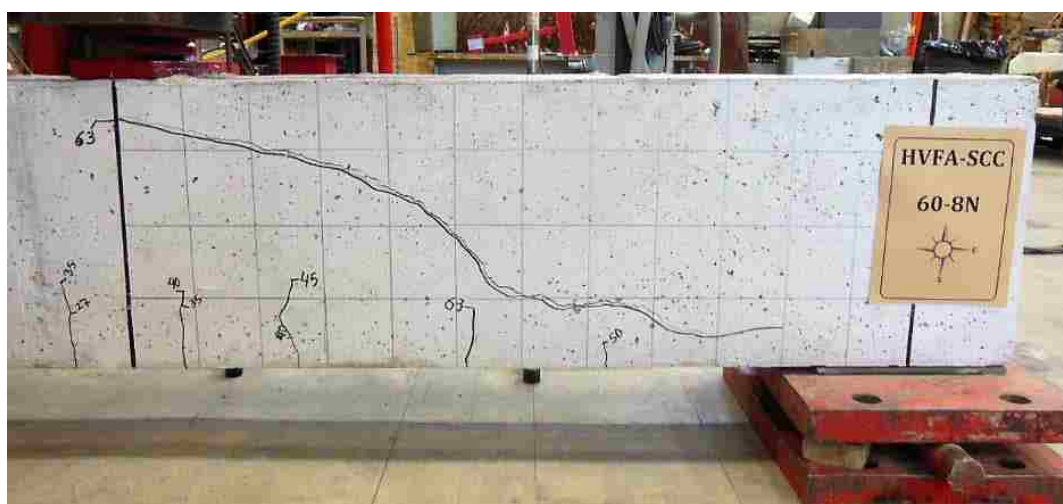


Figure B-12. Cracking Shear in Specimen 60-8N

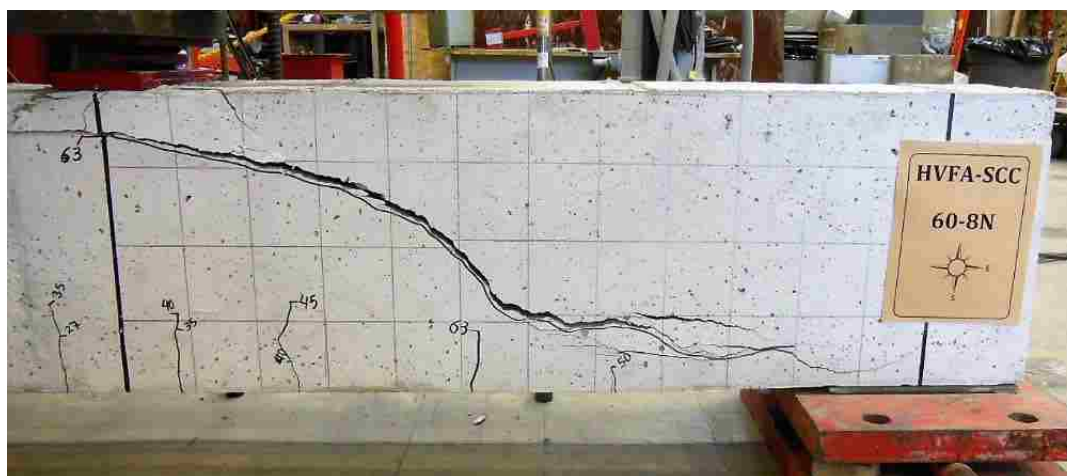


Figure B-13. Ultimate Shear in Specimen 60-8N

## 60-8S

Stage	Shear Force, kips
Cracking Shear (Diagonal Crack)	36.5
Ultimate Shear $V_c$ (Failure)	73.59
Angle of Critical Crack, ( $\phi$ ), deg.	28
Failure Side	West

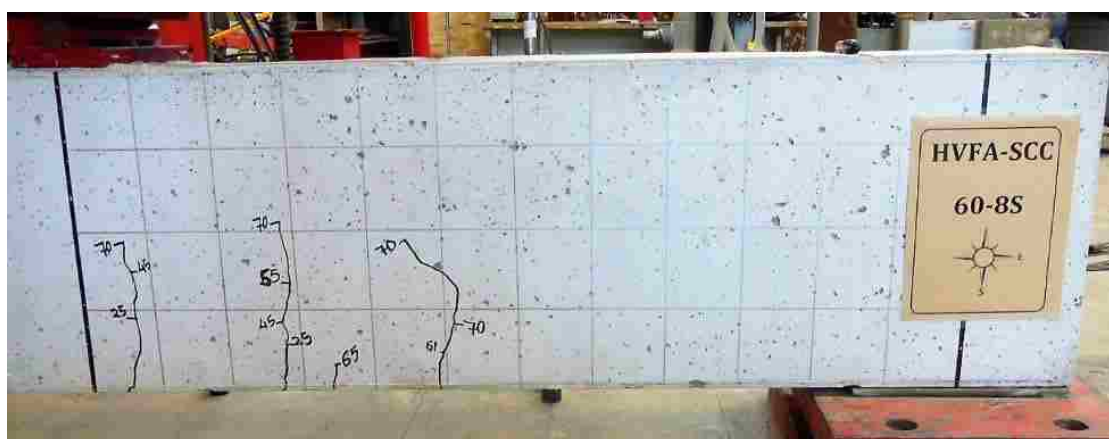


Figure B-14. Cracking Shear in Specimen 60-8S

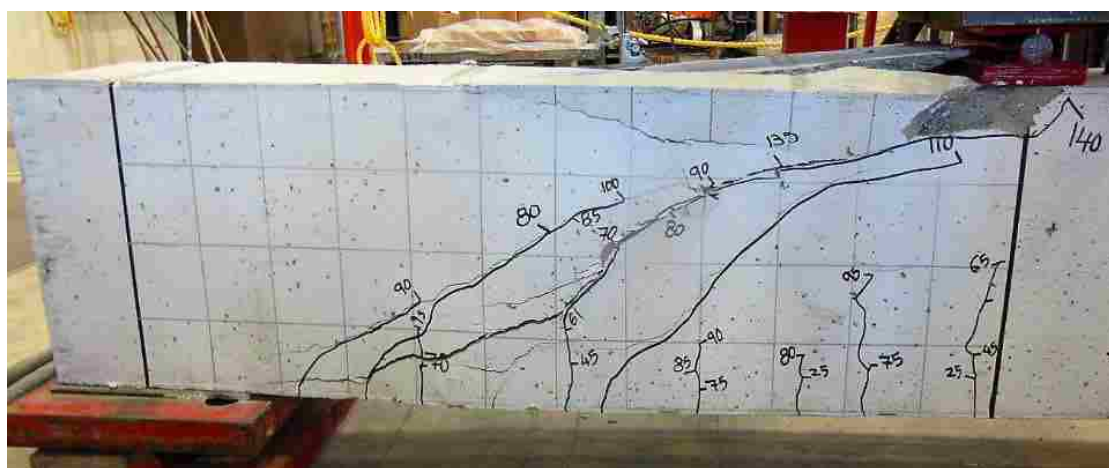


Figure B-15. Ultimate Shear in Specimen 60-8S

## 70-5N

Stage	Shear Force, kips
Cracking Shear (Diagonal Crack)	29
Ultimate Shear $V_c$ (Failure)	32.96
Angle of Critical Crack, ( $\phi$ ), deg.	24
Failure Side	West

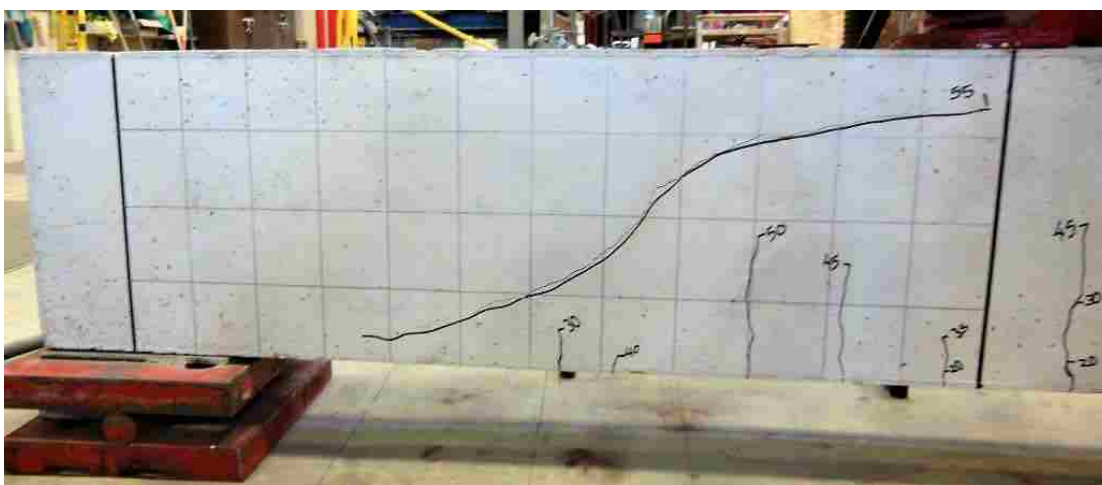


Figure B-16. Cracking Shear in Specimen 70-5N

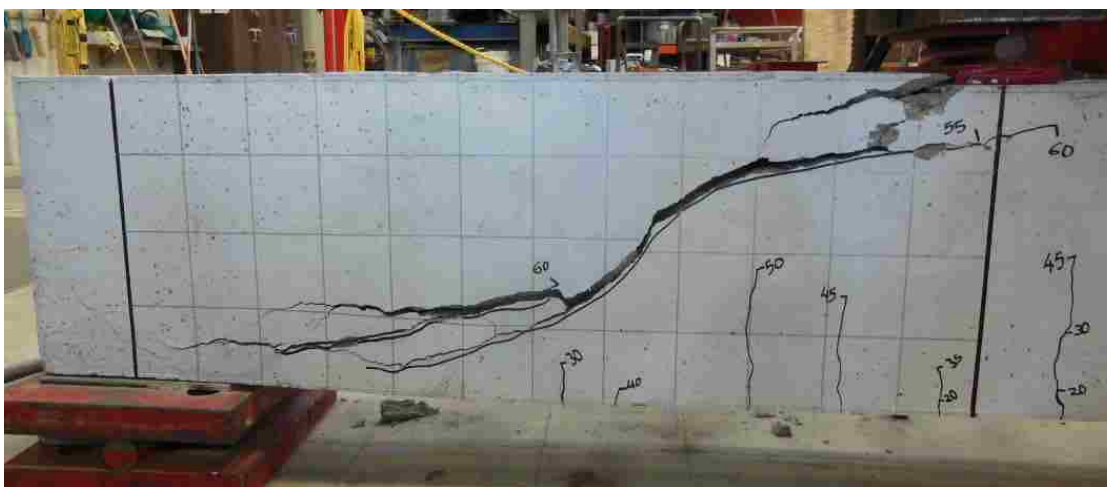


Figure B-17. Ultimate Shear in Specimen 70-5N

## 70-6N

Stage	Shear Force, kips
Cracking Shear (Diagonal Crack)	31.5
Ultimate Shear $V_c$ (Failure)	36.46
Angle of Critical Crack, ( $\phi$ ), deg.	24
Failure Side	East



Figure B-18. Cracking Shear in Specimen 70-6N



Figure B-19. Ultimate Shear in Specimen 70-6N

## 70-8N

Stage	Shear Force, kips
Cracking Shear (Diagonal Crack)	32
Ultimate Shear $V_c$ (Failure)	34.79
Angle of Critical Crack, ( $\phi$ ), deg.	25
Failure Side	East



Figure B-20. Cracking Shear in Specimen 70-8N



Figure B-21. Ultimate Shear in Specimen 70-8N

## 70-8S

Stage	Shear Force, kips
Cracking Shear (Diagonal Crack)	36.5
Ultimate Shear $V_c$ (Failure)	79.61
Angle of Critical Crack, ( $\phi$ ), deg.	28
Failure Side	East



Figure B-22. Cracking Shear in Specimen 70-8S



Figure B-23. Ultimate Shear in Specimen 70-8S

APPENDIX C.

SHEAR DATABASE



The material in Appendix C presents in detail the collected database of experimental shear test results in the literature. Part of this data was used to conduct a database comparison with shear test results of HVFA-SCC beams (Paper II).

The following abbreviations are presented in the Tables for the specimens in the shear test database:

**NG** = Natural Gravel

**CD** = Crushed Dolomite

**CL** = Crushed Limestone

**NS** = Natural Stone

**NCS** = Natural Crushed Stone

**NA** = Natural Aggregate

**CAG** = Crushed Angular Granite

**RL** = Replacement Level

Table C-1. Shear Test Database of Self Consolidating Concrete Beams without Transverse Reinforcement

No.	Author (Year)	Specimen ID	V <sub>test</sub> (kN)	a/d	b <sub>w</sub> (mm)	h (mm)	d (mm)	Agg. Size (mm)	Agg. Type	Slump flow (mm)	Paste Volume (%)	f'c (MPa)	ρ (%)	f <sub>y</sub> (MPa)	V <sub>test</sub> /√f'c bd
1	Safan M.A. (2012)	D1/10	23.7	2.6	100	150	135	19	CD	700.0	31.80	75	1.16	555	0.20
2	Safan M.A. (2012)	D1/12	25.3	2.6	100	150	135	19	CD	700.0	31.80	75	1.68	430	0.22
3	Safan M.A. (2012)	G1/10	18	2.6	100	150	135	19	NG	720.0	31.80	56	1.16	555	0.18
4	Safan M.A. (2012)	G1/12	20.8	2.6	100	150	135	19	NG	720.0	31.80	56	1.68	430	0.21
5	Safan M.A. (2012)	D2/10	19.8	2.6	100	150	135	19	CD	650.0	32.60	64	1.16	555	0.18
6	Safan M.A. (2012)	D2/12	21.8	2.6	100	150	135	19	CD	650.0	32.60	64	1.68	430	0.20
7	Safan M.A. (2012)	G2/10	16.3	2.6	100	150	135	19	NG	670.0	32.60	47	1.16	555	0.18
8	Safan M.A. (2012)	G2/12	17.5	2.6	100	150	135	19	NG	670.0	32.60	47	1.68	430	0.19
9	Safan M.A. (2012)	D3/10	19.3	2.6	100	150	135	19	CD	610.0	33.30	53	1.16	555	0.20
10	Safan M.A. (2012)	D3/12	23.7	2.6	100	150	135	19	CD	610.0	33.30	53	1.68	430	0.24
11	Safan M.A. (2012)	G3/10	21.2	2.6	100	150	135	19	NG	640.0	33.30	37	1.16	555	0.26
12	Safan M.A. (2012)	G3/12	22.5	2.6	100	150	135	19	NG	640.0	33.30	37	1.68	430	0.27
13	Safan M.A. (2012)	D4/10	19	2.6	100	150	135	19	CD	660.0	33.98	55	1.16	555	0.19
14	Safan M.A. (2012)	D4/12	22.4	2.6	100	150	135	19	CD	660.0	33.98	55	1.68	430	0.22
15	Safan M.A. (2012)	G4/10	18.3	2.6	100	150	135	19	NG	655.0	33.98	37	1.16	555	0.22

Table C-1. Shear Test Database of Self Consolidating Concrete Beams without Transverse Reinforcement (Cont.)

No.	Author (Year)	Specimen ID	$V_{test}$ (kN)	a/d	$b_w$ (mm)	h (mm)	d (mm)	Agg. Size (mm)	Agg. Type	Slump flow (mm)	Paste Volume (%)	$f'_c$ (MPa)	$\rho$ (%)	$f_y$ (MPa)	$V_{test}/\sqrt{f'_c}bd$
16	Safan M.A. (2012)	G4/12	19	2.6	100	150	135	19	NG	655.0	33.98	37	1.68	430	0.23
17	Safan M.A. (2012)	D5/10	19.6	2.6	100	150	135	19	CD	640.0	34.72	51	1.16	555	0.20
18	Safan M.A. (2012)	D5/12	22.5	2.6	100	150	135	19	CD	640.0	34.72	51	1.68	430	0.23
19	Safan M.A. (2012)	G5/10	14.7	2.6	100	150	135	19	NG	650.0	34.72	33	1.16	555	0.19
20	Safan M.A. (2012)	G5/12	18.8	2.6	100	150	135	19	NG	650.0	34.70	33	1.68	430	0.24
21	Safan M.A. (2012)	D6/10	21.7	2.6	100	150	135	19	CD	670.0	34.10	48	1.16	555	0.23
22	Safan M.A. (2012)	D6/12	22.1	2.6	100	150	135	19	CD	670.0	34.10	48	1.68	430	0.24
23	Safan M.A. (2012)	G6/10	19	2.6	100	150	135	19	NG	680.0	34.10	30	1.16	555	0.26
24	Safan M.A. (2012)	G6/12	20.1	2.6	100	150	135	19	NG	680.0	34.10	30	1.68	430	0.27
25	Safan M.A. (2012)	D7/10	15.1	2.6	100	150	135	19	CD	650.0	34.83	41	1.16	555	0.17
26	Safan M.A. (2012)	D7/12	19.8	2.6	100	150	135	19	CD	650.0	34.83	41	1.68	430	0.23
27	Safan M.A. (2012)	G7/10	19.5	2.6	100	150	135	19	NG	650.0	34.83	26	1.16	555	0.28
28	Safan M.A. (2012)	G7/12	16.8	2.6	100	150	135	19	NG	650.0	34.83	26	1.68	430	0.24
29	A.A.A. Hassan et al. (2010)	1SCC150	74	2.5	400	150	102.5	10	CL	700	32.65	45	1	480	0.27
30	A.A.A. Hassan et al. (2010)	2SCC150	81	2.5	400	150	100	10	CL	700	32.65	45	2	480	0.30

Table C-1. Shear Test Database of Self Consolidating Concrete Beams without Transverse Reinforcement (Cont.)

No.	Author (Year)	Specimen ID	$V_{test}$ (kN)	a/d	$b_w$ (mm)	h (mm)	d (mm)	Agg. Size (mm)	Agg. Type	Slump flow (mm)	Paste Volume (%)	$f'_c$ (MPa)	$\rho$ (%)	$f_y$ (MPa)	$V_{test}/\sqrt{f'_c} bd$
31	A.A.A. Hassan et al. (2010)	2SCC250	128	2.5	400	250	197.5	10	CL	700	32.65	45	2	480	0.24
32	A.A.A. Hassan et al. (2010)	1SCC363	153	2.5	400	363	310.5	10	CL	700	32.65	45	1	480	0.18
33	A.A.A. Hassan et al. (2010)	2SCC363	166	2.5	400	363	305.5	10	CL	700	32.65	45	2	480	0.20
34	A.A.A. Hassan et al. (2010)	1SCC500	181	2.5	400	500	447.5	10	CL	700	32.65	45	1	480	0.15
35	A.A.A. Hassan et al. (2010)	2SCC500	226	2.5	400	500	442.5	10	CL	700	32.65	45	2	480	0.19
36	A.A.A. Hassan et al. (2010)	1SCC750	250	2.5	400	750	667.5	10	CL	700	32.65	45	1	480	0.14
37	A.A.A. Hassan et al. (2010)	2SCC750	315	2.5	400	750	650.5	10	CL	700	32.65	45	2	480	0.18
38	Ammar N.H. et al. (2014)	B M1 2k v1-1.65	68	1.65	180	250	211	10	CG	660	37.3	19.87	1.05	420	0.40
39	Ammar N.H. et al. (2014)	B M2 5F v1-1.83	109	1.83	180	250	190.5	10	CG	700	37.1	49.49	2.9	420	0.45
40	Ammar N.H. et al. (2014)	B M3 2F v1-1.83	111	1.83	180	250	190.5	10	CG	740	35.6	60.1	3.5	420	0.42
41	Assem A.A. et al. (2015)	0.7NS10	70.56	2.5	250	250	198	10	NCS	760	39.3	31	2.06	480	0.26
42	Assem A.A. et al. (2015)	0.9NS10	72.93	2.5	250	250	198	10	NCS	780	39.3	29.3	2.06	480	0.27
43	Assem A.A. et al. (2015)	1.2NS10	73.83	2.5	250	250	198	10	NCS	750	39.3	27.3	2.06	480	0.29
44	Assem A.A. et al. (2015)	0.7NS20	72.54	2.5	250	250	198	20	NCS	790	39.3	30.4	2.06	480	0.27
45	Assem A.A. et al. (2015)	0.9NS20	76.46	2.5	250	250	198	20	NCS	770	39.3	29	2.06	480	0.29

Table C-1. Shear Test Database of Self Consolidating Concrete Beams without Transverse Reinforcement (Cont.)

No.	Author (Year)	Specimen ID	V <sub>test</sub> (kN)	a/d	b <sub>w</sub> (mm)	h (mm)	d (mm)	Agg. Size (mm)	Agg. Type	Slump flow (mm)	Paste Volume (%)	f <sub>c</sub> (MPa)	ρ (%)	f <sub>y</sub> (MPa)	V <sub>test</sub> /√f <sub>c</sub> bd
46	Assem A.A. et al. (2015)	1.2NS20	85.06	2.5	250	250	198	20	NCS	790	39.3	27.5	2.06	480	0.33
47	Assem A.A. et al. (2015)	0.7HS10	120.79	2.5	250	250	198	10	NCS	695	36.6	72	2.06	480	0.29
48	Assem A.A. et al. (2015)	1.2HS10	121.15	2.5	250	250	198	10	NCS	700	36.6	70	2.06	480	0.29
49	Assem A.A. et al. (2015)	0.7HS20	126.01	2.5	250	250	198	20	NCS	690	36.6	69.7	2.06	480	0.30
50	Assem A.A. et al. (2015)	1.2HS20	120.52	2.5	250	250	198	20	NCS	700	36.6	68.8	2.06	480	0.29
51	L. Biolzi et al. (2014)	SCC40-S-N-1	113.9	1.5	170	300	260	15	NS	720	35.7	42.64	0.905	589.6	0.39
52	L. Biolzi et al. (2014)	SCC40-S-N-2	136.23	1.5	170	300	260	15	NS	720	35.7	42.64	0.905	589.6	0.47
53	L. Biolzi et al. (2014)	SCC40-M-N-1	51.85	2.5	170	300	260	15	NS	720	35.7	42.64	0.905	589.6	0.18
54	L. Biolzi et al. (2014)	SCC40-M-N-2	48.89	2.5	170	300	260	15	NS	720	35.7	42.64	0.905	589.6	0.17
55	L. Biolzi et al. (2014)	SCC40-L-N-1	47.29	3.5	170	300	260	15	NS	720	35.7	42.64	0.905	589.6	0.16
56	L. Biolzi et al. (2014)	SCC40-L-N-2	54.01	3.5	170	300	260	15	NS	720	35.7	42.64	0.905	589.6	0.19
57	L. Biolzi et al. (2014)	SCC40-XL-N-1	34.04	4.5	170	300	260	15	NS	720	35.7	42.64	0.905	589.6	0.12
58	L. Biolzi et al. (2014)	SCC40-XL-N-2	47.6	4.5	170	300	260	15	NS	720	35.7	42.64	0.905	589.6	0.16
59	Ezzell and Volz (2011)	SCC-NS-1	182	3.1	304	457	372	25.4	CL	620	27	60.3	4.5	493	0.21
60	Ezzell and Volz (2011)	SCC-NS-2	250	3.1	304	457	372	25.4	CL	620	27	60.3	4.5	493	0.28

Table C-1. Shear Test Database of Self Consolidating Concrete Beams without Transverse Reinforcement (Cont.)

No.	Author (Year)	Specimen ID	V <sub>test</sub> (kN)	a/d	b <sub>w</sub> (mm)	h (mm)	d (mm)	Agg. Size (mm)	Agg. Type	Slump flow (mm)	Paste Volume (%)	f'c (MPa)	ρ (%)	f <sub>y</sub> (MPa)	V <sub>test</sub> /√f'c bd
61	Ezzell and Volz (2011)	SCC-NS-3	208	3.1	304	457	372	25.4	CL	620	27	60.3	4.5	493	0.24
62	Arezoumandi and Volz (2014)	NS-4-1	129.9	3	300	460	400	19	CL	620	32.84	53.5	1.27	449	0.15
63	Arezoumandi and Volz (2014)	NS-4-2	128.1	3	300	460	400	19	CL	620	32.84	39.6	1.27	449	0.17
64	Arezoumandi and Volz (2014)	NS-6-1	177.9	3.1	300	460	387	19	CL	620	32.84	53.5	2.07	449	0.21
65	Arezoumandi and Volz (2014)	NS-6-2	169.5	3.1	300	460	387	19	CL	620	32.84	39.6	2.07	449	0.23
66	Arezoumandi and Volz (2014)	NS-8-1	210.4	3.1	300	460	387	19	CL	620	32.84	53.5	2.71	449	0.25
67	Arezoumandi and Volz (2014)	NS-8-2	185.5	3.1	300	460	387	19	CL	620	32.84	39.6	2.71	449	0.25
68	Lachemi et al. (2005)	S12-150a	15.7	2.14	100	150	124	12	CG	645	32.6	54	1.6	N.S.	0.17
69	Lachemi et al. (2005)	S12-150b	16.5	2.14	100	150	124	12	CG	675	32.9	53	1.6	N.S.	0.18
70	Lachemi et al. (2005)	S19-150a	12.8	2.14	100	150	124	19	CG	635	30	58	1.6	N.S.	0.14
71	Lachemi et al. (2005)	S19-150b	17.7	2.14	100	150	124	19	CG	637	29.6	58	1.6	N.S.	0.19
72	Lachemi et al. (2005)	S12-200a	32.7	1.53	100	200	174	12	CG	645	32.6	54	1.15	N.S.	0.26
73	Lachemi et al. (2005)	S12-200b	27.5	1.53	100	200	174	12	CG	675	32.9	53	1.15	N.S.	0.22
74	Lachemi et al. (2005)	S19-200a	31.5	1.53	100	200	174	19	CG	635	30	58	1.15	N.S.	0.24
75	Lachemi et al. (2005)	S19-200b	31	1.53	100	200	174	19	CG	637	29.6	58	1.15	N.S.	0.23

Table C-1. Shear Test Database of Self Consolidating Concrete Beams without Transverse Reinforcement (Cont.)

No.	Author (Year)	Specimen ID	$V_{test}$ (kN)	a/d	$b_w$ (mm)	h (mm)	d (mm)	Agg. Size (mm)	Agg. Type	Slump flow (mm)	Paste Volume (%)	$f'_c$ (MPa)	$\rho$ (%)	$f_y$ (MPa)	$V_{test}/\sqrt{f'_c bd}$
76	Lachemi et al. (2005)	S12-300a	64	1.05	100	300	253	12	CG	645	32.6	54	1.57	N.S.	0.34
77	Lachemi et al. (2005)	S12-300b	64	1.05	100	300	253	12	CG	675	32.9	53	1.57	N.S.	0.35
78	Lachemi et al. (2005)	S19-300a	48	1.05	100	300	253	19	CG	635	30	58	1.57	N.S.	0.25
79	Lachemi et al. (2005)	S19-300b	48	1.05	100	300	253	19	CG	637	29.6	58	1.57	N.S.	0.25

Table C-2. Shear Test Database of Self Consolidating Concrete Beams with Transverse Reinforcement

No.	Author (Year)	Specimen ID	V <sub>test</sub> (kN)	a/d	b <sub>w</sub> (mm)	h (mm)	d (mm)	Agg. Size (mm)	Agg. Type	Slump flow (mm)	Paste Volume (%)	f'c (MPa)	ρ (%)	A <sub>sv</sub> (mm <sup>2</sup> )	ρ <sub>v</sub> (%) =A <sub>s</sub> /S*b <sub>w</sub>	f <sub>yt</sub> (MPa)	f <sub>yl</sub> (MPa)
1	Ammar N.H. et al. (2014)	B M1 2k v2-1.65	72	1.65	180	250	211	10	CG	660	37.3	19.87	1.05	50.26	0.29	340	420
2		B M1 2k v3-1.65	81	1.65	180	250	211	10	CG	660	37.3	19.87	1.05	50.26	0.59	340	420
3		B M1 2k v4-1.65	86	1.65	180	250	211	10	CG	660	37.3	19.87	1.05	50.26	0.9	340	420
4		B M2 5F v5-1.83	133	1.83	180	250	190.5	10	CG	700	37.1	49.49	2.9	50.26	0.33	340	420
5		B M2 5F v6-1.83	160	1.83	180	250	190.5	10	CG	700	37.1	49.49	2.9	50.26	0.67	340	420
6		B M2 5F v7-1.83	168	1.83	180	250	190.5	10	CG	700	37.1	49.49	2.9	50.26	1	340	420
7		B M3 2F v5-1.83	145	1.83	180	250	190.5	10	CG	740	35.6	60.1	3.5	50.26	0.33	340	420
8		B M3 2F v6-1.83	170	1.83	180	250	190.5	10	CG	740	35.6	60.1	3.5	50.26	0.67	340	420
9		B M3 2F v7-1.83	172	1.83	180	250	190.5	10	CG	740	35.6	60.1	3.5	50.26	1	340	420
10	L. Biolzi et al. (2014)	SCC40-S-S-1	177.05	1.5	170	300	260	15	NA	720	35.7	42.64	0.905	28.3	0.222	589.6	589.6
11		SCC40-S-S-2	165.95	1.5	170	300	260	15	NA	720	35.7	42.64	0.905	28.3	0.222	589.6	589.6
12		SCC40-M-S-1	109.4	2.5	170	300	260	15	NA	720	35.7	42.64	0.905	28.3	0.222	589.6	589.6
13		SCC40-M-S-2	104.78	2.5	170	300	260	15	NA	720	35.7	42.64	0.905	28.3	0.222	589.6	589.6
14		SCC40-L-S-1	70.37	3.5	170	300	260	15	NA	720	35.7	42.64	0.905	28.3	0.222	589.6	589.6
15		SCC40-L-S-2	71.56	3.5	170	300	260	15	NA	720	35.7	42.64	0.905	28.3	0.222	589.6	589.6



Table C-2. Shear Test Database of Self Consolidating Concrete Beams with Transverse Reinforcement (Cont.)

No.	Author (Year)	Specimen ID	V <sub>test</sub> (kN)	a/d	b <sub>w</sub> (mm)	h (mm)	d (mm)	Agg. Size (mm)	Agg. Type	Slump flow (mm)	Paste Volume (%)	f'c (MPa)	ρ (%)	A <sub>sv</sub> (mm <sup>2</sup> )	ρ <sub>v</sub> (%) =A <sub>s</sub> /S*b <sub>w</sub>	f <sub>yt</sub> (MPa)	f <sub>yl</sub> (MPa)
16	L. Biolzi et al. (2014)	SCC40-XL-S-1	53.56	4.5	170	300	260	15	NA	720	35.7	42.64	0.905	28.3	0.222	589.6	589.6
17		SCC40-XL-S-2	55	4.5	170	300	260	15	NA	720	35.7	42.64	0.905	28.3	0.222	589.6	589.6
18	Ezzell and Volz (2011)	SCC-7-1	468.4	3.1	304	457	372	25.4	CL	620	27	56	4.5	71	0.263	467	493
19		SCC-7-2	514.2	3.1	304	457	372	25.4	CL	620	27	56	4.5	71	0.263	467	493
20		SCC-7-3	449.3	3.1	304	457	372	25.4	CL	620	27	56	4.5	71	0.263	467	493
21		SCC-5-1	563.14	3.1	304	457	372	25.4	CL	620	27	51.16	4.5	71	0.263	467	493
22		SCC-5-2	581.4	3.1	304	457	372	25.4	CL	620	27	51.16	4.5	71	0.263	467	493
23		SCC-5-3	537.35	3.1	304	457	372	25.4	CL	620	27	51.16	4.5	71	0.263	467	493

Table C-3. Shear Test Database of High Volume Fly Ash Concrete Beams without Transverse Reinforcement

No.	Author (Year)	Specimen ID	V <sub>test</sub> (kN)	a/d	bw (mm)	h (mm)	d (mm)	RL (%)	Agg. Size (mm)	Agg. Type	f'c (MPa)	ρ (%)	fy (MPa)	V <sub>test</sub> /√f'c bd
1	Rao et al. (2011)	FB1	39	2.5	100	200	180	50	20	CAG	32.64	0.58	N.P.	0.38
2	Rao et al. (2011)	FB2	55	2.5	100	200	180	50	20	CAG	32.64	1	N.P.	0.53
3	Rao et al. (2011)	FB3	65	2.5	100	200	180	50	20	CAG	32.64	2	N.P.	0.63
4	Rao et al. (2011)	FB4	70	2.5	100	200	180	50	20	CAG	32.64	2.94	N.P.	0.68
5	Ortega C. (2012)	HVFA-R1-NS-1	120	3.06	304	457	398	70	19	CL	22	1.59	480	0.21
6	Ortega C. (2012)	HVFA-R1-NS-2	106	3.06	304	457	398	70	19	CL	21.6	1.59	480	0.19
7	Ortega C. (2012)	HVFA-R2-NS-1	123	3.25	304	457	375	70	19	CL	22	2.03	480	0.23
8	Ortega C. (2012)	HVFA-R2-NS-2	113	3.25	304	457	375	70	19	CL	21.6	2.03	480	0.21
9	Ortega C. (2012)	HVFA-R3-NS-1	162	3.25	304	457	375	70	19	CL	22	2.71	480	0.30
10	Ortega C. (2012)	HVFA-R3-NS-2	154	3.25	304	457	375	70	19	CL	21.6	2.71	480	0.29
11	Ortega C. (2012)	HVFA-R4-NS-1	116	3.28	304	457	372	70	19	CL	29	4.5	493	0.19
12	Ortega C. (2012)	HVFA-R4-NS-2	226	3.28	304	457	372	70	19	CL	29	4.5	493	0.37
13	Ortega C. (2012)	HVFA-R4-NS-3	191	3.28	304	457	372	70	19	CL	29	4.5	493	0.31

Table C-3. Shear Test Database of High Volume Fly Ash Concrete Beams without Transverse Reinforcement (Cont.)

No.	Author (Year)	Specimen ID	$V_{test}$ (kN)	a/d	bw (mm)	h (mm)	d (mm)	RL (%)	Agg. Size (mm)	Agg. Type	$f'_c$ (MPa)	$\rho$ (%)	$f_y$ (MPa)	$V_{test}/\sqrt{f'_c} bd$
14	Arezoumandi and Volz (2013)	NS-5-1	134.3	3.06	305	457	398	70	19	CL	30.7	1.27	475	0.20
15	Arezoumandi and Volz (2013)	NS-5-2	122.8	3.06	305	457	398	70	19	CL	30.7	1.27	475	0.18
16	Arezoumandi and Volz (2013)	NS-6-1	150.4	3.25	305	457	375	70	19	CL	30.7	2.03	475	0.24
17	Arezoumandi and Volz (2013)	NS-6-2	168.1	3.25	305	457	375	70	19	CL	30.7	2.03	475	0.27
18	Arezoumandi and Volz (2013)	NS-8-1	162.4	3.25	305	457	375	70	19	CL	30.7	2.71	475	0.26
19	Arezoumandi and Volz (2013)	NS-8-2	201.5	3.25	305	457	375	70	19	CL	30.7	2.71	475	0.32

Table C-4. Shear Test Database of High Volume Fly Ash Concrete Beams with Transverse Reinforcement

No.	Author (Year)	Specimen ID	$V_{test}$ (kN)	a/d	$b_w$ (mm)	h (mm)	d (mm)	RL (%)	Agg. Size (mm)	Agg. Type	$f'_c$ (MPa)	$\rho$ (%)	$A_{sv}$ (mm <sup>2</sup> )	$\rho_v(\%) = A_s/S*b_w$	$f_{yt}$ (MPa)	$f_{yl}$ (MPa)
1	Ortega C. (2012)	HVFA-R3-7-1	290	3.25	304	457	375	70	19	CL	24.4	2.71	71	0.263	432	480
2	Ortega C. (2012)	HVFA-R3-7-2	320	3.25	304	457	375	70	19	CL	24.4	2.71	71	0.263	432	480
3	Ortega C. (2012)	HVFA-R3-7-3	324	3.25	304	457	375	70	19	CL	24.4	2.71	71	0.263	432	480
4	Ortega C. (2012)	HVFA-R4-7-1	270	3.28	304	457	372	70	19	CL	18.2	4.5	71	0.263	467	493
5	Ortega C. (2012)	HVFA-R4-7-2	321	3.28	304	457	372	70	19	CL	18.2	4.5	71	0.263	467	493
6	Ortega C. (2012)	HVFA-R4-7-3	291	3.28	304	457	372	70	19	CL	18.2	4.5	71	0.263	467	493
7	Ortega C. (2012)	HVFA-R4-5-1	435	3.28	304	457	372	70	19	CL	32.5	4.5	71	0.368	467	493
8	Ortega C. (2012)	HVFA-R4-5-2	407	3.28	304	457	372	70	19	CL	32.5	4.5	71	0.368	467	493
9	Ortega C. (2012)	HVFA-R4-5-3	362	3.28	304	457	372	70	19	CL	32.5	4.5	71	0.368	467	493
10	Arezoumandi and Volz (2013)	S-8-1	328.7	3.25	305	457	375	70	19	CL	34.7	2.71	71	0.258	380	475
11	Arezoumandi and Volz (2013)	S-8-2	337.2	3.25	305	457	375	70	19	CL	34.7	2.71	71	0.258	380	475

Table C-5. Shear Test Database of Conventional Concrete Beams without Transverse Reinforcement

No.	Author (Year)	Specimen ID	$V_{test}$ (kN)	a/d	$b_w$ (mm)	h (mm)	d (mm)	Agg. Size (mm)	Agg. Type	$f'_c$ (MPa)	$\rho$ (%)	$f_y$ (MPa)	$V_{test}/\sqrt{f'_c} bd$
1	A.A.A. Hassan et al. (2010)	1NC150	78	2.5	400	150	102.5	10	CL	47	1	480	0.28
2	A.A.A. Hassan et al. (2010)	2NC150	85	2.5	400	150	100	10	CL	47	2	480	0.31
3	A.A.A. Hassan et al. (2010)	1NC250	123	2.5	400	250	202.5	10	CL	47	1	480	0.22
4	A.A.A. Hassan et al. (2010)	2NC250	136	2.5	400	250	197.5	10	CL	47	2	480	0.25
5	A.A.A. Hassan et al. (2010)	1NC363	169	2.5	400	363	310.5	10	CL	47	1	480	0.20
6	A.A.A. Hassan et al. (2010)	2NC363	178	2.5	400	363	305.5	10	CL	47	2	480	0.21
7	A.A.A. Hassan et al. (2010)	1NC500	209	2.5	400	500	447.5	10	CL	47	1	480	0.17
8	A.A.A. Hassan et al. (2010)	2NC500	235	2.5	400	500	442.5	10	CL	47	2	480	0.19
9	A.A.A. Hassan et al. (2010)	1NC750	198	2.5	400	750	667.5	10	CL	47	1	480	0.11
10	A.A.A. Hassan et al. (2010)	2NC750	340	2.5	400	750	650.5	10	CL	47	2	480	0.19
11	Ammar N.H. et al. (2014)	B M4 2k v1-1.65	81	1.65	180	250	211	10	CG	23.21	1.05	420	0.44
12	Ezzell and Volz (2011)	Control-NS	305	3.1	304	457	372	25.4	CL	50.54	4.5	467	0.38
13	Ezzell and Volz (2011)	Control-7-2	204	3.1	304	457	372	25.4	CL	50.54	4.5	467	0.25

Table C-5. Shear Test Database of Conventional Concrete Beams without Transverse Reinforcement (Cont.)

No.	Author (Year)	Specimen ID	$V_{test}$ (kN)	a/d	$b_w$ (mm)	h (mm)	d (mm)	Agg. Size (mm)	Agg. Type	$f'_c$ (MPa)	$\rho$ (%)	$f_y$ (MPa)	$V_{test}/\sqrt{f'_c} bd$
14	Ezzell and Volz (2011)	Control-7-3	218	3.1	304	457	372	25.4	CL	50.54	4.5	467	0.27
15	Arezoumandi and Volz (2014)	NS-4-1	106.8	3	300	460	400	19	CL	34	1.27	449	0.15
16	Arezoumandi and Volz (2014)	NS-4-2	123.2	3	300	460	400	19	CL	34.5	1.27	449	0.17
17	Arezoumandi and Volz (2014)	NS-6-1	155.7	3.1	300	460	387	19	CL	34	2.07	449	0.23
18	Arezoumandi and Volz (2014)	NS-6-2	165.5	3.1	300	460	387	19	CL	34.5	2.07	449	0.24
19	Arezoumandi and Volz (2014)	NS-8-1	152.6	3.1	300	460	387	19	CL	34	2.71	449	0.23
20	Arezoumandi and Volz (2014)	NS-8-2	191.3	3.1	300	460	387	19	CL	34.5	2.71	449	0.28
21	Mohan et al. (2011)	CB1	46	2.5	100	200	180	20	CAG	43.84	0.58	N.P.	0.39
22	Mohan et al. (2011)	CB2	72	2.5	100	200	180	20	CAG	43.84	1	N.P.	0.60
23	Mohan et al. (2011)	CB3	79	2.5	100	200	180	20	CAG	43.84	2	N.P.	0.66
24	Mohan et al. (2011)	CB4	82	2.5	100	200	180	20	CAG	43.84	2.94	N.P.	0.69
25	Ortega C. (2012)	CC-R1-NS-1	119	3.06	304	457	398	19	CL	34.5	1.59	477	0.17
26	Ortega C. (2012)	CC-R1-NS-2	130	3.06	304	457	398	19	CL	32	1.59	477	0.19

Table C-5. Shear Test Database of Conventional Concrete Beams without Transverse Reinforcement (Cont.)

No.	Author (Year)	Specimen ID	$V_{test}$ (kN)	a/d	$b_w$ (mm)	h (mm)	d (mm)	Agg. Size (mm)	Agg. Type	$f'_c$ (MPa)	$\rho$ (%)	$f_y$ (MPa)	$V_{test}/\sqrt{f'_c} bd$
27	Ortega C. (2012)	CC-R1-NS-1	165.6	3.25	304	457	375	19	CL	34.5	2.03	477	0.25
28	Ortega C. (2012)	CC-R2-NS-2	135.5	3.25	304	457	375	19	CL	32	2.03	477	0.21
29	Ortega C. (2012)	CC-R3-NS-1	211	3.25	304	457	375	19	CL	34.5	2.71	477	0.32
30	Ortega C. (2012)	CC-R3-NS-2	138	3.25	304	457	375	19	CL	32	2.71	477	0.21
31	Ortega C. (2012)	CC-R4-NS-1	305	3.28	304	457	372	19	CL	50.5	4.5	493	0.38
32	Ortega C. (2012)	CC-R4-NS-2	204	3.28	304	457	372	19	CL	50.5	4.5	493	0.25
33	Ortega C. (2012)	CC-R4-NS-3	218	3.28	304	457	372	19	CL	50.5	4.5	493	0.27
34	Arezoumandi and Volz (2013)	NS-5-1	119.7	3.06	305	457	398	19	CL	29	1.27	475	0.18
35	Arezoumandi and Volz (2013)	NS-5-2	113.9	3.06	305	457	398	19	CL	26.5	1.27	475	0.18
36	Arezoumandi and Volz (2013)	NS-6-1	153.5	3.25	305	457	375	19	CL	29	2.03	475	0.25
37	Arezoumandi and Volz (2013)	NS-6-2	144.6	3.25	305	457	375	19	CL	26.5	2.03	475	0.25
38	Arezoumandi and Volz (2013)	NS-8-1	147.7	3.25	305	457	375	19	CL	29	2.71	475	0.24
39	Arezoumandi and Volz (2013)	NS-8-2	143.7	3.25	305	457	375	19	CL	26.5	2.71	475	0.24

Table C-6. Shear Test Database of Conventional Concrete Beams with Transverse Reinforcement

No.	Author (Year)	Specimen ID	V <sub>test</sub> (kN)	a/d	b <sub>w</sub> (mm)	h (mm)	d (mm)	Agg. Size (mm)	Agg. Type	f'c (MPa)	ρ (%)	A <sub>sv</sub> (mm <sup>2</sup> )	ρ <sub>v</sub> (%) =A <sub>s</sub> /S*b <sub>w</sub>	f <sub>yt</sub> (MPa)	f <sub>yl</sub> (MPa)
1	Ezzell and Volz (2011)	Control-7-1	272.7	3.1	304	457	372	25.4	CL	49.7	4.5	71	0.263	467	493
2	Ezzell and Volz (2011)	Control-7-2	434.15	3.1	304	457	372	25.4	CL	49.7	4.5	71	0.263	467	493
3	Ezzell and Volz (2011)	Control-7-3	435.5	3.1	304	457	372	25.4	CL	49.7	4.5	71	0.263	467	493
4	Ezzell and Volz (2011)	Control-5-1	482.63	3.1	304	457	372	25.4	CL	38.7	4.5	71	0.263	467	493
5	Ezzell and Volz (2011)	Control-5-2	453	3.1	304	457	372	25.4	CL	38.7	4.5	71	0.263	467	493
6	Ezzell and Volz (2011)	Control-5-3	418.6	3.1	304	457	372	25.4	CL	38.7	4.5	71	0.263	467	493
7	Ortega C. (2012)	CC-R3-7-1	333.7	3.25	304	457	375	19	CL	34.6	2.71	71	0.263	432	480
8	Ortega C. (2012)	CC-R3-7-2	359.4	3.25	304	457	375	19	CL	34.6	2.71	71	0.263	432	480
9	Ortega C. (2012)	CC-R3-7-3	344.2	3.25	304	457	375	19	CL	34.6	2.71	71	0.263	432	480



Table C-6. Shear Test Database of Conventional Concrete Beams with Transverse Reinforcement (Cont.)

No.	Author (Year)	Specimen ID	$V_{test}$ (kN)	a/d	$b_w$ (mm)	h (mm)	d (mm)	Agg. Size (mm)	Agg. Type	$f'_c$ (MPa)	$\rho$ (%)	$A_{sv}$ (mm <sup>2</sup> )	$\rho_v(\%) = A_s/S*b_w$	$f_{yt}$ (MPa)	$f_{yl}$ (MPa)
10	Ortega C. (2012)	CC-R4-7-1	407.8	3.28	304	457	372	19	CL	49.7	4.5	71	0.263	467	493
11	Ortega C. (2012)	CC-R4-7-2	434.2	3.28	304	457	372	19	CL	49.7	4.5	71	0.263	467	493
12	Ortega C. (2012)	CC-R4-7-3	435.3	3.28	304	457	372	19	CL	49.7	4.5	71	0.263	467	493
13	Ortega C. (2012)	CC-R4-5-1	482.4	3.28	304	457	372	19	CL	38.6	4.5	71	0.368	467	493
14	Ortega C. (2012)	CC-R4-5-2	452.9	3.28	304	457	372	19	CL	38.6	4.5	71	0.368	467	493
15	Ortega C. (2012)	CC-R4-5-3	418.4	3.28	304	457	372	19	CL	38.6	4.5	71	0.368	467	493
16	Arezoumandi and Volz (2013)	S-8-1	299.8	3.25	305	457	375	19	CL	29	2.71	71	0.258	380	475
17	Arezoumandi and Volz (2013)	S-8-2	319.8	3.25	305	457	375	19	CL	26.5	2.71	71	0.258	380	475

APPENDIX D.

ADDITIONAL DETAILS OF BOND BEHAVIOR STUDY

The material in Appendix D is additional details to HVFA-SCC bond test results presented in Paper III. The Cracking load was recorded at the observation of the first crack. However, the failure considers splitting when a small clear cover or small spacing between reinforced bars exists and the slippage failure occurs when the reinforcing bar slips.

**REF-50**

Stage	Applied Load, kips
Cracking Load	23
Ultimate Load (Failure)	110
Failure Mode	Flexural (Yielding)

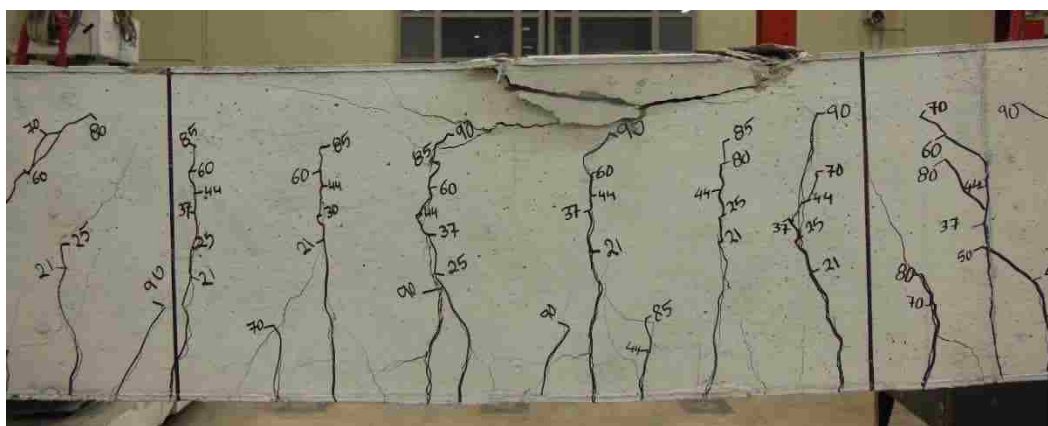


Figure D-1. Crack Pattern of Specimen REF-50 (Side View)



Figure D-2. Crack Pattern of Specimen REF-50 (Bottom View)

**BWOC-50**

Stage	Applied Load, kips
Cracking Load	21
Ultimate Load (Failure)	52
Failure Mode	Splitting

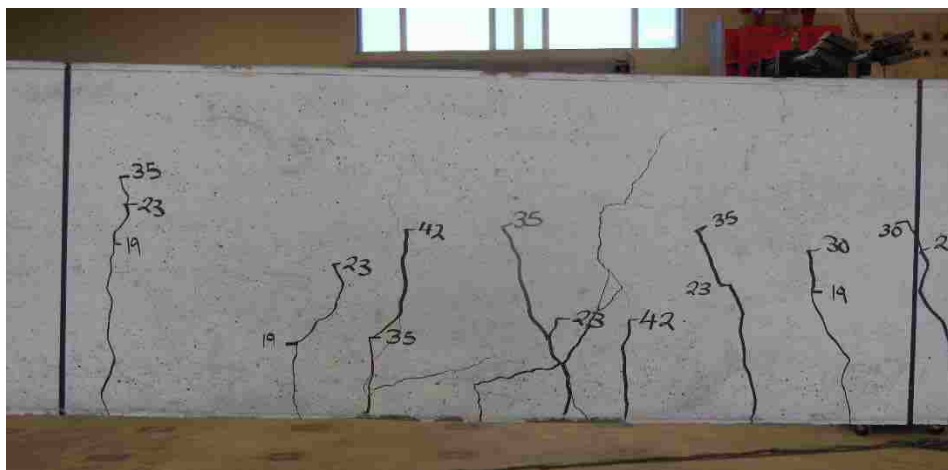


Figure D-3. Crack Pattern of Specimen BWOC-50 (Side View)



Figure D-4. Crack Pattern of Specimen BWOC-50 (Bottom View)

**BWC-50**

Stage	Applied Load, kips
Cracking Load	22
Ultimate Load (Failure)	54
Failure Mode	Slippage

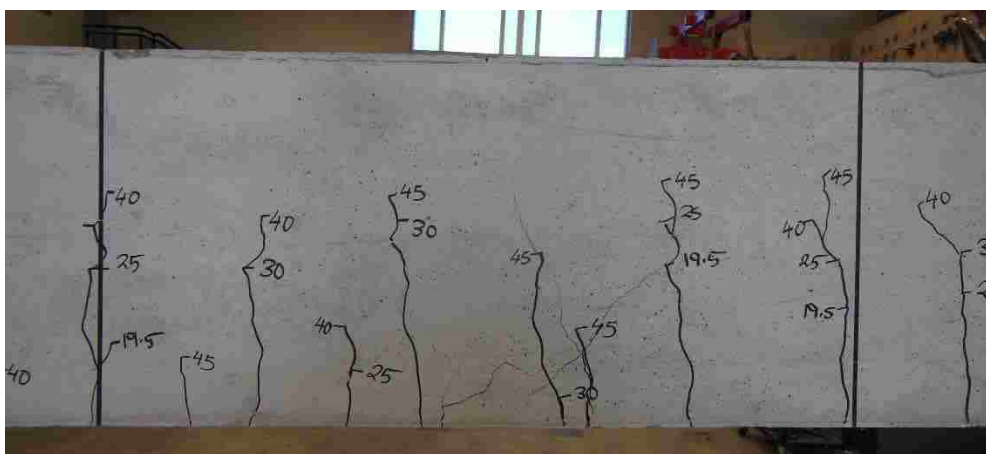


Figure D-5. Crack Pattern of Specimen BWC-50 (Side View)



Figure D-6. Crack Pattern of Specimen BWC-50 (Bottom View)

**TWOC-50**

Stage	Applied Load, kips
Cracking Load	17
Ultimate Load (Failure)	53
Failure Mode	Splitting

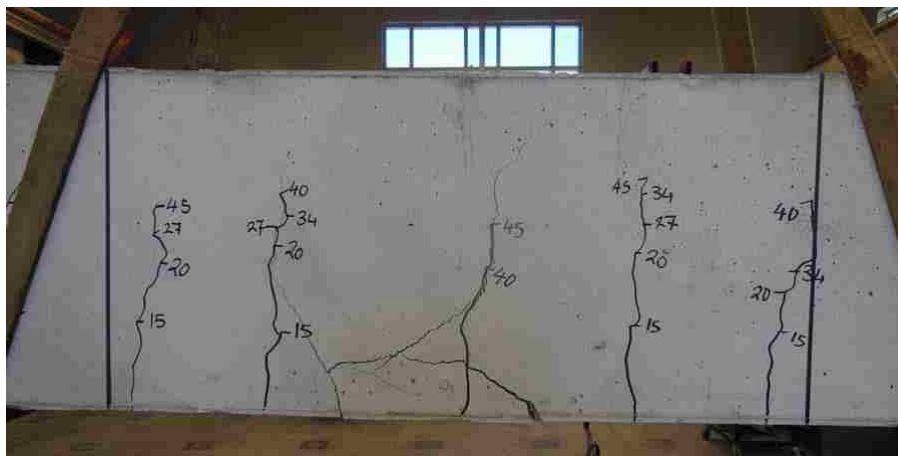


Figure D-7. Crack Pattern of Specimen TWOC-50 (Side View)

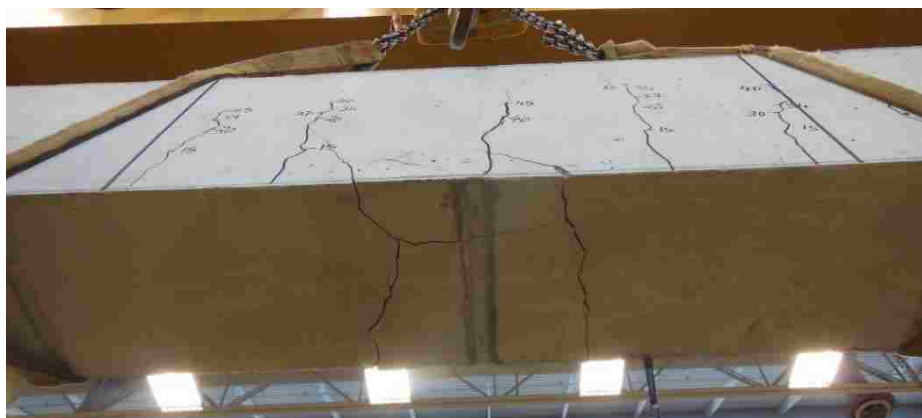


Figure D-8. Crack Pattern of Specimen TWOC-50 (Bottom View)

**REF-60**

Stage	Applied Load, kips
Cracking Load	19
Ultimate Load (Failure)	103
Failure Mode	Flexural (Yielding)

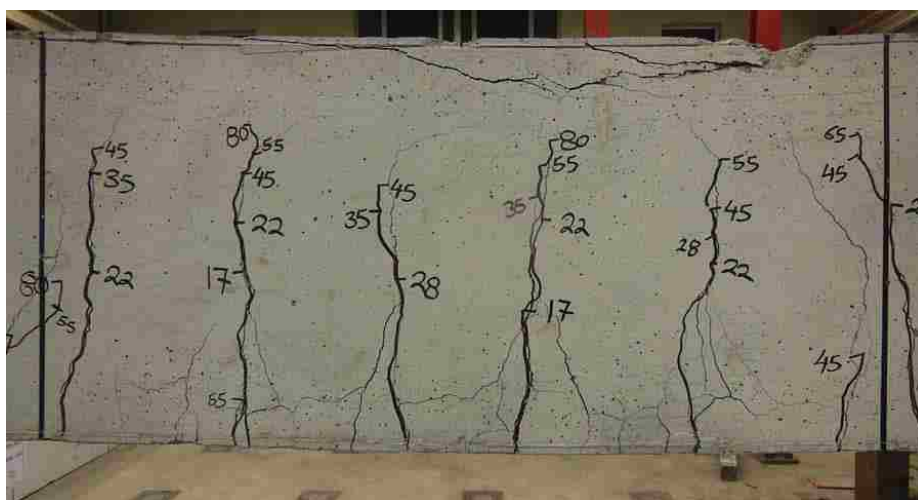


Figure D-9. Crack Pattern of Specimen REF-60 (Side View)

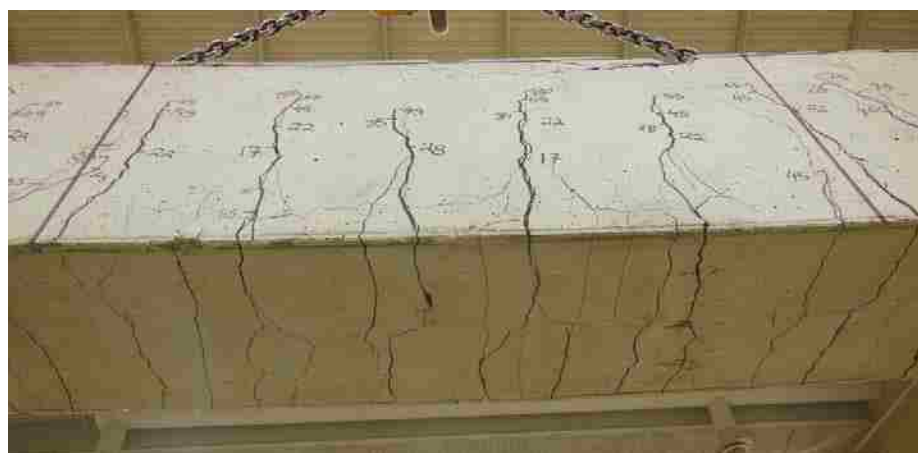


Figure D-10. Crack Pattern of Specimen REF-60 (Bottom View)



**BWOC-60**

Stage	Applied Load, kips
Cracking Load	23
Ultimate Load (Failure)	57
Failure Mode	Splitting

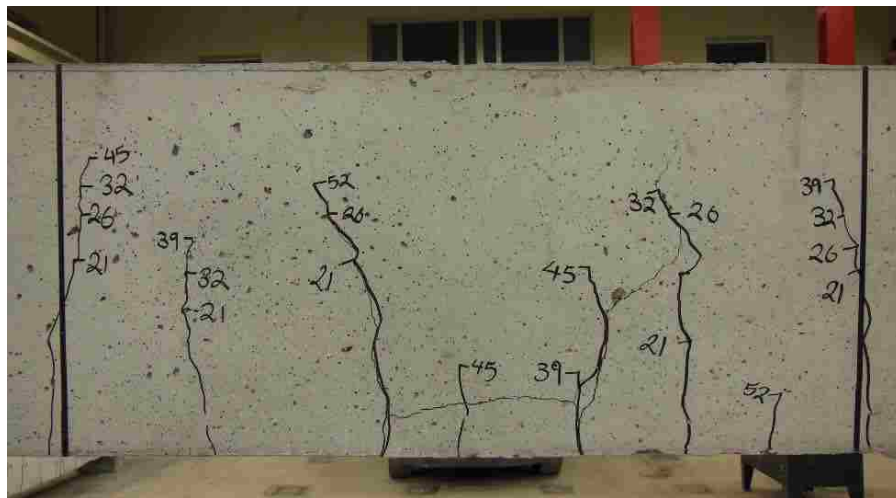


Figure D-11. Crack Pattern of Specimen BWOC-60 (Side View)



Figure D-12. Crack Pattern of Specimen BWOC-60 (Bottom View)

**BWC-60**

Stage	Applied Load, kips
Cracking Load	21
Ultimate Load (Failure)	55
Failure Mode	Slippage

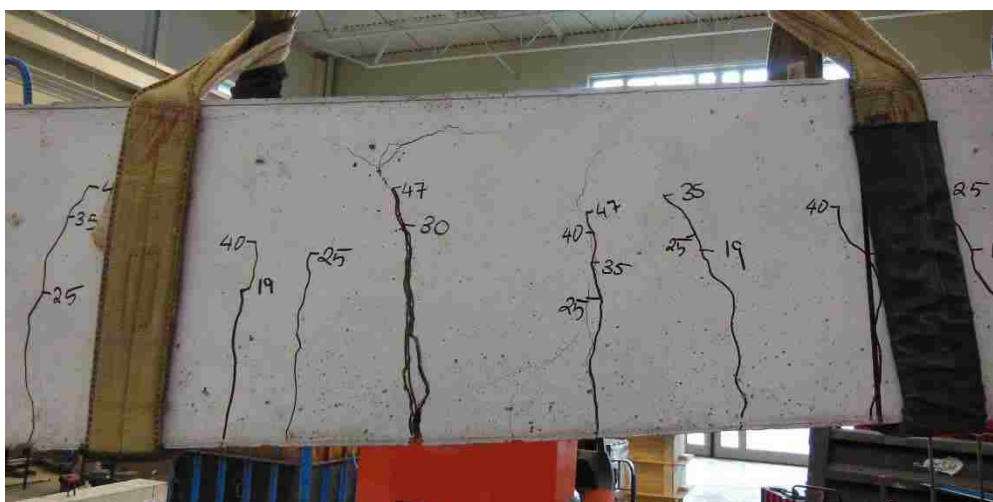


Figure D-13. Crack Pattern of Specimen BWC-60 (Side View)



Figure D-14. Crack Pattern of Specimen BWC-60 (Bottom View)

**TWOC-60**

Stage	Applied Load, kips
Cracking Load	15
Ultimate Load (Failure)	57
Failure Mode	Splitting

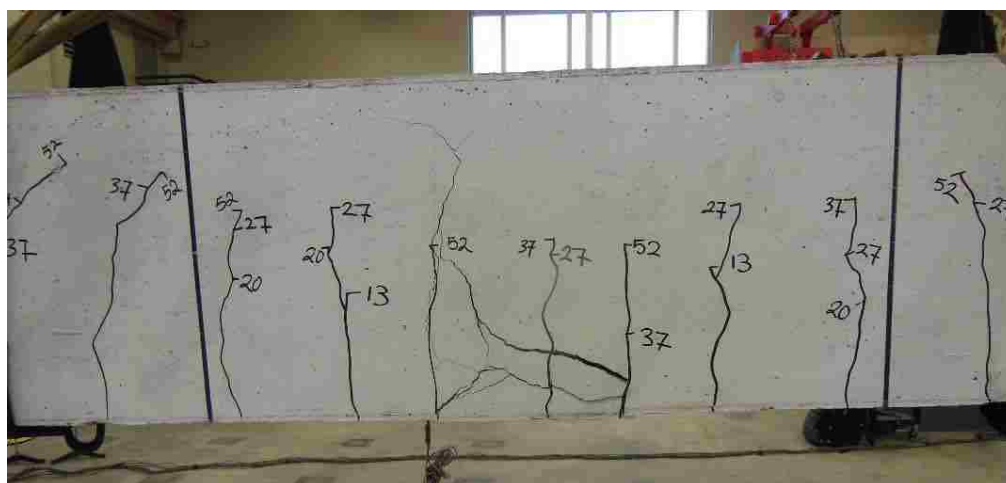


Figure D-15. Crack Pattern of Specimen TWOC-60 (Side View)

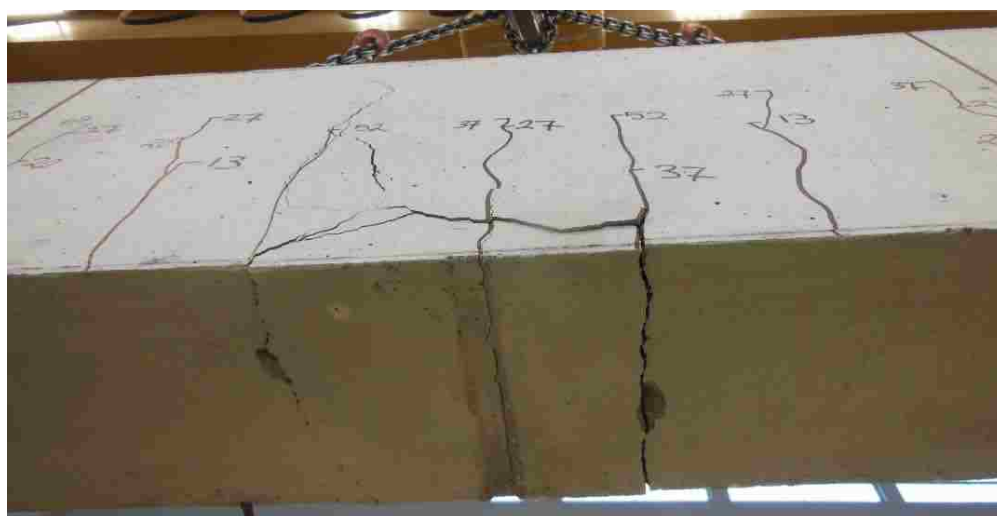


Figure D-16. Crack Pattern of Specimen TWOC-60 (Bottom View)

**REF-70**

Stage	Applied Load, kips
Cracking Load	22
Ultimate Load (Failure)	107
Failure Mode	Flexural (Yielding)

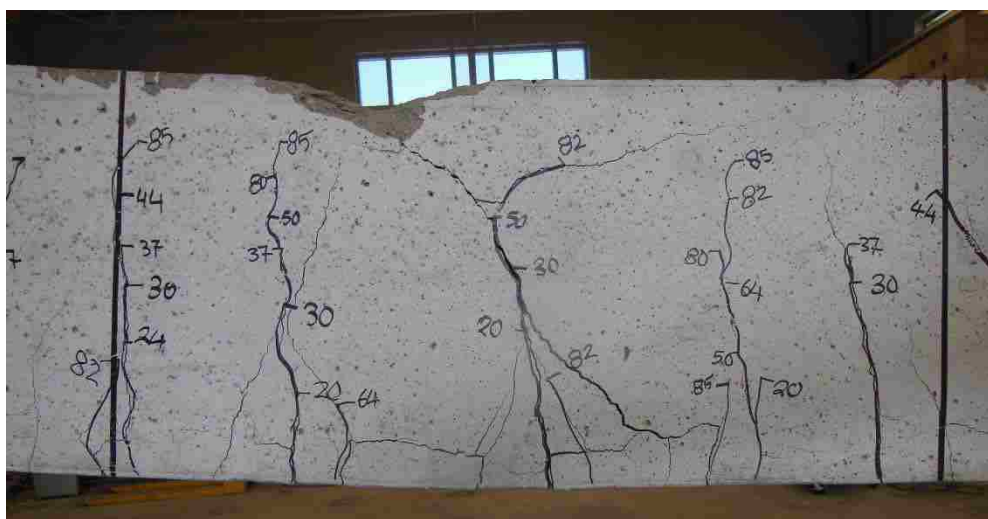


Figure D-17. Crack Pattern of Specimen REF-70 (Side View)



Figure D-18. Crack Pattern of Specimen REF-70 (Bottom View)

**BWOC-70**

Stage	Applied Load, kips
Cracking Load	20
Ultimate Load (Failure)	61
Failure Mode	Splitting

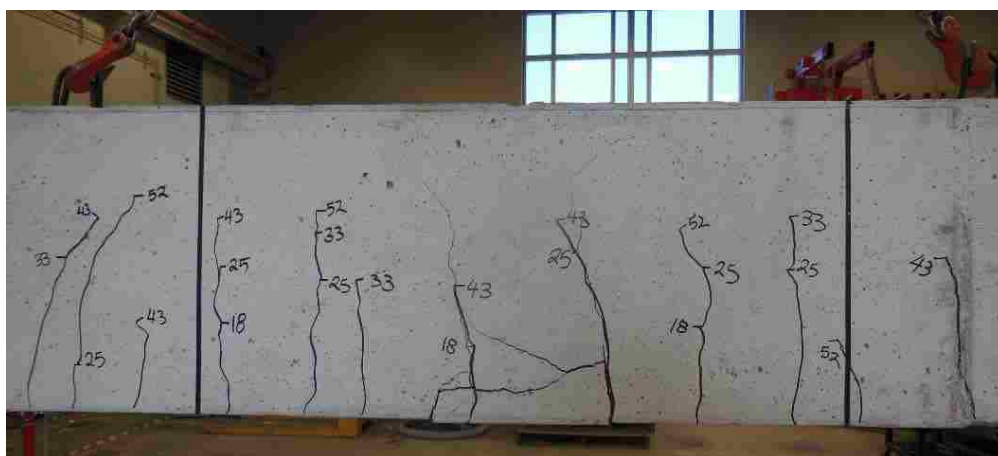


Figure D-19. Crack Pattern of Specimen BWOC-70 (Side View)



Figure D-20. Crack Pattern of Specimen BWOC-70 (Bottom View)

**BWC-70**

Stage	Applied Load, kips
Cracking Load	19
Ultimate Load (Failure)	58
Failure Mode	Slippage

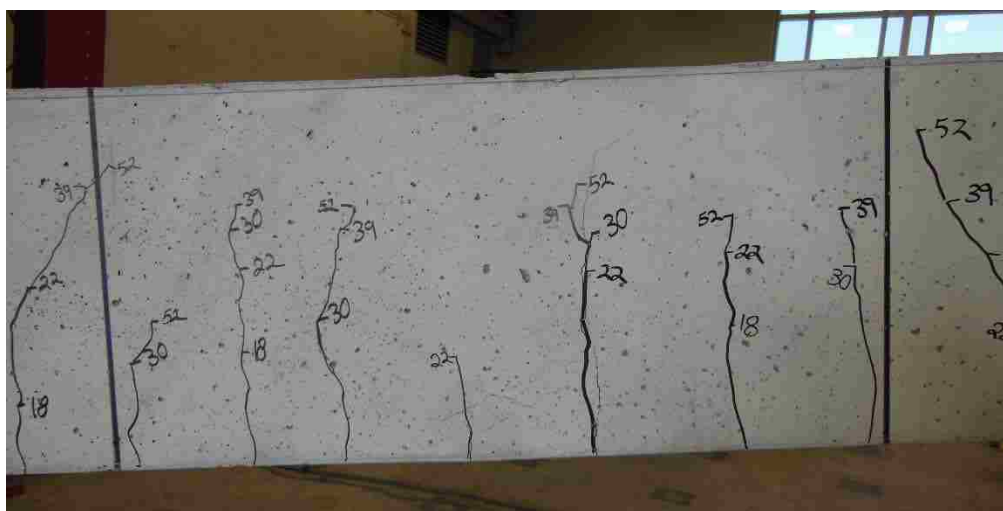


Figure D-21. Crack Pattern of Specimen BWC-70 (Side View)



Figure D-22. Crack Pattern of Specimen BWC-70 (Bottom View)

**TWOC-70**

Stage	Applied Load, kips
Cracking Load	20
Ultimate Load (Failure)	63
Failure Mode	Splitting + Yielding

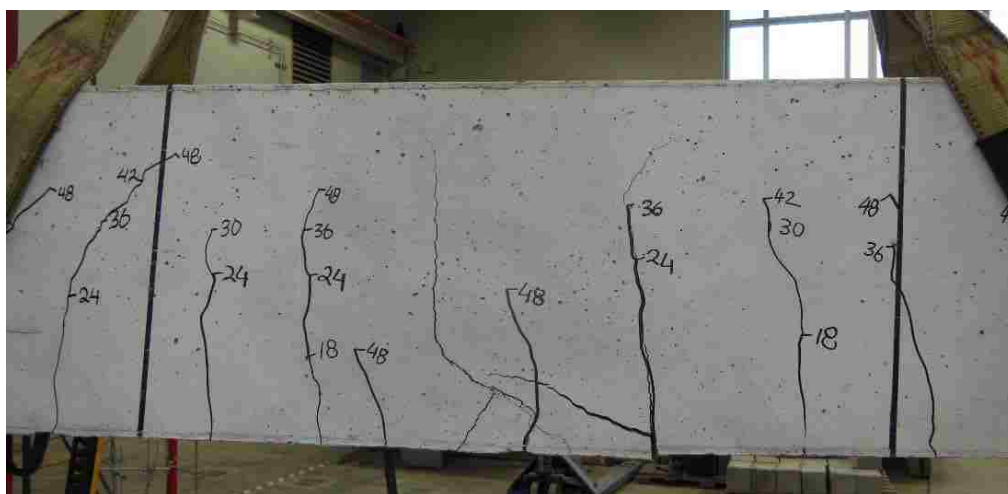


Figure D-23. Crack Pattern of Specimen TWOC-70 (Side View)

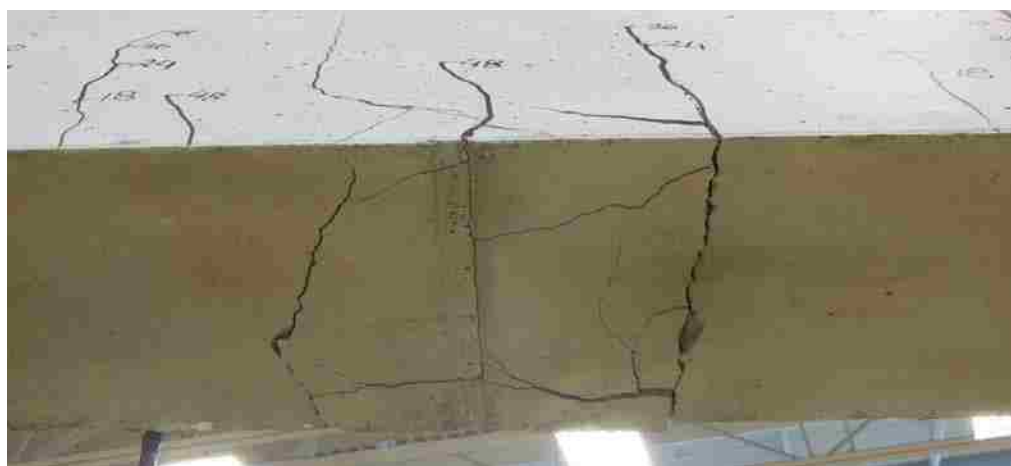


Figure D-24. Crack Pattern of Specimen TWOC-70 (Bottom View)

APPENDIX E.

PRESTRESS LOSSES DATABASE



## PRESTRESS LOSSES DATABASE

A wide range experimental database containing 65 pretensioned girders and beams was assembled and tabulated in this section. The majority of the collected data extracted from field studies conducted on bridges in the United States. The purpose of this effort was to compare and evaluate the prestress loss of bridge A7957 (particularly for the HS-SCC girders) with collected data, and check whether the total prestress losses of bridge A7957 fall within the collected data range and whether any trends appear (the comparison is presented in Paper IV). The collected data represents a wide range of environmental conditions, concrete mechanical properties, curing regimes, and geometries. Various prestress loss measurement techniques were utilized on the specimens; however, a vibrating wire strain gauge was used for most of the collected data. A selected number of important variables were taken from each study to be reported in the database. The definition of every selected variables is summarized below:

- $A_g$  = area of gross section (in.<sup>2</sup>).
- $L$  = length of beam or girder (ft).
- $f'_c$  = compressive strength of concrete at 28 days (ksi).
- $E_c$  = concrete modulus of elasticity (ksi).
- ES loss = elastic shortening loss (ksi).
- Age at final = age of specimens at last measurement (day).
- Total prestress losses = the total measured prestress losses, including elastic shortening, creep of concrete, shrinkage of concrete, and relaxation of the tendon (ksi).
- % losses = (total prestress losses / nominal jacking stress) \* 100 (%).

Table 1-E. Total Prestress Loss Database (1-3)

No.	Source	Concrete Type	Ag	L	f'c	Ec	Age at Final	Total Prestress Loss	% Losses	Comments
1	NCHRP 496 (Nebraska G1)	HSC	903.8	127	9.025	5088	470	31.96	15.8	Measured E <sub>c</sub>
2	NCHRP 496 (Nebraska G2)	HSC	903.8	127	9.025	5088	469	35.65	17.6	Measured E <sub>c</sub>
3	NCHRP 496 (New Hampshire G3)	HSC	875.2	110	10.05	5396	490	43.51	21.5	Measured E <sub>c</sub>
4	NCHRP 496 (New Hampshire G4)	HSC	875.2	110	10.05	5369	490	42.33	20.9	Measured E <sub>c</sub>
5	NCHRP 496 (Texas G7)	HSC	1121	129.2	10.67	7395	400	25.35	12.5	Measured E <sub>c</sub>
6	NCHRP 496 (Washington G18)	HSC	972	159	10.28	6114	380	42.06	20.8	Measured E <sub>c</sub>
7	NCHRP 496 (Washington G19)	HSC	972	159.8	10.28	6114	380	39.98	19.7	Measured E <sub>c</sub>
8	Gross et al. (1998) (W14)	HSC	788.4	128.96	10.13	5630	772	34.67	17.1	Measured E <sub>c</sub>
9	Gross et al. (1998) (W15)	HSC	788.4	128.96	10.13	5630	772	34.41	17.0	Measured E <sub>c</sub>
10	Gross et al. (1998) (W16)	HSC	788.4	128.96	10.13	5630	772	32.68	16.1	Measured E <sub>c</sub>
11	Gross et al. (1998) (W17)	HSC	788.4	128.96	10.26	5360	767	30.51	15.1	Measured E <sub>c</sub>
12	Myers et.al (2010) (HSC)	HSC	888	48	12.231	4538	365	9.84	6.2	Measured E <sub>c</sub>
13	Roller et.al. (2011) (S43)	HSC	1105	131.2	10.85	6100	651	35.07	18.8	Measured E <sub>c</sub>
14	Trejo et.al (2008) (CC-R)	HSC	276	40	8.95	5500	130	11.5	5.7	Approximated E <sub>c</sub>
15	Trejo et.al (2008) (CC-L)	HSC	276	40	9.19	5500	130	20.9	10.3	Approximated E <sub>c</sub>
16	Ruiz et al. (2008) (HSC-3)	HSC	78	18	12.52	6952	265	28.6	14.1	Calculated E <sub>c</sub>
17	Ruiz et al. (2008) (HSC-5)	HSC	78	18	10.7	6315	258	22.8	11.3	Calculated E <sub>c</sub>
18	Ruiz et al. (2008) (HSC-6)	HSC	78	18	13.1	7155	258	23.8	11.8	Calculated E <sub>c</sub>

Table 1-E. Total Prestress Loss Database (2-3)

No.	Source	Concrete Type	Ag	L	f'c	Ec	Age at Final	Total Prestress Loss		Comments
19	Gross et al. (1998) (N32)	HPC	1120	134.18	13.63	5730	762	43.11	21.3	Measured Ec
20	Gross et al. (1998) (S15)	HPC	1120	119.44	14.32	6680	749	37.86	18.7	Measured Ec
21	Gross et al. (1998) (S16)	HPC	1120	121.02	13.29	6930	1263	40.26	19.9	Measured Ec
22	Gross et al. (1998) (S25)	HPC	1120	133.4	13.41	6460	1222	33.81	16.7	Measured Ec
23	Gross et al. (1998) (E13)	HPC	788.4	128.95	13.7	6460	423	50.61	25.0	Measured Ec
24	Gross et al. (1998) (E14)	HPC	788.4	128.95	13.7	6460	423	57.24	28.3	Measured Ec
25	Gross et al. (1998) (E24)	HPC	788.4	153.34	14.24	5560	405	51.51	25.4	Measured Ec
26	Gross et al. (1998) (E25)	HPC	788.4	153.34	14.83	6540	747	51.95	25.7	Measured Ec
27	Gross et al. (1998) (E34)	HPC	788.4	146.32	13.75	5680	317	57.43	28.4	Measured Ec
28	Gross et al. (1998) (E35)	HPC	788.4	146.32	14.49	6490	310	58.17	28.7	Measured Ec
29	Gross et al. (1998) (E44)	HPC	788.4	145.67	14.55	6110	306	55.63	27.5	Measured Ec
30	Myers et al (2004) (B13)	HPC	310.6	50.26	11.647	6775	601	42.21	20.8	Measured Ec
31	Myers et al (2004) (B14)	HPC	310.6	50.26	11.647	6775	601	42.79	21.1	Measured Ec
32	Myers et al (2004) (B23)	HPC	310.6	55.18	12.808	6534	613	43.72	21.6	Measured Ec
33	Myers et al (2004) (B24)	HPC	310.6	55.18	12.808	6534	613	39.05	19.3	Measured Ec
34	Barr P. et. al. (2000) (1A)	HPC	747	80	10**	5700	200	33.36	16.5	Designed and Ec
35	Barr P. et. al (2000) (1C)	HPC	747	80	10**	5700	200	32.34	16.0	Designed f'c and Ec
36	Barr P. et. al (2000) (2A)	HPC	747	137	10**	5700	200	53.52	26.4	Designed f'c and Ec
37	Barr P. et. al (2000) (2B)	HPC	747	137	10**	5700	200	49.75	24.6	Designed f'c and Ec
38	Barr P. et. al (2000) (2C)	HPC	747	137	10**	5700	200	60.63	29.9	Designed f'c and Ec
39	Waldron et.al. (2004) (B1)	HPC	788.4	82.3	8	4583	890	36.9	18.2	
40	Waldron et.al. (2004) (B2)	HPC	1013	64	8		650	30.6	15.1	(2.4 RE assumed)
41	Waldron et.al. (2004) (B3)	HPC	1013	64	10		650	30.3	15.0	(2.9 RE Assumed), ES assumed depends on first beam
42	Waldron et.al. (2004) (B4)	HPC	746.7	62	8.7		400	33.8	16.7	(3 RE assumed), ES assumed depends on first beam

Table 1-E. Total Prestress Loss Database (3-3)

No.	Source	Concrete Type	Ag	L	f'c	Ec	Age at Final	Total Prestress Loss		Comments
43	Myers et.al (2010) (HS-SCC)	HS-SCC	726	34	10.131	4872	365	7.691	4.9	Measured Ec
44	Paul et.al (2009) (G1A)	HS-SCC	1085	132.2	12.836	5510	300	29.8	14.7	Measured Ec
45	Paul et.al (2009) (G1B)	HS-SCC	1085	132.2	12.836	5510	300	29.8	14.7	Measured Ec
46	Paul et.al (2009) (G1C)	HS-SCC	1085	132.2	12.836	5510	300	29.8	14.7	Measured Ec
47	Paul et.al (2009) (G3A)	HS-SCC	1085	82.2	12.836	5510	210	16.1	8.0	Measured Ec
48	Paul et.al (2009) (G3B)	HS-SCC	1085	82.2	12.836	5510	210	16.1	8.0	Measured Ec
49	Paul et.al (2009) (G3C)	HS-SCC	1085	82.2	12.836	5510	210	16.1	8.0	Measured Ec
50	Trejo et.al (2008) (SCC-R)	HS-SCC	276	40	11.66	6000	130	12.6	6.2	Approximated Ec
51	Trejo et.al (2008) (SCC-L)	HS-SCC	276	40	11.8	6000	130	17.1	8.4	Approximated Ec
52	Kukay et.al. (2007)	HS-SCC	788.4	89.25	11.5		300	23.2	11.5	Average of 4 girders SCC
53	Ruiz et al. (2008) (SCCI-3)	HS-SCC	78	18	11.32	6536	290	25.1	12.4	Calculated Ec
54	Ruiz et al. (2008) (SCCI-5)	HS-SCC	78	18	11.42	6571	286	21.3	10.5	Calculated Ec
55	Ruiz et al. (2008) (SCCI-6)	HS-SCC	78	18	11.74	6680	286	24.1	11.9	Calculated Ec
56	Ruiz et al. (2008) (SCCI-7)	HS-SCC	78	18	11	6422	274	24.6	12.1	Calculated Ec
57	Ruiz et al. (2008) (SCCI-8)	HS-SCC	78	18	12.03	6785	274	23.5	11.6	Calculated Ec
58	Ruiz et al. (2008) (SCCIII-3)	HS-SCC	78	18	10.34	6186	270	28.2	13.9	Calculated Ec
59	Ruiz et al. (2008) (SCCIII-5)	HS-SCC	78	18	12.89	7079	255	28.2	13.9	Calculated Ec
60	Brewe and Myers (2010) (1)	HS-SCC	66	15	9.026	4635		66.5	32.8	Measured Ec
61	Brewe and Myers (2010) (2)	HS-SCC	69	15	9.026	4635		70.7	34.9	Measured Ec
62	Brewe and Myers (2010) (3)	HS-SCC	72	15	9.026	4635		64.5	31.9	Measured Ec
63	Brewe and Myers (2010) (4)	HS-SCC	75	15	9.026	4635		62.9	31.1	Measured Ec
64	Brewe and Myers (2010) (5)	HS-SCC	78	15	9.026	4635		67.4	33.3	Measured Ec
65	Brewe and Myers (2010) (6)	HS-SCC	81	15	9.026	4635		57.7	28.5	Measured Ec

**REFERENCES**

Tadros, M.K., Al-Omaishi, N., Seguirant, S.J., and Gallt, J.G., (2003). "Prestress losses in pretensioned high-strength concrete bridge girders." National Cooperative Highway Research Program Report 496, TRB. National Research Council, Washington, DC.

Roller, J. J., Russell, H. G., Bruce, R. N., and Alayam W. R., (2011). "Evaluation of prestress losses in high strength concrete Bulb-Tee girders for the Rigolets Pass bridge." PCI Journal, Vol. 56, No. 1, pp. 110-134.

Myers, J.J., Yang, Y., (2005). "High performance concrete for bridge A6130-Route 412 Pemiscot County, MO." UTC R39.

Barr, P., Fekete, E., Eberhard, M., Stanton, J., Khaleghi, B., and Hsieh, J.C., (200). "High performance concrete in Washington State SR 18/SR 516 Overcrossing: final report on girder monitoring." Report No. FHWA-RD-00-070, Washington State Transportation Center (TRAC).

Waldron, G. J., (2004). "Investigation of long –term prestress losses in pretensioned high performance concrete girders." Virginia Polytechnic institute and State University, Ph.D. Dissertation.

Trejo, D., Hueste, M., Kim, Y., and Atahan, H., (2008). "Characterization of self-consolidating concrete for design of precast prestressed bridge girders (Report 0-5134-2)." Texas A&M University, College Station, Texas.

Barr, P., Halling, M., Boone, S., Toca, R., and Angomas, F., (2009). "UDOT's calibration of AASHTO's new prestress loss design equations." UTCM 09-10. Utah State University.

Kukay, B., Barr, P. J., and Halling, M.W., (2007). "Comparison of time dependent prestress losses in a two-span, prestressed concrete bridge." ASCE Structure Congress. California, USA.

Myers, J.J. and Bloch, K.E., (2010). "Innovative concrete bridging systems for pedestrian bridges: implementation and monitoring." Missouri University of Science and Technology, National University Transportation Center (NUTC) Report R250.

Myers, J.J. and Brewe, J.E., (2010). "High-strength self-consolidating concrete girders subjected to elevated fiber stresses part I: prestress loss and camber behavior." PCI Journal, Chicago, Illinois, Vol. 55 No.4, pp. 59-77.

Ruiz, E.D., Floyd, R.W., Staton, B.W., Do, N.H., and Hale, W.M., (2008). "Prestress losses in prestressed bridge girders cast with self- consolidating concrete." MBTC-2071, USDO.

Gross, S.P., (1999). "Field performance of prestressed high performance concrete highway bridges in Texas." University of Texas at Austin, Ph.D. Dissertation.

APPENDIX F.  
HEALTH MONITORING SYSTEM  
(PCI BIG BEAM)

## **INTRODUCTION**

The materials presented in Appendix F is reproduced from a report submitted for the Precast/Prestressed Concrete Institute (PCI) Big Beam Competition which is part of the PCI Engineering student design competition for the 2016-2017 academic year. The objective of this contest consisted of designing, fabricating, and testing a PC/PS beam with a desired strength capacity set forth in the rules of the competition. As part of the competition, a report was submitted outlining the health monitoring system used to accurately measure the total prestress losses developed in HS-SCC used in the beam. The content in this appendix is related to the Paper IV of this dissertation.

## **HEALTH MONITORING SYSTEM**

A structural health monitoring system was implemented in this contest to measure the real behavior of PC/PS beam (19 ft length) constructed with high strength-self consolidating concrete (HS-SCC) and compare results to those predicted using design code equations. This section describes the instrumentations employed and results found.

### **Electrical Resistive Strain Gages**

Four strain gauges were installed on the prestressing tendons to measure the prestress losses (Locations B1, B2, M1, and M2 in Figure 1). A linear strain gauge, model ED-DY 125 BT-350/LE by Micro Measurements, was used in the beam. The gauge has a constantan foil with a tough, flexible, polyimide backing, with pre-attached leads and encapsulation. In addition, the gauge has a resistance of  $350 \pm 0.6\%$  ohms and a usable temperature range of  $-320$  °F to  $+400$  °F ( $-195$  °C to  $+250$  °C). The gauge has an overall length of 0.37 in. (9.4 mm) and an overall width of 0.16 in. (4.1 mm). One gauge



was applied to each strand at mid-span. A standard coating kit by Vishay Measurements was used to adhere and protect the gauges from the concrete. The tendons were sanded, wiped clean, and then applied with Teflon® tape and a rubber sealant. A neoprene rubber dough material was molded around the gauge.

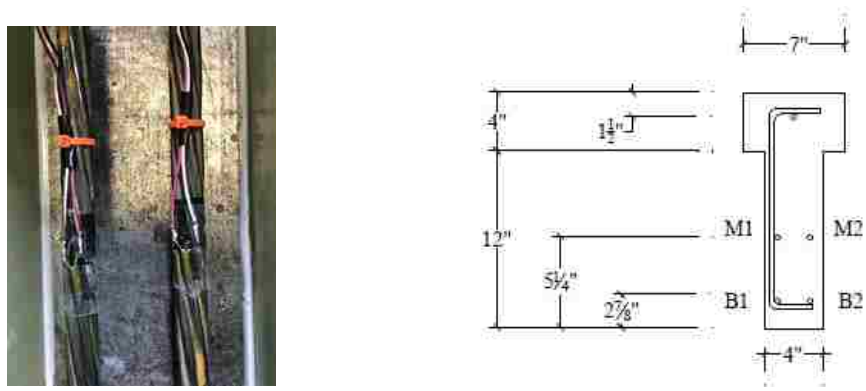


Figure F-1. Strain Gauge Installation Details

**Load cell**

A load cell (Figure 2) was used to verify the jacking force in the strand and any prestress losses before the strands were release. A 50-kips (22.4 kN) load cell was attached to one prestressing strand during the fabrication of beam and connected with data acquisition system for force monitoring.



Figure F-2. Load Cell Installation Detail

## Data Acquisition System

Data acquisition system (DAS) was used for strain and temperature data collection during the fabrication and testing of the beam. This DAS was custom-built by the researchers at Missouri University of Science and Technology. DAS was a compact RIO system with a NI9214 High Accuracy. Before the strands were tensioned, the strain gauges were connected to the DAS to start collecting the data. Figure 3 shows the DAS with computer collecting data at the precast plant.



Figure F-3. DAS Collecting Data at Precast Plant

## Thermocouples

A thermocouple is a temperature-sensing device that produces a voltage that is transmitted as a measure of temperature. Thermocouples are junctions of specific metals (wires) which have a predictable and repeated relation between voltage and temperature. These wires are coupled simply by tightly twisting thermocouple wire. Figure 4 shows these wires. The temperature range is reported to be  $-450$  to  $500$  °F ( $-267$  to  $260$  °C) by the manufacturer. The accuracy of measurements was stated to be  $\pm 1.8$  °F ( $\pm 1.0$  °C) for the thermocouple used.

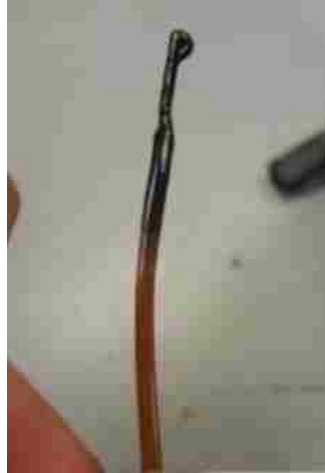


Figure F-4. Thermocouple Sensor

## **MATERIAL PROPERTIES**

### **Strands**

The low-relaxation strands of 0.5-in. diameter were selected as the prestressing reinforcement. These strands were passed through formwork holes at the end block. Then, the three strands were held at both ends inside the prestressing unit (Figure 10). The 0.5-in. diameter strands were tensioned to 32.32 kip to account for slippage losses. The specified jacking force was achieved after initial losses and this value corresponded to an initial stress of  $0.75 f_{pu}$  (31.98 kip/strand).

### **High Strength-Self Consolidating Concrete**

#### ***Mix Design***

Based on accessing to historical data of different concrete mix designs provided by the precast plant, HS-SCC mix was selected because of its robustness and excellent past performance. The concrete mixture met the beam design criteria (target compressive strength at release of 8280 psi and final compressive strength of 9810 psi). The HS-SCC

mixture was necessary to use because it is a highly flowable concrete that could spread easily into place due to the compacted shape and high prestressing steel congestion in the formwork, as well as to ensure the fabrication of a beam specimen with a smooth surface finishing free of honeycombing. A compressive strength of 9800 psi was specified as the target design value. The proportions of HS-SCC mix are presented in Table 1. It should be noted that Type-III cement was used as part of the mix to achieve a high early strength gain.

Table F-1. Mix Design Proportions

Material	Type	HS-SCC
Coarse Aggregate (lb/yd <sup>3</sup> )	<sup>3</sup> / <sub>4</sub> " Crushed stone, Grade E Limestone	1485
Fine Aggregate (lb/yd <sup>3</sup> )	Kaw Sand	1190
Water (lb/yd <sup>3</sup> )	Tap water	273
Cement (lb/yd <sup>3</sup> )	Portland Cement, Type III	850
Chemical Admixtures (oz/yd <sup>3</sup> )	1400 (Air entrainment)	15
	DCI (Mid-Range Water Reducer)	32
	585 (High Range Water Reducer)	102

### ***Fresh and Hardened Properties***

Fresh properties assessed were consistency, passing ability, filling ability, unit weight, temperature, and air content. Table 2 displays the fresh properties of HS-SCC mixture.

Table F-2. HS-SCC Fresh properties

Property	Specification	HS-SCC
Slump flow, in.	ASTM C1611	27
T50, sec		1.9
J-Ring, in.	ASTM C1621	26.5
Unit weight, lb/yd <sup>3</sup>	ASTM C138	142
Visual stability index (VSI)	ASTM 1611	0.5
Air content, %	ASTM C231	5.3
Concrete Temperature, °F	ASTM C1064	81

The HS-SCC's measured hardened properties included: compressive strength, modulus of elasticity (MOE), and the flexural strength of concrete. Two specimens were tested to obtain the compressive strength, modulus of elasticity and flexural strength of the mixture.



a)



b)



c)

Figure F-5. Mechanical Properties of Hardened Concrete. (a) Compressive Strength. (b) Modulus of Elasticity. (c) Modulus of Rupture (Flexural Strength)

Table F-3. Hardened Tests of HS-SCC

Tests	Test Method	Specimens	Concrete Age	Results
Compressive Strength, psi	ASTM C39	Cylinder (4 x 8 in.)	Release (3 day)	8280
			7 days	9250
			14 days	9810
Modulus of Elasticity, ksi	ASTM C469		Release (3 days)	4850
			14 days	5700
Modulus of Rupture, psi	ASTM C78		Beams (6 x 6 x 21 in.)	Release (3 days)
		14 days	1630	

## MEASUREMENT AND RESULTS

### Hydration profiles

The temperature development profiles were recorded from the start of pour using thermocouple wires. The thermocouples were embedded in two locations (First one at 1/3L and second one at 2/3L). Figure 6 presents hydration profiles of HS-SCC. The peak of the hydration curve occurred after 8 hours from adding water to cement. The maximum peak temperature was 109 °F (42.75 °C).

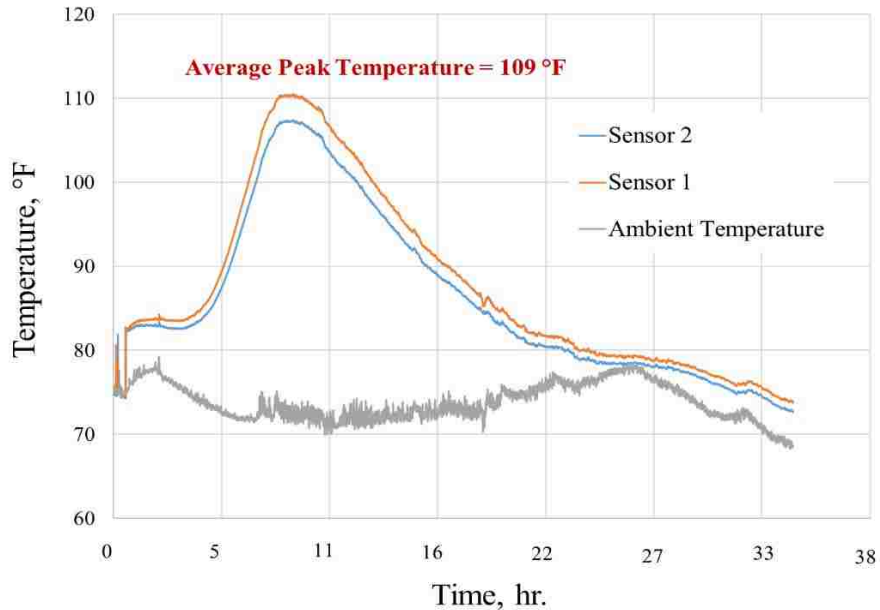


Figure F-6. Hydration Profile of HS-SCC Mixture

### Prestress Losses

The prestress losses are the losses that occur in the tensile stress of prestress steel. These losses affect a prestressed section's performance. The tensile force in the tendon does not remain constant from the recorded value in the jacking gauge. It changes with time. These losses are classified into two categories: immediate and either long-term or time-dependent. Immediate losses take place when prestressing the tendon and then transferring the prestress to the concrete member. Both the elastic shortening (ES) and anchorage slip are immediate losses. In contrast, losses produce by creep of the concrete (CR), shrinkage of the concrete (SH), and relaxation of the tendon (RE) are considered time-dependent losses. A simple equation is presented in Equation (1) used to determine the total Prestress losses within concrete beam (PCI, 2010).

$$\Delta f_{\text{Total}} = \Delta f_{\text{ES}} + \Delta f_{\text{SH}} + \Delta f_{\text{CR}} + \Delta f_{\text{RE}} \quad (1)$$

Measurements were successfully recorded on strands to measure prestress losses in the prestressing tendons using the strain gauges and the DAS. The measurements were divided into three stages. Chuck slippage measurement was conducted first using the strain gauges. As mentioned above, the chuck slippage was estimated using the load cell measurements. Results of both measurements are presented in Table 4. As a practical way to compensate the loss corresponding to chuck slippage, the strands were over stretch for slightly higher force than design. However, measurement showed that extra applied load was 1.35 kips and measured slippage was 1.68 kips. This indicates that there was a 1.06% loss caused by the chuck slippage.

Table F-4. Measured Loss Before Casting Caused by Chuck Slippage

Measured		Average, kips	Extra load for Chuck Slippage	Diff., kips	Loss, %
Using Load Cell, kips	Using Strain Gauges, kips				
1.64	1.72	1.68	1.35	0.33	1.06

Elastic shortening was measured next. These measurements were obtained by subtracting the strain reading immediately after release from the baseline strain measurement recorded just before release. The total prestress losses were obtained by comparing strain readings immediately before testing day to baseline strain measurement recorded after release. The measured total prestress loss was 32.3 % of the jacking stressing (202.5 ksi). Table 5 summarized the measured total prestress losses in addition to predicted total prestress losses using PCI models. In addition, Table 5 shows that the measured elastic shortening loss represents 38% of total prestress losses. From the ratio



of measured to predicted total prestress losses, 19% error can be estimated when predicted values use in the beam design.

Table F-5. Total Measured and Predicted prestress loss of HS-SCC beam

Loss Components	Measured		Predicted		Ratio (Meas. /Pred.)
	Loss as stress, ksi	% of Jacking force	Loss as force, ksi	% of Jacking force	
Chuck Slippage	2.16	1.06	----	----	----
ES	25.1	12.4	16.0	7.91	1.56
SH + CR + RE	38.3	18.9	38.9	19.2	0.98
Total Losses (TL)	65.56	32.36	54.9	27.11	1.19

## REFERENCES

- AASHTO LRFD, (2012). "Bridge Design Specifications and Commentary (6<sup>th</sup> Ed.)", customary U.S. units. American Association of State Highway and Transportation Officials. Washington, DC: AASHTO.
- Abid, S. R., Tayşi, N., and Özakça, M., (2016). "Experimental analysis of temperature gradients in concrete box-girders." *Construction and Building Materials*, V. 106, pp.523-532.
- ACI Committee 232, (2003). "Use of Fly Ash in Concrete." American Concrete Institute, Farmington Hills, MI.
- ACI Committee 237R, (2007). "Self-Consolidating Concrete," American Concrete Institute, Farmington Hills, MI.
- ACI Committee 318, (2014). "Building code requirements for structural concrete and commentary," American Concrete Institute, Farmington Hills, MI.
- ACI Committee 408R, (2003). "Bond and Development of Straight Reinforcing Bars in Tension," American Concrete Institute, Farmington Hills, MI.
- Alghazali, H. H., and Myers, J. J., (2015). "Creep and shrinkage of ecological self-consolidating concrete". In *Second International Conference on Performance-based and Life-cycle Structural Engineering (PLSE 2015) Proceedings*, Brisbane, Australia. St. Lucia, Australia: University of Queensland.
- American Coal Ash Association, (2016). "Coal ash recycling reaches 52 percent as production and use trends shift," <[www.aaa-usa.org](http://www.aaa-usa.org)>.
- ASCE Foundation, (2017). 2017-Infrastructure Report Card-Bridges. <https://www.infrastructurereportcard.org/wp-content/uploads/2017/01/Bridges-Final.pdf>.
- Aslani, F. and Nejadi, S., (2012). "Bond behavior of reinforcement in conventional and self-consolidating concrete." *Advance in Structural Engineering Journal*, Vol 15, No. 12, pp 2033-2051.
- ASTM C 618, (2017). "Standard Specification for Coal Fly Ash and Raw or Calcined Natural Pozzolan for Use in Concrete" ASTM, West Conshohocken, PA, 3 pp.
- Barr, P. J., Stanton, J. F., and Eberhard, M. O., (2005). "Effects of temperature variations on precast, prestressed concrete bridge girders." *Journal of Bridge Engineering*, V. 10(2), pp.186-194.
- Benhelal, E., Zahedi, G., Shamsaei, E., and Bahadori, A., (2013). "Global strategies and potentials to curb CO<sub>2</sub> emissions in cement industry." *Journal of Cleaner Production*, Vol. 51, 142-161.

- Daczko, J. A., (2012) "Self-consolidating concrete: applying what we know," CRC Press, 1<sup>st</sup> Ed.
- Damtoft, J. S., Lukasik, J., Herfort, D., Sorrentino, D., and Gartner, E. M., (2008). "Sustainable development and climate change initiatives." *Cement and concrete research*, 38(2), pp. 115–127.
- Elbadry, M. and Ghali, A., (1986). "Thermal Stresses and Cracking of Concrete Bridges." *ACI Journal (Technical Paper)*, Vol. 83, No. 6, pp. 1001-1009.
- Gross, S. P., (1999). "Field performance of prestressed high performance concrete highway bridges in Texas." PhD diss., University of Texas at Austin.
- Hawkins, N. and Kuchma, D., (2007). "Application of LRFD bridge design specifications to high-strength structural concrete: shear provisions (NCHRP 579)." *Transportation Research Board*, Washington, D.C.
- Headwaters Resources, (2017). Fly Ash for Concrete. Brochure.  
<http://flyash.com/data/upfiles/resource/Fly%20Ash%20for%20Concrete%202014.pdf>
- Imbsen, R. A., Vandershof, D. E., Schamber, R. A., and Nutt, R. V., (1985). "Thermal effects in concrete bridge superstructures." NCHRP Report No. 276. *Transportation Research Record*, Washington, DC.
- Khayat, K., and Mitchell, D. (2009). "Self-consolidating concrete for precast, prestressed concrete bridge elements (NCHRP 628)". *Transportation Research Board*, Washington, D.C.
- Larsson, O., and Thelandersson, S., (2011). "Estimating extreme values of thermal gradients in concrete structures," *Materials and Structures*, V. 44(8), pp. 1491-1500.
- Myers, J. J., and Bloch, K. E., (2010). "Innovative concrete bridging systems for pedestrian bridges: implementation and monitoring." *Missouri University of Science and Technology, National University Transportation Center (NUTC) Report R250*.
- Myers, J.J. and Yang, Y., (2004). "High performance concrete for Bridge A6130-route 412, Pemiscot County, MO," UTC R39.
- Nawy, E. G., (2009). *Prestressed Concrete: A Fundamental Approach*. (5<sup>th</sup> Ed.). Upper Saddle River, NJ: Prentice Hall.
- Onyemelukwe, O. and Kunnath, S., (1997). "Field measurement and evaluation of time-dependent losses in prestressed concrete bridges." *Florida Department of Transportation*, Project No. WPI 0510735.

Ortega C. A., (2012)., "Shear and fracture behavior of high-volume fly ash reinforced concrete for sustainable construction". Doctoral Dissertations. Missouri University of Science and Technology. Paper 2259.

Ozawa, K., Maekawa, K., Kunishima, M, and Okamura, H., (1989). "Development of high performance concrete based on the durability design of concrete structures." In Proceedings of the Second East-Asia and Pacific Conference on Structural Engineering and Construction (EASEC-2), Vol. 1, pp. 445-450.

Pandurangan, K., Kothandaraman, and Sreedaran, D., (2010). "A study on the Bond of Tension Lap Splices in Self Compacting Concrete." Materials and Structures Journal-RILEM, Vol. 43, pp 1113-1121.

Precast/Prestressed Concrete Institute, (2010). "PCI Design Handbook." MNL-120. (7<sup>th</sup> Ed). Chicago, IL.

Richardson, D.N., Beckemeier, K.W., and Volz, J.S., (2015). "Effects of powder additive on high volume fly ash mixtures." ACI Materials Journal. 112(4).

Rubenstein, M., (2012). "Emissions from the cement industry." The Earth Institute of Columbia University. <<http://blogs.ei.columbia.edu>>

Swenty M. K., (2003). "Contamination effects on the bond strength of reinforcing bars under pullout tests." Thesis. Missouri University of Science and Technology.

Tadros, M. K., Al-Omaishi, N., Seguirant, S. J., and Gallt, J. G., (2003). "Prestress losses in pretensioned high-strength concrete bridge girders". National Cooperative Highway Research Program Report 496 (NCHRP Report 496). Transportation Research Program. Washington, DC.

Wight, J.K., and MacGregor, J.G., (2009). "Reinforced Concrete Mechanics and Design (6<sup>th</sup> Ed.). Pearson-Prentice Hall.

Wilson, M. L., Kosmatka, S. H., (2011). "Design and control of concrete mixtures." Portland Cement Association, 15th edition. Washington, DC.

## VITA

Hayder Hussein Alghazali was born in Iraq. He earned his bachelor's degree in civil engineering from the University of Kufa, Iraq, in July 2004. He then attended the University of Technology in Baghdad, Iraq, and started his studies as a master's student of construction and materials engineering with emphasis on Structural Engineering. Hayder received his master's degree in March 2007. Over the course of his study, Hayder held the highest grade-point average and was awarded as the best outgoing student in the University of Technology. In 2012, Hayder received a prestigious fellowship from Iraq's government (HCED-Iraq Fellowship) to complete his PhD in the United States. He started his PhD program at the Department of Civil, Architecture, and Environmental Engineering at Missouri University of Science and Technology (Missouri S&T) under the supervision of Professor John J. Myers. Upon the completion of his PhD, He was selected as an excellent awardee of the Franklin-Cheng Teaching Scholar Program in 2017 to nourish graduate students to be recognized as academic leaders in the future. He had the opportunity to teach Structural Analysis I as an instructor and was a GTA for three semesters. At Missouri S&T, he received an Outstanding PhD Student Achievement Award, 2017 National Graduate Student Fellowship, ACI Missouri Chapter Honored Abdeldjelil "DJ" Belarbi Scholarship, and several travel grants and best poster awards. At Missouri S&T, Hayder was the president of Iraqi Student Association, vice president of the Chi-Epsilon Honor Society Organization, and vice president of the American Society of Civil Engineering (ASCE). Hayder is an affiliate member of ASCE, member in ACI, member in PCI, and a member in the Chi-Epsilon honor society.

In May 2018, he received his PhD in Civil Engineering from Missouri S&T.